GEOMECHANICAL DEVELOPMENT OF FRACTURED RESERVOIRS DURING GAS PRODUCTION

A Dissertation

by

JIAN HUANG

Submitted to the Office of Graduate Studies of
Texas A&M University
in partial fulfillment of the requirements for the degree of

DOCTOR OF PHILOSOPHY

Approved by:

Chair of Committee,	Ahmad Ghassemi
Committee Members,	Charles P. Aubeny
	Walter B. Ayers
	Stephen A. Holditch
	Jerome J. Schubert
Head of Department,	A. Daniel Hill

May 2013

Major Subject: Petroleum Engineering

ABSTRACT

Within fractured reservoirs, such as tight gas reservoir, coupled processes between matrix deformation and fluid flow are very important for predicting reservoir behavior, pore pressure evolution and fracture closure. To study the coupling between gas desorption and rock matrix/fracture deformation, a poroelastic constitutive relation is developed and used for deformation of gas shale. Local continuity equation of dry gas model is developed by considering the mass conservation of gas, including both free and absorbed phases. The absorbed gas content and the sorption-induced volumetric strain are described through a Langmiur-type equation. A general porosity model that differs from other empirical correlations in the literature is developed and utilized in a finite element model to coupled gas diffusion and rock mass deformation.

The dual permeability method (DPM) is implemented into the Finite Element Model (FEM) to investigate fracture deformation and closure and its impact on gas flow in naturally fractured reservoir. Within the framework of DPM, the fractured reservoir is treated as dual continuum. Two independent but overlapping meshes (or elements) are used to represent these kinds of reservoirs: one is the matrix elements used for deformation and fluid flow within matrix domain; while the other is the fracture element simulating the fluid flow only through the fractures. Both matrix and fractures are assumed to be permeable and can accomodate fluid transported. A quasi steady-state function is used to quantify the flow that is transferred between rock mass and fractures. By implementing the idea of equivalent fracture permeability and shape-factor within the

transfer function into DPM, the fracture geometry and orientation are numerically considered and the complexity of the problem is well reduced. Both the normal deformation and shear dilation of fractures are considered and the stress-dependent fracture aperture can be updated in time.

Further, a non-linear numerical model is constructed by implementing a poroviscoelastic model into the dual permeability (DPM)-finite element model (FEM) to investigate the coupled time-dependent viscoelastic deformation, fracture network evolution and compressible fluid flow in gas shale reservoir. The viscoelastic effect is addressed in both deviatoric and symmetric effective stresses to emphasize the effect of shear strain localization on fracture shear dilation. The new mechanical model is first verified with an analytical solution in a simple wellbore creep problem and then compared with the poroelastic solution in both wellbore and field cases.

ACKNOWLEDGEMENTS

It is my great pleasure to thank my committee members, colleagues, friends and family, whose support enables to me to complete this dissertation.

I owe my deepest gratitude to my Ph.D. supervisor, Dr. Ahmad Ghassemi, for his brilliant guidance and earnest help during the course of this project. I would like to thank my committee members, Dr. Aubeny, Dr. Ayers, Dr. Holditch, and Dr. Schubert for their serious supervision and profound advice in this research. This dissertation would not have been possible without their support throughout the whole process.

I would like to express my gratitude to the faculty and staff in the Petroleum Engineering Department for providing great atmosphere and enough assistantship for actualizing this research work.

I would also want to extend my appreciation to my friends and colleagues, Jun Ge, Chakra Rawal, Reza Safari, Sonia Wang, Vahid Serajian, Wenxu Xue and other members in the geomechanics group, who were always willing to help and offer their best suggestion.

Thanks also go to my parents, two elder sisters and their families, who give their warm-hearted encouragement in a number of ways. I offer my blessings to my parents-in-law for their solid support during this work.

Finally, thanks to my wife, Qin Wang, for her support and my little boy, Matthew Q. Huang, for giving me strength.

TABLE OF CONTENTS

Page

LIST OF FIGURES

Page

LIST OF TABLES

Page

CHAPTER I

INTRODUCTION

1.1 Overview

Methane is becoming an important and reliable global natural energy resource. Its demand and production have been significantly promoted over the last decade. As shown in the resource triangle (Figure 1), unconventional reservoirs, like coalbed methane (CBM), gas shale and gas hydrates, make up a great portion of the gas resources in the world (Holditch, 2009).

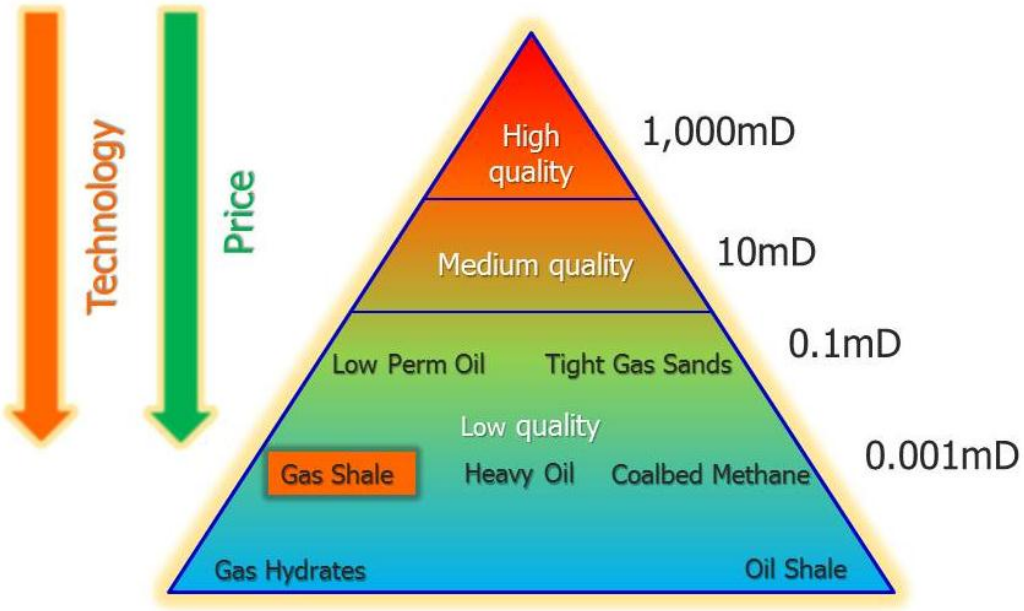

Figure 1 Resource triangle for gas (after Holditch, 2009)

Gas shale is one of the major unconventional reservoirs for natural gas, mostly methane. Currently, natural gas production is proven to be commercially possible in different gas

shale reservoirs across United States (Figure 2). Numerous operations have been conducted in Barnett shale, Eagle Ford shale and Haynesville shale.

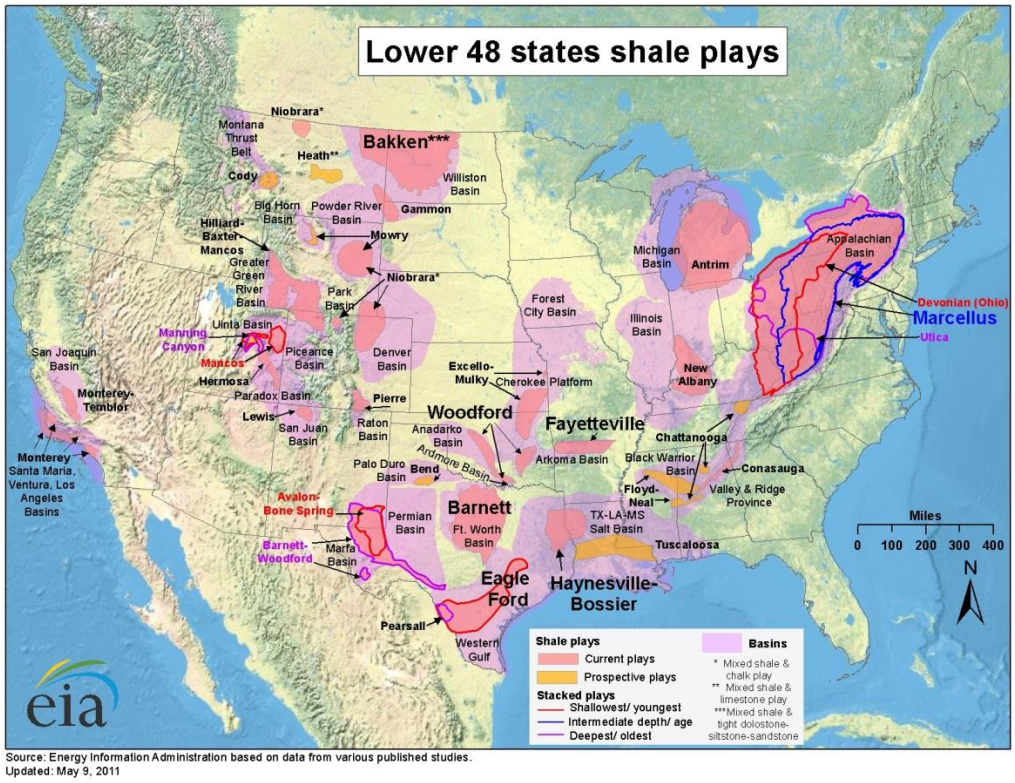

Source: Energy Information Administration based on data from various published studies.
Updated: May 9, 2011

Figure 2 Locations of major gas shale reservoirs in the U.S. (Energy Information Administration, 2012)

According to the updated discoveries of gas reserves and the application of innovative technologies in the development of gas reservoirs, annual natural gas production in the U.S. is believed to increase to 27.9 trillion cubic feet by 2035. Compared to the 21.6 trillion cubic feet gas production in 2010, a considerable 29% increase is projected in the following two decades. And the shale gas production is predicted to significantly increase from only 5.0 trillion cubic feet in 2010 to 13.6 trillion cubic feet in 2035,

which would supply 49% of domestic gas production in the U.S. by 2035 (Energy Information Administration, 2012). It is obvious that the promising development of gas shale reservoirs will contribute almost all the growth of domestic gas production in the U.S.

Among all the domestic gas shale reservoirs shown in Figure 2, the Barnett Shale is the most well studied and developed one. Its commercial gas production was first established by Mitchell Energy and Development Corporation in 1981 (Curtis, 2002; Martineau, 2007). Since then, numerous wells have been drilled by more than 200 operators, which resulted in a rapid increase of annual gas production in Barnett Shale in the past decade (Figure 3). By July 19, 2012, the total number of operated gas wells was 16,213 in this area (Texas Railroad Commission, 2012). Its gas production contributes nearly 9% domestic gas production at present (Energy Information Administration, 2012).

The Barnett Shale is located in the Fort Worth Basin, which is a north-south elongated basin in north-central Texas (Figure 2). Its productive part covers nearly 5,000 square miles (13,000 km^2), which characterizes it as the largest onshore natural gas field in the U.S. (Martineau, 2007; Zhao et al., 2007; Texas Railroad Commission, 2012). The major producing area of Barnett Shale is Newark East field (Hill and Nelson, 2000; Martineau, 2007). The Barnett Shale is of Mississippian age and was deposited in a foreland basin (Thompson, 1988; Jarvie et al., 2007; Pollastro et al., 2007; Zhao et al., 2007). In Barnett shale, organic-rich shale is the primary source and reservoir for gas accumulation (Montgomery et al., 2005; Pollastro, 2007). The depth of Barnett Shale ranges from

6,500 to 8,500 ft (1,981-2,591m) and its net thickness varies between 50 and 200 ft (15-61m) in Newark East field (Curtis, 2002).

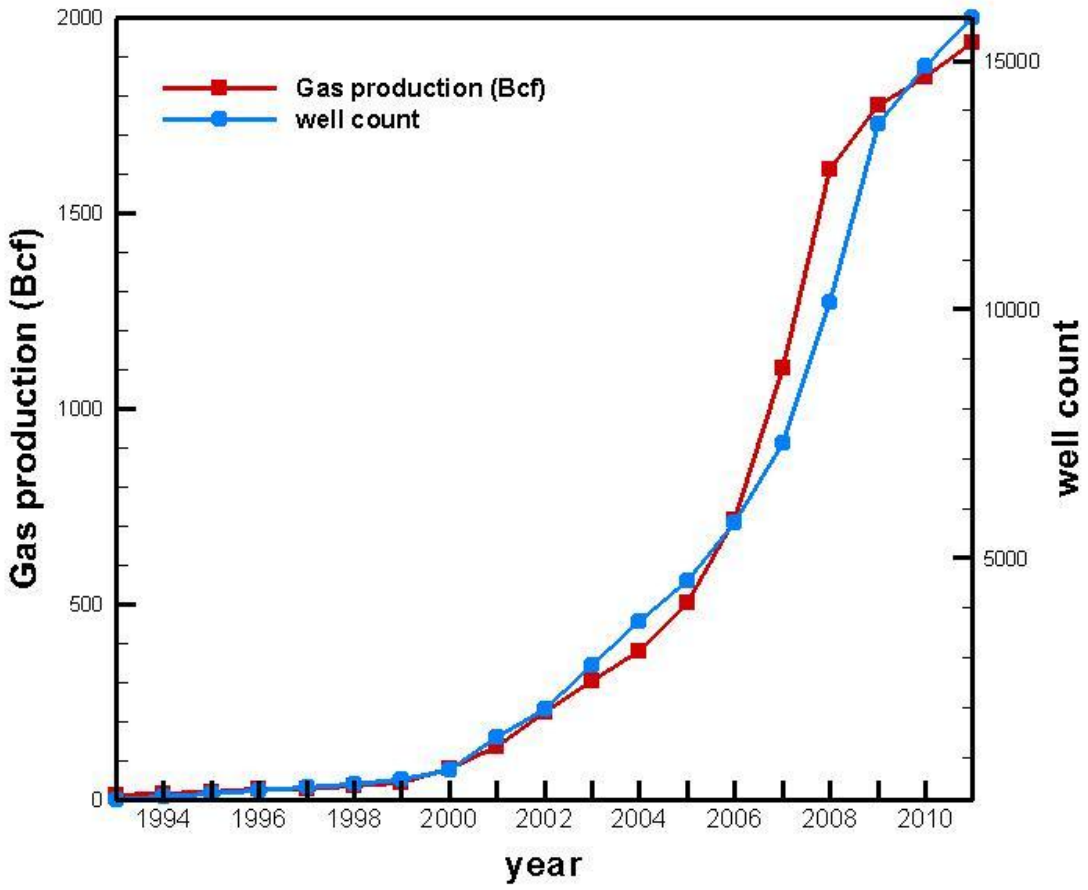

Figure 3 Gas production and well count history of Barnett Shale between 1993 and 2011 (from Texas Railroad Commission, 2012)

1.2 Motivation

Gas shale reservoirs are quite different among and within sedimentary facies. They differ in mineral composition or geological evolution, but they are all characterized by very fine grain texture and hence extremely low matrix permeability (Curtis, 2002; Vermylen, 2011). The matrix permeability of these shales typically varies from microdarcy to nanodarcy, which makes natural gas hard to be extracted from gas shale reservoir. Therefore, hydraulic fracturing and horizontal drilling are necessary for economic production from this kind of formation (Vanorsdale, 1987; Martineau, 2007; Cramer, 2008; Holditch, 2009; Vermylen, 2011; Sone, 2012).

Hydraulic fracturing treatment is handled by injecting water and/or gel into the wellbore at sufficiently high pressure and rate to create and propagate multiple fractures in the rock. During the hydraulic fracturing process, the contacted surface area of reservoir rock will be increased by connecting to pores and natural fractures, and hence, the pore pressure in the matrix rock adjacent to the fractures will be lowered and allow trapped gas molecules to flow into the wellbore. Fracturing can be carried out in horizontal wells, whose laterals vary between 1,000 and 3,500ft (304.8-1,066.8m). Such wells were first drilled in the Barnett Shale in 2003 (Martineau, 2007). Multi-stage hydraulic fracturing is performed in horizontal wells to maximize the drainage area of gas shale. By applying these advanced technologies, both the number of operations and the productivity in gas shale could be greatly promoted. However, many challenges remain unsolved in the fracture design and reservoir simulation work.

In practice, production from fractured stimulated wells of Barnett Shale rapidly decreases within several months after reaching early peak (Vermylen, 2011). In Figure 4, this type of decline takes place not only in the Barnett Shale but also in other gas shale plays, as the Woodford shale and so on (Kozier, 1984; McBane and Thompson, 1984; Vanorsdale, 1987; Baihly et al., 2010; Medeiros et al., 2010; Ambrose et al., 2011; Cook, 2011; Jayakumar et al., 2011; Martin et al., 2011). Among the four typical gas shale reservoirs (Figure 4), the Barnett Shale presents the lowest initial production rate but flattest curve. An important question is the cause(s) of the decline and how soon does it occur in a given well? Gas release mechanism and/or the time-dependent geo-mechanical behavior of the fractures more than likely play an important role.

The mechanical response of a gas shale reservoir to hydraulic fracturing is quite different from that of conventional or other unconventional resource. The conventional hydraulic fracturing is envisioned as a bi-wing shape fracture developed in the direction normal to the minimum principal stress. Whereas, according to the microseismic monitoring events, a complex fracture network is often developed in gas shale reservoirs, resulting from the interaction between natural fractures and the hydraulic fracture upon stimulation (Mayerhofer et al., 2006; Warpinski et al., 2008; Cipolla et al., 2009; Cipolla et al., 2010; Du et al., 2010; Chaudhri, 2012; Olorode et al., 2012; Zhou et al., 2012). This irregular and complicate fracture network should be considered in the reservoir simulator to predict future production and assess fracture design.

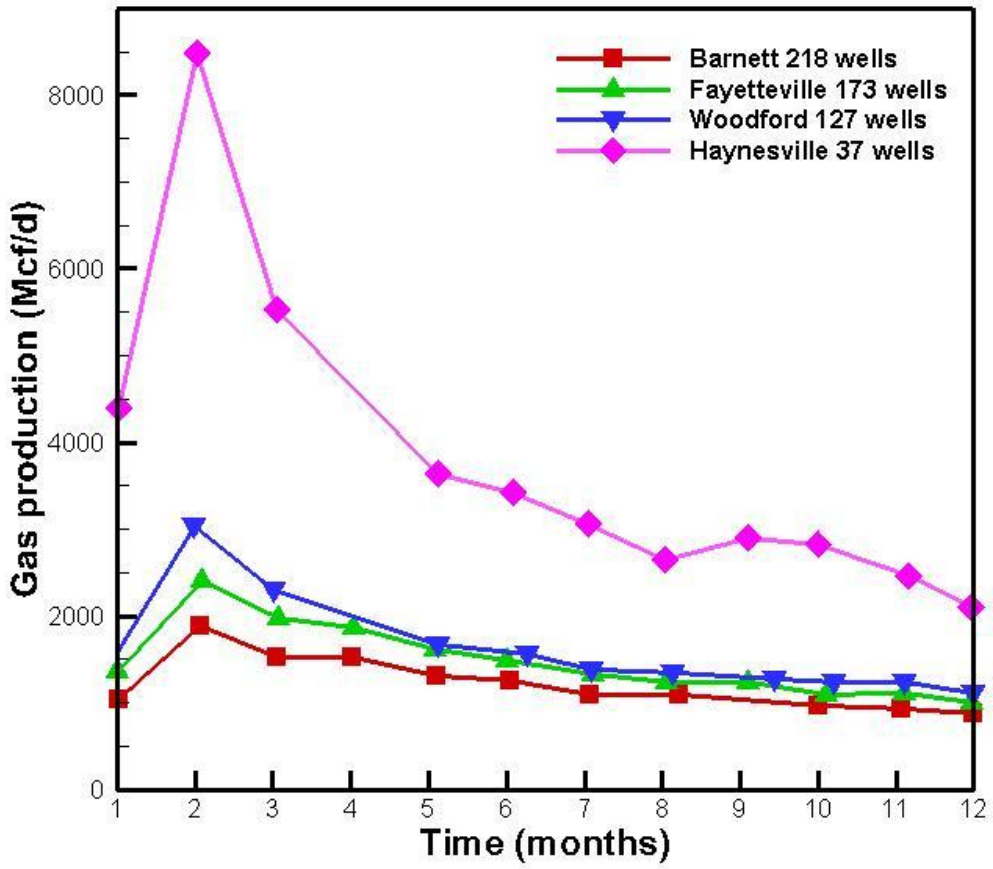

Figure 4 First year gas production rate from four different shale plays in 2008 (source: SPE 135555)

In many reservoir simulators for gas shale, only the elastic deformation of reservoir rock and fractures is considered. The elastic properties of the rock formations are obtained from core and log analyses prior to the simulation work. However, many experiment studies and field investigations indicated that shale undergoes viscoelastic deformation under in-situ stress condition (Olsson, 1980; Blanton and Teufel, 1983; Huang et al.,

1987; Warpinski, 1989; Zhou et al., 1992; Remvik, 1995; Bloch et al., 1999; Sone and Zoback, 2011). This time dependent response of reservoir rock is important in predicting reservoir performance, especially long-term performance. Neglecting this time-dependent reservoir behavior during production may underestimate reservoir compaction and lead to incorrect forecast production (Hagin and Zoback, 2007).

Due to the distinct nature of gas shale reservoirs, a full understanding of the mechanical behavior of gas shale is required to evaluate and enhance gas production. However, a comprehensive geomechanical reservoir simulator, which is capable of incorporating in-situ stress, gas desorption, reservoir compaction, nonideal fracture network and viscoelastic deformation, is not available in literature.

1.3 Previous work

1.3.1 Storage and flow mechanisms

Geomechanical reservoir performance and gas flow mechanism are critical issues for shale gas production, especially in fractured reservoirs. In addition, gas shale has a gas storage and release mechanism, which is quite different from that of conventional reservoirs that ought to be coupled to rock deformation. During gas production, pore pressure decrease along fractures (both natural and induced fractures) causes the increase of the effective in-situ stress. The increase in effective in-situ stress can compact the reservoir and reduce the fracture aperture and hence lower the reservoir permeability. However, the adsorbed gas is released from gas shale matrix and diffused into fractures

by the reduction of pore pressure. This gas desorption process results in the shrinkage of shale matrix and enhances the permeability in both matrix and fractures. The permeability evolution of gas shale reservoir is governed by these two coupled but competitive processes.

Gas in shale exists not only in small pores and open fractures (free gas), like conventional reservoirs, but is also adsorbed onto the surface of shale matrix. The amount of adsorbed gas is quantified through Langmuir isotherms (Bumb and McKee, 1988; Nguyen, 1989; Lane et al., 1990; Lu et al., 1995; Zhao et al., 2004; Ross and Bustin, 2007; Bustin et al., 2008; Lewis and Hughes, 2008; Zhang et al., 2008). Langmuir isotherms are commonly used to describe the relationship between the adsorption of methane molecules onto coal or shale surface and gas pressure at reservoir temperature. As a major gas storage mechanism in gas shale, releases of adsorbed gas should be considered in shale mechanical response. Neglecting the desorption process may result in significant errors in production prediction, especially for stimulated wells in gas shale reservoirs (Lane et al., 1990; Montgomery et al., 2005; Ross and Bustin, 2009; Schepers et al., 2009).

1.3.2 Dynamic permeability

The matrix porosity changes during production, causing permeability variation during gas production. Therefore, permeability changes in response to both sorption-induced matrix deformation and free gas depletion, and variation in in-situ stress conditions

(Seidle and Huitt, 1995; Palmer and Mansoori, 1998; Shi and Durucan, 2004; Cui and Bustin, 2005; Robertson and Christiansen, 2006, 2008; Zhang et al., 2008). Such coupling must be incorporated in rock deformation.

McKee et al. (1988) developed a relation between permeability change and stress variation based on Carmen-Kozeny equation.

$$\frac{k}{k_0} = \frac{e^{-3\bar{c}_p \Delta\sigma}}{1-\phi_0\left(1-e^{-\bar{c}_p \Delta\sigma}\right)} \tag{1.1}$$

where $\bar{c}_p$ is the average pore compressibility; $\Delta\sigma$ is the change of effective stress. In this model, the compressibility of solid grains is omitted by assuming it is very small compared to the porosity change in shale.

Liu and Civan (1995) proposed the following correlation by modifying the Kozeny equation.

$$\frac{k}{k_0} = \left((1-f)k_p + f\frac{\phi}{\phi^*} \right)^3 \tag{1.2}$$

where the dimensionless parameter k_p denotes the conductivity of fluid seepage within plugged pores; f represents the fraction of unplugged pore throats; ϕ^* is the porosity which is affected by mechanical loading. In this model, the particle plugging effects are taken into consideration. If the flow factor, f, is set to 1, this model is exactly the same as the cubic function.

Seidle and Huitt (1995) attributed all the real time porosity variation to the sorption-induced strain by excluding elastic strain of the matrix. This assumption might not be

proper for gas shale, whose desorption gas content is not as significant as that of coalbed methane.

$$\frac{\phi}{\phi_0} = 1 + \left(1 + \frac{2}{\phi_0}\right) C_m V_m \left(\frac{bp_0}{1+bp_0} - \frac{bp}{1+bp}\right) \tag{1.3}$$

$$\frac{k}{k_0} = \left\{1 + \left(1 + \frac{2}{\phi_0}\right) C_m V_m \left(\frac{bp_0}{1+bp_0} - \frac{bp}{1+bp}\right)\right\}^3 \tag{1.4}$$

where ϕ is the porosity at pressure p; ϕ_0 is the initial porosity at initial reservoir pressure p_0; C_m represents the swelling coefficient of matrix; V_m is maximum amount of adsorption; b is a Langmuir constant.

The Palmer-Mansoori model (1998) took both stress-caused elastic deformation and desorption-induced swelling into consideration. This model was developed for uniaxial strain conditions, and its expression was given as:

$$\frac{\phi}{\phi_0} = 1 + \frac{c_m}{\phi_0}(p - p_0) + \frac{\varepsilon_l}{\phi_0}\left(\frac{K}{M} - 1\right)\left(\frac{bp}{1+bp} - \frac{bp_0}{1+bp_0}\right) \tag{1.5}$$

$$\frac{k}{k_0} = \left\{1 + \frac{c_m}{\phi_0}(p - p_0) + \frac{\varepsilon_l}{\phi_0}\left(\frac{K}{M} - 1\right)\left(\frac{bp}{1+bp} - \frac{bp_0}{1+bp_0}\right)\right\}^3 \tag{1.6}$$

where c_m is the compressibility of pore space; ε_l represents the maximum volumetric strain when pressure goes to infinite; K and M denote the rock's bulk and constrained axial modulus respectively. The second term in the right hand side (RHS) of equation

1.05 represents the mechanical deformation caused by the change of effective stress, while the third term reflects the desorption-induced matrix swelling.

The Shi-Durucan model (2004) was derived for uniaxial strain conditions.

$$\frac{k}{k_0}=\exp\left\{3c_f\left[\frac{\nu}{1-\nu}\left(p-p_0\right)+\frac{E\varepsilon_l}{1-\nu}\left(\frac{p_0}{P_L+p_0}-\frac{p}{P_L+p}\right)\right]\right\} \tag{1.7}$$

where c_f is the compressibility of cleat volume; ε_l represents the maximum volumetric strain when pressure goes to infinite; E is Young's modulus and ν denotes Poisson's ratio.

The Cui-Bustin model (2005) showed porosity was a general function of bulk modulus of rock and pore space, mean stress and pore pressure:

$$\frac{\phi}{\phi_0}=\exp\left\{\left(\frac{1}{K}-\frac{1}{K_p}\right)\left[\left(\bar{\sigma}-\bar{\sigma}_0\right)-\left(p-p_0\right)\right]\right\} \tag{1.8}$$

$$\frac{k}{k_0}=\exp\left\{-\frac{3}{K_p}\left[\left(\bar{\sigma}-\bar{\sigma}_0\right)-\left(p-p_0\right)\right]\right\} \tag{1.9}$$

where K_p denotes the bulk modulus for the pore space; $\bar{\sigma}$ and $\bar{\sigma}_0$ are the current and initial mean stresses respectively. Assuming K and K_p are constants, this model is derived by integrating the following equation with time:

$$\frac{d\phi}{\phi}=\left(\frac{1}{K}-\frac{1}{K_p}\right)\left(d\bar{\sigma}-dp\right) \tag{1.10}$$

Under the uniaxial strain conditions, this model can be transformed to a function which is close to Palmer-Mansoori model.

The Robertson-Christiansen model (2006) was set up for hydrostatic stress condition to resemble the lab conditions for permeability measurement of core samples, while the overburden pressure was assumed be a constant.

$$\frac{k}{k_0} = \exp\left\{3c_0 \frac{1-e^{\alpha(p-p_0)}}{-\alpha} + \frac{9}{\phi_0}\left[\frac{1-2\nu}{E}(p-p_0) - \frac{\varepsilon_l P_L}{P_L+p_0}\ln\left(\frac{P_L+p}{P_L+p_0}\right)\right]\right\} \qquad (1.11)$$

where c_0 is the initial fracture compressibility; α is the change rate of fracture compressibility. Without specifying any stress conditions, a general porosity model, taking both in-situ stress conditions and gas desorption mechanisms into account, was developed within the framework of Biot's poroelasticity theory (Biot, 1935) and was utilized in the numerical model of this work.

1.3.3 Analytical and numerical simulators

Numerous analytical and semi-analytical models are available in literature to investigate the flow behavior in reservoirs using the dual continuum concept (either a dual porosity or dual permeability model). Some analytical models treated a fractured reservoir as an equivalent homogeneous porous medium (Bumb and McKee, 1988; Carlson, 1994) or just modeled a single fracture performance in this formation (Gringarten et al., 1974; Nobakht and Clarkson, 2012b, 2012a). Xu et al. (2009) developed a hydraulic fracture network model to handle the growth of multiple fractures in gas shale reservoir and

solved it analytically or semi-analytically based upon a quasi-steady fluid flow approximation. Xu et al. (2011) presented several analytical models to estimate the gas production from fractured shale gas reservoirs and validated them with commercial simulators. Ambrose et al. (2011) provided hybrid methods by combining both analytical and empirical approaches to predict post-fracturing well performance in both homogeneous and heterogeneous cases. However, gas desorption was omitted in these analytical models.

Several more advanced analytical and semi-analytical were developed to capture fracture complexity and/or gas desorption. Medeiros et al. (2006) discretized the highly heterogeneous reservoir into grids to represent substructures by assuming local homogeneity and coupling the analytical and pressure transient solutions within each grid. Samandarli et al. (2011b) used the analytical solution of dual porosity model, in which fractures are the only conduit for fluid flow and rock matrix acts as source of fluid, to history match the production of fractured gas shale reservoirs and took gas properties variation and gas desorption into account. Thompson et al. (2011) utilized the trilinear flow model to predict production in multi-fractured horizontal wells and simulated regional permeability within stimulated reservoir volume (SRV) and adsorbed gas contribution. Zhou et al. (2012) proposed a semi-analytical model on discretized fracture plane to manage the local heterogeneity and non-darcy flow was considered. Whereas, nonlinear gas compressibility, fluid exchange between matrix and fracture and fracture aperture variation still remained unsolved in these models. By assuming constant fracture aperture and regular-shaped fracture network, another widely used

model in literature is analytical dual porosity (Gatens III et al., 1985; Lee and Gatens III, 1985; Gatens III et al., 1989; Spivey and Semmelbeck, 1995; Bello and Wattenbarger, 2008; Lewis and Hughes, 2008; Samandarli et al., 2011a).

Due to the limitation in fully describing the gas flow mechanism and pressure dependent reservoir response to gas depletion, more and more numerical simulators have been constructed and applied in the studies of gas shale and other unconventional reservoirs. Some numerical models were successfully used in history match of gas production (King, 1993; Freeman et al., 2009; Freeman et al., 2010; Jayakumar et al., 2011; Olorode et al., 2012). However, only fluid transport is considered during gas production by neglecting rock deformation, which means an uncoupled or partially couple process is considered. In reality, pore pressure variation leads to either expansion or contraction of the rock and will affect fracture aperture during reservoir life. It is inadequate to separate one from the other in reservoir simulation. This coupling is considered by poroelastic theory.

1.3.4 Coupled flow/rock deformation for shale

Biot (1935; 1941) was the first to propose a linear poroelastic theory to describe the coupled hydro-mechanical process during rock consolidation. Rice and Cleary (1976) took fluid compressibility into account and extended this theory to both drained and undrained condition. Detournay and Cheng (1993) applied this theory to solve various boundary value problems and provided lots of analytical and numerical solutions, which

can be used to verify our numerical model. Heidug and Wong (1996) proposed a fully coupled constitutive model to simulate hydration swelling of water-absorbing rocks by using non-equilibrium thermodynamics and Gibbs-Duhem equation to quantify the swelling, osmosis and solute flow processes. Diek and Ghassemi's work (2004) extended this chemo-poroelastic theory by fully coupling the four processes of mechanical, hydraulic, chemical and thermal in transversely isotropic porous media saturated by a compressible and thermally expansible solution composed of a solvent and one or more solute. Zhang et al. (2008) and Zhao et al.(2004) developed Biot-type models to simulate gas transportation and coupled matrix deformation for coal seam. However, only an ideal gas law was used in their model, and gas compressibility was ignored. Huang and Ghassemi (2011) improved their work by utilizing a real gas law and focusing on adsorbed gas within shale matrix. In that work, a non-linear fully coupled poroelastic finite element model was constructed and then applied in performing poroelastic analysis of gas production from gas shale. However, fracture network and deformation was not taken into account in the production process.

1.3.5 Fracture network consideration

Many numerical methods have been developed to study the fracture deformation and interaction between natural and hydraulic fractures. The discrete fracture network (DFN) approach is a widely used approach for handling fracture propagation and interaction (Lee et al., 1999; Dershowitz et al., 2000; Karimi-Fard and Firoozabadi, 2001; Sarda et al., 2001; Sarda et al., 2002; Karimi-Fard and Firoozabadi, 2003; Tamagawa and

Tezuka, 2004; Li and Lee, 2006; Kim and Schechter, 2007; Li and Lee, 2008; Bang and Jeon, 2009; Kim and Schechter, 2009; Meyer and Bazan, 2011; Moinfar et al., 2011; Moinfar et al., 2012; Zeng et al., 2012). However, when using the DFN within the framework of FEM and FDM, the matrix domain needs to be explicitly discretized. This requires a refinement of mesh which could significantly increase the computational density and time consumption and hence withdraws its applications in highly fractured reservoirs.

Displacement-discontinuity method (DDM) is another popular way to model the fracture deformation (Wardle and Enever, 1983; Priest, 1984; Wardie, 1984; Curran and Carvalho, 1987; Nakagawa et al., 1999; Yacoub and Curran, 1999; Lavrov et al., 2005; Regueiro, 2006; Tao et al., 2009; Zhou and Ghassemi, 2009; Marji et al., 2010; Verde and Ghassemi, 2013). This is an indirect boundary element method by assuming continuous stress field whereas discontinuous displacement across fracture. The DD approach addresses the matrix description implicitly so mesh refinement is not an issue. An accurate analytical solution for displacement discontinuity in a homogeneous rock system is a prerequisite for the application of this method.

The continuum method is appropriate for simulating fracture deformation in naturally fractured medium. In the conventional continuum approach, a fractured reservoir was treated as an equivalent homogeneous porous medium. Regarding the existence of fractures, faults or cracks, this approach was not applicable for highly heterogeneous porous medium (Lee et al., 1999) like gas shale. Instead, the dual continuum concept would be a suitable candidate to quantify fluid flow within fractured porous medium.

The dual continuum concept was introduced by Barenblatt et al. (1960) and first applied to reservoir simulation by Warren and Root (1963). In this method, the fractured reservoir was treated as a dual continuum. Two independent but overlapping grids (or elements) were used to represent the fractured reservoir: one was the matrix elements denoting the reservoir deformation and fluid flow within the matrix domain while the other was the fracture elements to simulate fluid flow only through them. The fluid flow in fracture element and matrix element was independent from each other and only coupled by a transfer term, which was used to quantify the fluid exchange between matrix block and its adjacent fractures. These authors built the mathematical framework for modeling single-phase flow within fractured medium and simulating its interaction between fractures and matrix. Later, this approach was extended to simulate multiphase flow (Kazemi et al., 1976; Rossen, 1977; Saidi, 1983). Since then, a number of reservoir simulators have been constructed by using the dual continuum concept in either finite difference method (FDM) or finite element method (FEM). Kazemi et al. (1992) incorporated an empirical transfer function (pseudo-capillary-pressure function) into dual porosity simulator to solve field problems.

Lee et al. (1999) applied both the dual porosity model and discrete fracture network model to study the fluid flow in fractured aquifers and established the correlation between the two methods. Ganzer (2002) proposed to keep the elements without fractures as a conventional single permeability grid to get the discretized fractured reservoir more close to the real geological formation. Guo et al. (2004) constructed a multi-medium model by modeling the mass transfer between matrix block and macro-

fracture through the micro-fracture network. Ramirez et al. (2009) derived a transfer function to quantify the fluid exchange between matrix and fractures which was driven by capillary pressure, gravity and diffusion in dual porosity model. In that work, the matrix block was in sugar-cube or match-stick shape. Al-kobaisi et al. (2009) provided an analytical approximation of the transfer function to the differential equation and adjust the transfer function to investigate the surfactant flow and early mass transfer in matrix and fractures. Zhang et al. (2009) upscaled the DFN model to dual porosity model by using matrix-fracture coupling term (sigma). Zhang et al. (2011) modeled the fracture permeability with different fracture connectivity pattern on a cell-by-cell basis and implemented shear displacement induced fracture permeability change into dual permeability model and used the effective permeability concept to simulate the mechanical deformation of both connected and unconnected fractures during waterflooding.

Note that the dual continuum concept can be classified into two different approaches in literature: 1) dual porosity model; 2) dual permeability model (DPM). For the dual porosity model, fractures need to be connected as the fluid is assumed to flow only through fractures and rock matrix only acts as source of fluid (da Silva, 1989; Fung, 1993; Gurpinar et al., 1999; Lee et al., 1999; Gurpinar and Kossack, 2000; Donato et al., 2003; Guo et al., 2004; Al-kobaisi et al., 2009; Ramirez et al., 2009; Zhang et al., 2009).

Blaskovich et al. (1983) and Hill and Thomas (1985) improved the dual porosity model by introducing fluid interaction between matrix blocks, which is the key divergence between dual porosity model and dual permeability model. Within the DPM framework,

both matrix and fractures are assumed to be permeable and the fluid can be transported via these two (Blaskovich et al., 1983; Hill and Thomas, 1985; Dean and Lo, 1988; Chawathe et al., 1996; Al-Huthali and Datta-Gupta, 2004; Cicek, 2005; Ding et al., 2006; Alamdari et al., 2012). By allowing fluid exchange between adjacent matrix block, these simulator, developed with finite difference method, can provide a more accurate simulation of the flow path than the dual porosity model.

In the early dual permeability models (Blaskovich et al., 1983; Hill and Thomas, 1985), fluid flow, which was uncoupled or partially coupled with rock deformation, was modeled solely in the reservoir simulation. The interactions between fluid flow and rock deformation were usually neglected. Aifantis (1977) proposed a couple model in dual porosity/permeability medium for single phase flow by adopting mixture theory, but no unified formulation was given. Bai et al. (1993) and Ghafouri and Lewis (1996) implemented the dual permeability model into a fully coupled finite element model by taking both displacement and pore pressure as primary variables in the formulation. Lewis and Ghafouri (1997) further extended this approach for modeling multiphase flow in a heterogeneous media and revealed the strong influence of the coupling process between fluid flow and rock deformation by comparing the numerical results with those of uncoupled simulators. Lamb et al. (2010) modified this model to address displacement discontinuity by incorporating extended finite element method (XFEM). Huang and Ghassemi (2011) proposed a fully coupled poroelastic model by using a real gas law and focusing on the impact of adsorbed gas on matrix porosity and permeability evolution. In that work, a non-linear fully coupled poroelastic finite element model was

developed and applied in performing poroelastic analysis of gas shale deformation. However, that model was built up on a single porosity basis and fluid transport equation for fractures was not given. Compared with DFN and dual porosity model, DPM can overcome the limitations in mesh refinement and fracture network connectivity. However, the interactions between nonlinear gas compressibility, gas desorption, pressure dependent fracture aperture and irregular-shaped fracture network, which coexist within gas shale reservoirs, cannot be simultaneously captured by these previously mentioned models.

1.4 Objective

Within fractured reservoirs, coupled processes between matrix deformation and fluid flow are important for predicting reservoir behavior, pore pressure evolution and fracture closure. However, it remains difficult to model fluid flow interaction between fractures and matrix and displacement discontinuity simultaneously in reservoir simulation.

The primary objective of this work was to develop a numerical model, based on dual permeability method, for simulating coupled fluid flow and geomechanical processes associated with gas shale development. To accomplish this goal, I

1) developed constitutive relationships for the coupled gas flow and rock deformation within fractured reservoirs to simulate elastic and viscoelastic effects and compressible fluid flow mechanics;

2) investigated the interactions among rock matrix deformation – pressure dependent fracture geometry – gas flow physics that can be incorporated into numerical simulators;

3) conducted numerical studies for various degrees of branching and interconnectivity of fracture networks and identified reservoir properties that cause the loss of fracture area and conductivities and hence impact production.

CHAPTER II

FULLY COUPLED POROELASTIC MODEL

Desorption is a major mechanism for gas production for shale reservoirs and can impact the mechanical reservoir response. To study the coupling between gas desorption and rock matrix/fracture deformation, a poroelastic constitutive relation is developed and used for deformation of gas shale. Local continuity equation of dry gas model is developed by considering the mass conservation of gas, including both free and absorbed phases. In contrast to previous works which use an ideal gas law and neglect the gas compressibility, a real gas law is employed herein by using the Z-factor and gas formation volume factor Bg. The absorbed gas content and the sorption-induced volumetric strain are described through Langmiur-type equation. Without assuming a particular stress conditions, a general porosity model that differs from other empirical correlations in the literature, is developed and utilized in a finite element model to coupled gas diffusion and rock mass deformation. As the natural gas properties vary with pressure and appear in the stiffness matrix, a nonlinear iterative method is incorporated in the finite element procedure. The model is used to study the time evolution of gas desorption, stress-dependent porosity and permeability during gas depletion process. The model is verified through the comparison with the analytical solution for the methane depletion of the Barnett shale. In chapter 3, this model will be further developed by incorporating dual permeability concept to study the gas desorption influences, the dynamic fracture closure and gas flow in naturally fractured reservoir.

2.1 Introduction

Gas shale is a major unconventional source of natural gas production. Gas shales have ultra-low permeability thus necessitating hydraulic fracturing from horizontal wells. However, most often production from fractured wells rapidly declines (Lane et al., 1990; Montgomery et al., 2005; Ross and Bustin, 2009; Schepers et al., 2009). In many cases this can be attributed to the time-dependent behavior of the rock fracture/matrix system related to coupled diffusion/deformation phenomena and particular rheological characteristics.

Gas in shale is stored not only in small pores and open fractures (free gas), as conventional reservoirs, but is also adsorbed onto the pore surface or is confined onto the rock grains in shale matrix (Figure 5) as solid solution. Based on field and lab data of Devonian shales, 50% or more of gas in place may be stored as adsorbed gas (Kuuskraa et al., 1985; Lane et al., 1989; Lane et al., 1990).

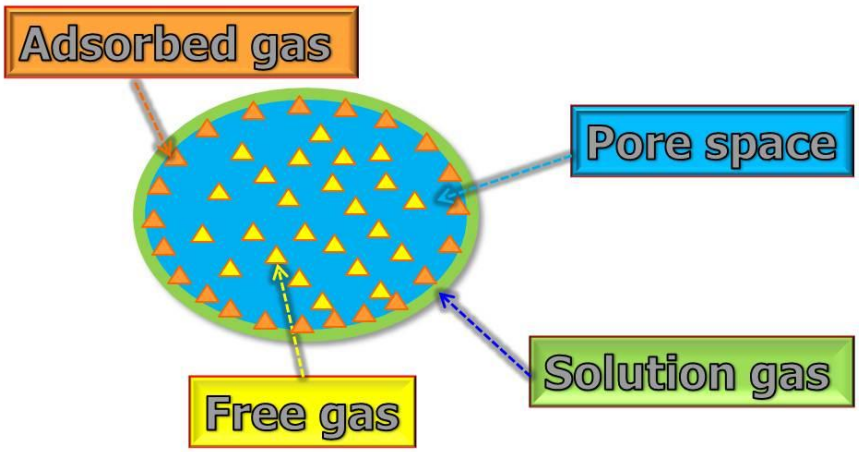

Figure 5 Illustration of the coexistence of free gas (yellow), adsorption gas and solution gas (green) in gas shale reservoir in the pore space.

Langmuir isotherms is always employed to quantify the amount of adsorbed gas in literature (Bumb and McKee, 1988; Nguyen, 1989; Rushing et al., 1989; Lane et al., 1990; Lu et al., 1995; Zhao et al., 2004; Ross and Bustin, 2007; Bustin et al., 2008; Lewis and Hughes, 2008; Zhang et al., 2008). Langmuir isotherms are empirical correlations to model the gas adsorption capacity of coal or shale without temperature variation, which is depended on reservoir pressure and petrophysical properties. As an important gas storage mechanism in gas shale and some other unconventional reservoirs, release process of adsorbed gas need to be implemented into numerical reservoir simulator to accurately capture gas store and flow mechanics. Neglecting desorption process of adsorbed gas may eventually lead to significant errors in predicting reservoir performance and final production, typically for stimulated wells in gas shale (Lane et al., 1990; Montgomery et al., 2005; Ross and Bustin, 2009; Schepers et al., 2009).

Gas transportation and coupled hydromechanical process have been studied for coal seam (Zhao et al., 2004; Zhang et al., 2008). A similar approach is adopted in this dissertation and is applied to gas shale. In contrast to previous works, which use an ideal gas law and ignore gas compressibility (Zhao et al., 2004; Zhang et al., 2008) in the gas transport equation, a real gas law is applied herein by considering the pressure-dependent Z-factor and gas formation volume factor Bg. Also, a general porosity model that is different from other empirical correlations in the literature (Seidle and Huitt, 1995; Palmer and Mansoori; Shi and Durucan, 2004; Cui and Bustin, 2005; Robertson and Christiansen, 2006, 2008) is derived and used in our finite element model. The

porosity is treated as a function of reservoir pressure, rock mechanical properties, and gas desorption isotherm parameters in this study.

The main work in this chapter is to construct a fully coupled poroelastic model that considers the time evolution of gas desorption, stress-dependent permeability and porosity during gas depletion process to quantify the influences of gas sorption induced fracture/matrix deformation under the in-situ stress conditions. Then, the model is further improved to handle complex fracture network in the following chapters.

2.2 Gas adsorption

Adsorption refers to the process that gas molecules, like methane and carbon dioxide, are attracted to surface of a porous medium, like gas shale and CBM. Desorption is the opposite of adsorption, during which gas molecules are released from the surface as a result of a pressure drop. These surface phenomena are highly related to the internal surface area of solid. Normally, for a porous medium with very small pore space (nanometer-scale in Figure 6), its internal surface area will significantly increase with the decrease of pore size and hence exhibits the rise of gas adsorption capacity. The adsorption ability of a porous rock is also dominated by its composition, as the weight percent of organic kerogen. Gas shale has both tiny pore size (nanometer-scale) and high concentration of organic kerogen. Thus, gas shale commonly demonstrates greater gas adsorption potential compared to the conventional reservoirs. Adsorption gas always plays an important role in the estimation of gas-in-place and actual production from gas shale reservoirs. Its release also impact rock mechanical response of reservoir.

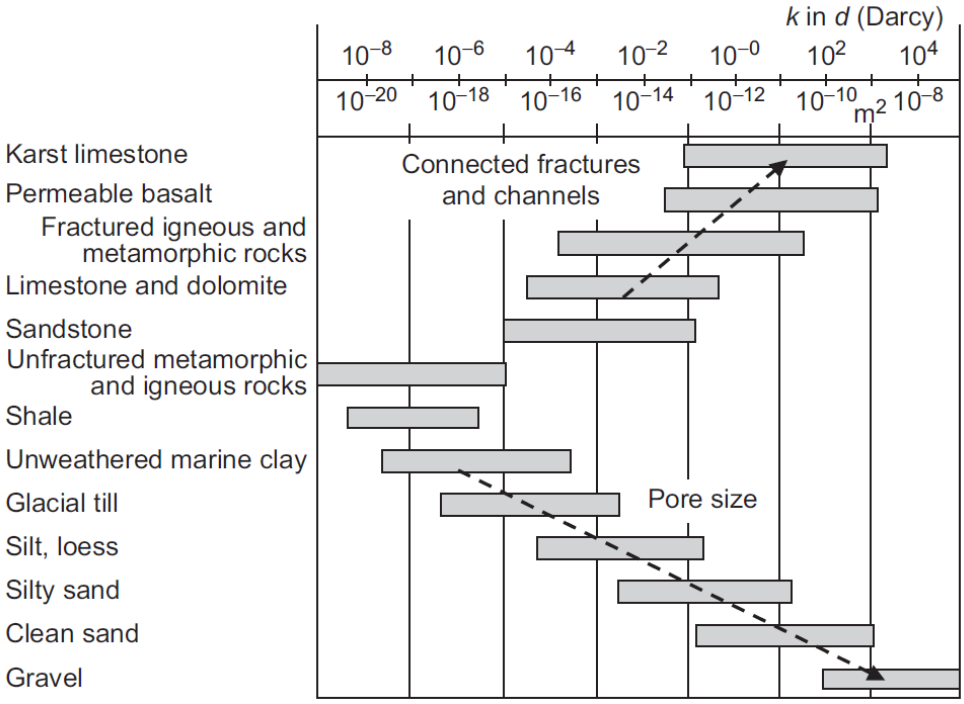

Figure 6 Magnitude ranges of permeability and pore size trends for different rock types (Schön, 2011)

To quantify the amount of adsorbed gas in a rock, Langmuir isotherms are widely used in biology, chemistry, petroleum engineering and so on. They are founded by measuring the amount of adsorption gas under different pressures while keeping invariant temperature and fitting the results to a theoretical model. Their shape and magnitude are determined by the adsorption capability and mechanism of the medium. Langmuir (1916) first proposed a semi-empirical isotherm to model gas adsorption. His model was derived based on the kinetic mechanism of gas motion and assumed that gas molecules could be only adsorbed on to a single layer and there was no interaction between neighboring molecules. In literature, his model is usually named as Langmuir or Type I

isotherm (Figure 7). The fitted curve of Langmuir isotherm can be described through the following two-parameter equation:

$$V(p) = \frac{V_L p}{p + P_L} \tag{2.1}$$

where $V(p)$ is the volume of adsorbed gas per unit mass of medium; V_L and P_L represent Langmuir volume and pressure constant respectively; p is the gas pressure in pore space. And this model is only valid for the material that presents a monolayer of adsorbed gas molecules for a specific gas.

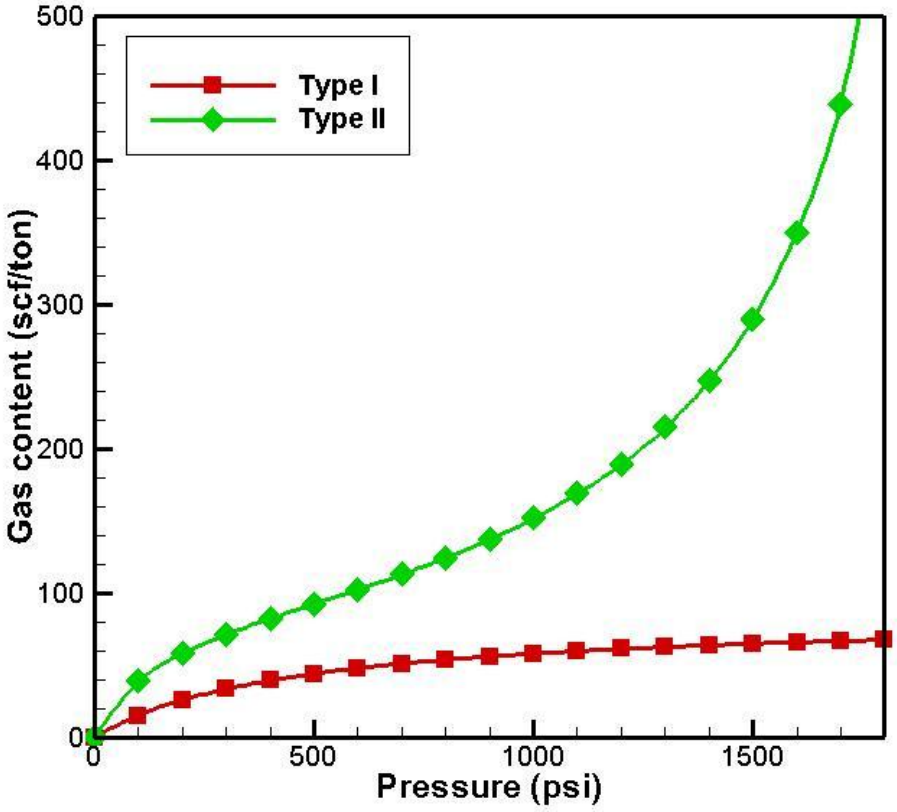

Figure 7 Type I and II adsorption isotherms

In reality, it is highly possible that gas molecules can be attracted onto the already adsorbed molecules to form multilayers of adsorption. In that situation, the monolayer Langmuir model is not applicable. Brunauer et al. (1938) presented another isotherm model to take this into consideration. This multilayer model is called BET or Type II isotherm (Figure 7). Like the Langmuir isotherm, this BET isotherm can also be modeled by an equation:

$$V(p) = \frac{V_m C p}{(p_0 - p)\left[1 + (C-1)\, p / p_0\right]} \tag{2.2}$$

where $V(p)$ is the volume of adsorption gas per unit mass of medium; V_m is the maximum adsorption of a single layer; p_0 denotes the saturation pressure of gas; p is the gas pressure in pore space; C represents a dimensionless constant which depends on temperature. Both the Type I and II isotherms are derived for single phase system and can be further developed for binary or multiphase system (Chen et al., 2009; Lin, 2010).

The adsorption of nature gas, mostly CH_4, onto the internal surface of coal and gas shale, usually fits Langmuir-type isotherm, which can be supported by experiment results. Lu et al. (1995) measured gas (CH_4) adsorption capability for the samples gathered from Devonian shale and Antrim shale. And their results for adsorption isotherms resembled Langmuir-type isotherm. The Barnett Shale core samples also displayed Langmuir-type methane adsorption isotherm (Lancaster et al., 1992; Montgomery et al., 2005; Kang et al., 2010; Vermylen, 2011). However, the adsorption isotherm of CO_2 on shale and coal surface did not fit Langmuir-type (Lin, 2010; Vermylen, 2011). It may follow BET-type isotherm or some other complicated models. In this project, our work will focus on the

gas production, mostly methane, from gas shale reservoirs. Therefore, only Langmuir-type isotherm will be considered in building up the numerical simulator.

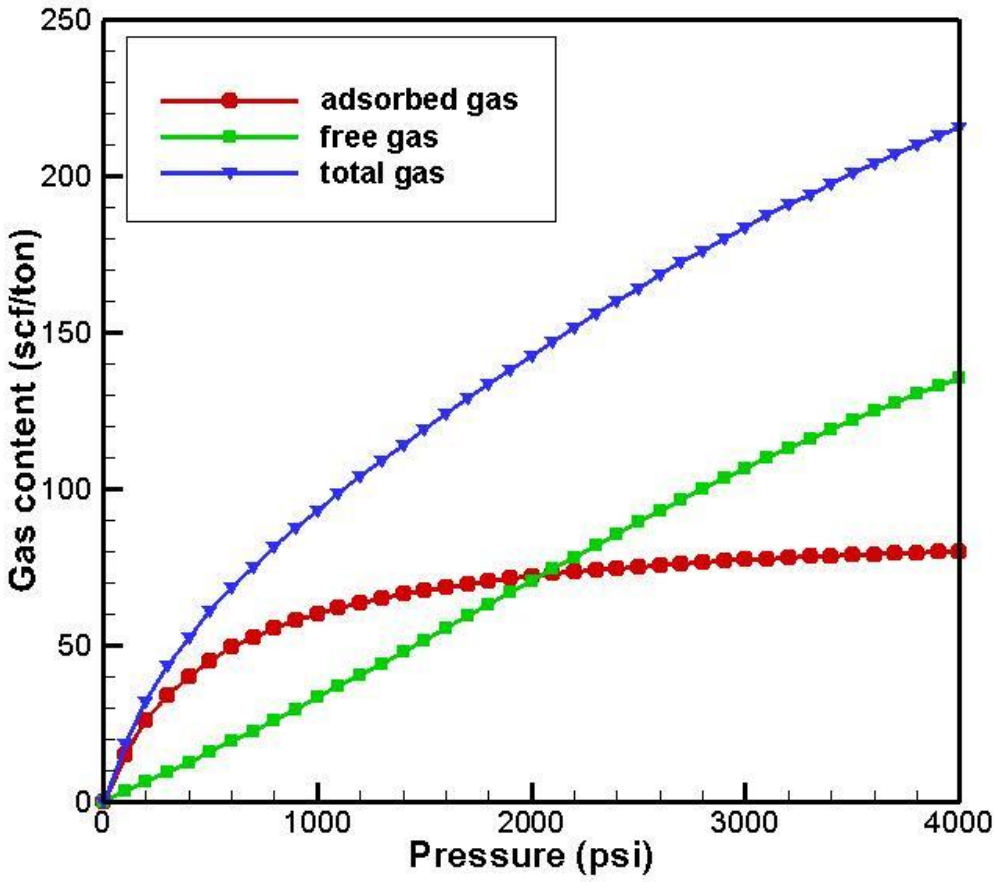

Figure 8 A typical example of gas content in the Barnett Shale

The relationship between gas content, including both free gas and adsorbed gas, and reservoir pressure is demonstrated in Figure 8 for a typical Barnett Shale sample (Montgomery et al., 2005). The free gas, sometimes called porosity gas, shows a nearly straight line while the adsorbed gas presents a nonlinear curve, which is identical to a

Langmuir-type isothermal. For an ordinary reservoir pressure (3,800psi) in the Barnett Shale, almost 38% total gas is stored as adsorption gas in this case. However, this significant amount of adsorbed gas demonstrates a nearly flatten pattern curve at high reservoir pressure, more than 1000 psi, when compared with free gas. It implies that, when reservoir pressure is high, the adsorbed gas is hard to release and only contributes to a minor portion of production, although it covers a considerable portion in gas-in-place of gas shale reservoir.

A resultant volumetric strain is generated during the gas adsorption/desorption process, which has been proven by experiment work (Harpalani and Schraufnagel, 1990; Cui and Bustin, 2005; Robertson, 2005). This sorption-induced strain can project non-negligible mechanical influence on the deformation of matrix rock, like coal seam and gas shale. Previously mentioned experiments showed that the isotherm curves of gas sorption-induced strain could also be classified as Langmuir-type curves. So, a Langmuir type equation is widely used to describe gas sorption-induced strain (Shi and Durucan, 2004; Robertson and Christiansen, 2006, 2008; Zhang et al., 2008; Chen et al., 2009; Liu et al., 2010).

$$\varepsilon_s = \varepsilon_L \frac{p}{P_L + p} \tag{2.3}$$

where ε_s is defined as gas sorption-induced strain; ε_L is the Langmuir volumetric strain, which denotes the maximum volumetric strain that could be induced in the bulk rock

when fully saturated with gas; P_L represents Langmuir pressure at which half of the ε_L can be measured.

This function is only valid for a single phase system and assumes that only volumetric strain is affected by gas desorption, i.e., gas sorption-induced strain has the same influence in all directions and also the three normal stress components.

2.3 Poroelastic model

A poroelastic formulation considering gas desorption has been previously developed for coal-bed methane. This was accomplished based on a direct analogy between poroelastic dilation and thermal contraction in order to study the coupling response between gas desorption and rock matrix/fracture deformation (Shi and Durucan, 2004; Zhang et al., 2008). We build on these works by applying the same poroelastic formulation to gas shale, considering that gas shale is a system composed by shale matrix and gas, including both free and absorbed phase gas.

Then, a set of governing equations of the non-linear poroelastic model are constructed to prescribe the shale matrix deformation, gas flow mechanism and their interactions.

The following important assumptions are made in defining the fundamental field equations for the system: (i) shale is a linearly elastic, isotropic and homogeneous medium; (ii) shale is fully saturated with gas; (iii) complete isothermal conditions with no chemical perturbation; (iv) dry gas is considered so that only gas flows through the

wellbore; (v) Darcy flow is valid for the system; (vi) plane strain conditions with infinitesimal strains are applicable; (vii) gravity effect on gas flow is negligible.

2.3.1 Constitutive equation

Diek and Ghassemi's (2004) chemo-thermo-poroelastic theory is an improvement of the Heidug and Wong's (1996) work and is derived from the potential energy of wetted clay matrix, i.e., the differences between the internal energy of fluid saturated porous medium and that of the pore fluid. In the case of complete isotropy and without chemical influences, the constitutive equation for an isotropic thermo-poroelatic porous medium is given as *(tension is considered positive):*

$$\dot{\sigma}_{ij} = (K - \frac{2G}{3})\dot{\varepsilon}_{kk}\delta_{ij} + 2G\dot{\varepsilon}_{ij} - \alpha \dot{p}\delta_{ij} - K\delta_s \dot{T}\delta_{ij} \tag{2.4}$$

where K , G represent the rock's bulk and shear modulus respectively; α is the Biot's poroelastic coefficient; δ_s denotes the volumetric thermal expansion coefficient of the solid matrix. The above linearization of rock-fluid constitutive equations (2.4) express the total stresses σ_{ij} with respect to three variables, the solid strain ε_{ij} , the pore pressure p , and the temperature T and the dots above variables represent time derivatives.

Considering the macro matrix shrinkage, a direct analogy between poroelastic dilation and thermal contraction could be proposed to describe the constitutive relation between gas desorption and rock matrix/fracture deformation for deformed gas shale (Shi and Durucan, 2004)

$$\sigma_{ij} = (K - \frac{2G}{3})\varepsilon_{kk}\delta_{ij} + 2G\varepsilon_{ij} - \alpha p\delta_{ij} - K\varepsilon_s\delta_{ij} \tag{2.5}$$

where ε_s is defined as gas sorption-induced strain. Again, only the three normal stress components are affected by thermal contraction/gas desorption and no shear is induced.

The strain-displacement expression is defined as:

$$\varepsilon_{ij} = \frac{1}{2}(u_{i,j} + u_{j,i}) \tag{2.6}$$

where u_i represents the solid displacement vector (denoting the movement of the porous rock with respect to a reference configuration).

By applying Eq. (2.6) into Eq. (2.5), the strain-stress relation is given as:

$$\varepsilon_{ij} = \frac{1}{2G}\sigma_{ij} - \left(\frac{1}{6G} - \frac{1}{9K}\right)\sigma_{kk}\delta_{ij} + \frac{\alpha}{3K}p\delta_{ij} + \frac{\varepsilon_s}{3}\delta_{ij} \tag{2.7}$$

where σ_{kk} is the trace of stress tensor. Then, the volumetric strain of the gas shale ($\varepsilon_v = \varepsilon_{xx} + \varepsilon_{yy} + \varepsilon_{zz}$) is readily obtained from Eq. (2.7):

$$\varepsilon_v = \frac{1}{3K}\sigma_{kk} + \frac{\alpha}{K}p + \varepsilon_s \tag{2.8}$$

With tension positive, the mean compressive stress is defined as:

$$\bar{\sigma} = -\sigma_{kk}/3 \tag{2.9}$$

After putting Eq. (2.9) into Eq. (2.8), the volumetric strain of the gas shale can be rewritten as:

$$\varepsilon_v = -\frac{1}{K}(\bar{\sigma} - \alpha p) + \varepsilon_s \tag{2.10}$$

The component of effective stress is also given as:

$$\sigma_{ij}^{'} = \sigma_{ij} + \alpha p \delta_{ij} \tag{2.11}$$

With body force, the momentum balance equation is expressed as:

$$\sigma_{ij,j} + f_i = 0 \tag{2.12}$$

where f_i represents the components of body force.

Substituting the constitutive Eq. (2.5) into the equilibrium Eq. (2.12) with Eq. (2.6), a set of Navier-type equations is obtained:

$$G\nabla^2 u_i + \frac{G}{1-2\nu} u_{k,ki} - \alpha p_{,i} - K\varepsilon_{s,i} + f_i = 0 \tag{2.13}$$

2.3.2 Mass conservation of gas

In the case of complete isotropy and without chemical influences, the fluid transport equation for an isotropic thermo-poroelatic porous medium is given as *(tension is considered positive):*

$$\dot{\zeta} = \alpha \dot{\varepsilon}_{kk} + \frac{1}{M}\dot{p} \tag{2.14}$$

where ζ represents the variation of fluid content per unite reference volume; α is the Biot's effective stress coefficient which measures the ability of the pore pressure to act against compressional stresses; M stands for the Biot modulus, defined as the inverse of

a storage coefficient with the expression of $\frac{1}{M}=\frac{\partial\zeta}{\partial p}\Big|_{\varepsilon}$; the dots above variables represent time derivatives.

The mass conservation equation of fluid is given by (Diek and Ghassemi, 2004)

$$\dot{\zeta}+\nabla\cdot v=\gamma \tag{2.15}$$

where v denotes Darcy's filter velocity; γ denotes the source density.

And the fluid content variation could be expressed by:

$$\zeta=\frac{m_f-m_{f0}}{\rho_g} \tag{2.16}$$

where m_f defines the total fluid mass; m_{f0} is the fluid mass at reference configuration; ρ_g is the gas density. And the time evolution of fluid content variation is obtained:

$$\dot{\zeta}=\frac{\dot{m}_f}{\rho_g} \tag{2.17}$$

Combinig Eq.(2.15) and Eq.(2.17), local continuity equation is developed by considering the mass conservation of gas content:

$$\frac{\partial m}{\partial t}+\nabla\cdot(\rho_g v)=\gamma \tag{2.18}$$

where $v=\frac{q}{A}$ is the fluid velocity; ρ_g is the gas density; γ denotes the source density (rate of injected gas content per unit volume of the porous medium); m represents the gas content remaining within a unit volume of rock, including both free and absorbed gas (Saghafi et al., 2007)

$$m = \rho_g \phi + \rho_{sc} \rho_r \frac{V_L p}{p + P_L} \tag{2.19}$$

where ϕ represents the porosity; ρ_g is the gas density at reservoir condition; ρ_{sc} denotes gas density at standard condition; ρ_r is the density of gas shale; V_L and P_L represent Langmuir volume and pressure constant respectively; p is the gas pressure in pore space. The first term in the right hand side (RHS) of equation 2.19 represents the free gas content which is stored in pore space, while the second term reflects the adsorbed gas that is attracted onto the internal surface of matrix.

Based on the real gas law, the gas density could be expressed as:

$$\rho_g = \frac{pM_g}{ZRT} \tag{2.20}$$

where M_g is the gas molecular mass; Z is the compressibility factor with $Z_{sc} \approx 1$ at standard conditions; R represents the universal gas constant. Then, the gas density at standard condition yields as:

$$\rho_{sc} = \frac{p_{sc} M_g}{RT_{sc}} \tag{2.21}$$

with p_{sc} and T_{sc} denoting the pressure and temperature under standard condition.

By neglecting the gravity effect, the gas superficial velocity could be given from Darcy's law:

$$v = -\frac{k}{\mu} \nabla p \tag{2.22}$$

where k stands for gas permeability of the formation; μ is the gas viscosity. Substituting Eq. (2.19)-(2.22) into Eq. (2.18), it yields:

$$\frac{\partial}{\partial t}\left(\frac{p\phi}{Z}\right)+\frac{p_{sc}\rho_r V_L P_L}{(p+P_L)^2}\frac{T}{T_{sc}}\frac{\partial p}{\partial t}=\nabla\cdot(k_a\frac{p}{\mu Z}\nabla p)+\gamma\frac{RT}{M_g} \tag{2.23}$$

Therefore, the gas flow equation of dry gas model is developed by considering the mass conservation of gas content, including both free and absorbed phase gas. This Biot-type equation is quite different from the models that we can find in literature, which utilized an ideal gas law and neglected the gas compressibility (Zhao et al., 2004; Zhang et al., 2008). Then, the rock constitutive equation (Eq. (2.13)) and gas flow equation (Eq. (2.23)) are coupled through the following general porosity model.

2.4 Porosity model

During the gas depletion process, the reduction of pore pressure causes a rise in effective stress in the reservoir. This increase of effective stress can compact the reservoir and hence reduce its porosity and permeability. Simultaneously, the reduction of pore pressure also results in the release of adsorbed gas, whose effect on the porosity and permeability of the system is the reverse of pore pressure decrease (since effective stress is reduced by it). So the net change of porosity and permeability in the reservoir is the outcome of these two competing processes.

The matrix porosity is an essential factor to simulate reservoir permeability evolution during gas production. Due to the complex gas storage and flow mechanism within gas

shale, it is a function of rock mechanical properties, gas desorption capability and in-situ stress condition. In the following, different porosity models, which can be found in literature, are discussed briefly for gas sorption-bearing rocks.

2.4.1 Seidle-Huitt model

Seidle-Huitt model (1995) assumed that only sorption-induced strain caused changes in porosity in the coalbed with matchstick geometry, which excluded all elastic strain generated by stress variation within the matrix. This might not be the proper case for gas shale, whose desorped gas does not cover a significant portion of production as that of coalbed methane.

$$\frac{\phi}{\phi_0} = 1 + \left(1 + \frac{2}{\phi_0}\right) C_m V_m \left(\frac{bp_0}{1 + bp_0} - \frac{bp}{1 + bp}\right) \tag{2.24}$$

where ϕ is the porosity at pressure p; ϕ_0 is the initial porosity at initial reservoir pressure p_0; C_m represents the swelling coefficient of matrix; V_m is maximum amount of adsorption; b is a Langmuir constant. In this model, the gas adsorption is given by the following Langmuir equation:

$$V(p)_{ads} = \frac{V_m bp}{1 + bp} \tag{2.25}$$

And the volumetric strain ($\varepsilon_v(p)$) is set proportional to amount of adsorption gas by a swelling coefficient, C_m

$$\varepsilon_v(p) = C_m \frac{V_m bp}{1+bp} \tag{2.26}$$

2.4.2 Palmer-Mansoori model

Palmer-Mansoori model (1998) considered both stress-caused elastic deformation and desorption-induced swelling. This model was developed under uniaxial strain conditions and was given as:

$$\frac{\phi}{\phi_0} = 1 + \frac{c_m}{\phi_0}(p - p_0) + \frac{\varepsilon_l}{\phi_0}\left(\frac{K}{M} - 1\right)\left(\frac{bp}{1+bp} - \frac{bp_0}{1+bp_0}\right) \tag{2.27}$$

where c_m is the compressibility of pore space, defined as the change of pore volume with pore pressure; ε_l represents the maximum volumetric strain when pressure goes to infinite; K and M denote the rock's bulk and constrained axial modulus respectively.

The second term in the right hand side (RHS) of equation 2.27 represents the mechanical deformation caused by the change of effective stress, while the third term reflects the desorption-induced matrix swelling.

2.4.3 Cui-Bustin model

Cui-Bustin model (2005) showed the porosity was a general function of bulk modulus of rock and pore space, mean stress and pore pressure:

$$\frac{\phi}{\phi_0} = \exp\left\{\left(\frac{1}{K} - \frac{1}{K_p}\right)\left[\left(\bar{\sigma} - \bar{\sigma}_0\right) - \left(p - p_0\right)\right]\right\} \tag{2.28}$$

where K_p denotes the bulk modulus for the pore space; $\bar{\sigma}$ and $\bar{\sigma}_0$ are the current and initial mean stress respectively. Assuming K and K_p are constants, this model is derived by integrating the following equation with time

$$\frac{d\phi}{\phi} = \left(\frac{1}{K} - \frac{1}{K_p} \right) \left(d\bar{\sigma} - dp \right) \tag{2.29}$$

2.4.4 General model

To avoid any stress or strain restrictions for the application of porosity model, a general model is derived from poroelasticity theory (Detournay and Cheng, 1993), by taking both gas desorption mechanism and in-situ stress condition into account (Huang and Ghassemi, 2011).

For the initial condition, we assume the initial volumetric strain is zero ($\varepsilon_{v0} = 0$). So, in the following discussion, we are dealing with the increments of all strain and stress components, which are indicated by the "$\cdot$" script on top of variables. The volumetric response of the porous medium with respect to loading {P, p} (mechanical and fluid loading, respectively) can be expressed by the following relations (Detournay and Cheng, 1993):

$$\frac{\Delta V}{V} = -\frac{1}{K}(\dot{P} - \alpha \dot{p}) \tag{2.30}$$

$$\frac{\Delta V_p}{V_p} = -\frac{1}{K_p}(\dot{P} - \beta \dot{p}) \tag{2.31}$$

where K and K_p denote bulk modulus for the medium and the pore space respectively; V_p is the volume of pore space; α is the Biot's poroelastic coefficient; β is a dimensionless coefficient with the expression $\beta = 1 - \frac{K_p}{K_s}$; K_s represents the bulk modulus of solid constituent.

Recalling Eq. (2.10), a similar expression could be stated in this case study:

$$\frac{\Delta V}{V} = -\frac{1}{K}(\dot{\bar{\sigma}} - \alpha \dot{p}) + \dot{\varepsilon}_s \tag{2.32}$$

If we assume that sorption-induced strain projects the same effect on bulk rock and pore space, another relation for pore space could be proposed:

$$\frac{\Delta V_p}{V_p} = -\frac{1}{K_p}(\dot{\bar{\sigma}} - \beta \dot{p}) + \dot{\varepsilon}_s \tag{2.33}$$

By applying Betti-Maxwell reciprocal theorem:

$$\frac{\partial V}{\partial p}\Big|_{\bar{\sigma}} = -\frac{\partial V_p}{\partial \bar{\sigma}}\Big|_p \tag{2.34}$$

The following equation could be obtained:

$$K_p = \frac{\phi}{\alpha} K \tag{2.35}$$

Applying the definition $V = V_p + V_s$ and $\phi = V_p / V$, the following equations could be readily developed (Detournay and Cheng, 1993)

$$\frac{\Delta V}{V} = \frac{\Delta V_s}{V_s} + \frac{\Delta \phi}{1-\phi} \tag{2.36}$$

$$\frac{\Delta V_p}{V_p} = \frac{\Delta V_s}{V_s} + \frac{\Delta \phi}{\phi(1-\phi)} \tag{2.37}$$

By combining Eq. (2.32)-(2.37), $\Delta\phi$ could be solved:

$$\Delta\phi = \phi(\frac{1}{K} - \frac{1}{K_p})(\dot{\bar{\sigma}} - \dot{p}) \tag{2.38}$$

This expression is identical to the Eq. (2.29) that is used for developing Cui-Bustin model (2005). In that work, Cui-Bustin model was derived by assuming constant K and K_p and integrating the equation over time. However, K_p is also a function of porosity (as shown in Eq. (2.35)). We substitute Eq. (2.9) and (2.35) into Eq. (2.38) to get the following expression of porosity:

$$\Delta\phi = (\alpha - \phi)(\dot{\varepsilon}_v - \dot{\varepsilon}_s + \frac{\dot{p}}{K_s}) \tag{2.39}$$

With the initial condition of the system, $\varepsilon_{v0} = 0$:

$$\dot{\varepsilon}_v = \varepsilon_v - \varepsilon_{v0} = -\frac{1}{K}(\dot{\bar{\sigma}} - \alpha\dot{p}) + \dot{\varepsilon}_s \tag{2.40}$$

Then the following relation could be revealed:

$$\phi - \phi_0 = \Delta\phi \tag{2.41}$$

Substituting Eq. (2.38) and (2.39) into Eq. (2.40), we can get:

$$\phi = \frac{1}{1+S-S_0}[\phi_0 + \alpha(S-S_0)] \tag{2.42}$$

with $S = \varepsilon_v - \varepsilon_s + \frac{p}{K_s}$ and $S_0 = \frac{p_0}{K_s} - \varepsilon_{s0} = \frac{p_0}{K_s} - \varepsilon_L \frac{p_0}{P_L + p_0}$ and script " $_0$ " indicating initial conditions.

The total volumetric deformation (ε_v) of the porous medium consists of the pore space deformation (ε_p), the deformation of the solid porous matrix (ε_{sm}) and gas sorption-induced strain (ε_s). The deformation of the solid porous matrix is due to the fluid pressure and effective stress loading:

(i) the effect of fluid pressure (the compression stress or strain is negative)

$$\varepsilon_{sm1} = -\frac{p}{K_s}(1-\phi) \tag{2.43}$$

(ii) the effect of effective stress loading

$$e_{sm2} = \frac{\sigma'_{kk}}{3K_s} \tag{2.44}$$

where K_s is the bulk modulus of the solid and ϕ is the porosity. The mean effective stress ($\sigma'_{kk}/3$) has the following relation with the volumetric strain and pore pressure:

$$\frac{\sigma'_{kk}}{3} = \frac{\sigma'_{xx} + \sigma'_{yy} + \sigma'_{zz}}{3} = K(\varepsilon_v - \varepsilon_s) + \frac{K}{K_s} p \tag{2.45}$$

where K ($K < K_s$) is the bulk modulus of the porous matrix. Combining Eq. (2.43) and (2.44), and substituting Eq. (2.45) result in the deformation of the solid porous matrix:

$$\varepsilon_{sm} = \frac{K}{K_s}(\varepsilon_v - \varepsilon_s) + \frac{p}{K_s}\left[\frac{K}{K_s} - (1-\phi)\right] \tag{2.46}$$

The pore space volumetric strain is obtained by subtracting the volumetric deformation of the solid porous matrix from the total volumetric strain and using the definition of Biot's coefficient ($\alpha = 1 - K / K_s$):

$$\varepsilon_p = \alpha(\varepsilon_v - \varepsilon_s) + (\alpha - \phi)\frac{p}{K_s} \tag{2.47}$$

This general porosity model is a key component to control reservoir permeability distribution and time evolution, which will be discussed in the following. And it is also an indispensable function to further expand the gas flow equation (Eq. (2.22)) to obtain the fully coupled poroelastic model for developing numerical simulator of gas shale.

2.5 Permeability model

Both porosity and permeability of gas shale are essential mechanical properties that govern gas deliverability through reservoirs. In reality, porosity and permeability are the function of the reservoir stresses condition, reservoir pressure, gas adsorption and rock properties and they cannot stay invariant during gas depletion. Some commonly used porosity models are briefly introduced and a general porosity model is derived for gas sorption-bearing rocks, based on poroelasticity theory. Then, a general porosity model is utilized to estimate permeability field within reservoir.

Validated with numerous experiment results, several empirical functions have been developed to correlate permeability with porosity in the literature. Commonly, a cubic

function can be used to calculate rock matrix permeability change during production. This correlation was adopted in Seidle-Huitt model (1995) and Palmer-Mansoori model (1998) for computing permeability after developing porosity model.

$$k = k_0 \left(\frac{\phi}{\phi_0} \right)^3 \tag{2.48}$$

where the subscript "0" represents the initial value of the variables.

Liu and Civan (1995) proposed the following correlation by modifying the Kozeny equation.

$$\frac{k}{k_0} = \left((1 - f) k_p + f \frac{\phi}{\phi^*} \right)^3 \tag{2.49}$$

where the dimensionless parameter k_p denotes the conductivity of fluid seepage within plugged pores; f represents the fraction of unplugged pore throats; ϕ^* is the porosity which is affected by mechanical loading. In this model, the particle plugging effects is taking into consideration. If the flow factor f is set to 1, this model is exactly the same as the above cubic function.

McKee et al. (1988) developed another correlation based on Carmen-Kozeny equation.

$$\frac{k}{k_0} = \frac{e^{-3\bar{c}_p \Delta\sigma}}{1 - \phi_0 \left(1 - e^{-\bar{c}_p \Delta\sigma} \right)} \tag{2.50}$$

where $\bar{c}_p$ is the average pore compressibility; $\Delta\sigma$ is the change of effective stress. In this model, the compressibility of solid grains is omitted as it is assumed to be negligible compared to pore compressibility.

For most gas shale reservoir, its porosity $\phi_0 << 1$, which is just on order of 1%. Therefore, Eq. (2.50) can be simplified to:

$$\frac{k}{k_0} = e^{-3\bar{c}_p \Delta\sigma} \tag{2.51}$$

This function is similar to the correlation developed in Shi-Durucan model (2004), Cui-Bustin model (2005) and Robertson-Christiansen model (2006).

Shi-Durucan model (2004) was derived under uniaxial strain conditions.

$$\frac{k}{k_0} = \exp\left\{3c_f\left[\frac{\nu}{1-\nu}(p-p_0) + \frac{E\varepsilon_l}{1-\nu}\left(\frac{p_0}{P_L+p_0} - \frac{p}{P_L+p}\right)\right]\right\} \tag{2.52}$$

where c_f is the compressibility of cleat volume; ε_l represents the maximum volumetric strain when pressure goes to infinite; E is Young's modulus and ν denotes Poisson's ratio.

Cui-Bustin model (2005) was established by using cubic law. However, this model was similar to Eq. (2.51). This model was obtained by assuming constant values of K and K_p over time. Under uniaxial strain condition, this permeability model can be transformed to a function which was close to Shi-Durucan model.

$$\frac{k}{k_0} = \exp\left\{-\frac{3}{K_p}\left[(\bar{\sigma}-\bar{\sigma}_0) - (p-p_0)\right]\right\} \tag{2.53}$$

Robertson-Christiansen (2006) developed a model for hydrostatic stress condition to resemble the lab condition for permeability measurement on core, while the overburden pressure was assumed be a constant.

$$\frac{k}{k_0}=\exp\left\{3c_0\frac{1-e^{\alpha(p-p_0)}}{-\alpha}+\frac{9}{\phi_0}\left[\frac{1-2\nu}{E}(p-p_0)-\frac{\varepsilon_l P_L}{P_L+p_0}\ln\left(\frac{P_L+p}{P_L+p_0}\right)\right]\right\} \tag{2.54}$$

where c_0 is the initial fracture compressibility; α is the change rate of fracture compressibility.

2.5.1 Klinkenberg model

The conventional Klinkenberg model (Klinkenberg, 1941) was proposed based on the assumption that the gas molecule velocity was non-zero at the porous media surface due to slip. This occurs when the magnitude of gas molecule's mean free path approaches the pore diameter. The onset of slip is, when the mean free path increases (e.g., at low pressure), becoming less two orders of magnitude smaller than the capillary radius (Kundt and Warburg, 1875). Utilizing the kinetic theory of gases and straight tube flow geometry, Florence et al. (2007) presented a detailed derivation of Klinkenberg equation:

$$q_g=\frac{\pi R_c^{\,4}}{8\mu}\frac{\Delta p}{L_c}\left[1+\frac{4c\bar{\lambda}}{R_c}\right] \tag{2.55}$$

where q_g is the volumetric gas flow rate; R_c denotes the pipe radius; L_c is the length of the flow tube; μ stands for viscosity of the gas; Δp is the differential pressure; c is a constant which is slightly lower than 1 (Kundt and Warburg, 1875); $\bar{\lambda}$ represents the mean free path of gas molecules. Based on this model, the apparent gas permeability is given as (Florence et al., 2007):

$$k_a = k_\infty \left[1 + \frac{b_K}{\bar{p}} \right] \tag{2.56}$$

where $b_K = \frac{4c\bar{\lambda}\bar{p}}{R_c}$ is termed as "gas slippage factor".

2.5.2 Beskok-Karniadakis microflow model

A unified flow model was proposed by Beskok and Karniadakis (1999) to predict volumetric gas flow rate through micro tubes:

$$q_g = \frac{\pi R_c^4}{8\mu} \frac{\Delta p}{L_c} \left[1 + \alpha Kn \right] \left[1 + \frac{4Kn}{1 - bKn} \right] \tag{2.57}$$

where α represents the dimensionless rarefaction coefficient; b is dimensionless slip coefficient; Kn is the *Knudsen number* defined as:

$$Kn = \frac{\bar{\lambda}}{R_c} \tag{2.58}$$

where R_c denotes the pipe radius; $\bar{\lambda}$ is the mean free path of gas molecules; it is defined by Loeb (1934) as:

$$\bar{\lambda}(\bar{p}, T) = \frac{\mu}{\bar{p}} \sqrt{\frac{\pi RT}{2M}} \tag{2.59}$$

where $\bar{p}$ is the mean gas pressure ; T is the absolute temperature; μ is the viscosity of gas at $\bar{p}$ and T ; R is the universal gas constant; M is the molecular mass of the gas.

Based on Kn, various flow regimes could be classified by Schaaf and Chambre (1961): continuum fluid flow ($Kn \le 0.001$), slip flow ($0.001 < Kn \le 0.1$), transition flow ($0.1 < Kn \le 10$) and free molecular flow ($Kn \ge 10$).

The parameter α is a function of Kn through the following empirical correlation (Beskok and Karniadakis, 1999):

$$\alpha(Kn) = \alpha_0 \frac{2}{\pi} \tan^{-1}\left[c_1 Kn^{c_2}\right] \tag{2.60}$$

where $c_1 = 4.0$ and $c_2 = 0.4$ and:

$$\alpha_0 \equiv \alpha_{Kn\to\infty} = \frac{64}{3\pi\left(1-\frac{b}{4}\right)} = \frac{64}{15\pi} \tag{2.61}$$

Then the parameter α could be simplified to:

$$\alpha(Kn) = \frac{128}{15\pi^2} \tan^{-1}\left[4Kn^{0.4}\right] \tag{2.62}$$

Based on this model, the apparent gas permeability could be expressed as (Civan, 2010):

$$k_a = k_\infty \left[1+\alpha Kn\right]\left[1+\frac{4Kn}{1-bKn}\right] \tag{2.63}$$

where k_∞ stands for the intrinsic permeability of porous medium given as:

$$k_\infty = \frac{\phi R_c^2}{8\tau_c} \tag{2.64}$$

with $\tau_c = L_c / L$ (2.65) denoting the tortuosity factor of flow path. The intrinsic permeability is independent of flow condition and fluid type.

Let $b = -1$ and $\alpha(Kn) = 0$ for a slip flow regime, Eq. (2.54) could be simplified to:

$$q_g = \frac{\pi R_c^4}{8\mu} \frac{\Delta p}{L_c} \left[1 + \frac{4Kn}{1+Kn} \right] \tag{2.66}$$

Eq.(2.63) is given as: $$k_a = k_\infty \left[1 + \frac{4Kn}{1+Kn} \right] \tag{2.67}$$

for $0.001 < Kn \le 0.1$, $\frac{4Kn}{1+Kn} \approx 4Kn$, then the above equations can be expressed as:

$$q_g = \frac{\pi R_c^4}{8\mu} \frac{\Delta p}{L_c} \left[1 + 4Kn \right] \tag{2.68}$$

$$k_a = k_\infty \left[1 + 4Kn \right] \tag{2.69}$$

According to Eq. (2.58), Eq. (2.68) could be rewritten as:

$$q_g = \frac{\pi R_c^4}{8\mu} \frac{\Delta p}{L_c} \left[1 + \frac{4\bar{\lambda}}{R_c} \right] \tag{2.70}$$

Considering c is very close to 1, it could be suggested that the conventional Klinkenberg model is a good analogue to Beskok-Karniadakis microflow model under this circumstance.

Based on the Klinkenburg model, the apparent gas permeability could be stated as (Florence et al., 2007): $$k_a = k_\infty \left[1 + \frac{b_K}{\bar{p}} \right] \tag{2.71}$$

where b_K is termed as "gas slippage factor". Comparing Eq.(2.69) with Eq.(2.71), one can get

$$b_K = 4\bar{p}K_n = \frac{4\bar{\lambda}\bar{p}}{R_c} \tag{2.72}$$

Substituting $\bar{\lambda}$ with Eq.(2.59), Eq.(2.72) can be given as:

$$b_K = \frac{4\mu}{R_c}\sqrt{\frac{\pi RT}{2M}} \tag{2.73}$$

From Eq.(2.64), the hydraulic pipe radius R_c is expressed as:

$$R_c = \sqrt{\frac{8\tau_c k_\infty}{\phi}} \tag{2.74}$$

Substituting Eq.(2.74) into Eq.(2.73), the following equation is derived:

$$b_K = \mu\sqrt{\frac{\pi RT}{\tau_c M}}\sqrt{\frac{\phi}{k_\infty}} \tag{2.75}$$

Letting $\beta = \mu\sqrt{\frac{\pi RT}{\tau_c M}}$ (2.76)

Eq.(2.75) can be rewritten as a "square root" model: $b_K = \beta\left(\frac{k_\infty}{\phi}\right)^{-0.5}$ (2.77)

Civan (2010) proposed the following correlation to compute β term for various gases under isothermal condition (assumed to be 298K) in SI unites:

$$\beta = 2.79 \times 10^3 \frac{\mu}{\sqrt{M}} \tag{2.78}$$

In Figure 9, the linear relationship between the term β / μ and M for various gases is shown in log-log diagram. The data for hydrogen, helium, nitrogen, are and carbon dioxide are collected from Florence et al.(2007); while gas properties of methane is obtained from literature and its β term is calculated from Eq.(2.78). All the gas properties and computed data are listed in Table 1.

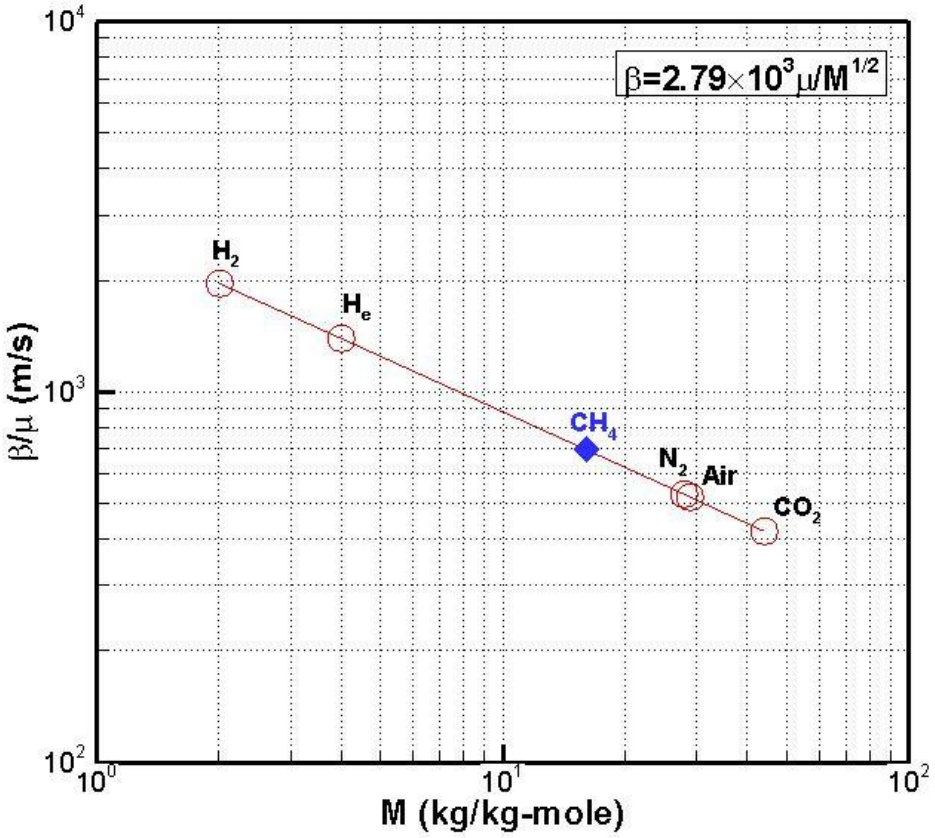

Figure 9 Correlation between β / μ and M for various gases.

Gas	Viscosity at 1atm and 298K (Pa·s)	Molecular Weight(Kg/Kg-mole)	β (Pa·m)
Hydrogen	8.845E-06	2.0159	1.74E-02
Helium	1.985E-05	4.0026	2.77E-02
Nitrogen	1.781E-05	28.01348	9.39E-03
Air	1.842E-05	28.9586	9.55E-03
Carbon dioxide	1.503E-05	44.0095	6.32E-03
Methane	1.100E-05	16.043	7.66E-03

Table 1 Computed β term based on the data of Florence et al.(2007)

By taking the empirical correlation (Eq.(2.78), the computed β term (isothermal conditions, T=298K) for pure methane is plotted as red curve in Figure 10. If assuming the intrinsic permeability $k_\infty = 1\mu D$ and porosity $\phi = 0.04$, the dimensionless permeability k_a / k_∞ can be calculated from Eq.(2.71) and (2.77) and is demonstrated as blue curve in Figure 10. It can be seen that β term decreases while the gas permeability (k_a) increases with gas depletion.

If taking the temperature term into conderation, Eq.(2.78) can be extended into the computation of β term under any reservoir conditions.

$$\beta = \frac{2.79\times10^3}{\sqrt{298}}\mu\sqrt{\frac{T}{M}} = 161.62\mu\sqrt{\frac{T}{M}} \tag{2.79}$$

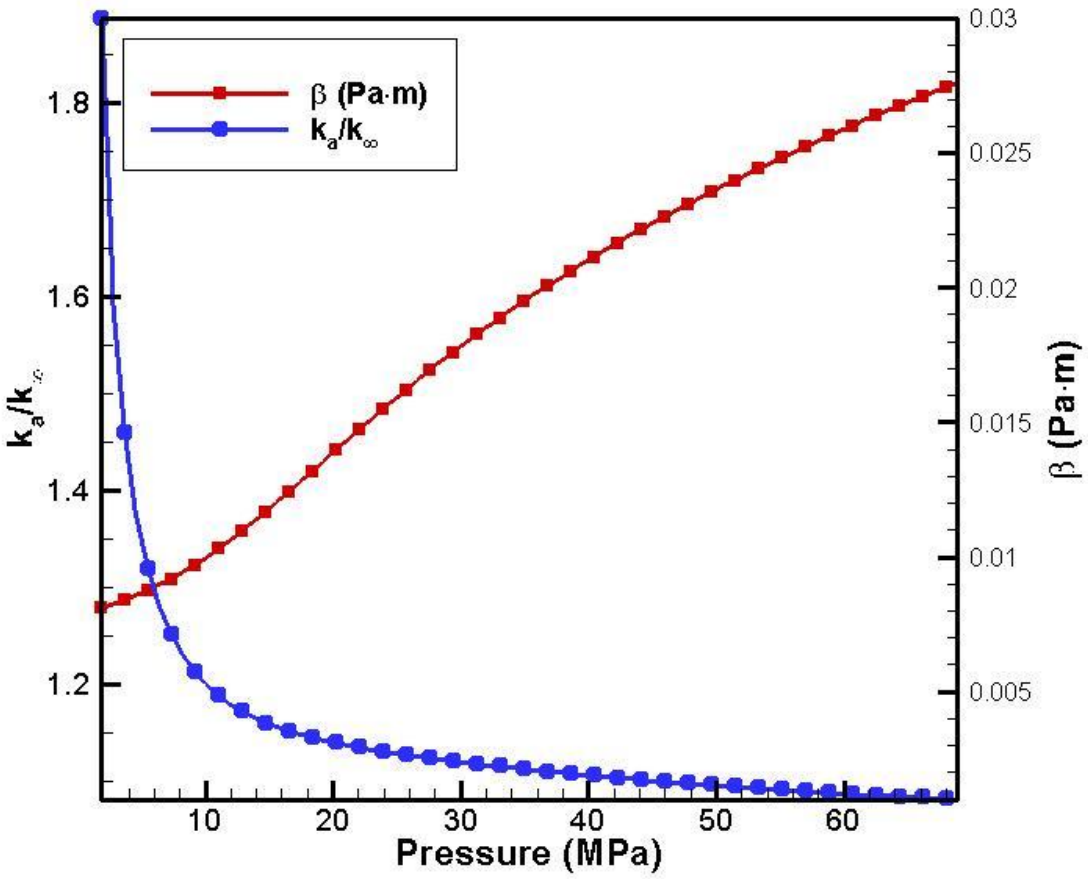

Figure 10 Calculated β term and k_a / k_∞ under different reservoir pressure for methane.

2.5.3 Forchheimer's model for non-Darcy flow

The above models are only applicable for *low velocity gas flow*, which is adequate for Darcy's law. As for high velocity gas flow, Non-Darcy flow effect should be taken into account. Forchheimer equation (1901) was developed to describe this nonlinear fluid flow phenomena by incorporating a quadratic term into conventional Darcy's law:

$$-\frac{dp}{dx}=\frac{\mu}{k}v+\beta\rho v^2 \tag{2.80}$$

where $v=\frac{q}{A}$ is the gas velocity; β is called beta factor or *turbulence factor*.

Then, the apparent permeability could be presented as (Huang and Ayoub, 2008):

$$\frac{1}{k_a}=-\frac{1}{\mu v}\frac{dp}{dx}=\frac{1}{k}+\beta\frac{\rho v}{\mu} \tag{2.81}$$

Apparently, β is the slope of the Forchheimer graph ($\frac{1}{k_a}$ vs. $\frac{\rho v}{\mu}$) .This is the conventional way to estimate it in oil and gas industry (Huang and Ayoub, 2008).

For dry gas, its velocity could be expressed at standard condition by taking the gas expansion into account:

$$v=\frac{q_{res}}{A}=\frac{q_{sc}}{A}B_g \tag{2.82}$$

where q_{res} and q_{sc} stand for the volumetric flow rate at reservoir condition and standard condition respectively; B_g is the gas formation volume factor with the definition as:

$$B_g=\frac{V}{V_{sc}}=\frac{p_{sc}}{p}\frac{T}{T_{sc}}\frac{Z}{Z_{sc}} \tag{2.83}$$

where Z is the compressibility factor ($Z_{sc}\approx 1$).

Then, $\frac{\rho}{\rho_{sc}}=\frac{V_{sc}}{V}=\frac{1}{B_g}\Rightarrow\rho=\rho_{sc}/B_g$ (2.84)

Substituting Eq. (2.82) and Eq. (2.84) into Eq. (2.81) yields:

$$-\frac{dp}{dx}=\frac{\mu}{k}\frac{q_{sc}}{A}B_g+\beta\rho_{sc}\frac{{q_{sc}}^2}{A^2}B_g \tag{2.85}$$

Integration of the above equation needs special treatment as the gas properties are not constant with pressure change, the pseudo-pressure is introduced(Al-Hussainy et al., 1966): $m(p)=2\int_{p_1}^{p_2}\frac{p}{\mu Z}dp$ (2.86)

By applying Liebnitz's rule to differentiate the above integral, we obtain:

$$\frac{\partial m(p)}{\partial x}=2\frac{p}{\mu Z}\frac{\partial p}{\partial x} \tag{2.87}$$

Replacing $\frac{dp}{dx}$ in Eq. (2.85) by Eq. (2.87) and B_g by its definition (Eq.(2.83)):

$$-\frac{T_{sc}}{2p_{sc}T}\frac{\partial m(p)}{\partial x}=\left[\frac{1}{k}\frac{q_{sc}}{A}+\beta\rho_{sc}\frac{{q_{sc}}^2}{\mu A^2}\right] \tag{2.88}$$

Separating variables and integrating on each side:

$$-\frac{T_{sc}}{2p_{sc}T}\int_{p_1}^{p_2}dm(p)=\int_0^L\left[\frac{1}{k}\frac{q_{sc}}{A}+\beta\rho_{sc}\frac{{q_{sc}}^2}{\mu A^2}\right]dx$$

One can get $$\frac{m(p_1)-m(p_2)}{2p_{sc}T/T_{sc}}=\left[\frac{1}{k}\frac{q_{sc}}{A}+\beta\rho_{sc}\frac{{q_{sc}}^2}{\bar{\mu}A^2}\right]L \tag{2.89}$$

From Darcy's law: $q_{sc}B_g=-\frac{k_aA}{\mu}\frac{dp}{dx}$ (2.90)

For steady state laminar flow: $q_{sc} = \frac{k_a A}{2L} \frac{m(p_1) - m(p_2)}{p_{sc} T / T_{sc}}$ (2.91)

Combining Eq. (2.89) with Eq. (2.91), it is obtained:

$$\frac{1}{k_a} = \frac{1}{k} + \beta \rho_{sc} \frac{q_{sc}}{\bar{\mu} A} \tag{2.92}$$

where $\bar{\mu}$ is taken at mean pressure.

2.6 Finite element model

After developing the general porosity model, we will incorporate it into the field equation (Eq. (2.23)). By expanding the first term on the LHS of Eq. (2.23) and taking Eq. (2.20) and (2.47) into account, one can obtain:

$$\frac{\partial}{\partial t}\left(\frac{p\phi}{Z}\right) = \frac{p}{Z}\left(\frac{\phi}{K_g} + \alpha\left(\frac{\partial \varepsilon_v}{\partial p} - \frac{\varepsilon_L P_L}{(P_L + p)^2}\right) + \frac{\alpha - \phi}{K_s}\right)\frac{\partial p}{\partial t} \tag{2.93}$$

where K_g is the gas bulk modulus.

As $\frac{\phi}{K_g} + \frac{\alpha - \phi}{K_s} = \frac{1}{M}$ where M is the Biot modulus, Eq.(2.93) could be rewritten as:

$$\frac{\partial}{\partial t}\left(\frac{p\phi}{Z}\right) = \frac{p}{Z}\left(\frac{1}{M} + \alpha \frac{\partial \varepsilon_v}{\partial p} - \alpha \frac{\varepsilon_L P_L}{(P_L + p)^2}\right)\frac{\partial p}{\partial t} \tag{2.94}$$

B_g is the gas formation volume factor with the definition in Eq.(2.83) and Z is the compressibility factor which is shown in the gas flow equation in Zhang et al.(2008).

By substituting Eq. (2.94) and (2.83) into the LHS of Eq. (2.23), it yields:

$$\frac{p}{Z}\left(\frac{1}{M}+\alpha\frac{\partial\varepsilon_v}{\partial p}-\alpha\frac{\varepsilon_L P_L}{(P_L+p)^2}\right)\frac{\partial p}{\partial t}+\frac{B_g\rho_r V_L P_L}{(p+P_L)^2}\frac{p}{Z}\frac{\partial p}{\partial t}=\nabla\cdot(k_a\frac{p}{\mu Z}\nabla p)+\gamma\frac{RT}{M_g} \quad (2.95)$$

By taking the derivative of pseudo-pressure (Eq.(2.86)) with respect to time, we obtain:

$$\frac{\partial m(p)}{\partial t}=2\frac{p}{\mu Z}\frac{\partial p}{\partial t} \quad (2.96)$$

Substituting Eq.(2.87) and (2.96) into Eq.(2.95) and assuming constant k_a, finally we get:

$$\alpha\frac{2p}{\mu Z}\frac{\partial\varepsilon_v}{\partial t}+\left(\frac{1}{M}+\frac{\left(B_g\rho_r V_L-\alpha\varepsilon_L\right)P_L}{(p+P_L)^2}\right)\frac{\partial m(p)}{\partial t}=\frac{k_a}{\mu}\nabla^2 m(p)+\gamma\frac{2RT}{\mu M_g} \quad (2.97)$$

Taking Eq. (2.3) and (2.87) into the Navier-type equation (2.13), it could be rewritten as:

$$G\nabla^2 u_i+\frac{G}{1-2\nu}u_{k,ki}-\left(\alpha+K\frac{\varepsilon_L P_L}{(P_L+p)^2}\right)\frac{\mu Z}{2p}m(p)_{,i}+f_i=0 \quad (2.98)$$

Therefore, a coupled poroelastic model (Eq. (2.97) and (2.98)) is constructed to describe the interaction between gas diffusivity and rock mass deformation.

The above coupled set of equations can be rewritten as the follows by eliminating the body force and source/sink terms (γ):

$$\left(K+\frac{G}{3}\right)\nabla(\nabla\cdot\mathbf{u})+G\nabla^2\mathbf{u}-\mathbf{M}\left(\alpha+K\frac{\varepsilon_L P_L}{(P_L+p)^2}\right)\frac{\mu Z}{2p}\nabla m(p)=0 \quad (2.99)$$

$$\alpha\frac{2p}{\mu Z}\frac{\partial\varepsilon_v}{\partial t}+\left(\frac{1}{M}+\frac{\left(B_g\rho_r V_L-\alpha\varepsilon_L\right)P_L}{(p+P_L)^2}\right)\frac{\partial m(p)}{\partial t}-\frac{k_a}{\mu}\nabla^2 m(p)=0 \quad (2.100)$$

where $\mathbf{u}$ represents the displacement vector, $\mathbf{M}=[1,1,0]^{\mathrm{T}}$ for plane strain cases and $\mathbf{M}=[1,1,1,0,0,0]^{\mathrm{T}}$ for three dimension applications.

Since the coefficients, such as p, μ and Z, are not constant and are incorporated in the coefficients of the field equations (Eq. (2.99) and (2.100)), the system is non-linear and hence not amenable to analytical solutions. Thus, a numerical method is required to solve these non-linear partial differential equations (PDE) with certain initial and boundary conditions.

Considering this is a non-linear poroelastic problem, the finite element method is adopted in this study. Eight-node quadrilateral elements are used to compute solid displacement vector, $\boldsymbol{u}$, while four-node quadrilateral element is applied to calculate pseudo-pressure $\boldsymbol{m}(\boldsymbol{p})$. The unknowns ($\boldsymbol{u}$ and $\boldsymbol{m}(\boldsymbol{p})$) can be approximated by the following functions:

$$u=N_u\tilde{u} \qquad\qquad m(p)=N_p m(\tilde{p}) \tag{2.101}$$

where N_u and N_p are the conventional shape functions and $\tilde{u}$ and $m(\tilde{p})$ are the vectors of the nodal displacement and pseudo-pressure respectively. Galerkin's finite element method (GFEM) is then used to discretize the field equations in spatial domain.

$$K\dot{\tilde{u}} - A\cdot m(\dot{\tilde{p}}) = \dot{f} \tag{2.102}$$

$$L^T\dot{\tilde{u}} + Sm(\dot{\tilde{p}}) + H_H m(\tilde{p}) = 0 \tag{2.103}$$

where

$$K = \int_{V_e} B^{\mathrm{T}} DB dV \tag{2.104}$$

$$A = \int_{V_e} [B]^{\mathrm{T}} \left[M\left(\alpha + K\frac{\varepsilon_L P_L}{(P_L+p)^2} \right)\frac{\mu Z}{2p} \right] [N_p] dV \tag{2.105}$$

$$L = \int_{V_e} [B]^{\mathrm{T}} \left[\alpha \frac{2p}{\mu Z} \mathrm{M} \right] \left[\mathrm{N}_p \right] dV \tag{2.106}$$

$$S = \int_{V_e} \left[\mathrm{N}_p \right]^{\mathrm{T}} \left[\frac{1}{M} + \frac{\left(B_g \rho_r V_L - \alpha \varepsilon_L \right) P_L}{(p + P_L)^2} \right] \left[\mathrm{N}_p \right] dV \tag{2.107}$$

$$H_H = \int_{V_e} \left[\nabla \mathrm{N}_p \right]^{\mathrm{T}} \left[\frac{k_a}{\mu} \right] \left[\nabla \mathrm{N}_p \right] dV \tag{2.108}$$

Within the complete expression of each term, V_e represents the element area, f denotes the external applied forces, B and D are the strain-displacement matrix and stress-strain matrix respectively.

For the temporal discretization, the following equation is taken into Eq. (2.102) and (2.103) with an implicit variable θ.

$$\tilde{\mathrm{p}}_{n+1} = \tilde{\mathrm{p}}_n + \theta(\Delta t)\dot{\tilde{\mathrm{p}}}$$

where Δt is the time increment; the variable θ is bounded between 0.5 (Crank-Nicolson implicit scheme) and 1.0 (fully implicit scheme) for stability; subscript n represents the last time step. After some algebraic work, we finally obtain the following discretization equations:

$$\begin{bmatrix} K & -A \\ -L^T & -\left(S + \theta \Delta t H_H \right) \end{bmatrix} \begin{bmatrix} \Delta \tilde{\mathrm{u}} \\ \Delta \mathrm{m}(\tilde{\mathrm{p}}) \end{bmatrix} = \begin{Bmatrix} \Delta \mathrm{f} \\ H_H \mathrm{m}(\tilde{\mathrm{p}})_{t_{n-1}} \Delta t \end{Bmatrix} \tag{2.109}$$

where Δt is the time increment; implicit variable θ is bounded between 0.5 and 1.0 for stability; subscript t_{n-1} represents the time of last step. It is obvious that the "stiffness" matrix of the above FEM formula is unsymmetrical. Thereafter, an unsymmetrical solver

is utilized to solve the above equations (Smith and Griffiths, 1997). For the far-field boundary, a no flow condition is applied.

As the natural gas properties which are not constant and change with $\tilde{p}_{t_n}$ (pore pressure at current time step), are included in the "stiffness" matrix, a nonlinear iterative method (see Appendix VI) is needed in the numerical procedure. A tolerance value (0.2%) is set to check the convergence in every iteration process during each time step.

In this finite element model, the nodal variables u and $m(p)$ can be solved directly from Eq. (2.109). Then, the total and effective stresses, which are not primary variables, can be computed through Eq. (2.5) and (2.11) at Gauss integration points of each element.

2.7 Verification

The finite element model for gas flow is verified by comparing its predictions with the analytical solution of production from a well in a poroelastic rock by assuming that gas properties are linear function of pressure and temperature. In this numerical analysis, the reservoir dimension is $10\text{m} \times 10\text{m}$. Considering the axial symmetry of the wellbore geometry and trying to reduce the computational density, only a quadrant of reservoir is running to simulate gas flow and reservoir deformation, as shown in Figure 11. The finite element mesh and element geometry are also presented in Figure 11.

Under plane strain conditions, the production of gas within the wellbore can be simulated by decreasing the pore pressure on the wellbore wall at very initial (as t=0). Then, a wellbore with radius ($a = 0.1\text{m}$) is located in the center of the reservoir and its bottom hole pressure (BHP) should be set lower than the reservoir pressure since gas production.

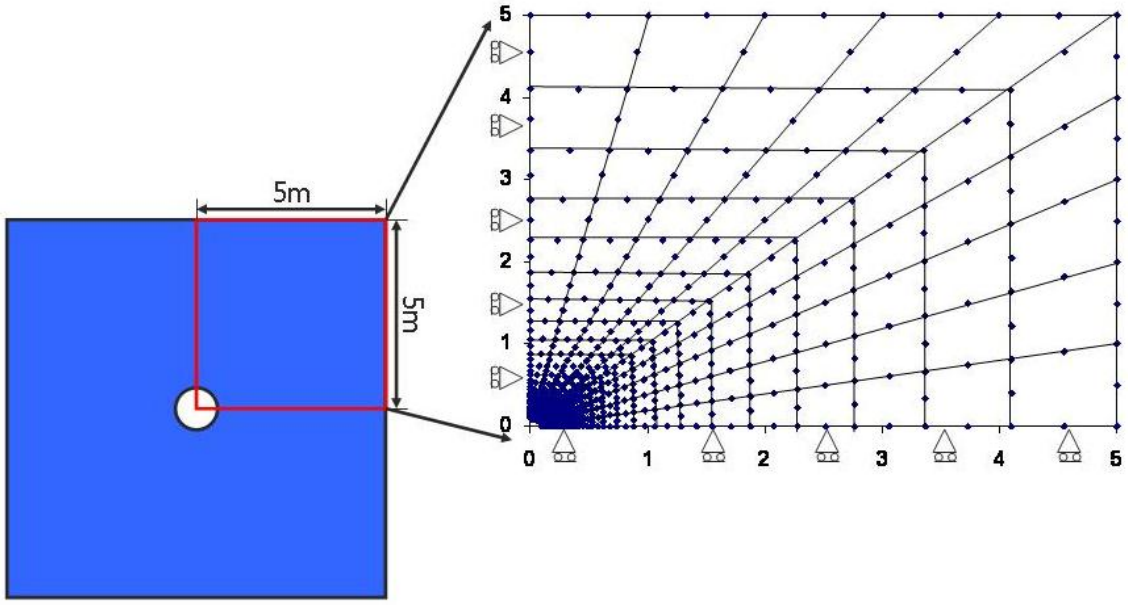

Figure 11 Reservoir and mesh geometry

In order to solve field equation (2.99) and (2.100), proper initial and boundary conditions need to be specified first. In this study, the initial reservoir pressure is set to be 28.27MPa and the BHP at wellbore is 15 MPa and kept constant with time under isothermal conditions.

As for the far field boundary, constant pressure is maintained. And there is no mechanical loading acting on any part of the reservoir. In order to highlight the matrix deformation caused by gas flow, the in-situ stress state is assumed to be isotropic during the verification process. All reservoir parameters and gas properties for the FEM are given in Table 2, which are mainly extracted from Palmer et al. (2007), Zhang et al. (2008), Montgomery et al. (2005) and Kale et al. (2010).

In the poroelastic model, the BHP at the wellbore is suddenly reduced from 28.27MPa and maintain at 15 MPa for gas production. The profiles of the pore pressure variation and induced total radial and tangential stresses (*compression is considered positive*) around the wellbore are depicted in Figure 12, 13, and 14, respectively. The analytical solution (given in Appendix) is also shown for comparison. It can be seen that tensile tangential stress can be generated close to the wellbore due to gas depletion. From the figures, it is obvious that all the finite element results match very well with the analytical solution at early stage. However, as time goes by, the difference between the two results becomes significant. This difference is caused by the gas compressibility and non-linearity of the natural gas properties, which are not included in the analytical solution.

Poisson's ratio, ν	0.25
Young's modulus, E	20.68GPa
Shear modulus, G	8.27GPa
Initial porosity, ϕ	0.04
Biot's coefficient, α	0.64
Initial permeability, k	0.1 μD
Bulk modulus, K	13.79GPa
Solid bulk modulus, K_s	37.82GPa
Initial reservoir pressure, p_0	28.27MPa
Average system temperature, T	$90^0 C$
Density of gas shale, ρ_r	2.40×10^3 kg/m^3
Min in-situ stress, σ_h	39.01MPa
Max in-situ stress, σ_H	43.34MPa
Langmuir pressure constant, P_L	6.11MPa
Langmuir volume constant, V_L	1.50×10^{-2} m^3/kg
Langmuir volumetric strain constant, ε_L	2.30×10^{-2}

Table 2 Input parameter for single permeability model

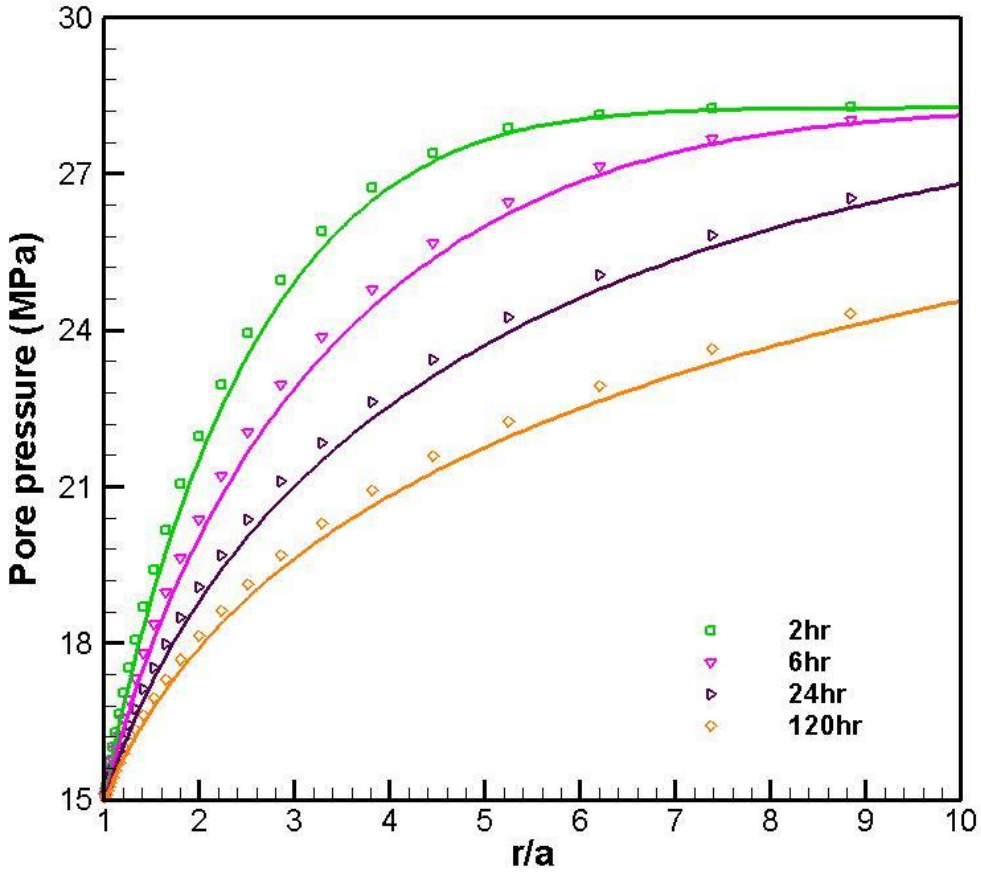

Figure 12 Comparison of numerical results (solid curves) with analytical solution (data markers) for the distribution of induced pore pressure around the wellbore.

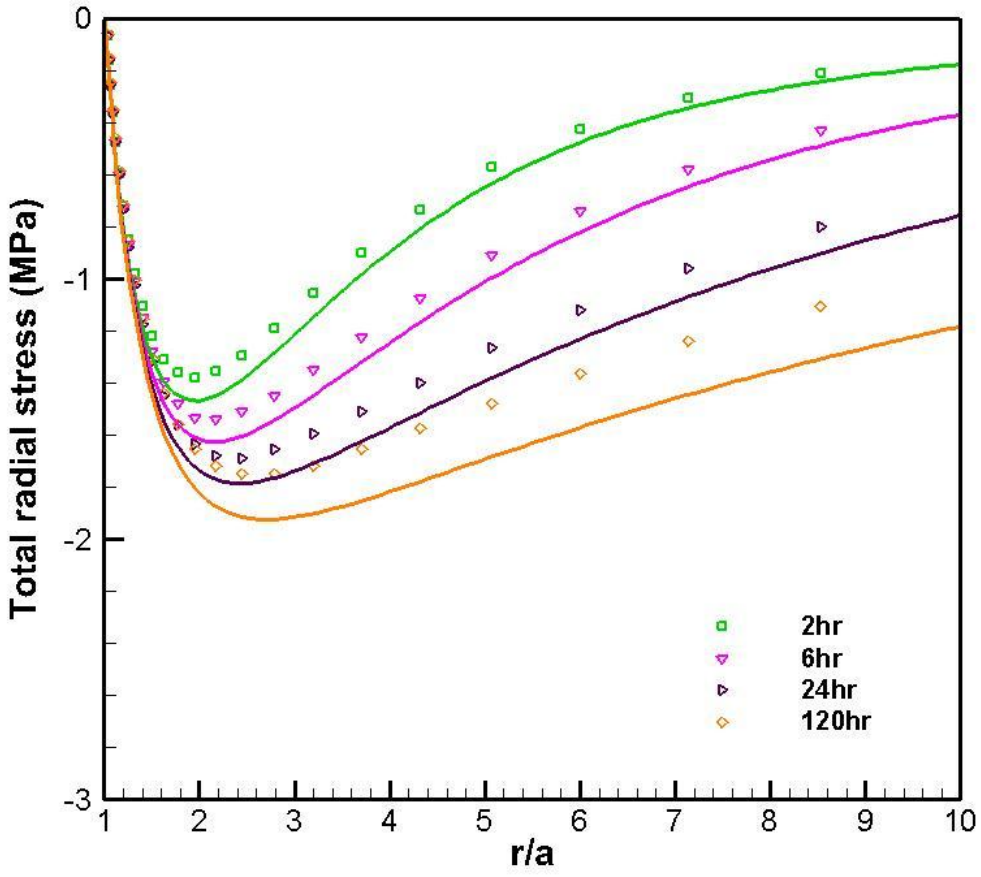

Figure 13 Comparison numerical (solid curves) and analytical solutions (data markers) for induced total radial stress around the wellbore.

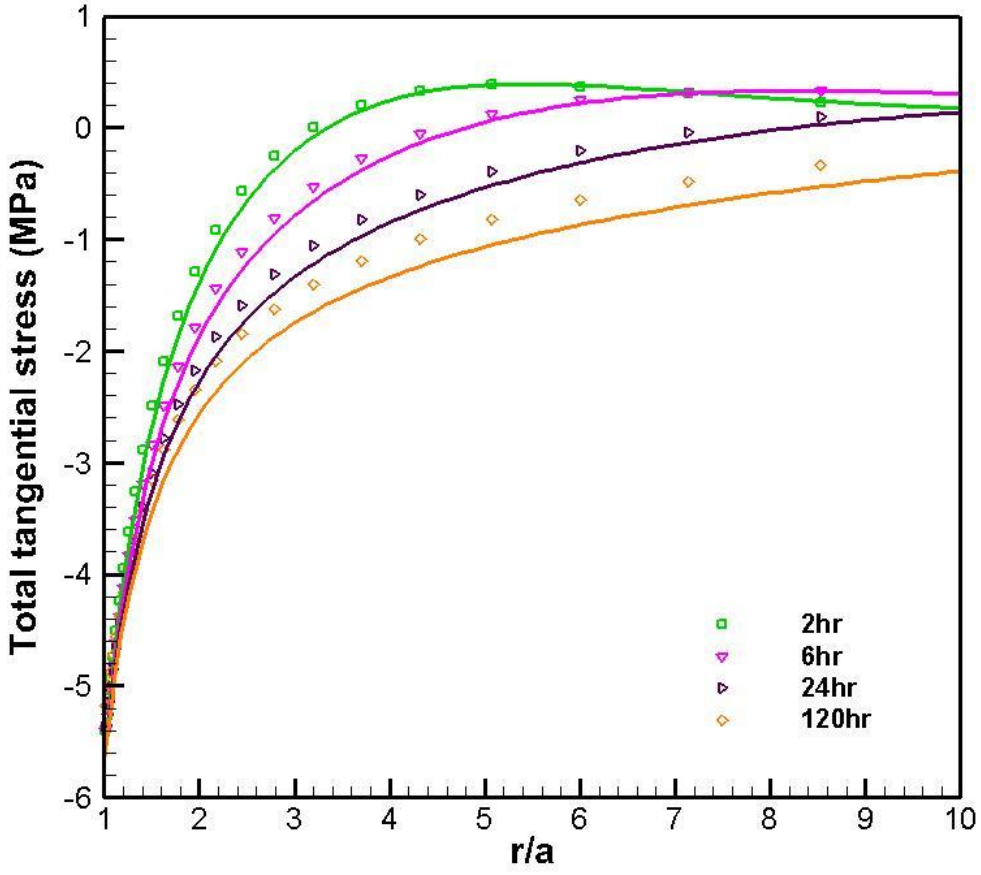

Figure 14 Comparison of numerical (solid curves) and analytical solutions (data markers) for induced total tangential stress.

2.8 Conclusion

In this chapter, a coupled poroelastic model has been successfully constructed to simulate geomechanical reservoir response to gas production process by considering free and adsorbed gas within shale matrix. The gas transport equation for single phase flow has been developed by considering the mass conservation of gas content, including both free and absorbed phase gas, and a real gas law. The amount of adsorbed gas is determined through Langmuir isotherms. The rock constitutive equation and gas transport equation are coupled through the general porosity model and matrix permeability is also simulated during production based on the Beskok-Karniadakis microflow model. These have been implemented in a non-linear coupled poroelastic FEM model in which the nodal variables u and $m(p)$ are treated as unknowns. The model has been verified by comparing its results with the appropriate analytical solution.

CHAPTER III

DUAL PERMEABILITY MODEL

In gas shale and tight sand reservoirs, coupled process between matrix deformation and fluid flow is important for predicting reservoir behavior, pore pressure evolution and fracture closure. In this chapter the dual permeability method (DPM) is implemented in a Finite Element Model (FEM) to investigate fracture deformation and closure and its impact on gas flow in a fractured reservoir. Within the framework of DPM, the fractured rock is treated as dual continuum. Two independent but overlapping meshes (or elements) are used to represent the fractured rock mass: one is the matrix elements used to describe the reservoir matrix deformation and fluid flow within the matrix domain; while the other is the fracture element simulating the fluid flow only through fractures. Both matrix and fractures are assumed to be permeable and the fluid can be exchanged and transported via these two. A quasi steady-state function is used to quantify the flow between the rock matrix and the fractures. By implementing the concept of equivalent fracture permeability, and the shape-factor within the transfer function into DPM, the fracture geometry and orientation are numerically considered and the complexity of the problem is reduced. The stress-dependent fracture aperture is updated as time elapses. Simulation results show that the time evolutions of gas pressure, effective stresses, fracture aperture and permeability are strongly affected by desorption gas during production, especially in the near-wellbore region. Gas desorption retards the influence of the effective stress increase associated with pore pressure reduction during

production. Combination of in-situ stress condition and gas desorption mechanism governs the fracture deformation behavior in fractured reservoirs.

3.1 Introduction

Gas shale is one of the major unconventional reservoirs for natural gas. However, gas production on a fracture network is controlled by the interaction of natural fractures and hydraulic fractures. Experience has shown that often production from fractured wells rapidly declines (Lane et al., 1990; Montgomery et al., 2005; Ross and Bustin, 2009; Schepers et al., 2009). The production decline is believed to be closely related to the fracture permeability evolution with time. In many cases, the fracture permeability is impacted by the time-dependent geomechanical behavior of rock fracture/matrix system. As a result, rock mechanical properties and coupled rock (matrix/fracture) deformation and gas flow are important to predict the reservoir behavior such as pore pressure evolution and fracture closure.

Due to the limitation in fully capturing coupled process of gas flow and pressure dependent mechanical behavior of fractured reservoir within gas shale in analytical and semi-analytical models, many numerical simulators have been developed and applied to gas shale and other unconventional reservoirs.

The discrete fracture network (DFN) is broadly adopted in reservoir simulators to manage fracture propagation and fracture network development, for either hydraulic or natural fracture (Lee et al., 1999; Dershowitz et al., 2000; Karimi-Fard and Firoozabadi, 2001; Sarda et al., 2001; Sarda et al., 2002; Karimi-Fard and Firoozabadi, 2003;

Tamagawa and Tezuka, 2004; Li and Lee, 2006; Kim and Schechter, 2007; Li and Lee, 2008; Bang and Jeon, 2009; Kim and Schechter, 2009; Meyer and Bazan, 2011; Moinfar et al., 2011; Moinfar et al., 2012; Zeng et al., 2012). The DFN approach can provide realistic visualization of fracture network in naturally fractured reservoir. While, the geometry and location of individual fracture is outlined by using unstructured elements and its mechanical influence on fluid flow is imposed explicitly for most DFN cases. Moreover, when using FEM or FDM, the matrix domain needs to be explicitly discretized to fully capture the evolution of fracture network, especially for the area near fractures. Consequently, the computational effort and time consumption is greatly increased by this mesh refinement and hence reduces its applications in highly fractured reservoirs for field cases.

Displacement-discontinuity method (DDM) is another widely accepted approach to address the mechanical performance of fractures during fluid flow process within naturally fractured reservoir (Wardle and Enever, 1983; Priest, 1984; Wardie, 1984; Curran and Carvalho, 1987; Nakagawa et al., 1999; Yacoub and Curran, 1999; Lavrov et al., 2005; Regueiro, 2006; Tao et al., 2009; Zhou and Ghassemi, 2009; Marji et al., 2010). Compared to DFN, the major advantage of this method is that only the fractures (boundary) are discretized which can reduce the computational density greatly. However, this is an indirect boundary element method based on the assumption of homogeneity and continuous stress field whereas discontinuous displacement through fractures.

The continuum method is a good candidate for simulating fracture deformation in naturally fractured medium. Considering the presence of fractures, faults or cracks, a fractured reservoir cannot be treated as an equivalent homogeneous porous medium, as in the conventional continuum model. Alternatively, the dual continuum concept is an extensively used and efficient way to quantify fluid flow within fractured porous media. Within the framework of dual continuum method, the displacement discontinuity behavior of the fractures is neglected and the fluid exchange between matrix and fracture is handled by a transfer term (Barenblatt et al., 1960; Warren and Root, 1963; Kazemi et al., 1976). Compared with DFN, the dual continuum method does not require mesh refinement and no accurate analytical solution for displacement is demanded as DDM. The dual continuum concept can be grouped into two different categories: 1) the dual porosity model; 2) the dual permeability model (DPM). In some papers, these two terms refer to the same method. Theoretically, they are dissimilar in the way the flow channels within the reservoir are set up. In the porosity model, fractures are the only conduits for fluid flow so they need to be connected to deliver fluid to the wellbore; whereas, in DPM, fractures are the major fluid flow channel but the fluid can also move through the permeable matrix block. Fracture network connectivity is not a prerequisite in DPM, when compared with the dual porosity model.

In this chapter, the dual permeability method (DPM) is implemented into the non-linear fully coupled poroelastic finite element model to investigate fracture deformation and closure and its impact on gas flow in naturally fractured reservoir. The primary objective of this work is to simulate the time evolution of gas pressure, effective stresses, fracture

aperture and permeability during fluid depletion process and quantify the influence of matrix and fracture deformation in the vicinity of the wellbore on gas production.

3.2 Dual permeability method

Fluid flow mechanism in a fractured shale reservoir is quite different from that of conventional reservoirs, particularly for gas reservoirs. Two distinct flow regimes coexist in a heterogeneous gas reservoir, as illustrated in Figure 15.

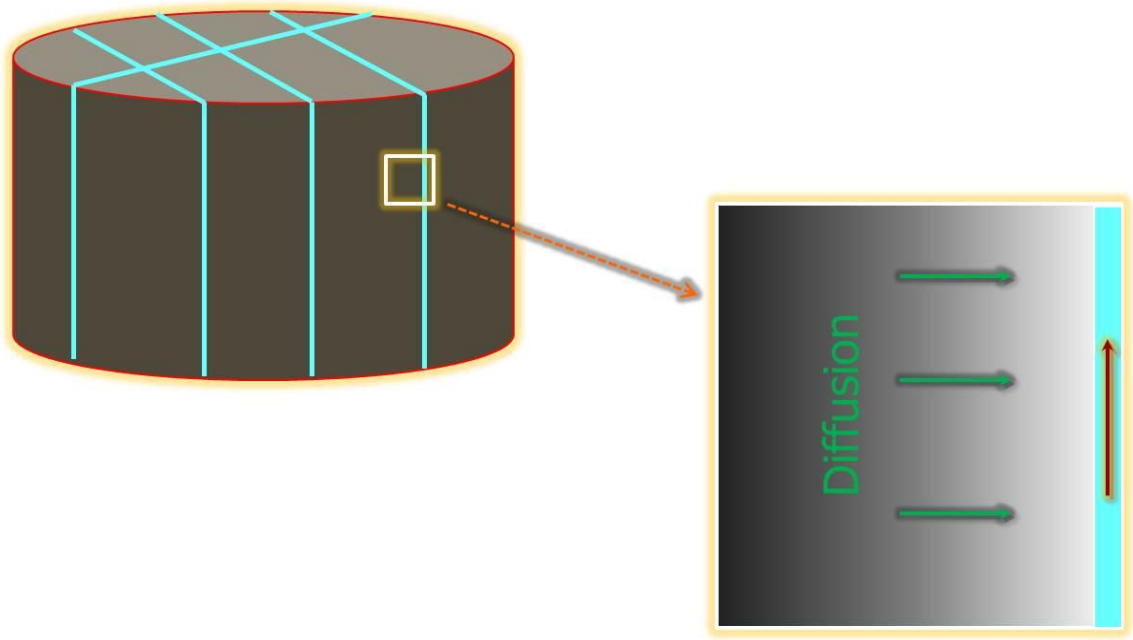

Figure 15 Different flow mechanisms coexist within fractured reservoir

One is the fast flow flushing toward the wellbore through fractures by the imposed appropriate boundary condition for production. The second flow is due to the pressure difference or gradient that is created between the matrix gas and the fracture free gas.

The gas within the matrix pores, including both free gas and adsorbed gas as discussed in Chapter 2, moves out to the adjacent fractures via a "diffusion" process. However, this diffusive flow occurs at a low rate due to the ultra-low permeability of shale matrix.

3.2.1 Dual continuum treatment

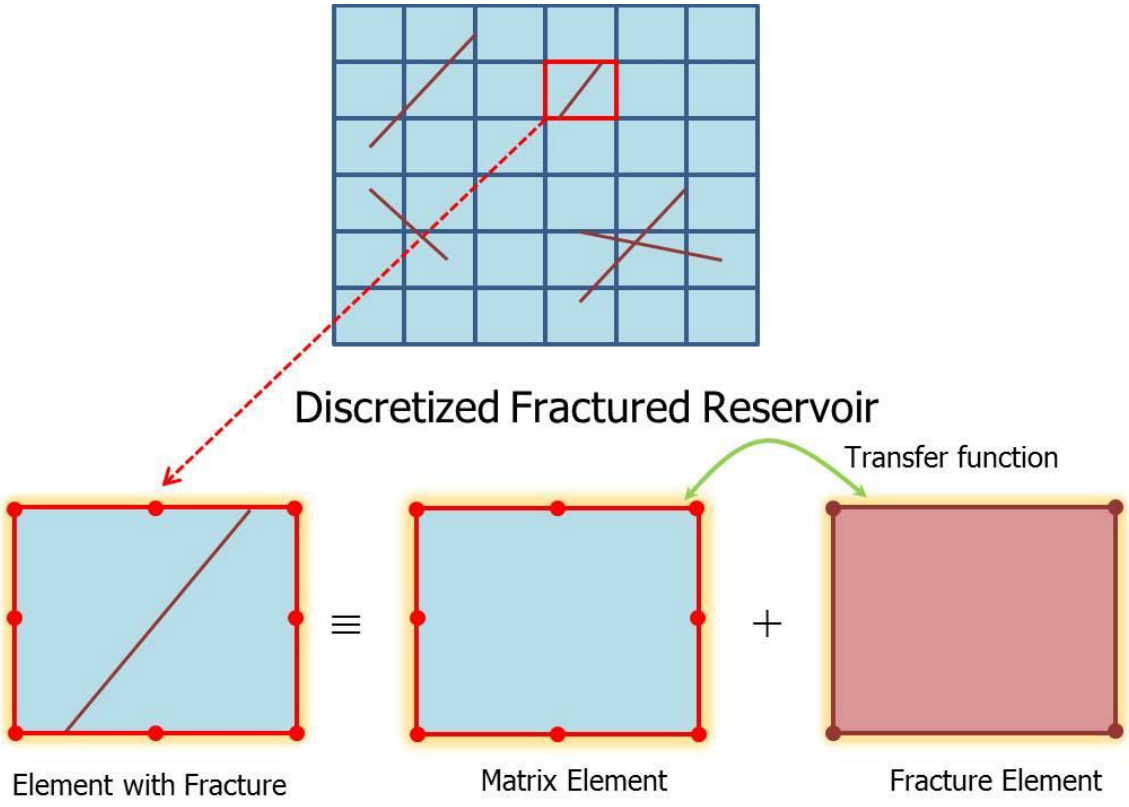

Figure 16 General representation of dual continuum method for discretized fractured reservoir

To simulate this complicated flow phenomenon in fractured porous medium, the dual continuum concept was first introduced to literature by Barenblatt et al. (1960) and incorporated into reservoir simulation by Warren and Root(1963). In this method, the fractured reservoir is treated as a dual continuum in Figure 16. Two independent but

overlapping meshes (or elements) are used to represent the fractured reservoir: one is for the matrix, denoting the reservoir deformation and fluid flow within the matrix domain while the other is for the fractures to simulate fluid flow only through them. The fluid flow within fracture element and matrix element is independent from each other and are only coupled by a transfer term which is used to quantify the two-way fluid exchange between matrix block and its adjacent fractures. Both fracture element and matrix element are characterized in porosity, permeability, pore pressure and other mechanical properties. The fracture elements are distinguished from matrix elements by their high permeability but very low storage. In early works, the geometry of matrix/fracture network was represented by a regular sugar cube and the dual continuum model was only set up for simulating single-phase flow within fractured medium. Kazemi et al. (1976), Rossen (1977), and Saidi (1983) extended the application of this dual continuum theory into developing numerical simulator for modeling multiphase flow. Later, several simulators were developed for more complex situations, like multi-dimension and/or two or multi-phase flow, by employing either finite difference method(FDM) or finite element method(FEM) (Kazemi et al., 1992; Zhang et al., 1996; Lee et al., 1999; Guo et al., 2004; Al-kobaisi et al., 2009; Ramirez et al., 2009; Zhang et al., 2009; Lamb et al., 2010; Moinfar et al., 2011; Zhang et al., 2011). The dual continuum treatment is widely employed in various reservoir simulators, either analytical model or numerical model, to deal with the simultaneous flows in different scales within these highly heterogeneous reservoirs.

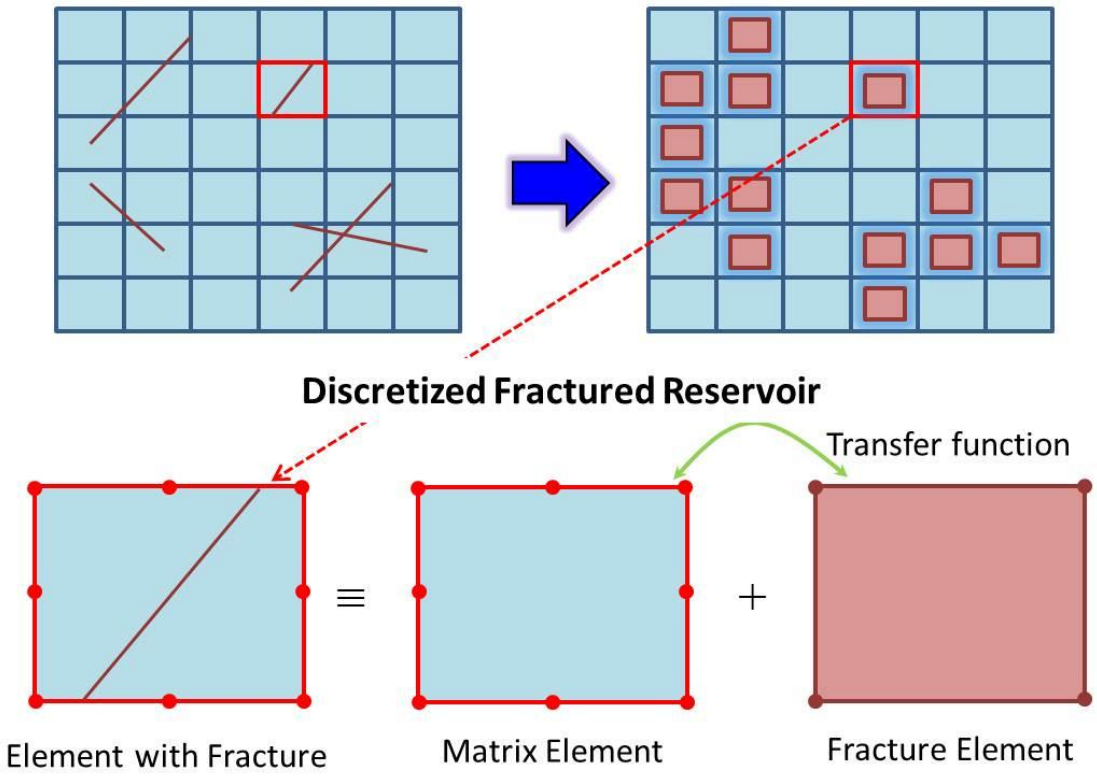

Figure 17 Dual permeability treatment for a fractured reservoir

In the early publications (Barenblatt et al., 1960; Warren and Root, 1963; Kazemi et al., 1976), fractures were assumed to be uniformly distributed within fractured medium and an identical dual permeability was applied to each matrix subdomain. Ganzer (2002) suggested that the elements without fracture could be treated as conventional single permeability (porosity) grid to make the discretized fractured reservoir closer to the complicated geological formation. Thus, the dual permeability treatment is only required for the elements with fractures. As for the elements without fractures, this treatment is not necessary, which is not taken into consideration in conventional dual permeability model. To get the discretized fractured reservoir closer to the real geological formation,

the elements without fractures are kept as conventional single permeability grid as illustrated in Figure 17. This significantly reduces the computational density and efficiently handles the fracture properties and reservoir heterogeneity on an element by element basis.

3.2.2 Dual porosity vs. dual permeability

Under many circumstances, dual porosity and dual permeability mean the same way to deal with fluid flow in heterogeneous fractured reservoir based on the dual continuum concept. However, they are distinguished from each other by treating flow path within matrix block. The key divergence between dual porosity model and dual permeability model is that in the conventional dual porosity model, *global* fluid flow takes place only within the fracture elements. *Local* fluid flow only occurs between matrix element and the intersecting fracture element because of the pressure gradient between matrix pore gas and fracture free gas. As shown in Figure 18, matrix elements only act as source for fluid flow within their adjacent fractures. All matrix elements are isolated from each other and no local fluid exchange between nearby matrix elements is allowed in the dual porosity model. Fractures are the only fluid channels that need to be interconnected with each other to transmit fluid flow through reservoir (da Silva, 1989; Fung, 1993; Gurpinar et al., 1999; Lee et al., 1999; Gurpinar and Kossack, 2000; Donato et al., 2003; Guo et al., 2004; Al-kobaisi et al., 2009; Ramirez et al., 2009; Zhang et al., 2009). The boundary condition is only imposed on the fracture subdomain.

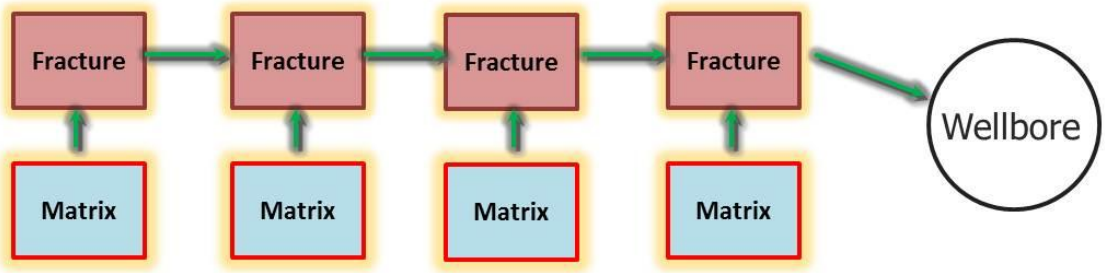

Figure 18 Schematic representation of flow path in dual porosity model

Whereas, Blaskovich et al. (1983) and Hill and Thomas (1985) improved the dual porosity model by introducing fluid interaction between matrix subdomains. Later, series of research works were carried out to investigate the fluid transportation in fractured medium by adopting this dual permeability (modified dual porosity) idea (Blaskovich et al., 1983; Hill and Thomas, 1985; Dean and Lo, 1988; Chawathe et al., 1996; Al-Huthali and Datta-Gupta, 2004; Cicek, 2005; Ding et al., 2006; Alamdari et al., 2012).

In the *dual permeability* model, both matrix and fractures are assumed to be permeable and allowing fluid transport. Fracture elements are still the major channel for delivering the most portion of global fluid flow to the production well. The fluid flow through matrix only contributes a minor part of production due to the low permeability of matrix rock. The local fluid flow can take place between matrix element and fracture element, as in dual porosity model, but it can also move from one matrix block to its neighboring matrix blocks because of the pressure difference between two. Unlike the dual porosity model, matrix element serves as both flow channels and source and storage in dual permeability model, which is closer to reality than the dual porosity model. Both the

fracture and matrix subdomain need to be subjected to boundary conditions in the dual continuum (DC) approach.

In DC model, fracture network connectivity is not a must. Hence, unconnected or isolated fractures can also be considered and contribute to the production, which cannot be dealt in dual porosity model. Though the fluid flushes at an extremely low velocity through matrix blocks, it might address significant influence on the final production and reservoir mechanical response, considering the existence of great heterogeneity and complexity of fracture network within gas shale reservoirs. This effect might not be negligible for long term prediction of production, especially for a field case work. Moreover, the dual permeability model can provide a more accurate description of the flow path in the reservoir than that in the dual porosity model.

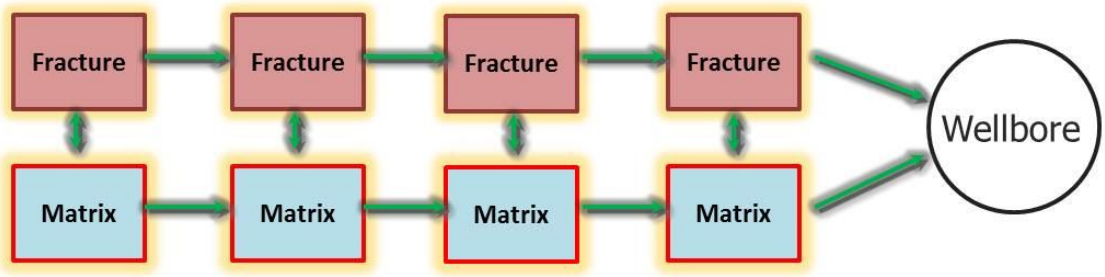

Figure 19 Schematic representation of flow path in dual permeability model

3.2.3 Transfer function

Although dual porosity model and dual permeability model are quite different in theory, they both are based on the dual continuum concept, as depicted in Figure 19, and are all classified as dual continuum method. In the dual continuum treatment, a fractured porous rock is supposed to be composed of two independent but overlapping elements, matrix and fracture element, as discussed previously. For a fracture matrix system, the superposition of those two distinct elements needs to be addressed. The matrix and fracture sub-systems are linked by the fluid interaction between them, which is the heart of dual continuum approach. Both dual porosity and dual permeability models use the same approach to estimate the fluid exchange between matrix and fracture along the open surface of fractures.

A quasi steady-state function, derived by Barenblatt et al. (1960), is commonly used to quantify the fluid transferred between the rock matrix and fractures. Transfer rate per unit matrix volume, $q_{mf}\,(1/s)$, is given as the following expression:

$$q_{mf} = \psi \frac{k_m}{\mu}\left(p_m - p_f\right) \tag{3.1}$$

where $\psi\,(\mathrm{m}^{-2})$ is the shape-factor for reservoir simulation and denotes the area effect of matrix and fracture geometry on the mass transfer between the two; k_m denotes the matrix permeability; μ stands for the fluid viscosity; p_m is the pore pressure within matrix and p_f is the fluid pressure along the fracture. This function is only valid for single phase flow (ignoring capillary effects).

Warren and Root (1963) used a stacked-cubes model to represent a fractured reservoir. In their model, fractures are evenly distributed and act as boundaries between matrix elements. They proposed an analytical solution to estimate the shape factor for single-phase flow:

$$\psi = \frac{4N\left(N+2\right)}{L^2} \tag{3.2}$$

where $N = 1, 2 \, or \, 3$ represents the total number of sets of parallel fractures around one matrix block (as shown in Figure 20); L denotes the characteristic length of a rectangular matrix grid, which is given as:

$$L = \begin{cases} L_x & N = 1 \\ 2L_xL_y / \left(L_x + L_y\right) & N = 2 \\ 3L_xL_yL_z / \left(L_xL_y + L_xL_z + L_yL_z\right) & N = 3 \end{cases} \tag{3.3}$$

where L_x, L_y and L_z represent the matrix block size in three different directions. For the case of a cube, $L = L_x = L_y = L_z$ hence the shape factor equals to $\frac{12}{L^2}$, $\frac{32}{L^2}$ and $\frac{60}{L^2}$ corresponding to 1, 2 and 3 sets of parallel fractures.

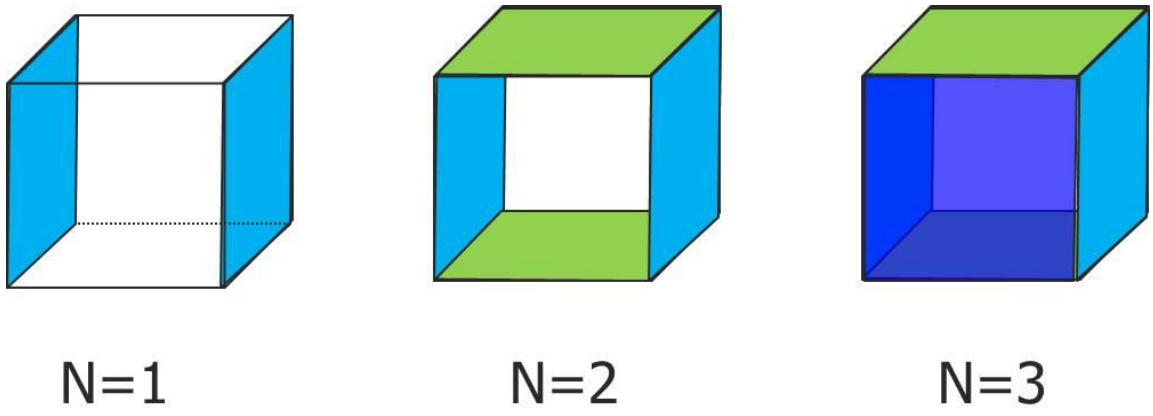

Figure 20 Schematic representation of different sets of fractures

Kazemi et al. (1976) extended Warren and Root's model into simulating multiphase flow. They developed a numerical simulator by using finite difference method. Based on a seven point finite difference scheme, they obtained an expression for shape factor in three-dimension:

$$\psi = 4\left(\frac{1}{L_x^2}+\frac{1}{L_y^2}+\frac{1}{L_z^2}\right) \tag{3.4}$$

In this model, a linear pressure distribution was assumed between the fracture and matrix element center.

Lim and Aziz (1995) derived a shape factor for a non-linear pressure gradient between the fracture and matrix element center. Analytical solution for pressure diffusion within cylindrical block was used to approximate the pressure distribution within matrix block. Without assuming pseudo steady-state flow within matrix, the fracture geometry was combined with the fluid flow mechanism. In their work, the general expression of shape factor for an anisotropic, rectangular shape matrix element was reported as

$$\psi = \frac{\pi^2}{\bar{k}}\left(\frac{k_x}{L_x^2}+\frac{k_y}{L_y^2}+\frac{k_z}{L_z^2}\right) \tag{3.5}$$

where $\bar{k} = \left(k_x k_y k_z\right)^{1/3}$ is the equivalent isotropic permeability for matrix block.

For an isotropic case, the above expression can be simplified to

$$\psi = \pi^2\left(\frac{1}{L_x^2}+\frac{1}{L_y^2}+\frac{1}{L_z^2}\right) \tag{3.6}$$

Eq.(3.6) is quite similar to Eq.(3.4) except for the coefficient term.

Within each fractured element, after calibrating with experimental results, the shape-factor could be computed as (Kazemi et al., 1992; Zhang et al., 1996):

$$\psi = \frac{1}{V}\sum_{j=1}^{J}\frac{A_j}{d_j} \tag{3.7}$$

where A_j is the surface area for one fracture and d_j stands for the distance between the element center and the fracture; J represents the total number of fractures within the element; V is the volume of the element.

3.3 DPM-Poroelastic model

In the early dual permeability models (Blaskovich et al., 1983; Hill and Thomas, 1985), fluid flow, which was uncoupled or partially coupled with rock deformation, was modeled solely in the reservoir simulation. The interactions between fluid flow and rock deformation were usually neglected. However, fluid production from underground

reservoir concerned a fully coupled hydro-mechanical process. During fluid depletion, pore pressure change and reservoir rock/fracture deformation, could inevitably affect each other during the whole reservoir life. Therefore, it is often inappropriate to artificially detach fluid flow from matrix deformation in reservoir simulation.

Naturally, the dual permeability formulation, formed in a fully coupled manner, was required to investigate the realistic response of fractured reservoir to wellbore completion and production. Aifantis (1977) proposed a coupled model in dual porosity/permeability medium without giving formulation. Bai et al. (1993) and Ghafouri and Lewis (1996) derived the constitutive equations to describe the mechanical response of a fractured reservoir to single phase flow. In their work, the dual permeability formulation had been developed and incorporated into a finite element model to construct a numerical simulator for single phase flow. Later, Lewis and Ghafouri (1997) extended this model for simulating multiphase flow through a fractured reservoir and revealed the strong influence of the coupling process between fluid flow and rock deformation by comparing the numerical results with those of uncoupled simulators. Lamb et al.(2010) further improved the model to solve displacement discontinuity within fractured porous medium by incorporating extended finite element method (XFEM). In all of these coupled dual permeability models, only incompressible or slightly compressible fluid was taken into consideration and gas desorption and gas compressibility were not included in the fundamental formulation of these work. Thus, these models are not suitable for predicting reservoir performance and production in gas shale.

Then, Huang and Ghassemi (2011) proposed a fully coupled poroelastic model by using a real gas law and focusing on the impact of adsorbed gas on matrix porosity and permeability evolution, as discussed in chapter 2. In that work, a non-linear fully coupled poroelastic finite element model was developed and applied in performing poroelastic analysis of gas shale deformation. However, that model was built on a single porosity basis and fluid transport equation for fractures was not given.

To take the fracture network and deformation into account, the dual permeability idea is implemented into the non-linear fully coupled poroelastic model, which is derived in Chapter 2 and the fractures are elastic. The governing equation for matrix deformation is identical to that of the single porosity model (Eq.(2.92)).

$$\left(K+\frac{G}{3}\right)\nabla(\nabla\cdot\mathbf{u})+G\nabla^2\mathbf{u}-\mathbf{M}\left(\alpha+K\frac{\varepsilon_L P_L}{(P_L+p_m)^2}\right)\frac{\mu Z}{2p_m}\nabla m(p_m)=0 \qquad (3.8)$$

where p_m is the gas pore pressure within matrix elements; $\mathbf{M}=[1,1,0]^{\mathrm{T}}$ for plane strain cases and $\mathbf{M}=[1,1,1,0,0,0]^{\mathrm{T}}$ for three dimension applications; all other terms use the same definition as in Chapter 2.

In the DPM theory, two distinct but overlapping elements are used to represent the fractured reservoir: one is for the matrix blocks characteristic in high storage but low permeability while the other is for the fracture segments featured in high permeability but low storage. In the mathematic formulation, two different ways are needed to derive fluid continuity equation for matrix element and fracture element.

The transfer term (Eq. (3.1)) is treated as sink for the matrix and a source for the fracture in DPM, respectively. By putting the transfer term as a sink term in Eq.(2.92), the continuity equation for gas shale in a matrix element is given by Eq.(3.9).

$$\alpha \frac{2p_m}{\mu Z}\frac{\partial \varepsilon_v}{\partial t}+\left(\frac{1}{M}+\frac{\left(B_g\rho_r V_L-\alpha\varepsilon_L\right)P_L}{(p_m+P_L)^2}\right)\frac{\partial m(p_m)}{\partial t}-\frac{k_m}{\mu}\nabla^2 m(p_m)=-q_{mf} \tag{3.9}$$

The first term of Eq. (3.9) represents the volumetric strain change of matrix subdomain, whose presence denotes the coupling between fluid flow and rock mechanical response. In the second term, $\frac{1}{M}=\frac{\phi}{K_g}+\frac{\alpha-\phi}{K_s}$ is the inverse of Biot's modulus (under certain conditions represent storage coefficient) of the matrix subdomain and $\frac{\left(B_g\rho_r V_L-\alpha\varepsilon_L\right)P_L}{(p+P_L)^2}$ represents the influence of adsorbed gas on fluid accumulation and the whole second term denotes the fluid accumulation in the matrix blocks. The third term stands for the fluid interaction between adjacent matrix subdomains, which does not show up in the dual porosity model. The RHS term is the fluid exchange between matrix and fracture continua.

By ignoring the gas desorption and coupled matrix deformation and changing the sink term to source term in Eq.(3.9), the gas transportation equation for fracture element is obtained from Eq. 3.9 as below (Bai et al., 1993; Lamb et al., 2010):

$$\frac{1}{M_f}\frac{\partial m(p_f)}{\partial t}=\frac{k_f}{\mu}\nabla^2 m(p_f)+q_{mf} \tag{3.10}$$

where p_f is the gas pore pressure along fracture elements and k_f is the permeability of fracture elements. As $K_g \ll K_s$, the Biot modulus M_f in Eq.(3.10) is expressed as:

$$\frac{1}{M_f} \approx \frac{\phi_f}{K_g} \tag{3.11}$$

with ϕ_f denoting the porosity of fracture and K_g representing the gas bulk modulus in fracture elements. Detailed derivation of fluid continuity equation will be given in Appendix III for free gas case by using the general porosity model given in Chapter 2.

After incorporating the DPM theory into fully coupled poroelastic model for gas shale, the governing equations, including one for matrix rock deformation (Eq.(3.9)) and two for fluid flow through the matrix (Eq.(3.10)) and fracture (Eq.(3.11)), respectively, are successfully derived and are ready for further numerical implementation. In this work, these governing equations are discretized and solved by finite element method later. A DPM-FEM numerical simulator, modeling single phase flow (dry gas) through fractured gas shale, will be developed based on these fully coupled governing equations.

3.4 Fracture permeability

In reservoir formations, both natural fractures and hydraulic fractures usually possess irregular shape and rough surfaces and sometimes are partially closed, as demonstrated in Figure 21. To simplify the computation, a fracture is ideally represented by a set of parallel plates to study the fluid flow through it (Snow, 1965; Witherspoon et al., 1980; Bai et al., 1993).

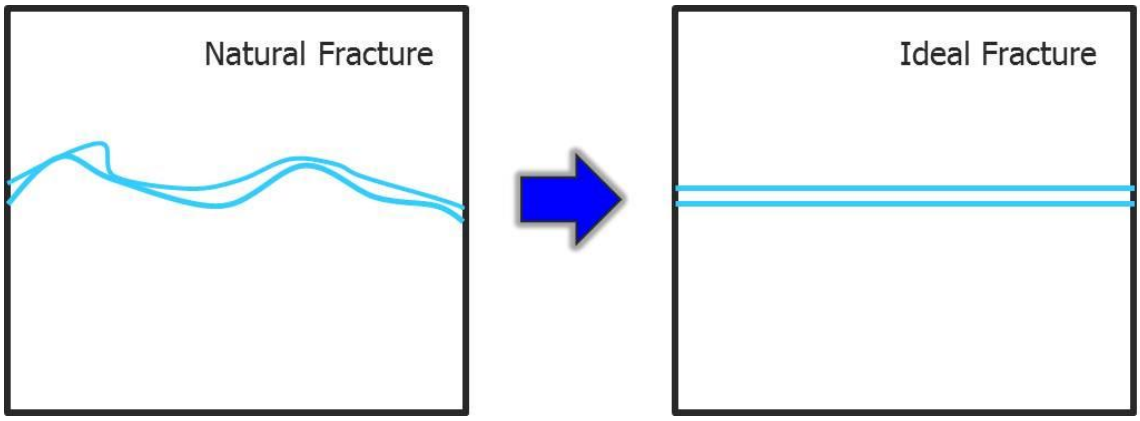

Figure 21 A real natural fracture and its idealized shape for numerical simulation

By assuming laminar flow between two smooth parallel plates, as shown in Figure 22, the analytical solution of Navier-stokes equation in this model yields the following widely used cubic law (Snow, 1965; Witherspoon et al., 1980):

$$Q = -\frac{a^3 w}{12\mu}\frac{\Delta p}{L} \tag{3.12}$$

where Q is the total flux flushing through the fracture space; a is the fracture aperture, which is the distance between two fracture walls, as depicted in Figure 22; w is height of the plate and L is the fracture length; μ is the fluid viscosity; Δp is the pressure drop along the flow direction.

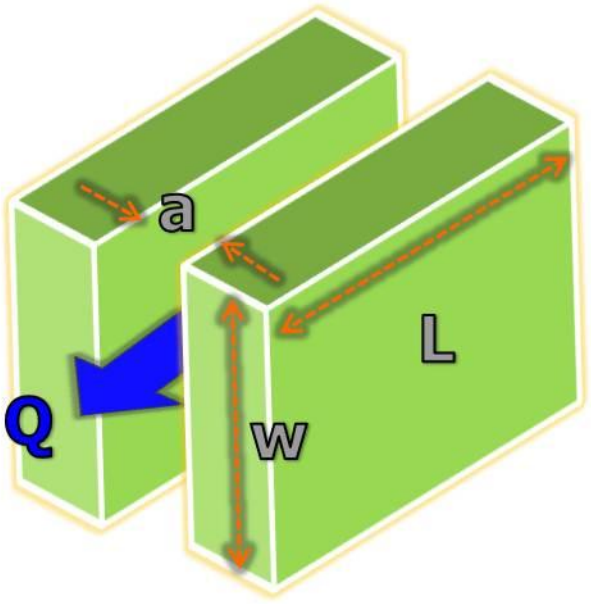

Figure 22 Volumetric flux (Q) between parallel plates with apertures (a), plate height (w) and plate lengths (L)

In one dimension, Darcy's law for fluid flow is given as

$$Q = -\frac{k_{fl} A}{\mu} \frac{\Delta p}{L} \tag{3.13}$$

where k_{fl} is the fracture permeability in the direction parallel to the fluid flow; A is cross-section of fracture perpendicular to the flux, which equals to wa.

From Eq. (3.12) and Eq.(3.13), k_{fl} can be easily derived from the cubic law:

$$k_{fl} = \frac{a^2}{12} \tag{3.14}$$

This relation between fracture aperture and its corresponding permeability is derived from the simple parallel plate model. In the model, the two fracture walls are assumed to be smooth and parallel to each other and separated by a uniform aperture. The flow

through the fracture space is laminar due to the uniform pressure gradient within fracture plane. However, the natural fractures departure these assumptions by their rough surfaces and partially closure at finite points, as shown in Figure 21. All these characteristics of natural fractures diminish the total hydraulic flow passing fracture open space and hence lower the equivalent hydraulic aperture. Therefore, it is inadequate to directly use the Eq.(3.14) to compute fracture permeability for natural fractures.

After validating with the experiment results, Witherspoon et al. (1980) incorporated a friction term into the ideal cubic law to account for the reduction of hydraulic flow. This effective cubic law was proven to be independent with rock type and stress history in their work. The relation between hydraulic aperture and permeability is given as:

$$k_{fl} = \frac{a^2}{12 f} \tag{3.15}$$

where f is the friction term and ranges between 1.04 and 1.65.

Gas deliverability is highly related to the fracture permeability in naturally fractured gas shale reservoir. From Eq. (3.15), it can be seen that the fracture permeability is dependent on hydraulic aperture for either natural fracture or hydraulic fracture. In the conventional dual porosity/permeability models, fracture aperture/permeability as well as some other mechanical properties, are given or computed uniformly over the whole reservoir, as given in Figure 23(I). This reservoir-level equivalent aperture can be only valid for the fracture systems with regular distribution and connection of small scale fractures. This equivalent aperture over reservoir volume is too coarse to confirm real

observation and capture details in local flow phenomena, especially for large scale fractures. However, in gas shale reservoir, hydraulic fractures usually extend hundreds of feet in completion process. If uniform hydraulic aperture is presumed for these large scale fractures in dual permeability model, inaccurate simulation results might be presented (Moinfar et al., 2012).

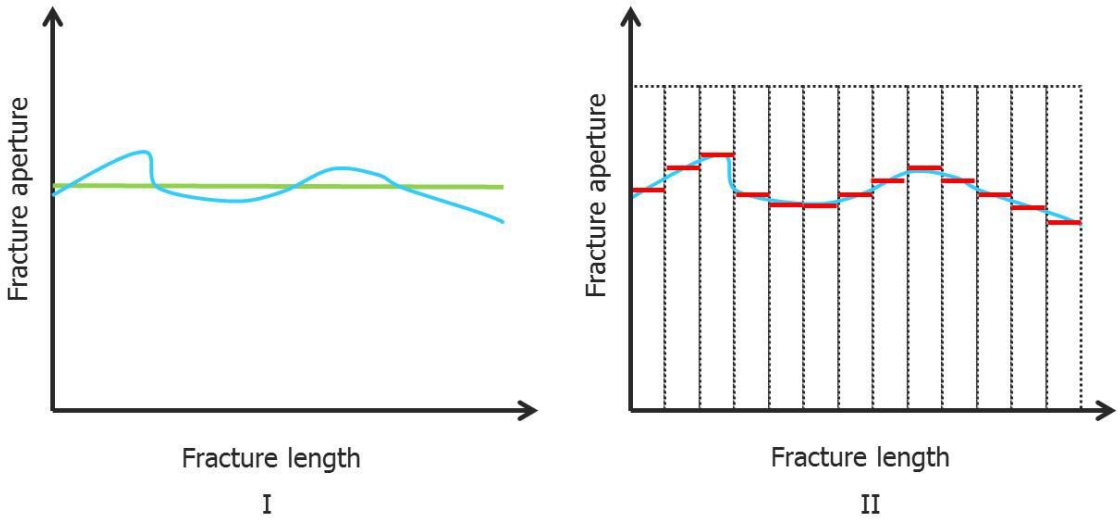

Figure 23 Equivalent fracture aperture: (I) whole reservoir-level average (green line); (II) segmented element-level average (red lines); blue curves represent real fracture aperture along its length.

To fully handle the heterogeneity of complex fractured reservoir and describe the realistic behavior of large scale fractures, these large scale fractures can be discretized into small segmented fractures (Clemo and Smith, 1989). As shown in Figure 23(II), a large scale fracture is modeled as a curve in two-dimension and intersects multiple elements after spatial discretization of whole matrix domain. The intersection of matrix

element and fracture is first determined for dual permeability treatment in this work. Then, within the element containing pieces of fracture, the parallel plate model is applied to represent the segment of fracture by assuming a uniform aperture along the fracture segment only within the corresponding fractured element. This element-level averaged aperture is later used to compute the corresponding fracture permeability only within the intersected elements. However, across the whole reservoir, this element-level averaged aperture varies with position (Figure 23(II)) and time for a single fracture. By discretizing large scale fractures into small segments, the fracture aperture and hence its permeability is no longer constant along the facture length, which better conforms to reality.

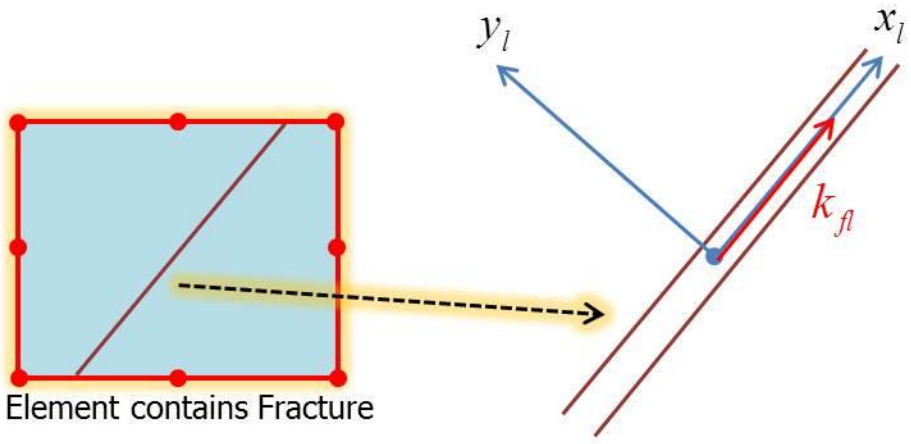

Figure 24 Fracture permeability in local coordinate

Following fracture discretization, fracture permeability (k_{fl}) within each intersected element can be calculated by employing cubic law (Eq.(3.15)). In two dimensions, this is

just the permeability component in the direction parallel to the fracture length, as depicted in Figure 24. By using parallel plate model, the fracture wall is assumed to be impermeable with no slip boundary condition. Thus, the permeability tensor of fracture, aligned to local coordinate system, is given as:

$$\left[k_f\right]=\begin{bmatrix} k_{fl} & 0 \\ 0 & 0 \end{bmatrix} \tag{3.16}$$

It can be seen in Figure 24, as for local coordinate system, x_l-axis is parallel to the fracture length and y_l-axis is normal to the fracture length. k_{fl} is the permeability along x_l direction and can be calculated through Eq.(3.15). The permeability in y_l direction is set to be zero.

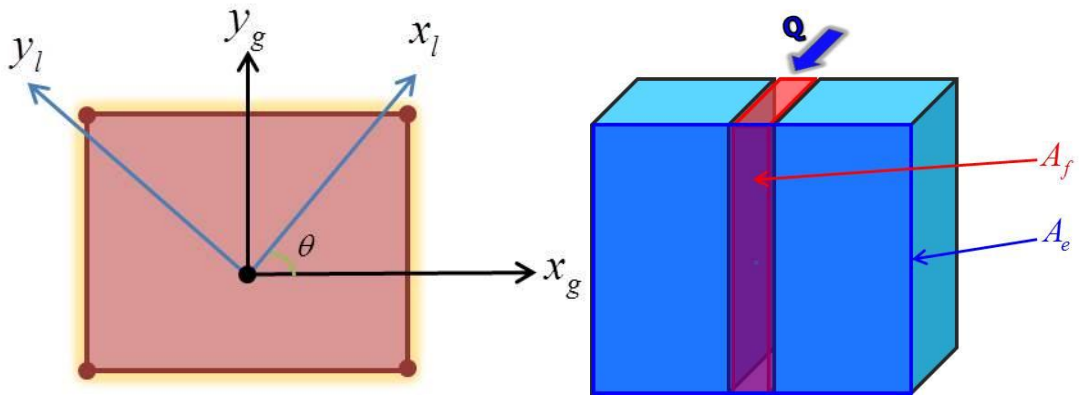

(I) (II)

Figure 25 (I) Rotating local coordinate system to global coordinate system; (II) geometry of fracture in 3D

In most cases, this local coordinate system is not parallel to the global coordinate system of the whole reservoir, especially for complex fracture network. As shown in Figure 25

(I), there always exists a rotation angle θ between the two coordinate systems. As we need to handle and solve the problem in global coordinate, the permeability tensor of every fracture should be stated in global coordinate system.

$$\left[k_{fg}\right]=\left[R\right]^{T}\left[k_{f}\right]\left[R\right] \tag{3.17}$$

where $R=\begin{bmatrix}\cos\theta & \sin\theta\\ -\sin\theta & \cos\theta\end{bmatrix}$ is the rotation tensor. (3.18)

In the rotation tensor, the counter-clockwise rotation direction is defined as positive.

In the framework of dual permeability model, an artificial element is used to compute the fluid flow through the discrete fracture contained within the matrix element. By assuming homogeneous permeability field within the fractured element, an equivalent permeability tensor can be obtained on the element (Lamb et al., 2010):

$$\left[k_{fe}\right]=\frac{A_{f}}{A_{e}}\left[k_{fg}\right] \tag{3.19}$$

where k_{fe} is the equivalent permeability tensor of the fractured element; A_f is the surface area (line length in 2D) of the fracture within the element; A_e denotes the element area (Figure 25 (II)); k_{fg} is the permeability tensor of fracture in the global coordinate system, which is computed from the local permeability tensor of fracture (k_{fl}) through coordinate rotation.

This equivalent permeability tensor is an averaged tensor over the area of the fracture element. By doing so, the fluid flow through the fracture element is a good analogue to the flow through the fracture. In this way, the total fluxes via fractures are evaluated over

the element volume to ensure the mass conservation for each fracture element. For a complex fracture network, the matrix block might be intersected by several fractures which are not uniformly distributed in the matrix element. In this case, a generalized expression of equivalent fracture permeability tensor is given as

$$\left[k_{fe}\right]=\sum_{i=1}^{n}\frac{A_{fi}}{A_e}\left[k_{fgi}\right] \tag{3.20}$$

where n represents the total number of fractures within a fracture element; A_{fi} is the surface area for one fracture and k_{fgi} is its permeability tensor aligned to global coordinate system.

In the dual permeability treatment, the equivalent fracture permeability is only computed within each fractured element (grid) by assuming homogeneous permeability field within the corresponding fractured element and matrix element. Each element can have a different permeability field as the whole reservoir is not homogenous (matrix and fracture properties can vary). By discretizing large scale fractures into discrete fragments, the fracture aperture and hence its permeability varies along the fracture length. In the application of equivalent fracture permeability, the fractures are not required to be well connected or regularly distributed. Inclined, isolated, or connected fractures and multi-scale fractures can be all handled over the control volume of fracture element.

By adopting the idea of discrete fracture, equivalent fracture permeability and shape-factor within the transfer function in the DPM, the complex fracture geometry and

orientation are numerically considered and the complexity of the problem is reduced. In this way, the mesh refinement is not required for DPM, even for a slightly coarse mesh. That is the reason this method is used herein to predict the geomechanical evolution of fractured reservoirs, which are highly heterogenous.

3.5 Fracture deformation

During gas production in gas shale reservoir, coupled gas flow and matrix deformation will cause a change in fracture aperture and consequently alter the fracture permeability with time. The time evolution of fracture permeability will simultaneously influence the fracture fluid flow and matrix deformation, especially for long term production. So the fracture deformation, either opening or closure, should be considered in the numerical simulator to sketch the real mechanical behavior of fractures.

The two walls of fractures are usually not smooth and contacts with each other at some finite points. These rough fractures will undergo two modes of deformation, normal or shear-dilation, which are determined by the stress state in the local coordinate system.

In the finite element formulation of DPM, the nodal variables u , $m(p_m)$ and $m(p_f)$ can be solved directly from Eq.(3.8), (3.9) and (3.10). Then, the total and effective stresses, which are not primary variables, can be computed at Gauss integration points through Eq.(3.21) and (3.22) (tension is considered positive).

$$\sigma_{ij} = (K - \frac{2G}{3})\varepsilon_{kk}\delta_{ij} + 2G\varepsilon_{ij} - \alpha p_m \delta_{ij} - K\varepsilon_s \delta_{ij} \tag{3.21}$$

$$\sigma_{ij}^{'} = \sigma_{ij} + \alpha p_m \delta_{ij} \tag{3.22}$$

After computing the total stress tensor of fracture (σ_f) aligned with the global coordinate system, the local total stress tensor of fracture σ_{fl} can be easily derived through coordinate rotation, which have been employed to compute fracture permeability in global coordinate:

$$\left[\sigma_{fl}\right] = \left[R\right]\left[\sigma_f\right]\left[R\right]^T \tag{3.23}$$

where $R = \begin{bmatrix} \cos\theta & \sin\theta \\ -\sin\theta & \cos\theta \end{bmatrix}$ in which θ is the rotation angle between the two coordinate systems with the counter-clockwise rotation direction defined as positive.

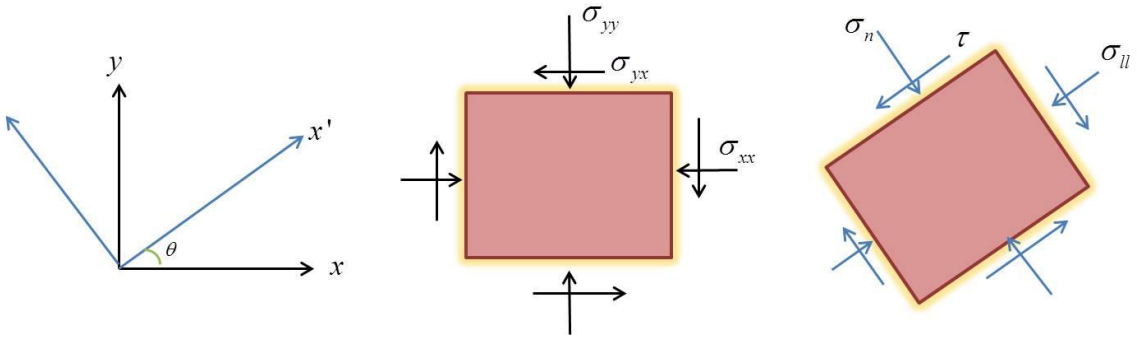

Figure 26 Rotating stress tensor from global coordinate system to local coordinate system, where x'-axis is parallel to a fracture surface and y'-axis is normal to it.

As shown in Figure 26, the stress tensor in global coordinate system is given as $\left[\sigma_f\right] = \begin{bmatrix} \sigma_{xx} & \sigma_{xy} \\ \sigma_{yx} & \sigma_{yy} \end{bmatrix}$; while stress tensor in local coordinate system is $\left[\sigma_{fl}\right] = \begin{bmatrix} \sigma_{ll} & \tau \\ \tau & \sigma_n \end{bmatrix}$.

The normal stress σ_n acting on the fracture surface is the second diagonal term of σ_{fl}

and shear stress τ is the off-diagonal term in the local total stress tensor. After that, the effective normal stress $\sigma_n^{'}$ on the same fracture surface can be calculated by the following equation (compression is considered as positive):

$$\sigma_n^{'} = \sigma_n - p_f \tag{3.24}$$

3.5.1 Normal deformation

Because of the discontinuity between two fracture walls, a fracture is easier to deform than the intact rock mass. The normal deformation is caused by the variation of effective normal stress $\sigma_n^{'}$ acting on the fracture surface: the fracture walls tend to move towards each other with increase of the effective normal stress, as shown in Figure 27; and the fracture walls will move apart due to the decrease of the effective normal stress. The magnitude of fracture opening or closure in normal direction is controlled by the effective normal stress as well as the fracture stiffness.

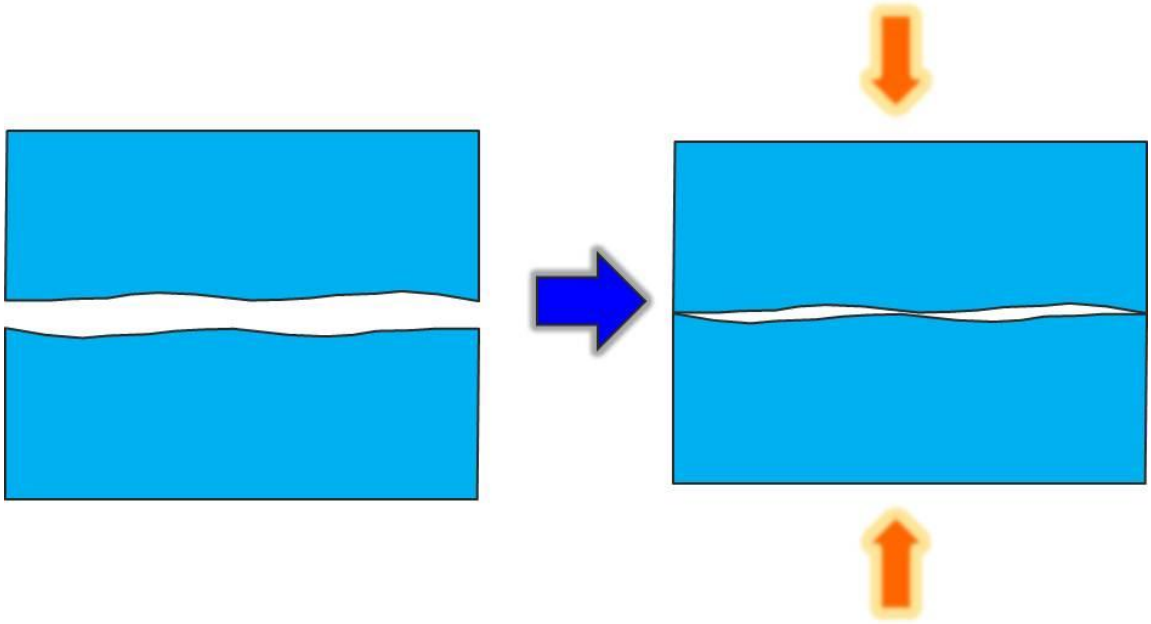

Figure 27 Normal deformation of a rough fracture

Goodman (1976) investigated the stress-displacement relationship for artificial fractures in rock samples. He proposed a hyperbolic relationship to describe the fracture closure in normal direction:

$$\frac{\sigma_n^{'} - \sigma_{ni}^{'}}{\sigma_{ni}^{'}} = A\left(\frac{u_n}{u_m - u_n}\right)^B \tag{3.25}$$

where $\sigma_{ni}^{'}$ is the initial effective normal stress; A and B are empirical constants; u_m represents the maximum normal displacement for fracture closure; u_n is the normal displacement under effective normal stress $\sigma_n^{'}$. In his model, the fracture closure is governed by the initial stress and maximum displacement of fracture.

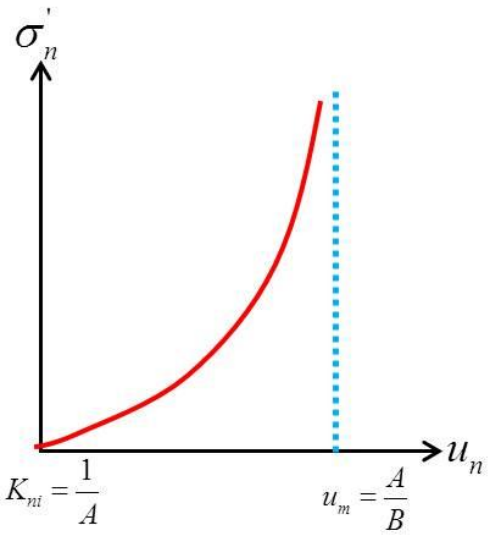

Figure 28 Hyperbolic relationship between stress and displacement of a fracture.

Barton et al. (1985) suggested another hyperbolic relationship to model the stress-deformation behavior of fractures based on experiment results of natural fractures within different rock types:

$$\sigma_n' = \frac{u_n}{A - Bu_n} \tag{3.26}$$

where A and B are empirical constants.

As shown in Figure 28, the initial fracture stiffness is given as:

$$K_{ni} = \frac{\sigma_n'}{u_n}\Big|_{u_n \to 0} = \frac{1}{A} \tag{3.27}$$

And the maximum normal displacement is expressed as: $u_m = \frac{A}{B}\Big|_{\sigma_n' \to \infty}$ (3.28)

Then, after substituting the constants A and B with Eq. (3.27) and (3.28), Eq.(3.26) can be stated as:

$$\sigma_n^{'} = K_{ni} \frac{u_n}{1 - u_n / u_m} \tag{3.29}$$

Eq.(3.29) can be rewritten as: $$u_n = \frac{u_m}{1 + K_{ni} u_m / \sigma_n^{'}} \tag{3.30}$$

Then, in Barton-Bandis constitutive model, the fracture closure is expressed as a function of effective normal stress and initial stiffness of fracture.

In Eq.(3.30), u_m and u_n are the normal joint displacements and can be expressed by the fracture aperture, which denotes the distance between two fracture walls.

$$a_m = u_m \tag{3.31}$$

$$a_n = u_m - u_n \tag{3.32}$$

where a_m is the aperture at zero normal stress and a_n is the fracture aperture under effective normal stress $\sigma_n^{'}$. By replacing u_m and u_n with Eq.(3.31) and (3.32) into Eq.(3.30) , one can get:

$$a_n = \frac{a_m}{1 + \sigma_n^{'} / (K_{ni} a_m)} \tag{3.33}$$

Barton et al. (1985) also offered the empirical formulae to compute K_{ni} and a_m in terms of fracture roughness (JRC), wall strength (JCS) and mean aperture. However, there are so many unknowns which need be specified or measured.

For the case of 90% fracture closure: $u_n = 0.9u_m$ (3.34)

By putting Eq.(3.34) and (3.31) into Eq.(3.29), the expression for 90% closure effective normal stress σ'_{ref} can be obtained:

$$\sigma'_{ref} = 9K_{ni}a_m \tag{3.35}$$

Substituting the term $K_{ni}a_m$ in Eq.(3.33) by Eq.(3.35), the fracture aperture can be calculated by:

$$a_n = \frac{a_m}{1+9\sigma'_n / \sigma'_{ref}} \tag{3.36}$$

This stress-aperture relationship is derived based on Barton-Bandis constitutive model and widely used in literature to model fracture normal deformation (Hicks et al., 1996; Willis-Richards et al., 1996; Rahman et al., 2002). Form Eq. (3.36), it can be seen that fracture aperture during normal loading is a function of effective normal stress (σ'_n), the stress-free aperture (a_m) and the 90% closure stress (σ'_{ref}). By using the relationship, the pressure-dependent fracture aperture in normal deformation can be updated explicitly as time elapse and stress changes.

3.5.2 Shear dilation

When subjected to shear stress under in-situ conditions, the fracture walls are likely to slip over each other in the direction parallel to the fracture surfaces. Due to the offset of the two uneven fracture walls, the aperture of the fracture might also change, as shown

in Figure 29. This shear-dilation induced aperture variation has been proven by the experiment results (Barton et al., 1985). Probably, this stimulated aperture, caused by shear slippage, can cause the enhancement of the fracture permeability and hence affect the hydro-mechanical behavior of rock mass. Thus, the shear-dilation behavior of natural fractures should be included in the geo-mechanical reservoir simulation.

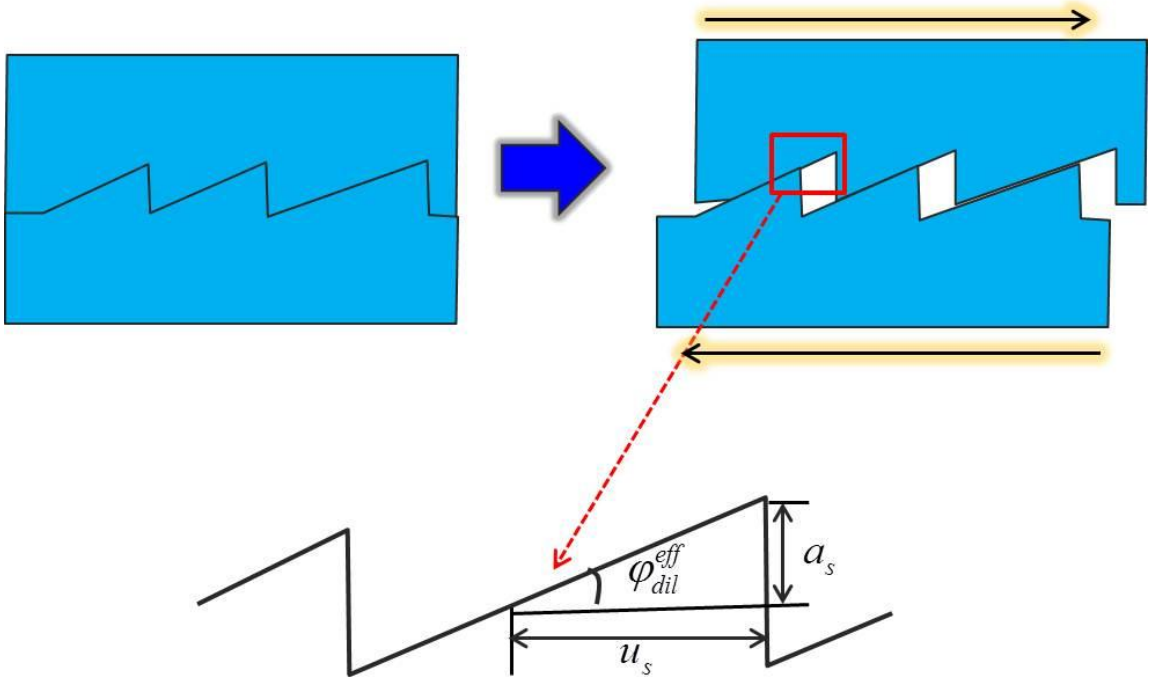

Figure 29 Shear-dilation of a rough fracture (Goodman, 1980)

The linear relationship (Hicks et al., 1996) between excess shear stress ($\Delta\tau$) and shear displacement (u_s) is given by:

$$\Delta\tau = K_{sh} u_s \tag{3.37}$$

where K_{sh} represents the shear stiffness of fracture.

In the Mohr-Coulomb criterion, shear failure or displacement can only take place when the shear stress (τ_n) is greater than the shear strength of the fracture (τ_p), which is a critical parameter to measure the resistance of fracture to shear slippage. The shear strength of the fracture can be approximated by combing Patton and Mohr-Coulomb criterion: (Willis-Richards et al., 1996; Rahman et al., 2002):

$$\tau_p = \sigma_n^{'} \tan(\varphi_f + \varphi_{dil}^{eff}) \tag{3.38}$$

where φ_f is the friction angle and typically varies between 30^0-40^0; φ_{dil}^{eff} represents the effective dilation angle and measures the roughness of the fracture surface, which is also termed as fracture roughness coefficient (JRC) by Barton et al. (1985). According to the laboratory measurement of dilation angle (φ_{dil}) under low effective stress (Willis-Richards et al., 1996), the expression of φ_{dil}^{eff} can be given as:

$$\varphi_{dil}^{eff} = \frac{\varphi_{dil}}{1 + 9\sigma_n^{'} / \sigma_{ref}^{'}} \tag{3.39}$$

Shear failure is taking place only if the shear stress exceeds the fracture shear strength:

$$\tau_n \geq \tau_p \Rightarrow \tau_n \geq \sigma_n^{'} \tan(\varphi_f + \varphi_{dil}^{eff}) \tag{3.40}$$

And the excess shear stress is defined as the difference between shear stress and shear strength (Willis-Richards et al., 1996): $\Delta\tau = \tau_n - \tau_p = \tau_n - \sigma_n^{'} \tan(\varphi_f + \varphi_{dil}^{eff})$ (3.41)

Combing Eq.(3.37), (3.40) and (3.41), it yields

$$u_s = \begin{cases} \dfrac{\tau_n - \sigma_n^{'} \tan(\varphi_f + \varphi_{dil}^{eff})}{K_{sh}} & (\tau_n \geq \sigma_n^{'} \tan(\varphi_f + \varphi_{dil}^{eff})) \\ 0 & (\tau_n < \sigma_n^{'} \tan(\varphi_f + \varphi_{dil}^{eff})) \end{cases} \tag{3.42}$$

From Figure 29, the fracture aperture induced by shear dilation (a_s) is related to the shear displacement through the following equation (Barton et al., 1985; Hicks et al., 1996; Willis-Richards et al., 1996):

$$a_s = u_s \tan(\varphi_{dil}^{eff}) \tag{3.43}$$

By replacing the term φ_{dil}^{eff} in Eq.(3.43) by Eq.(3.39), the fracture aperture due to shear dilation is expressed by:

$$a_s = \frac{u_s \tan(\varphi_{dil})}{1 + 9\sigma_n^{'} / \sigma_{ref}^{'}} \tag{3.44}$$

Finally, we can see that the shear displacement induced fracture aperture is a function of internal friction angle (φ_f), shear stiffness of fracture (K_{sh}), shear dilation angle (φ_{dil}), 90% closure stress ($\sigma_{ref}^{'}$) and effective normal stress ($\sigma_n^{'}$) acting on the fracture walls. After giving the expression of shear displacement by Eq. (3.42), the mechanical behavior of fractures during shear-dilation process can be mathematically assessed and readily incorporated into the numerical simulator.

Even with very high effective stress, the rough fracture surfaces are not in full contact with each other. Usually, there exists a residual aperture a_{res} to prevent complete closure of fractures to flow. This residue aperture is a very small quantity and always set to be zero in simulation work.

Taking the apertures caused by normal deformation and shear dilation and residual aperture into account, the total fracture aperture during mechanical deformation is formed as Eq.(3.45) and its schematic representation is given in Figure 30.

$$a = a_n + a_s + a_{res} = \frac{a_m + u_s \tan(\varphi_{dil})}{1 + 9\sigma_n^{'} / \sigma_{ref}^{'}} + a_{res} \tag{3.45}$$

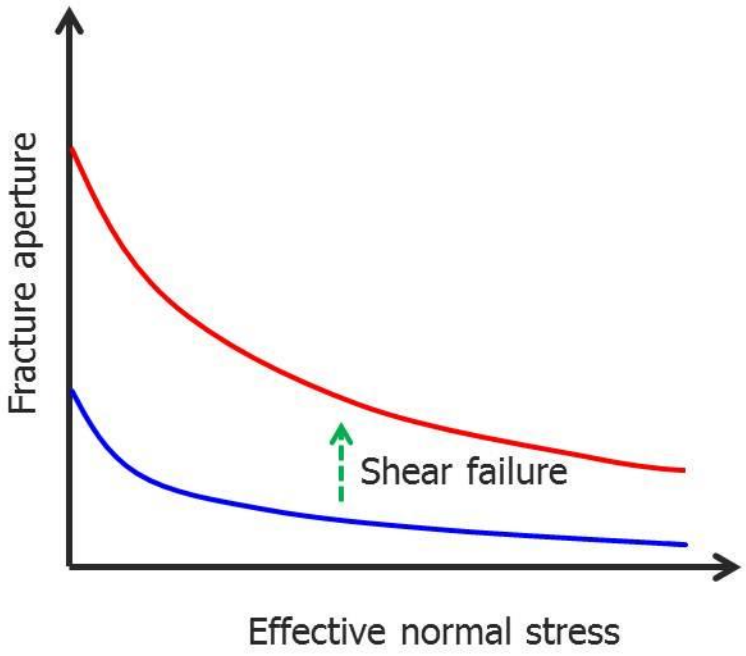

Figure 30 The relationship between fracture aperture and effective normal stress. The blue curve represents the stress-aperture relation before shear slip and red curve denotes the stress-aperture relation after the shear failure (Tezuka et al., 2005).

As plotted in Figure 30, the blue curve demonstrates the stress-aperture relation caused by normal deformation only and red curve represents the total fracture deformation induced by both normal deformation and shear dilation. This shear-dilation process can dramatically change the fracture mechanical behavior. The general expression of total aperture (Eq.(3.45)) provides a simple way to model the mechanical deformation of complex fracture network, some of which might suffer shear displacement.

3.6 Finite element model

Since the unknown variables such as p, μ and Z, appear in the coefficients of the field equations (Eq.3.8, 3.9 and 3.10) for this dual permeability model, the system is non-linear and hence not amenable to analytical solutions. Thus, a numerical method is required to solve these non-linear partial differential equations (PDE) with certain initial and boundary conditions.

The finite element method is used in this study. Eight-node quadrilateral element is used to compute solid displacement vector u, while four-node quadrilateral element is applied to calculate pseudo-pressure for fluid, either $m(p_m)$ or $m(p_f)$. The unknowns, u, $m(p_m)$ and $m(p_f)$), at any arbitrary point can be approximated by interpolating the variables at nodal points through the following functions (Smith and Griffiths, 1997):

$$u=N_u\tilde{u} \qquad m(p_m)=N_p m(\tilde{p}_m) \qquad m(p_f)=N_p m(\tilde{p}_f) \tag{3.46}$$

where N_u and N_p are the conventional shape functions and $\tilde{u}$, $m(\tilde{p}_m)$ and $m(\tilde{p}_f)$ are the vectors of the nodal displacement, pseudo-pressure within matrix and fracture respectively. Galerkin's finite element method (GFEM) is a widely used way to divide domain into elements and integrate the weak formulation over the element to minimize the solution residual. This method is then used to discretize the field equations in spatial domain.

$$K\dot{\tilde{u}} - A\cdot m(\dot{\tilde{p}}_m) = \dot{f} \tag{3.47}$$

$$L^T\dot{\tilde{u}} + S_1 m(\dot{\tilde{p}}_m) + H_{H1} m(\tilde{p}_m) = -Q(m(\tilde{p}_m) - m(\tilde{p}_f)) \tag{3.48}$$

$$S_2 m(\dot{\tilde{p}}_f) + H_{H2} m(\tilde{p}_f) = Q(m(\tilde{p}_m) - m(\tilde{p}_f)) \tag{3.49}$$

where

$$K = \int_{V_e} B^{\mathrm{T}} D B dV \tag{3.50}$$

$$A = \int_{V_e} [B]^{\mathrm{T}} \left[\mathrm{M} \left(\alpha + K \frac{\varepsilon_L P_L}{(P_L + p)^2} \right) \frac{\mu Z}{2p} \right] \left[\mathrm{N}_p \right] dV \tag{3.51}$$

$$L = \int_{V_e} [B]^{\mathrm{T}} \left[\alpha \frac{2p}{\mu Z} \mathrm{M} \right] \left[\mathrm{N}_p \right] dV \tag{3.52}$$

$$S_1 = \int_{V_e} \left[\mathrm{N}_p \right]^{\mathrm{T}} \left[\frac{1}{M} + \frac{\left(B_g \rho_r V_L - \alpha \varepsilon_L \right) P_L}{(p + P_L)^2} \right] \left[\mathrm{N}_p \right] dV \tag{3.53}$$

$$H_{H1} = \int_{V_e} \left[\nabla \mathrm{N}_p \right]^{\mathrm{T}} \left[\frac{k_a}{\mu} \right] \left[\nabla \mathrm{N}_p \right] dV \tag{3.54}$$

$$S_2 = \int_{V_e} \left[\mathrm{N}_p \right]^{\mathrm{T}} \left[\frac{1}{M_f} \right] \left[\mathrm{N}_p \right] dV \tag{3.55}$$

$$H_{H2} = \int_{V_e} \left[\nabla \mathrm{N}_p \right]^{\mathrm{T}} \left[\frac{k_f}{\mu_f} \right] \left[\nabla \mathrm{N}_p \right] dV \tag{3.56}$$

$$Q = \int_{V_e} \left[\mathrm{N}_p \right]^{\mathrm{T}} \left[\psi \frac{k_m}{\mu} \right] \left[\mathrm{N}_p \right] dV \tag{3.57}$$

Within the complete expression of each term, V_e represents the element area, f denotes the external applied forces, B and D are the strain-displacement matrix and stress-strain matrix respectively.

For the temporal discretization, Crank-Nicolson scheme is applied to Eq.(3.47-3.49) with an implicit variable θ. After some algebraic work, we finally obtain the following discretize equations:

$$\begin{bmatrix} K & -A & 0 \\ -L^T & -\left(S_1 + \theta\Delta t H_{H1} + \theta Q\Delta t\right) & Q\Delta t\theta \\ 0 & Q\Delta t\theta & -(S_2 + H_{H2}\theta\Delta t + Q\Delta t\theta) \end{bmatrix} \begin{bmatrix} \Delta\tilde{u} \\ \Delta m(\tilde{p}_m) \\ \Delta m(\tilde{p}_f) \end{bmatrix} = \begin{bmatrix} \Delta\tilde{f} \\ (H_{H1}\Delta t + Q\Delta t)m(\tilde{p}_m) - Q\Delta t m(\tilde{p}_f) \\ (H_{H2}\Delta t + Q\Delta t)m(\tilde{p}_f) - Q\Delta t m(\tilde{p}_m) \end{bmatrix} \tag{3.58}$$

where Δt is the time increment; implicit variable θ is bounded between 0.5 and 1.0; subscript t_{n-1} represents the time of last step. The "stiffness" matrix of the above FEM formula is not symmetrical. Thereafter, an optimized FORTRAN solver, called Pardiso will be utilized.

As the natural gas properties are not constant with pressure change, and $\tilde{p}_{t_n}$ (pore pressure at the current time step) are included in the "stiffness" matrix, a nonlinear iterative method is needed in the numerical procedure. This is done by using the unknowns computed from previous step to estimate the stiffness matrix in the current step (see Appendix IV). A tolerance value (0.2%) is used to check the convergence in every iteration during each time step. In this finite element model, the nodal variables u, $m(p_m)$ and $m(p_f)$ can be solved directly from Eq.(3.58). Then, the total and effective stresses at Gauss integration points, which are not primary variables, can be computed through Eq.(3.21) and (3.22).

3.7 Verification

The non-linear fully coupled poroelastic FEM model (single porosity) for simulating gas production from gas shale has been verified using analytical solutions in Chapter 2. However, as no analytical solutions are available, the program is verified by using a very low fracture aperture and comparing the dual permeability model to the analytical solution for a single permeability model.

In this numerical analysis, the reservoir dimension is 10m×10m. Considering the axial symmetry of the wellbore geometry, only a quadrant of the reservoir is simulated as shown in Figure 31. The finite element mesh and element geometry are also presented in Figure 31. And six near-wellbore fractures are considered in the verification process, as shown in Figure 31. Three of them are perpendicular to the minimum in-situ stress direction to represent hydraulic fractures. The others three are assumed to be pre-existing natural fractures.

In field, a producer with radius ($a = 0.1\text{m}$) is located in the center of the reservoir and its bottom hole pressure (BHP) is set lower than the reservoir pressure to initiate production. In this FEM model, under the plane strain conditions for the 2-D case, the production of gas within the wellbore can be simulated by decreasing the pore pressure on the wellbore wall at t=0. Flow rate at wellbore can be computed through Darcy's law.

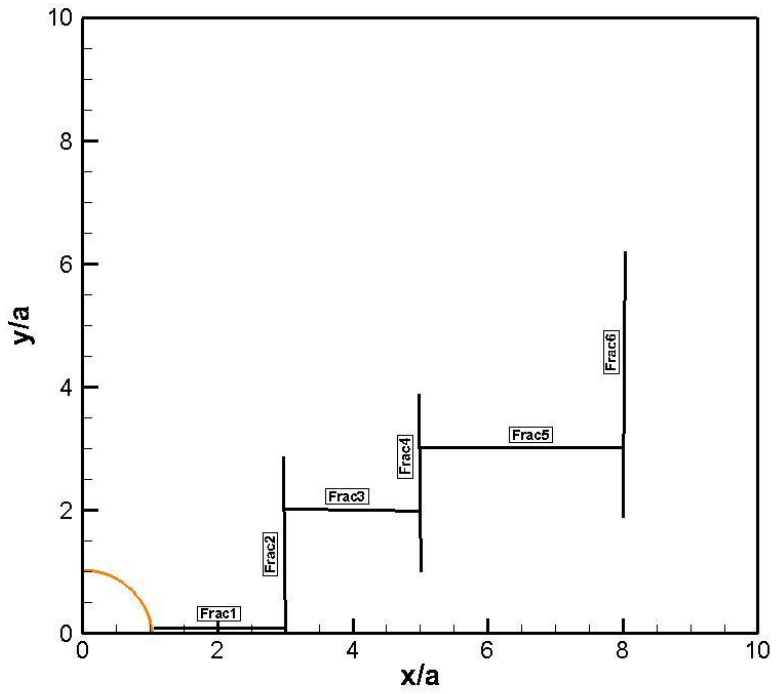

Figure 31 Wellbore and Fractures geometry

In order to solve these diffusion the initial reservoir pressure is set to be 8.27 MPa (1200psi) and the BHP at wellbore is 5.52 MPa (800psi) and is kept constant in time under isothermal conditions. For the far-field boundary, a no flow condition is applied.

In order to highlight the matrix deformation and gas flow only induced by pore pressureperturbation, the in-situ stress state is assumed to be isotropic during the verification process. All reservoir parameters and gas properties for the FEM are given in Table 3.

Poisson's ratio, ν	0.25	0.25
Young's modulus, E	20.684GPa	3.0×10^{6} psi
Shear modulus, G	8.274GPa	1.2×10^{6} psi
Initial porosity, ϕ	0.04	0.04
Biot's coefficient, α	0.6354	0.6354
Initial permeability, k	1.0×10^{-19} m^2	0.1 μD
Bulk modulus, K	13.790GPa	2.0×10^{6} psi
Solid bulk modulus, K_s	37.820GPa	5.5×10^{6} psi
Initial reservoir pressure, p_0	28.269MPa	4100psi
Bottom hole pressure, p_{wf}	15MPa	2176psi
Average system temperature, T	90^0C	194^0F
Density of gas shale, ρ_r	2.4×10^{3} kg/m^3	150lb/ft^3
Min in-situ stress, σ_h	39.011MPa	5658psi
Max in-situ stress, σ_H	43.340MPa	6286psi
Langmuir pressure constant, P_L	6.109MPa	886psi
Langmuir volume constant, V_L	0.015 m^3/kg	0.24ft^3/lb
Langmuir volumetric strain constant, ε_L	0.02295	0.02295
Aperture without any normal stress, a_0	0.0001m	3.94×10^{-3} in
Empirical constant, A	1.0	1.0
90% closure stress, B	50MPa	7252psi

Table 3 Input parameter for dual permeability model

In the verification process, the fracture aperture within the reservoir is assumed to be ultra-low and equal to $a_0 = 1.0 \times 10^{-6}\,\mathrm{m}$. In this way, the equivalent fracture permeability of the fractured elements resembles the matrix permeability and the result of the dual permeability model can be compared against the single permeability model. The profiles of the pore pressure distribution around the wellbore are depicted in Figure 32. In both models, it can be observed that the gas pressure decreases with time and decreases close to the wellbore pressure due to production. It can be seen that all the numerical results of DPM agree very well with those of the single permeability model.

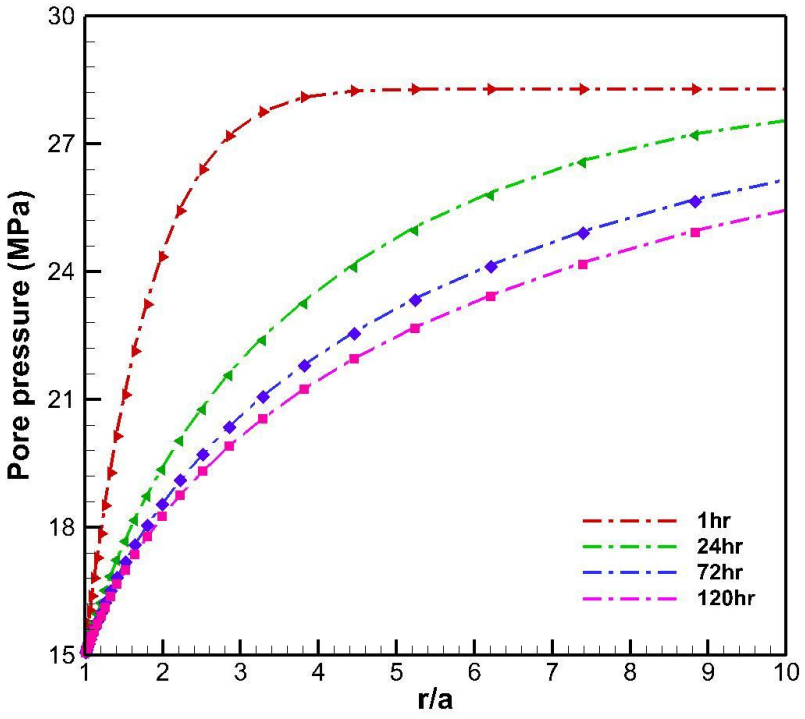

Figure 32 Comparison of dual permeability model results (dashed curves) with single permeability model results (data markers) for the distribution of induced pore pressure around the wellbore.

3.8 Conclusion

The response of fractured gas shale to gas diffusion in depletion process has been successfully studied using a non-linear coupled poroelastic model and considers adsorbed gas within shale matrix (Chapter 2). In this chapter, this single permeability model for simulating gas flow is further developed by incorporating the dual continuum concept to handle fracture network in heterogeneous reservoirs such as gas shale and coal-bed methane.

In the dual permeability model, elements without fracture will remain as conventional single permeability cells whereas the dual permeability treatment is needed for the elements intersected with fractures. In this newly created model, both matrix and fractures are set to be permeable, so that fluid can move through both. Within the framework of this DPM-FEM model, every element, either with or without fractures, can have its own permeability tensor and other mechanical properties.

The fractures, especially large scale fractures, are discretely represented by small segments and their geometry and mechanical behavior are considered on element-by element basis. Fracture aperture and hence its permeability is no longer constant along the fracture length. The stress-dependent fracture aperture, caused by both normal deformation and shear displacement, can be computed by a simple correlation and updated explicitly within the time loop of finite element model. And the implementation of DPM to the non-linear fully coupled poroelastic FEM model was verified with single permeability model.

CHAPTER IV

POROVISCOELASTICITY

In most reservoir simulators for gas shale, only the elastic deformation of reservoir rock and fractures is modeled. However, many experimental studies and field investigation indicated that shale might experience viscoelastic deformation before reaching plastic deformation under in-situ stress condition. Thus, in this work, a non-linear numerical simulator was constructed by incorporating a poroviscoelastic model into the dual permeability (DPM)-finite element model (FEM) to investigate the coupled time-dependent viscoelastic deformation, fracture network evolution and compressible fluid flow in gas shale reservoir. The viscoelastic effect was addressed in both deviatoric and mean effective stresses to emphasize the effect of shear strain localization on fracture shear dilation. In the strain damage model, shear viscosity was set to be proportional to the second invariant of the strain-rate for viscous rheology. The new mechanical model was first verified with an analytical solution in a simple consolidation problem and wellbore creep problem and then compared with the poroelastic solution under the same conditions. Comparing the case of poroelasticity and poroviscoelasticity showed that the pore pressure difference throughout the domain was small; however, the stress evolution was quite divergent, especially for the area close to the loading boundary. This numerical model was applied to a field case of fractured gas shale reservoir to understand the long term viscoelastic and damage effects on the gas production in gas shale.

4.1 Introduction

For successful drilling, completion and simulation of gas shale reservoirs, accurate measurement and estimation of rock mechanical properties is demanded in petroleum industry. Core sample tests and log data analyses are commonly used to acquire rock mechanical properties. Only elastic properties of reservoir rock can be extracted from these two methods. However, the geomechanical deformations of shale reservoirs usually demonstrate time-dependent behavior and follow viscoelastic, even viscoplastic, constitutive laws, which was proven by extensive experiment results (Olsson, 1980; Blanton and Teufel, 1983; Huang et al., 1987; Warpinski, 1989; Zhou et al., 1992; Remvik, 1995; Bloch et al., 1999; Sone and Zoback, 2011).

A non-negligible portion of the reservoir mechanical response occurs as viscoelastic deformation, which is non-linear in time and cannot be correctly described by linear elasticity theory. This time-dependent geomechanical behavior of rock matrix/fracture system can impact the dynamic permeability of the reservoir and hence affect the gas deliverability during production period, especially for a long-term prediction during reservoir life. Failure to handle this viscoelastic deformation of gas shale reservoirs may result in significant errors in predicting reservoir compaction and gas production. The viscoelastic theory and applications on nonporous medium are widely developed in literature, but seldom applied to the porous medium.

Biot (1956) initially proposed a poro-visco-elasticity theory to investigate the linear viscoelasticity and anisotropy of porous medium, which presented viscoelastic deformation of solid and viscous flow of pore fluid. The linearized formulation of Biot's

poro-visco-elasticity theory was established based on a thermodynamic approach, in which a generalized free energy as well as dissipation function was used to define thermodynamic systems. The linear operator, containing both elastic and viscous terms, between stress, strain, fluid content and pressure was given and applied to solve the field equations.

Abousleiman et al. (1993) introduced a micromechanical method to interpret Biot's poro-visco-elasticity theory. In their micromechanical approach, the generalized Kelvin's model (three parameters) was utilized to compute the bulk modulus of rock matrix (K) and solid constituent (K_s) in Laplace domain. In this way, the rock elastic and viscoelastic properties were considered at pore scale and applied to represent the coefficients in the poroviscoelastic constitutive equations. Then, an analytical solution for wellbore problem was derived to investigate the coupled process between fluid flow and rock viscoelastic deformation.

Bloch et al. (1999) applied the poroviscoelasticity theory to interpret anelastic strain recovery test by using modified Kelvin's model (three parameters). The rock mechanical properties, such as Young's modulus and bulk modulus were computed in a similar way to that of Abousleiman et al. (1993) to account for viscoelastic effect. Both the analytical solutions of poroviscoelastic and viscoelastic models were applied to predict the viscoelastic behavior among different rock types, sandstone, chalk and shale in that study. By comparing the results between poroviscoelastic and viscoelastic solutions, poroviscoelastic was advanced in forecasting the deformation of rock sample in time.

Simakin and Ghassemi (2005) developed another poroviscoelastic model by taking the relaxation in both deviatoric stress and the symmetric effective stress into consideration. In that work, a Maxwell linear viscoelastic model was employed to describe the mechanical nature of reservoir rock and shear viscosity was assumed to be proportional to the second invariant of the strain rate for viscous rheology in the damage model. Based on these assumptions, a numerical model was constructed to simulate the triaxial compressional test of rock, which melted partially under in-situ conditions. In this new mechanical model, the poroviscoelasticity was implemented with damage model to study the shear strain localization and fluid flow in rock.

In this chapter, a poroviscoelastic model with damage model is incorporated into the dual permeability (DPM)-finite element model (FEM) numerical simulator to study the coupled time-dependent viscoelastic deformation, fracture network evolution and compressible fluid flow in gas shale reservoir. The primary objective of this chapter is to simulate the time evolution of gas pressure, effective stresses, fracture aperture and permeability during gas depletion process and quantify the influence of shear strain localization on matrix and fracture deformation during gas production.

4.2 Linear viscoelasticity

In an elastic material, the stress and strain correlation is modeled by Hooke's law and demonstrates a linear relationship which is only dependent on the mechanical properties of the material and is invariant with time as shown in Figure 33. However, a viscoelastic material usually exhibits the elastic deformation as well as the viscous deformation,

which is time-dependent. According to the boundary condition, either stress relaxation or strain creep (Figure 33) can be presented by a viscoelastic material.

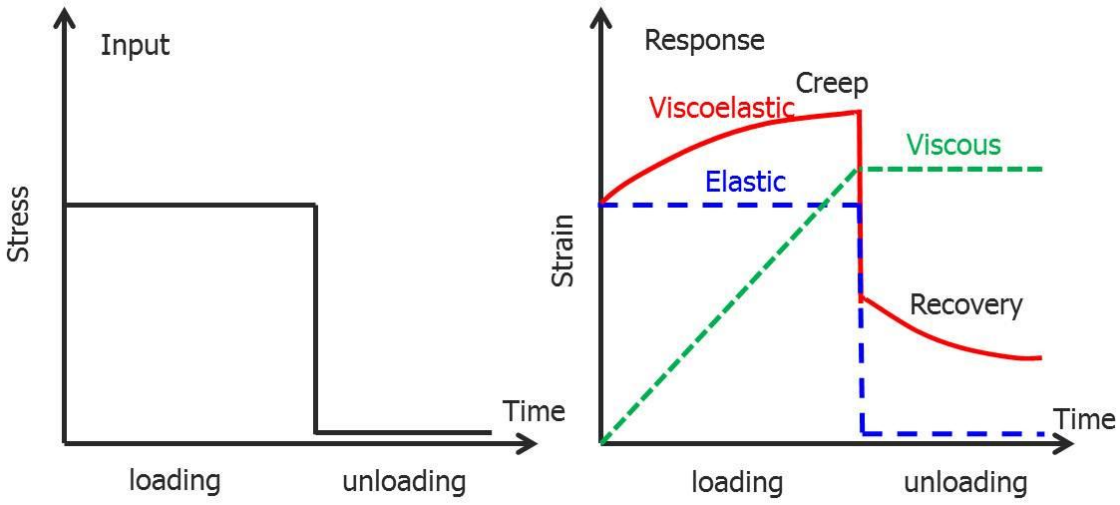

Figure 33 Schematic descriptions of stress-strain relationships in elastic, viscous and viscoelastic materials

In a relaxation test, if the applied strain is kept as constant, the stress of viscoelastic material decreases with time as illustrated in Figure 33; in a creep test, if applied stress on the boundary of the sample is held constant, the strain of viscoelastic material increases over time as shown in Figure 33. The relaxation and creep phenomena coexist inherently within viscoelastic materials.

Although the stress and strain relationship for viscoelastic materials is time dependent, it is assumed to be linear which is an ideal but widely used way to describe the complicated viscoelastic behavior in literature. However, the actual stress-strain response could be non-linear.

In the theory of linear viscoelasticity, two simple mechanical elements, spring and dashpot, are utilized to represent the elastic and viscous behavior respectively, as depicted in Figure 34.

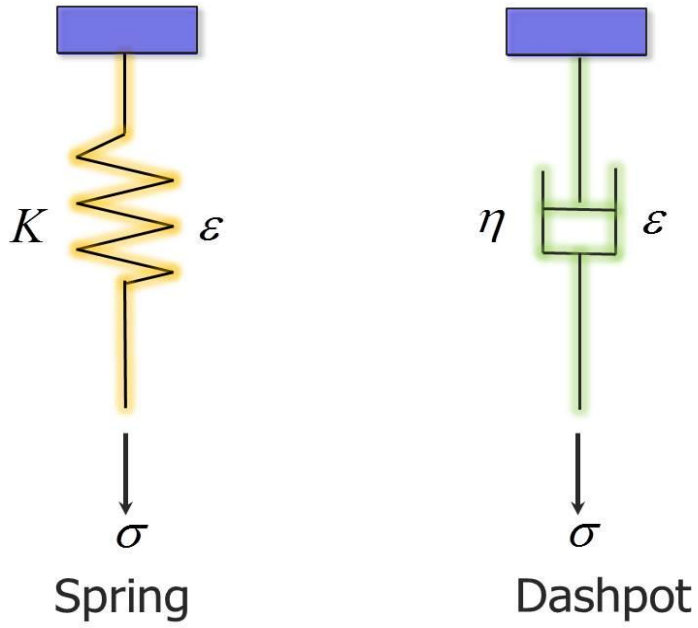

Figure 34 Two mechanical elements used in linear viscoelasticity

Spring is a representative of linear elastic solid. Its constitutive equation is given as below:

$$\sigma = K\varepsilon \tag{4.1}$$

where K is the stiffness of the spring. In a spring, strain is an instantaneous function of stress during loading process and it reduces to zero instantly when unloaded.

Dashpot works as a piston moving within a viscous medium and is used to describe the viscous behavior. For a dashpot, we have the following constitutive equation:

$$\sigma = \eta\dot{\varepsilon} = \eta\frac{d\varepsilon}{dt} \tag{4.2}$$

where η is the dashpot viscosity (creep compliance) and is a constant. It is obvious that stress is a linear function of strain rate in Eq. (4.2). Integrating Eq. (4.2) by assuming constant load σ_0 and zero initial strain, one can get:

$$\varepsilon = \frac{\sigma_0}{\eta} t \tag{4.3}$$

Strain depends not only in stress level, but also stress history in loading process. It can be seen that strain is accumulated linearly with time in Eq. (4.3). If the relationship between stress and strain rate in Eq. (4.2) becomes non-linear, a non-linear viscoelasticity theory will be developed, which will not be addressed in this study.

Two simple but typical models will be examined to demonstrate how to construct a linear viscoelastic model by employing linear spring and dashpot elements.

The Kelvin model consists of a spring and dashpot element, which are connected in *parallel* as shown in Figure 35 (I). In this parallel two-element model, the total stress and strain are given as:

$$\sigma = \sigma_e + \sigma_{ve} \tag{4.4}$$

$$\varepsilon = \varepsilon_e = \varepsilon_{ve} \tag{4.5}$$

By substituting Eq. (4.1) and (4.2) into Eq. (4.4), the governing equation of Kelvin model is expressed as: $\sigma = K\varepsilon + \eta\dot{\varepsilon}$ (4.6)

The Maxwell model is another typical two-element model which is composed of a spring and dashpot element that are connected in *series* as depicted in Figure 35 (II). The

components in series carry the same the total stress and their strains are added to find the total strain so that:

$$\sigma = \sigma_e = \sigma_{ve} \tag{4.7}$$

$$\varepsilon = \varepsilon_e + \varepsilon_{ve} \tag{4.8}$$

By taking Eq. (4.1) and (4.2) into Eq. (4.8), one can get the governing equation of Maxwell model:

$$\dot{\sigma} = K\dot{\varepsilon} - \frac{\sigma}{\eta / K} \tag{4.9}$$

In literature, numerous linear viscoelastic models are constructed based on different combination of spring(s) and dashpot(s). If a Kelvin and a Maxwell model are connected in series, the Burger's model is formed, as shown in Figure 35 (III). Normally, increasing the number of mechanical elements in a model can improve its quality in predicting the mechanical response of viscoelastic materials. Consequently, the number of necessary mechanical properties also rises, whose measurement might be difficult or even impossible through experiments. In the following section, the Maxwell model will be used to develop a linear poroviscoelastic model which is incorporated into a numerical reservoir simulator to study the viscoelastic effects during gas production.

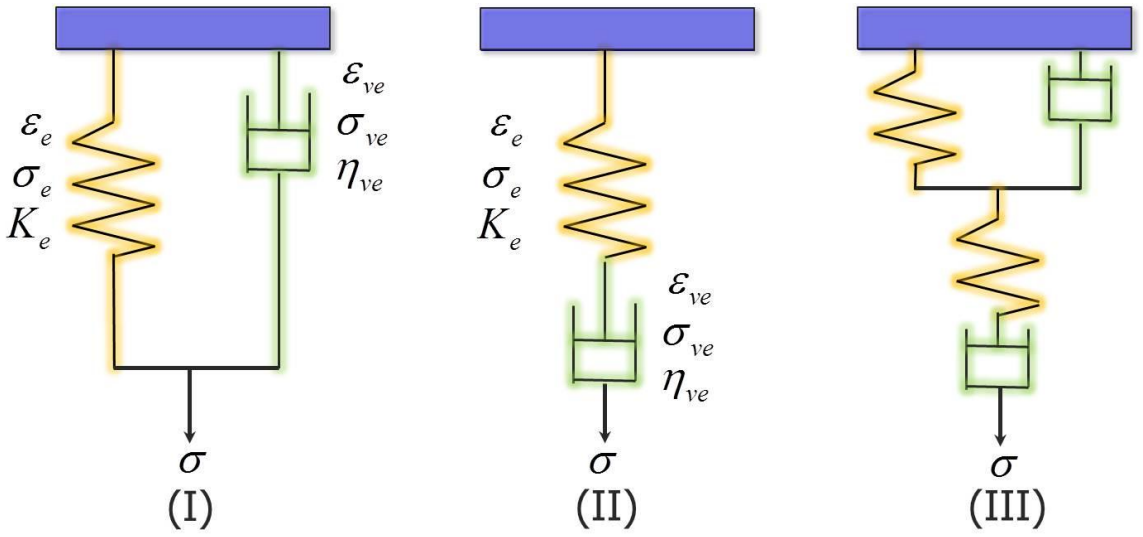

Figure 35 schematic representation of three liner-viscoelastic models: (I) Kelvin model; (II) Maxwell model; (III) Burger's model

4.3 Poroviscoelastic model

Diek and Ghassemi's (2004) chemo-poroelastic theory is an improvement of the Heidug and Wong (1996) work and is derived from the potential energy of wetted clay matrix, i.e., the differences between the internal energy of fluid saturated porous medium and that of the pore fluid. In the case of complete isotropy and without thermal and chemical influences, the constitutive equations for a poroelastic porous rock are given as *(tension is considered positive):*

$$\dot{\sigma}_{ij} = (K - \frac{2G}{3})\dot{\varepsilon}_{kk}\delta_{ij} + 2G\dot{\varepsilon}_{ij} - \alpha\dot{p}\delta_{ij} \tag{4.10}$$

$$\dot{\zeta} = \alpha\dot{\varepsilon}_{kk} + \frac{1}{M}\dot{p} \tag{4.11}$$

where K and G represent the rock's bulk and shear modulus respectively; α is the Biot's effective stress coefficient which measures the ability of the pore pressure to act against compressional stresses; M stands for the Biot modulus, defined as the inverse of a storage coefficient with the expression of $\frac{1}{M} = \frac{\partial \zeta}{\partial p}\Big|_{\varepsilon}$; the dots above variables represent time derivatives. With the isotropic thermodynamic response, coefficient α and M are given by:

$$\alpha = 1 - \frac{K}{K_s} \tag{4.12}$$

$$\frac{1}{M} = \frac{\phi}{K_f} + \frac{\alpha - \phi}{K_s} \tag{4.13}$$

where K_s and K_f stand for the solid matrix's bulk modulus and fluid modulus respectively; ϕ represents the porosity. The above linearization of rock-fluid constitutive equations (4.10) to (4.11) express the total stresses σ_{ij} and the variation of fluid content ζ with respect to two variables, the solid strain ε_{ij} and the pore pressure p in linear poroelasticity theory.

The components of *effective stress* tensor (σ'_{ij}) are given as the sum of the corresponding total stress (σ_{ij}) components and pore pressure of fluid (p):

$$\begin{aligned} \dot{\sigma}'_{ij} &= \dot{\sigma}_{ij} + \alpha \dot{p} \delta_{ij} \\ &= (K - \frac{2G}{3}) \dot{\varepsilon}_{kk} \delta_{ij} + 2G \dot{\varepsilon}_{ij} \quad i, j, k = x, y, z \end{aligned} \tag{4.14}$$

And, the 3D strain-stress relation is expressed as:

$$\dot{\varepsilon}_{ij} = \frac{1}{2G}\dot{\sigma}'_{ij} - \left(\frac{1}{6G} - \frac{1}{9K}\right)\dot{\sigma}'_{kk}\,\delta_{ij} \quad i, j, k = x, y, z \tag{4.15}$$

So the volumetric strain could be obtained as

$$\dot{\varepsilon}_v = \frac{1}{3K}\dot{\sigma}'_{kk} \tag{4.16}$$

In order to solve these linear equations by finite element method, the stress-strain relation need to be expressed in matrix form. In matrix form, the stress-strain relationship for an isotropic rock can be written as:

$$\begin{bmatrix} \dot{\sigma}'_{xx} \\ \dot{\sigma}'_{yy} \\ \dot{\sigma}'_{zz} \\ \dot{\sigma}'_{xz} \\ \dot{\sigma}'_{yz} \\ \dot{\sigma}'_{xy} \end{bmatrix} = \begin{bmatrix} K+\frac{4}{3}G & K-\frac{2}{3}G & K-\frac{2}{3}G & 0 & 0 & 0 \\ K-\frac{2}{3}G & K+\frac{4}{3}G & K-\frac{2}{3}G & 0 & 0 & 0 \\ K-\frac{2}{3}G & K-\frac{2}{3}G & K+\frac{4}{3}G & 0 & 0 & 0 \\ 0 & 0 & 0 & 2G & 0 & 0 \\ 0 & 0 & 0 & 0 & 2G & 0 \\ 0 & 0 & 0 & 0 & 0 & 2G \end{bmatrix} \begin{bmatrix} \dot{\varepsilon}_{xx} \\ \dot{\varepsilon}_{yy} \\ \dot{\varepsilon}_{zz} \\ \dot{\varepsilon}_{xz} \\ \dot{\varepsilon}_{yz} \\ \dot{\varepsilon}_{xy} \end{bmatrix} \tag{4.17}$$

Under plane strain condition, $\varepsilon_{zz} = \varepsilon_{xz} = \varepsilon_{yz} = 0$

so that the above stress-strain relation can be simplified to

$$\begin{bmatrix} \dot{\sigma}'_{xx} \\ \dot{\sigma}'_{yy} \\ \dot{\tau}_{xy} \end{bmatrix} = \begin{bmatrix} K+4G/3 & K-2G/3 & 0 \\ K-2G/3 & K+4G/3 & 0 \\ 0 & 0 & 2G \end{bmatrix} \begin{bmatrix} \dot{\varepsilon}_{xx} \\ \dot{\varepsilon}_{yy} \\ \dot{\varepsilon}_{xy} \end{bmatrix} \tag{4.18}$$

From Eq.(4.15), for plane strain condition,

$$\dot{\varepsilon}_{zz} = \frac{1}{2G}\dot{\sigma}'_{zz} - \left(\frac{1}{6G} - \frac{1}{9K}\right)\dot{\sigma}'_{kk}\,\delta_{ij} = 0 \tag{4.19}$$

the 3rd normal stress component due to Poisson effect can be easily derived

$$\dot{\sigma}'_{zz} = \frac{3K - 2G}{2(3K + G)}\left(\dot{\sigma}'_{xx} + \dot{\sigma}'_{yy}\right) \tag{4.20}$$

So the mean effective stress is given as:

$$\dot{\sigma}_m = \frac{\dot{\sigma}'_{kk}}{3} = \frac{3K}{2(3K + G)}\left(\dot{\sigma}'_{xx} + \dot{\sigma}'_{yy}\right) \tag{4.21}$$

In mechanics, any stress tensor can be decomposed into two parts, mean stress ($\sigma_m \mathrm{I}$) and deviatoric stress (s), through the following way:

$$\begin{bmatrix} \sigma_{xx} & \sigma_{xy} \\ \sigma_{yx} & \sigma_{yy} \end{bmatrix} = \sigma_m \mathrm{I} + s = \begin{bmatrix} \sigma_m & 0 \\ 0 & \sigma_m \end{bmatrix} + \begin{bmatrix} s_{xx} & s_{yx} \\ s_{xy} & s_{yy} \end{bmatrix} \tag{4.22}$$

where

$$s = \begin{bmatrix} s_{xx} & s_{yx} \\ s_{xy} & s_{yy} \end{bmatrix} = \begin{bmatrix} \dfrac{\sigma_{xx} - \sigma_{yy}}{2} & \sigma_{yx} \\ \sigma_{xy} & -\dfrac{\sigma_{xx} - \sigma_{yy}}{2} \end{bmatrix} \tag{4.23}$$

Letting $S_1 = \dfrac{\sigma_{xx} - \sigma_{yy}}{2}$ and $S_2 = \sigma_{xy} = \sigma_{yx}$, the deviatoric stress tensor can be given as:

$$s = \begin{bmatrix} S_1 & S_2 \\ S_2 & -S_1 \end{bmatrix} \tag{4.24}$$

A synthetic vector (Φ) can be formed by putting the hydrostatic (σ_m) and deviatoric stress (S_1 and S_2) components together in the following way:

$$\Phi = \begin{bmatrix} \sigma_m \\ S_1 \\ S_2 \end{bmatrix} \tag{4.25}$$

A linear operator (tensor C) is used to transform the stress tensor in plane strain (also in vector form) into vector Φ:

$$\Phi = \begin{bmatrix} \sigma_m \\ S_1 \\ S_2 \end{bmatrix} = [C] \begin{bmatrix} \sigma'_{xx} \\ \sigma'_{yy} \\ \tau_{xy} \end{bmatrix} \tag{4.26}$$

where

$$[C] = \begin{bmatrix} \dfrac{3K}{2(3K+G)} & \dfrac{3K}{2(3K+G)} & 0 \\ \dfrac{1}{2} & -\dfrac{1}{2} & 0 \\ 0 & 0 & 1 \end{bmatrix} \tag{4.27}$$

And its inverse is $[C]^{-1} = \begin{bmatrix} 1+\dfrac{G}{3K} & 1 & 0 \\ 1+\dfrac{G}{3K} & -1 & 0 \\ 0 & 0 & 1 \end{bmatrix}$ (4.28)

Correspondingly, another synthetic vector (Ψ) can be given by putting the plane strain "volumetric" ($\varepsilon_v = \varepsilon_{xx} + \varepsilon_{yy}$) and deviatoric strain ($\psi_1 = \dfrac{\varepsilon_{xx} - \varepsilon_{yy}}{2}$ and $\psi_2 = \varepsilon_{xy}$) components together in the same way:

$$\Psi = \begin{bmatrix} \varepsilon_v \\ \psi_1 \\ \psi_2 \end{bmatrix} \tag{4.29}$$

The above vector Ψ can be also transformed into the conventional strain tensor (in vector form) through a linear operator:

$$\Psi = \begin{bmatrix} \varepsilon_v \\ \psi_1 \\ \psi_2 \end{bmatrix} = \begin{bmatrix} 1 & 1 & 0 \\ \frac{1}{2} & -\frac{1}{2} & 0 \\ 0 & 0 & 1 \end{bmatrix} \begin{bmatrix} \varepsilon_{xx} \\ \varepsilon_{yy} \\ \varepsilon_{xy} \end{bmatrix} \tag{4.30}$$

The poro-viscoelastic constitutive law for the Maxwell model is given by Eq. (4.9). The difference between the constitutive equations of poroviscoelasticity and that of poroelasticity is the viscous term (the second term on the RHS of Eq. (4.9)), which is modeled by the linear dashpot element. The viscous behavior of reservoir rock can affect the time evolution of both the deviatoric and symmetric components of stress (Simakin and Ghassemi, 2005).

The deviatoric stress components (S_1 and S_2) contain two terms in the relation between stresses rate and strain rate: one is the conventional linear elastic deformation; the other is the viscous relation term, indicating the deviatoric stress decays with a relaxation time τ_s, which is proportional to the shear viscosity of the matrix (η_s).

$$\dot{\Phi}_i = 2G\dot{\Psi}_i - \frac{\Phi_i}{\tau_s} \qquad i = 2,3 \tag{4.31}$$

where $\tau_s = \frac{\eta_s}{G}$ and η_s is the shear viscosity, which describes a material's resistance to shear flow; the script dot indicates the time derivative of the corresponding term.

Similarly to the deviatoric part, the effective stresses-strain rate relation for the symmetric part (σ_m) can be expressed in terms of two terms: one is the linear elastic deformation and the other is another viscous relaxation term, showing that the symmetric

stress evolves with a characteristic time τ_v, which is proportional to the volumetric viscosity of the matrix (η_v).

$$\dot{\Phi}_i = K\dot{\Psi}_i - \frac{\Phi_i}{\tau_v} \qquad i = 1 \tag{4.32}$$

where $\tau_v = \frac{\eta_v}{K}$ and η_v is the volumetric viscosity, which measures a material's reaction to volume change.

Note that the last equations are written in terms of effective stress components and the "prime" has been omitted. In matrix form, the above equations (Eq. (4.31) and (4.32)) can be rewritten as:

$$\dot{\Phi} = \begin{bmatrix} \dot{\sigma}_m \\ \dot{S}_1 \\ \dot{S}_2 \end{bmatrix} = \begin{bmatrix} K & 0 & 0 \\ 0 & 2G & 0 \\ 0 & 0 & 2G \end{bmatrix} \begin{bmatrix} \dot{\varepsilon}_v \\ \dot{\psi}_1 \\ \dot{\psi}_2 \end{bmatrix} - \begin{bmatrix} \sigma_m / \tau_v \\ S_1 / \tau_s \\ S_2 / \tau_s \end{bmatrix} \tag{4.33}$$

According to Eq. (4.26), the *plane strain effective stresses (in vector form)* can be expressed as

$$\begin{bmatrix} \dot{\sigma}'_{xx} \\ \dot{\sigma}'_{yy} \\ \dot{\tau}_{xy} \end{bmatrix} = [C]^{-1}\dot{\Phi} \tag{4.34}$$

Taking Eq. (4.28), (4.30) and (4.33) into Eq.(4.34), it yields for *effective stresses*:

$$\begin{bmatrix} \dot{\sigma}'_{xx} \\ \dot{\sigma}'_{yy} \\ \dot{\tau}_{xy} \end{bmatrix} = \begin{bmatrix} 1+G/3K & 1 & 0 \\ 1+G/3K & -1 & 0 \\ 0 & 0 & 1 \end{bmatrix} \left\{ \begin{bmatrix} K & 0 & 0 \\ 0 & 2G & 0 \\ 0 & 0 & 2G \end{bmatrix} \begin{bmatrix} 1 & 1 & 0 \\ \frac{1}{2} & -\frac{1}{2} & 0 \\ 0 & 0 & 1 \end{bmatrix} \begin{bmatrix} \dot{\varepsilon}_{xx} \\ \dot{\varepsilon}_{yy} \\ \dot{\varepsilon}_{xy} \end{bmatrix} - \begin{bmatrix} \sigma_m / \tau_v \\ S_1 / \tau_s \\ S_2 / \tau_s \end{bmatrix} \right\}$$

$$= \begin{bmatrix} K+4G/3 & K-2G/3 & 0 \\ K-2G/3 & K+4G/3 & 0 \\ 0 & 0 & 2G \end{bmatrix} \begin{bmatrix} \dot{\varepsilon}_{xx} \\ \dot{\varepsilon}_{yy} \\ \dot{\varepsilon}_{xy} \end{bmatrix} - \begin{bmatrix} \frac{\tau_v+\tau_s}{2\tau_v\tau_s} & \frac{\tau_s-\tau_v}{2\tau_v\tau_s} & 0 \\ \frac{\tau_s-\tau_v}{2\tau_v\tau_s} & \frac{\tau_v+\tau_s}{2\tau_v\tau_s} & 0 \\ 0 & 0 & \frac{1}{\tau_s} \end{bmatrix} \begin{bmatrix} \sigma'_{xx} \\ \sigma'_{yy} \\ \tau_{xy} \end{bmatrix} \tag{4.35}$$

Let $$[D] = \begin{bmatrix} K+4G/3 & K-2G/3 & 0 \\ K-2G/3 & K+4G/3 & 0 \\ 0 & 0 & 2G \end{bmatrix} \tag{4.36}$$

represent the stiffness matrix for elasticity, and:

$$[V] = \begin{bmatrix} \frac{\tau_v+\tau_s}{2\tau_v\tau_s} & \frac{\tau_s-\tau_v}{2\tau_v\tau_s} & 0 \\ \frac{\tau_s-\tau_v}{2\tau_v\tau_s} & \frac{\tau_v+\tau_s}{2\tau_v\tau_s} & 0 \\ 0 & 0 & \frac{1}{\tau_s} \end{bmatrix} \tag{4.37}$$

represent the viscoelasticity component. Then, the increment of effective stress at current step can be expressed as:

$$\begin{bmatrix} \dot{\sigma}'_{xx} \\ \dot{\sigma}'_{yy} \\ \dot{\tau}_{xy} \end{bmatrix} = [D] \begin{bmatrix} \dot{\varepsilon}_{xx} \\ \dot{\varepsilon}_{yy} \\ \dot{\varepsilon}_{xy} \end{bmatrix} - [V] \begin{bmatrix} \sigma_{xx}' \\ \sigma_{yy}' \\ \tau_{xy} \end{bmatrix} \tag{4.38}$$

Or one can write it as $\dot{\sigma}' = D\dot{\varepsilon} - V\sigma'$ (4.39) for simplicity. Substituting Eq. (4.14) into Eq. (4.38), one can get

$$\begin{bmatrix} \dot{\sigma}_{xx} + \alpha \dot{p} \\ \dot{\sigma}_{yy} + \alpha \dot{p} \\ \dot{\tau}_{xy} \end{bmatrix} = [D] \begin{bmatrix} \dot{\varepsilon}_{xx} \\ \dot{\varepsilon}_{yy} \\ \dot{\varepsilon}_{xy} \end{bmatrix} - [V] \begin{bmatrix} \sigma_{xx} + \alpha p \\ \sigma_{xy} + \alpha p \\ \tau_{xy} \end{bmatrix} \tag{4.40}$$

Thus, for a fully coupled hydro-mechanical process, the increment of total stress at current stage is stated as:

$$\begin{bmatrix} \dot{\sigma}_{xx} \\ \dot{\sigma}_{yy} \\ \dot{\tau}_{xy} \end{bmatrix} = [D] \begin{bmatrix} \dot{\varepsilon}_{xx} \\ \dot{\varepsilon}_{yy} \\ \dot{\varepsilon}_{xy} \end{bmatrix} - [V] \begin{bmatrix} \sigma_{xx} + \alpha p \\ \sigma_{xy} + \alpha p \\ \tau_{xy} \end{bmatrix} - \begin{bmatrix} \alpha \dot{p} \\ \alpha \dot{p} \\ 0 \end{bmatrix} \tag{4.41}$$

For the mechanical equilibrium, the following equation should be satisfied by the total stresses, which are computed through Eq. (4.41):

$$\nabla \cdot \dot{\sigma} + \dot{f} = 0 \tag{4.42}$$

where f is the external body force.

Without a volume source, the conservation equation of fluid mass is given by (Diek and Ghassemi, 2004):

$$\dot{\zeta} + \nabla \cdot \dot{w} = 0 \tag{4.43}$$

where $\dot{w}$ denotes Darcy's filter velocity; The transport equation for isotropic flow without thermal and chemical osmosis is deduced:

$$\dot{w} = -\frac{k}{\mu_f} \nabla p \tag{4.44}$$

where k denotes the intrinsic permeability; μ_f represents the viscosity of the fluid.

Let $\kappa = \dfrac{k}{\mu_f}$ and substitute Eq. (4.44) into Eq. (4.43):

$$\dot{\zeta} = \kappa \nabla^2 p \tag{4.45}$$

Combining Eq.(4.11) and (4.45), a coupled fluid diffusion equation could be yielded:

$$\alpha(\nabla \cdot \dot{u}) + \frac{1}{M}\dot{p} = \kappa \nabla^2 p \tag{4.46}$$

Eq.(4.41) and (4.46) represent a coupled set for poroviscoelasticity. They can be used to simulate the interaction between viscoelastic deformation of rock mass and fluid flow in a fluid flow-mechanical process under plane strain condition. Neglecting the second term on the RHS of Eq. (4.41), this model becomes identical to the conventional poroelastic model (Biot, 1941; Rice and Cleary, 1976; Diek and Ghassemi, 2004).

4.4 Viscosity model for the rock

Based on the experiment data, shear viscosity during deformation can be expressed as (Rushmer, 1995; Tommasi et al., 2000)

$$\eta_s = \eta_{s0}(T)\left|\dot{e}\right|^{1/n-1} \tag{4.47}$$

where $\left|\dot{e}\right| = \left[\frac{\dot{\varepsilon}_{ij}\dot{\varepsilon}_{ij}}{2}\right]^{1/2}$ is the second invariant of strain rate; in plane strain, it is given as $\left|\dot{e}\right| = \left[\frac{\dot{\varepsilon}_{xx}^2 + \dot{\varepsilon}_{yy}^2}{2} + \dot{\varepsilon}_{xy}^2\right]^{1/2}$; n is set in the range of 3-10. Shear viscosity is a function of both temperature and strain rate.

Sleep (2002) proposed a damage rheology model by taking both strain weakening and healing process into consideration. In the model, the damage tensor (C) was expressed in the compliance form of viscosity.

$$\frac{\partial C}{\partial t} = Af\left(\left|\dot{e}\right|\right) - BC \tag{4.48}$$

The first term on the RHS of Eq.(4.48) represents the strain weakening process, which is proportional to the second invariant of strain rate; while the second term denotes the healing process of damage (as recrystallization). For an isotropic material, the damage tensor C can reduce to a scalar: $C = 1/\eta_s$ (4.49)

By substituting the function f in Eq. (4.48) by a power law formulation for viscous rheology with an exponent $m = 1 - 1/n$ and replacing the damage tensor with Eq.(4.49) into Eq.(4.48), a common power law for viscous rheology can be derived in the steady state asymptotic. This is used only in the verification case of consolidation problem (for reservoir problems, a simpler rheology is used) whose analytical solution was given by Simakin and Ghassemi (2005).

$$\eta_s = \frac{B}{A}|\dot{e}|^{-m} \tag{4.50}$$

where A ($A = 10^{-9} - 0.1$) and B ($B = 2\times10^{-9} - 0.2$) are empirical constants.

4.5 Finite element formulation

After developing the coupled poro-viscoelastic model (Eq.(4.41) and (4.46)) with damage rheology (Eq.(4.50)), this model features in the nonlinearity of stress-strain relationship and power law rheology, which is distinguished from direct analytical methods by using Laplace transformation (Abousleiman et al., 1993; Bloch et al., 1999). Due to the complexity (nonlinearity) of the model, analytical solution is not amenable to solve the field equations. Therefore, a numerical method, finite element method, is

needed to solve these coupled fluid flow and rock deformation equations with certain initial and boundary conditions.

For plane strain conditions considered herein, a corresponding stiffness matrix (D) is selected for the poroviscoelastic model. In this work, eight-node quadrilateral elements are used to compute solid displacement vector u, while four-node quadrilateral element is applied to calculate pore pressure p for fluid. By applying the FEM approximation, the unknowns (u and p) at gauss integration points can be computed through the following equaitons:

$$\mathrm{u} = \mathrm{N_u}\tilde{\mathrm{u}} \qquad\qquad \mathrm{p} = \mathrm{N_p}\tilde{\mathrm{p}} \tag{4.51}$$

where $\mathrm{N_u}$ and $\mathrm{N_p}$ are the shape functions for solid and fluid elements; $\tilde{\mathrm{u}}$ and $\tilde{\mathrm{p}}$ are the vectors of the displacement and pore pressure at nodal points respectively.

For the mechanical equilibrium, Galerkin's finite element method (GFEM) is used to discretize Eq. (4.41) in spatial domain and the total stresses should satisfy Eq.(4.42). In weak form formulation, the mechanical equilibrium equation (Eq.(4.42)) for the poroviscoelastic model is expressed as:

$$\int_{\Omega} B^T D B \dot{\tilde{u}} d\Omega - \int_{\Omega} B^T \alpha \mathrm{N_p} \dot{\tilde{p}} d\Omega = R_{\Omega} + f_{\Omega}^{ve} \tag{4.52}$$

where Ω represents the discretized domain; R_{Ω} denotes the external applied forces; $f_{\Omega}^{ve} = \int_{\Omega} B^T \left\{ V \sigma'_{n+1} \right\} d\Omega$ represents the internal force resulted from viscoelastic deformation; B is the strain-displacement matrix for solid element.

By running element by element assembling, Eq. (4.52) is given in matrix form

$$K\Delta\tilde{\mathrm{u}} - A\Delta\tilde{\mathrm{p}} = \left(\mathrm{R}_{\Omega e} + \mathrm{f}_{\Omega e}\right)\Delta t \tag{4.53}$$

Where

$$K = \int_{\Omega e} B^{\mathrm{T}} DB dV \tag{4.54}$$

$$A = \int_{\Omega e} \left[B\right]^{\mathrm{T}} \left[\alpha\right]\left[\mathrm{N}_{\mathrm{p}}\right] dV \tag{4.55}$$

where Ωe represents the area of an element.

For the fluid diffusion equation (Eq.(4.46)), its FEM formulation is expressed in matrix form by applying GFEM treatment:

$$A^T\dot{\tilde{\mathrm{u}}} + S\dot{\tilde{\mathrm{p}}} + H_H\tilde{\mathrm{p}} = 0 \tag{4.56}$$

where

$$S = \int_{\Omega e}\left[\mathrm{N}_{\mathrm{p}}\right]^{\mathrm{T}}\left[\frac{1}{M}\right]\left[\mathrm{N}_{\mathrm{p}}\right] dV \tag{4.57}$$

$$H_H = \int_{\Omega e}\left[\nabla\mathrm{N}_{\mathrm{p}}\right]^{\mathrm{T}}\left[\kappa\right]\left[\nabla\mathrm{N}_{\mathrm{p}}\right] dV \tag{4.58}$$

For the temporal discretization, the following equation is taken into Eq. (4.56) with an implicit variable θ.

$$\tilde{\mathrm{p}}_{n+1} = \tilde{\mathrm{p}}_n + \theta(\Delta t)\dot{\tilde{\mathrm{p}}} \tag{4.59}$$

where Δt is the time increment; implicit variable θ is bounded between 0.5 (Crank-Nicolson scheme) and 1.0 (fully implicit scheme) for stability; subscript n represents the last time step. After some algebraic work, we finally obtain the following discretize equation for fluid diffusion equation:

$$-A^T \Delta\tilde{\mathrm{u}} - \left(S + \theta \Delta t H_H\right) \Delta\tilde{\mathrm{p}} = H_H \tilde{\mathrm{p}}_n \Delta t \tag{4.60}$$

By assembling the mechanical equation (Eq.(4.53)) and fluid diffusion equation (Eq.(4.60)) into matrix form, the FEM formulation for the poroviscoelasticity theory is given as:

$$\begin{bmatrix} K & -A \\ -A^T & -\left(S + \theta \Delta t H_H\right) \end{bmatrix} \begin{bmatrix} \Delta\tilde{\mathrm{u}} \\ \Delta\tilde{\mathrm{p}} \end{bmatrix} = \begin{Bmatrix} \left(\mathrm{R}_{\Omega e} + \mathrm{f}_{\Omega e}\right) \Delta t \\ H_H \tilde{\mathrm{p}}_n \Delta t \end{Bmatrix} \tag{4.61}$$

Apparently, the rise of internal force is caused by the viscoelastic deformation, which can be treated as boundary conditions in the FEM formulation and updated at each time step for equilibrium purpose.

A new numerical model is constructed by implementing the coupled poro-viscoelastic model into a finite element formulation. This model is first verified with analytical solution in simple case and compared to the poroelastic results in consolidation problem. Then, gas flow and fracture network can be incorporated into the numerical model to investigate the geomechanical (viscoelastic) behavior of gas shale reservoir and mechanical deformation of contact surfaces during production.

4.6 Verification

4.6.1 Consolidation problem

Due to the complexity of the poroviscoelastic problem, no analytical solution is available to solve the problem in 3D case. So, a 1D consolidation problem having a simple geometry (Figure 36) will be considered and solved analytically to partially verify the numerical model of poroviscoelastic deformation.

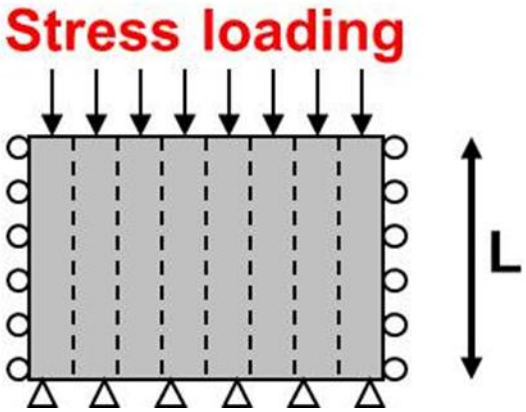

Figure 36 Geometry of consolidation problem for deriving analytical solution

A block of rock is subjected to a constant load (σ_{yy}) on the top surface. This mechanical load is greater than the internal fluid pressure of the sample and hence triggers the poroviscoelastic deformation. There is no any horizontal displacement or fluid leak-off on the right and left side boundary of the block, resulting in development of lateral confining pressure (σ_{xx}) during the loading process. However, the displacement and fluid leak-off is allowed on the top, in the y-axis (vertical) direction, which means the sample is under a uniaxial strain condition. The bottom side of the sample is impermeable and fixed for any vertical displacement. Then, the symmetric and deviatoric stress tensors can be given as

$$\sigma_s = \begin{bmatrix} \frac{\sigma_{xx}+\sigma_{yy}}{2} & 0 \\ 0 & \frac{\sigma_{xx}+\sigma_{yy}}{2} \end{bmatrix} \tag{4.62}$$

$$\sigma_d = \begin{bmatrix} \dfrac{\sigma_{xx} - \sigma_{yy}}{2} & 0 \\ 0 & \dfrac{\sigma_{xx} - \sigma_{yy}}{2} \end{bmatrix} \tag{4.63}$$

For a steady-state asymptotic solution, the following equations are obtained from Eq. (4.21), (4.31) and (4.32):

$$\frac{\sigma_{xx} + \sigma_{yy}}{2} + p = 2\eta_v \left(1 + \frac{G}{3K}\right)\left(\frac{\dot{\varepsilon}_{xx} + \dot{\varepsilon}_{yy}}{2}\right) \tag{4.64}$$

$$\frac{\sigma_{xx} - \sigma_{yy}}{2} = 2\eta_s \left(\frac{\dot{\varepsilon}_{xx} - \dot{\varepsilon}_{yy}}{2}\right) \tag{4.65}$$

For the consolidation problem, $\sigma_{yy} = \text{constant}$ without any body forces and $\dot{\varepsilon}_{xx} = 0$

Subtracting Eq. (4.63) from Eq.(4.62), one can get

$$\sigma_{yy} + p = \left(\eta_v \left(1 + \frac{G}{3K}\right) + \eta_s\right)\dot{\varepsilon}_{yy} \tag{4.66}$$

Applying the Laplacian operator on both sides of the Eq. (4.66), the following expression is obtained:

$$\frac{\partial^2 p}{\partial y^2} = \left(\eta_v \left(1 + \frac{G}{3K}\right) + \eta_s\right)\frac{\partial^2 \dot{\varepsilon}_{yy}}{\partial y^2} \tag{4.67}$$

Recalling the fluid diffusion equation (Eq.(4.46)), if taking $\dot{p} = 0$ for steady state and replacing the Laplacian of pore pressure by Eq.(4.67), one can get

$$\frac{k}{\mu_f}\left(\eta_v \left(1 + \frac{G}{3K}\right) + \eta_s\right)\frac{\partial^2 \dot{\varepsilon}_{yy}}{\partial y^2} = \alpha \dot{\varepsilon}_{yy} \tag{4.68}$$

Letting $\varphi = \sqrt{\dfrac{\alpha}{\dfrac{k}{\mu_f}\left(\eta_v\left(1+\dfrac{G}{3K}\right)+\eta_s\right)}}$, the above equation has a general solution

$$\dot{\varepsilon}_{yy}(y) = C_1 e^{\varphi y} + C_2 e^{-\varphi y} \tag{4.69}$$

By substituting this solution into Eq. (4.66), the following equation can be derived

$$\sigma_{yy} + p = \left(\eta_v\left(1+\frac{G}{3K}\right)+\eta_s\right)\left(C_1 e^{\varphi y} + C_2 e^{-\varphi y}\right) \tag{4.70}$$

Applying the boundary condition $p(0) = 0$ and $\left.\dfrac{\partial p}{\partial y}\right|_{y=L} = 0$, one can get the solution for mode I loading case:

$$\frac{p}{\sigma_{yy}} = \frac{e^{\varphi(y-2L)} + e^{-\varphi y}}{1+e^{-2\varphi L}} - 1 \tag{4.71}$$

For the mode 2 loading case ($\sigma_{yy} = 0$), the boundary condition is $p(0) = p_0$ and $\left.\dfrac{\partial p}{\partial y}\right|_{y=L} = 0$, then the solution will be expressed as:

$$\frac{p}{p_0} = \frac{e^{\varphi(y-2L)} + e^{-\varphi y}}{1+e^{-2\varphi L}} \tag{4.72}$$

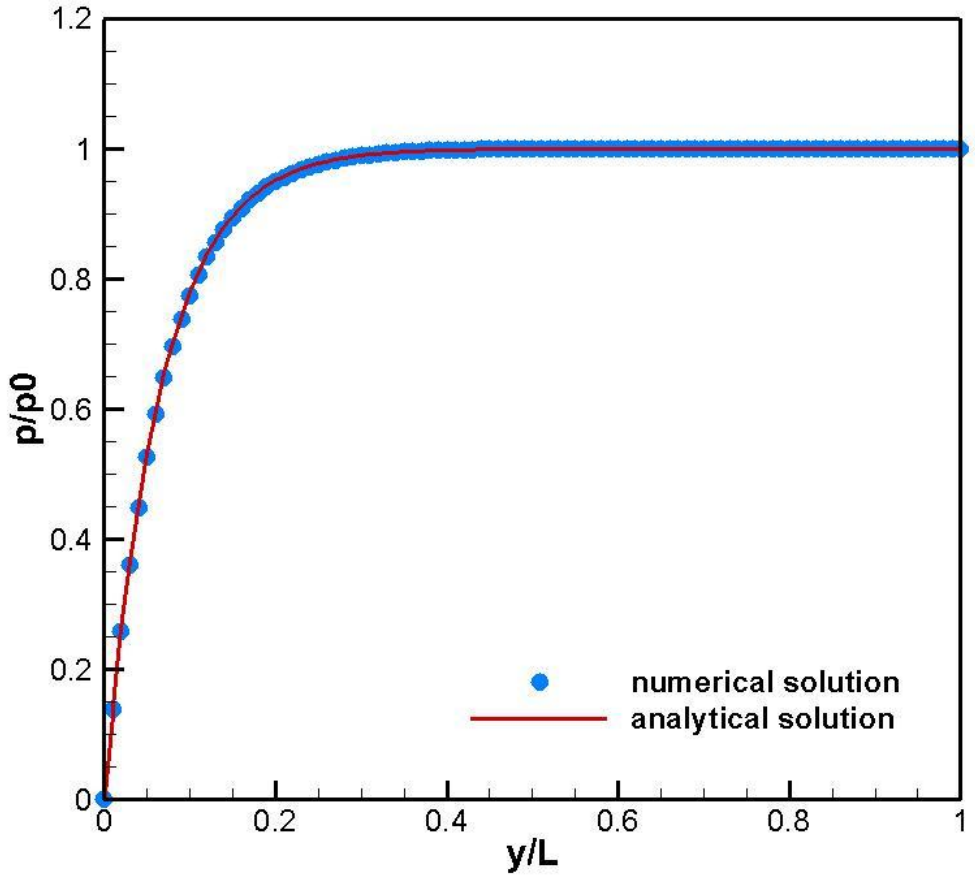

Figure 37 Comparison of numerical results (data markers) with analytical solution (solid curves) for the distribution of pore pressure in steady state.

By simulating the simple geometry and boundary conditions for a uniaxial strain problem, the analytical solution of pore pressure distribution is plotted together with that of numerical solution, as shown in Figure 37. All the required rock mechanical properties for both numerical and analytical tests are kept the same as listed in Table 2 for the verification and the shear viscosity, which is set to $\eta_s = 4.0\times10^{10}\,\mathrm{Pa}\cdot\mathrm{s}$. When pore pressure reached steady state (slight change of pore pressure and stress component

with respect to time), it can be seen that the analytical solution matches very well with the finite element results for fluid loading.

4.6.2 Wellbore problem (creep closure)

Under the plane strain condition for the 2-D case, the wellbore problem (geometry is given in Figure 38), is widely studied and analytically solved in literature. In this problem, uniform stress p_0 is acting on the far field boundary of the reservoir rock and the fluid pressure p_{wf} is maintained on the wellbore wall ($r = a = 0.1\text{m}$). The the fluid pressure p_{wf} is set lower than the far field stress p_0 to initialize the elastic or even viscoelastic deformation. For the elastic deformation, the analytical solution of radial displacement is available in literature (Jaeger et al., 2007):

$$u_r(r) = \frac{a^2}{2Gr}\left(p_0 - p_{wf}\right) \tag{4.73}$$

It can be seen that the response of displacement field to the stress loading is instantaneous. For the viscoelastic deformation, the analytical solution of radial displacement for the Maxwell viscoelatic model is given as (Christensen, 1971):

$$u_r\left(r,t\right) = \frac{a^2}{r}\left(p_0 - p_{wf}\right)\left(\frac{1}{2G} + \frac{t}{\eta}\right) \tag{4.74}$$

In this solution, the displacement field is a function of radius and time, which is quite different from that of the elastic case. This time dependent behavior corresponds to the viscoelastic creep of the formation, which can cause the closure of the wellbore with time. (Christensen, 1971)

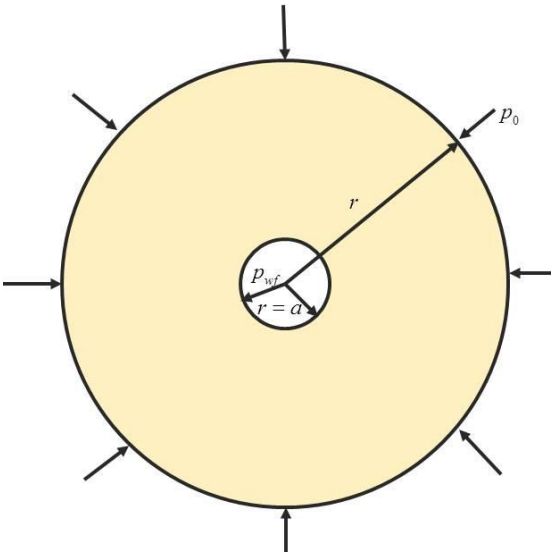

Figure 38 Geometry of wellbore problem

This analytical solution for Maxwell model (Eq. 4.74) can be employed to verify the numerical model of poroviscoelasticity in this study. By simulating the axisymmetric geometry and boundary conditions for the wellbore problem (mode II laoding), the analytical solutions of the radial displacement evolution at the wellbore wall ($r = 0.1\text{m}$) are plotted against those of numerical solution with different solid viscosity, as displayed in Figure 39. In the verification process, the difference between the far field stress p_0 and mud pressure p_{wf} is set to be 1.0 MPa and all necessary rock mechanical properties are extracted from Table 2. For the shear viscosity of the rock sample, three different values are used in the comparison. It can be seen that the analytical solutions agree very well with the finite element results of the Maxwell model for fluid loading. When the solid deformation gets close to elastic regime, as the viscosity is greater than $1.0\times10^{18}\text{pa}\cdot\text{s}$ in this study, the radial displacement of the wellbore wall becomes

invariant or slightly changes with time. The viscoelastic deformation (creep), hence the wellbore closure, becomes more significant with lower viscosity of the reservoir rock.

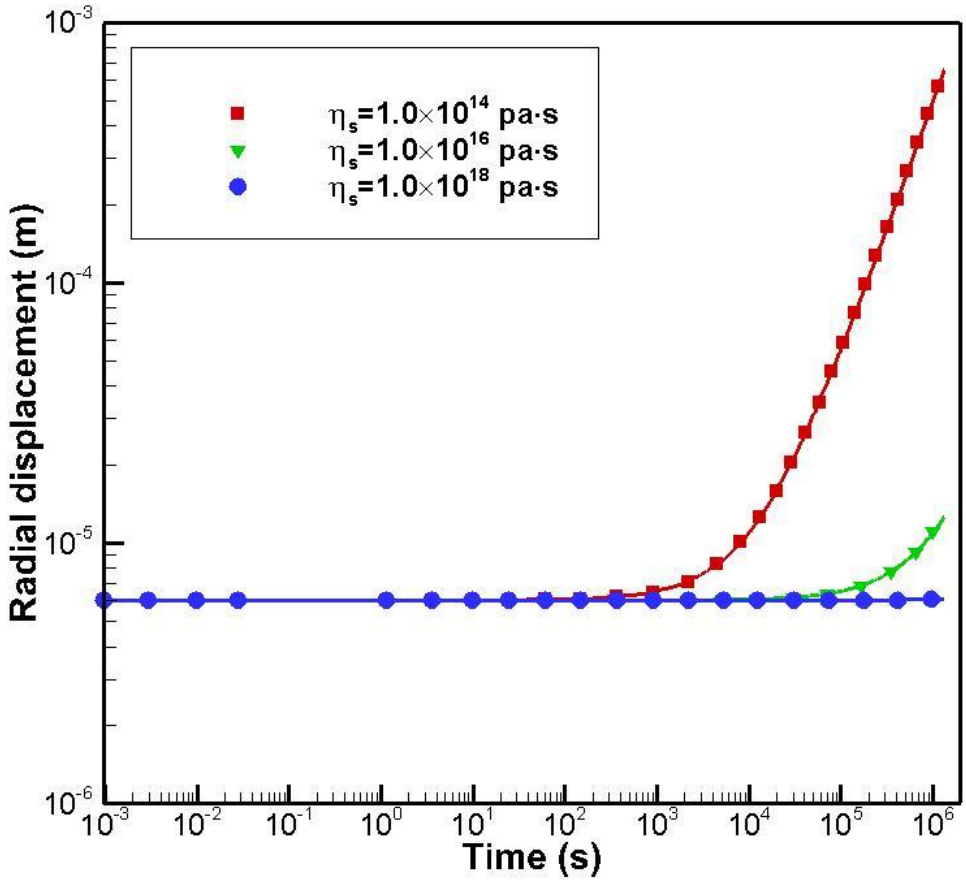

Figure 39 Comparison of numerical results (data markers) with analytical solution (solid curves) for the time evolution of the radial displacement at the wellbore wall with the variation of the viscosity of the reservoir rock.

4.7 Comparison

In order to highlight the influence of viscoelastic deformation in matrix mechanical performance, both the numerical models for poroviscoelasticity and poroelasticity are applied to simulate 1D consolidation of the same rock sample in Figure 36, whose properties are given in Table 4. Besides this, boundary conditions and loading history are kept the same as those in the verification process and assumed for both models. With these assumptions, a comparison is allowed between the two different models.

The results of numerical experiments are presented in Figure 40, 41 and 42. Figure 40 shows the distribution of pore pressure along vertical direction within the sample. The poroviscoelastic cases are given in data markers, while the poroelastic cases are shown in solid curves for comparison. The pore pressure responses for fluid loading in two cases overlap each other. It implies that the viscoelastic effect is insignificant (In the fluid diffusion equation, the coupled term is very small when compared to the fluid pressure gradient) in the pore pressure evolution which agrees with the results in Abousleiman et al. (1993), in which a three-parameter generalized Kelvin's model was used. Figure 41 depicts the distribution of effective stress σ'_{xx} along vertical direction and Figure 42 demonstrates the distribution of effective stress σ'_{yy} in the same direction. The difference in the stress responses between two cases becomes noticeable as time elapse. However, away from the loading boundary ($y = 0$), the difference in the stress responses between two cases reduces with dimensionless position (y / L). It indicates

that the viscoelastic deformation projects considerable influence in the development of stress field, especially for the area close to the loading boundary.

Drained Poisson's ratio, ν	0.219
Undrained Poisson's ratio, ν_u	0.461
Young's modulus, E	1.853GPa
Shear modulus, G	0.76GPa
Porosity, ϕ	0.2989
Biot's coefficient, α	0.966
Permeability coefficient, κ	$3.33\times10^{-16}\,\mathrm{m}^2/(\mathrm{Pa}\cdot\mathrm{s})$
Bulk modulus, K	1.10GPa
Solid bulk modulus, K_s	32.65GPa
Shear viscosity, η_s	$4.0\times10^{11}\,\mathrm{pa}\cdot\mathrm{s}$

Table 4 Rock mechanical properties used in the comparison

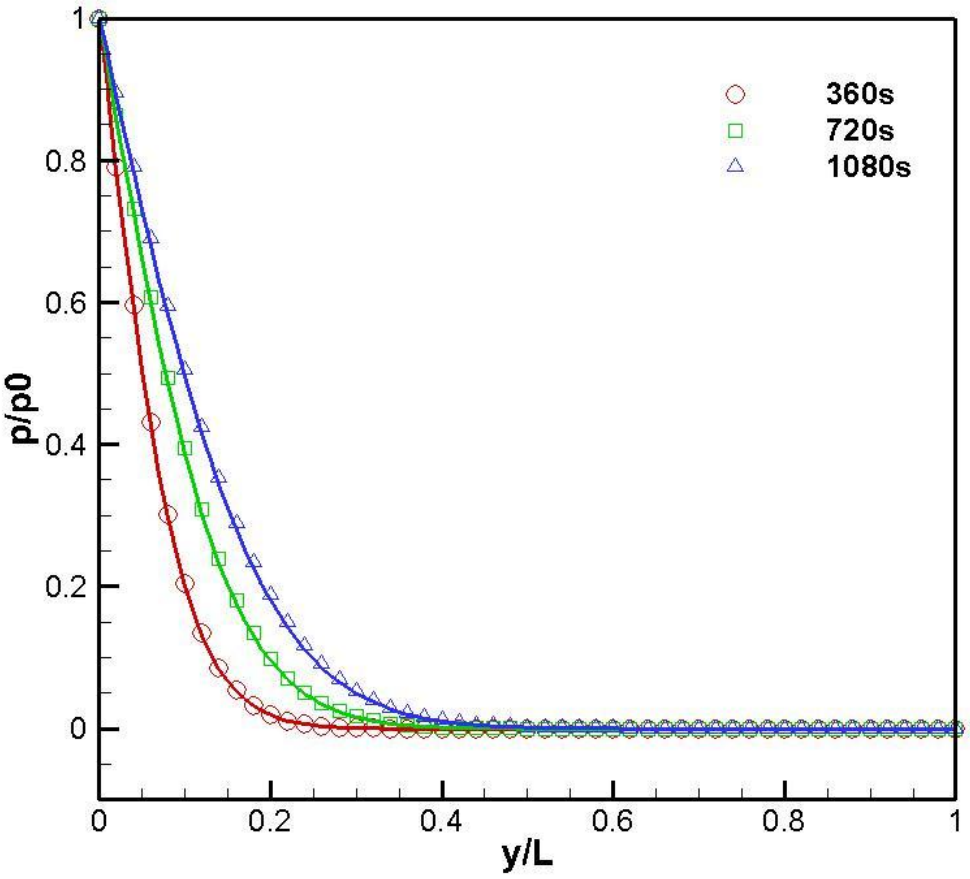

Figure 40 Influence of viscoelastic deformation on the distribution of pore pressure in vertical direction (solid curve: poroelasticity; data marker: poroviscoelasticity)

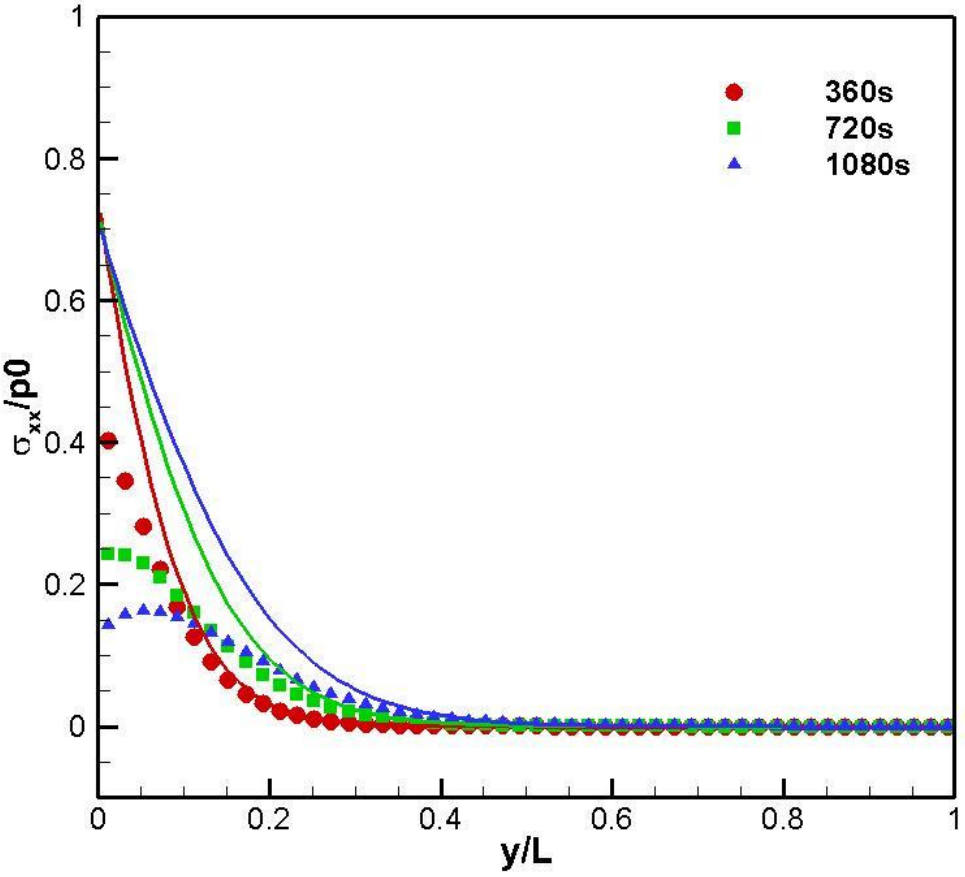

Figure 41 Influence of viscoelastic deformation on the distribution of effective stress σ'_{xx} along vertical direction (solid curve: poroelasticity; data marker: poroviscoelasticity)

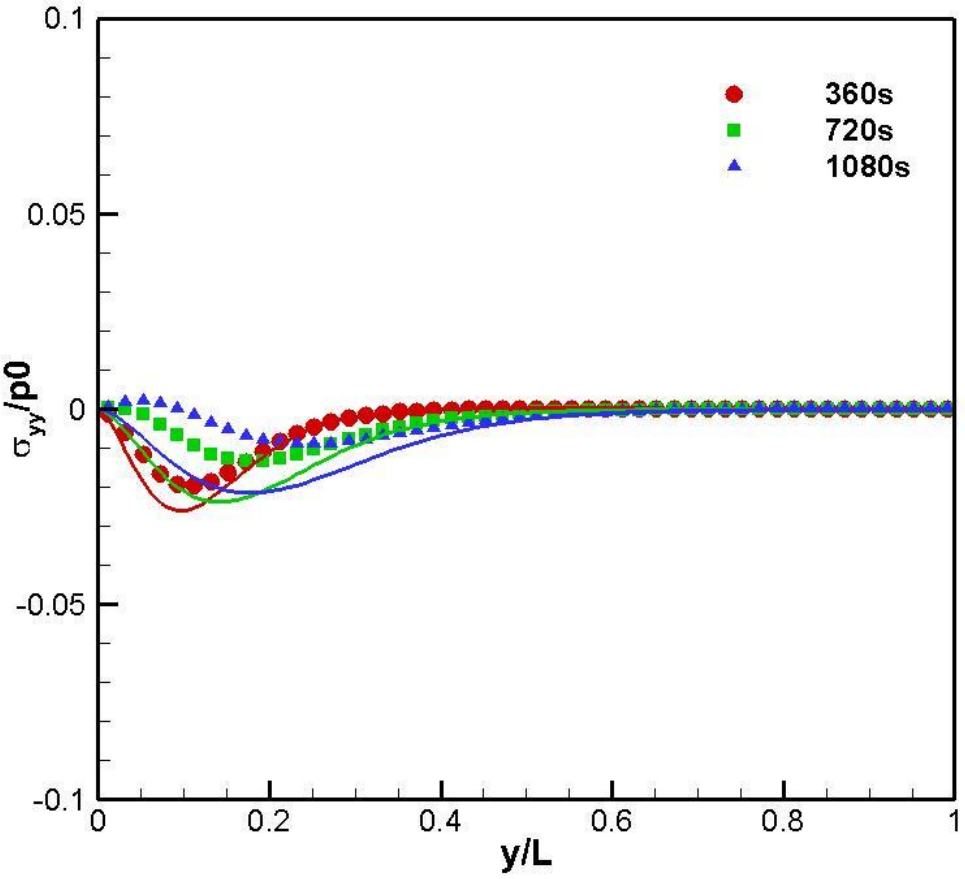

Figure 42 Influence of viscoelastic deformation on the distribution of effective stress σ'_{yy} along vertical direction (solid curve: poroelasticity; data marker: poroviscoelasticity)

4.8 Poroviscoelastic-DPM-FEM model

In Chapter 3, a DPM-FEM model was developed based on poroelastic constitutive law. However, the viscoelastic effect, which is proved to be essential in stress response in shale samples, was omitted in that model. In this chapter, a poroviscoelastic-FEM model is constructed based on the Maxwell model. By combining the DPM-FEM model and poroviscoelastic-FEM model (Eq.(4.41) and (4.46)), a poroviscoelastic-DPM-FEM model is proposed to handle the viscoelastic deformation, fracture network evolution, and gas storage and flow mechanism simultaneously in gas shale reservoir.

As stated before, the difference between FEM formulation of poroelasticity (Zhou and Ghassemi, 2009) and poroviscoelasticity (Eq.(4.61)) in the fluid-mechanical process is the internal force term, which is induced by the viscoelastic deformation. Thus, an internal force term ($\mathrm{f}^{\wedge}_{\Omega e}$) denoting the viscoelastic effect is added to Eq. (3.48); while the gas transportation equations for matrix (Eq.(3.49)) and fracture (Eq.(3.50)) elements are unaltered.

Therefore, the FEM formulation for the poroviscoelastic-DPM-FEM model is given as (Appendix VI):

$$\begin{bmatrix} K & -A & 0 \\ -L^T & -\left(S_1+\theta\Delta t H_{H1}+\theta Q\Delta t\right) & Q\Delta t\theta \\ 0 & Q\Delta t\theta & -(S_2+H_{H2}\theta\Delta t+Q\Delta t\theta) \end{bmatrix}\begin{bmatrix} \Delta\tilde{u} \\ \Delta m(\tilde{p}_m) \\ \Delta m(\tilde{p}_f) \end{bmatrix} = \begin{bmatrix} \left(\mathrm{R}_{\Omega e}+\mathrm{f}^{\wedge}_{\Omega e}\right)\Delta t \\ (H_{H1}\Delta t+Q\Delta t)m(\tilde{p}_m)-Q\Delta t m(\tilde{p}_f) \\ (H_{H2}\Delta t+Q\Delta t)m(\tilde{p}_f)-Q\Delta t m(\tilde{p}_m) \end{bmatrix} \tag{4.75}$$

where all the coefficients are defined by Eq.3.51-3.58; the internal force is computed by $f_{\Omega e} = \int_{\Omega e} B^T \left\{ V \sigma'_{n+1} \right\} d\Omega$ (4.73), whose detailed derivation is given in Section 5.

The procedure to solve the non-linear equations (Eq.(4.75)) is briefly given as below:

(i) Unknowns (u , $m(p_m)$ and $m(p_f)$) from a previous time step are used to "guess" the initial stiffness matrix in current time step; and the intial condition of the reservoir is used for the first guess;

(ii) In current time step, the FEM formulation (Eq.(4.72)) is solved to obtain the increment of unknown variables (Δu , $\Delta m(p_m)$ and $\Delta m(p_f)$);

(iii) The newly updated Δu , $\Delta m(p_m)$ and $\Delta m(p_f)$ is used to compute the strain, stress at current time step and then update the fracture aperture, boundary conditions and stiffness matrix;

(iv) Step (ii) is repeated to get the new Δu , $\Delta m(p_m)$ and $\Delta m(p_f)$ for the next iteration; if Δu , $\Delta m(p_m)$ and $\Delta m(p_f)$ are close enough to those in the presvious iteration, the iteration is terminated and the next time step is proceeded.

4.9 Conclusion

In this chapter, a coupled poroviscoelastic model is developed based on the Maxwell model and applied to investigate the interaction between viscoelastic deformation of rock mass and fluid flow in a fluid-mechanical process. The viscoelastic effect is addressed in both deviatoric and symmetric effective stresses.

The poroviscoelastic model has been implemented into a finite element formulation in plane strain condition. This newly constructed mechanical model has been verified with analytical solution in a uniaxial strain problem. And then it has been compared to the poroelastic results in consolidation problem under plane strain deformation. By comparing the case of poroelasticity and poroviscoelasticity, viscoelastic effect in pore pressure response throughout the whole sample is slight; however, viscoelastic effect in the stress evolution is noticeable, especially for the area near the loading boundary.

Finally, a non-linear numerical simulator is constructed by incorporating this poroviscoelastic model into the dual permeability (DPM)-finite element model (FEM) to study the long term viscoelastic effect in fracture network evolution and hence the gas production in gas shale reservoirs.

CHAPTER V

APPLICATION

5.1 Wellbore problem-single permeability

In this session, poroelastic analysis of gas production from gas shale is performed by using the non-linear fully coupled poroelastic finite element model (single permeability). The example considered Barnett Shale with properties given in Table 2. The finite element mesh used for the simulation is shown in Figure 11. The reservoir is assumed to be subjected to the following in-situ stress conditions: σ_H =43.34 MPa in the x-direction ($\theta = 0$) and σ_h =39.01 MPa in the y-direction ($\theta = \pi / 2$). In order to simplify the problem, only methane (single phase and single component) is considered. Two different cases are simulated to quantify the net influence of gas sorption and induced matrix deformation: (i) only free gas is produced; (ii) free and desorption gas are produced. The gas sorption influence on gas pressure distribution, time evolution of permeability, and the effect of gas desorption on effective stress field are studied simultaneously.

5.1.1 Gas pressure distribution

The spatial and temporal variations in gas pressure around the wellbore in response to gas depletion are presented in Figure 43. In both cases, with and without desorbed gas, the gas pressure decreases with time in a similar manner. However, the reduction of gas pressure for the desorption case is relatively slower than that of only free gas. This is attributed to the release of the sorption gas from the matrix.

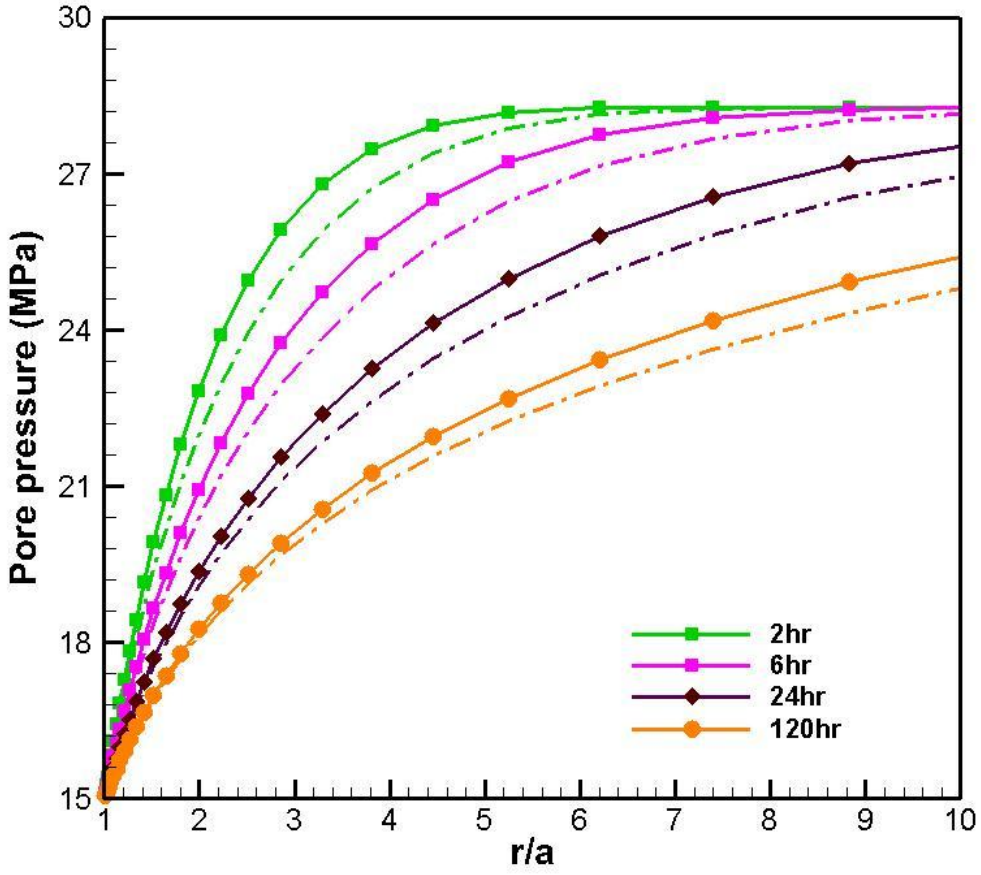

Figure 43 Influence of gas desorption on the distribution of gas pressure in the x-direction (solid curves: with desorption; dashed lines: without desorption).

5.1.2 Evolution of matrix permeability

The distributions of the permeability ratio (k / k_0) in time and space are depicted in Figure 44. For the no-desorption case, the permeability ratio decreases near the wellbore but, gradually increases with time and away from the well to approach unity. When desorption is included, the permeability ratio increases moderately, its highest value is at the wellbore wall and gradually decreases with distance from the well. The reduction of the permeability for the free gas case is associated with a pore pressure reduction that increases the effective stresses thus compressing the pore space. On the other hand, gas desorption induces tensile stresses that work against the influence of increases compressive effective stress associated with pore pressure reduction and thus, cause permeability enhancement within the near wellbore region. Close to the wellbore, a greater pore pressure drop is generated and so a larger amount of adsorbed gas is released which in turn, enhances the tensile stresses and causes a higher increases in permeability. The zone with a permeability ratio greater than 1 expands away from the wellbore with the elapse of time. It can be seen that if the gas desorption is omitted, the permeability and gas flow capabilities will be underestimated within the reservoir, especially for the area near the wellbore.

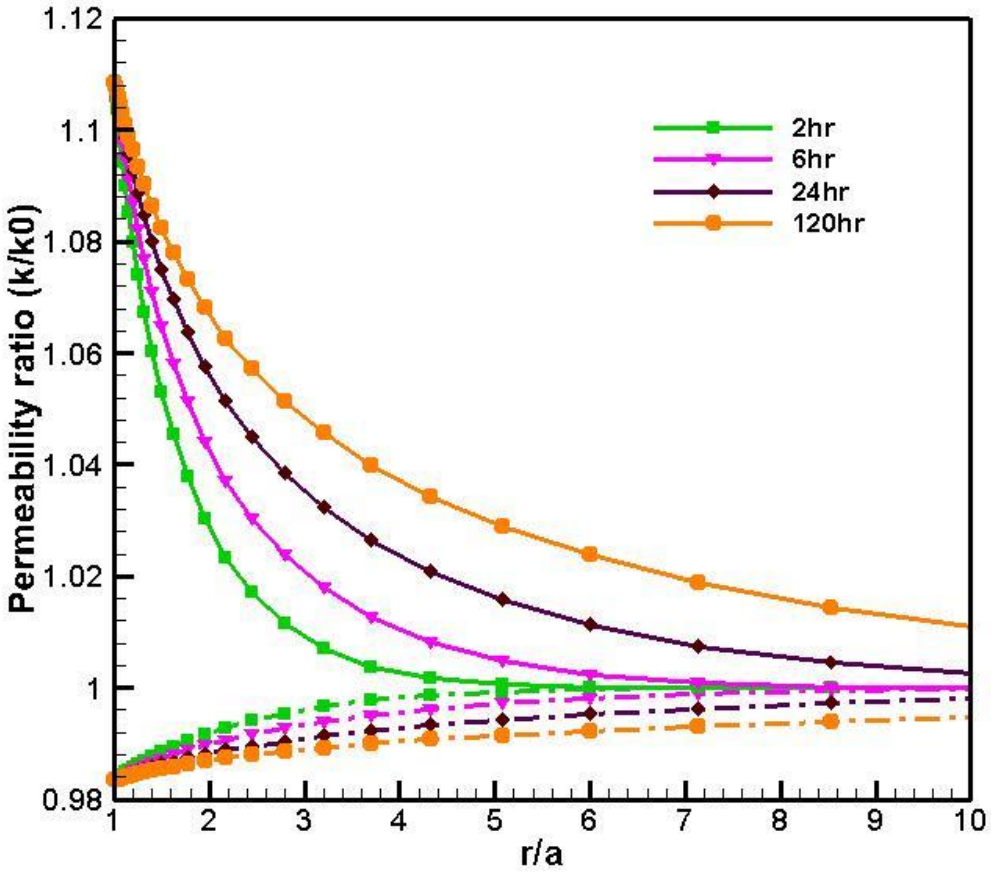

Figure 44 Influence of gas desorption on the evolution of gas permeability in the x-direction (solid curves: with desorption; dashed lines: without desorption).

5.1.3 Effective stress variation

Figure 45 and 46 show the distributions of the total effective radial and tangential stresses around the wellbore for with and without desorption cases. It can be seen that when including desorption, the compressive effective radial stresses around the wellbore are relatively lower than when desorption is excluded, irrespective of the spatial and temporal extent. However, the total effective tangential stresses in the no-desorption case is compressive and increases with time at every point. Its highest value is on the wellbore wall and is associated with the pore pressure drawdown. On the other hand, the total effective tangential stress for the desorption case is tensile near the wall (r/a=1), becoming more tensile with time. But, away from the wellbore wall, it increases and becomes compressive with time. Further, it can be seen that with desorption, the total effective tangential stresses are relatively lower in the near the wellbore region. In this tensile area, small fractures might open. However, But the effective tangential stresses in the with-desorption case are slightly higher than those in the without-desorption case in the far field at the same time, which implies that the fractures tends to close more easily and earlier with desorption gas within reservoir. All these differences can be related to the impacts of gas desorption mechanism.

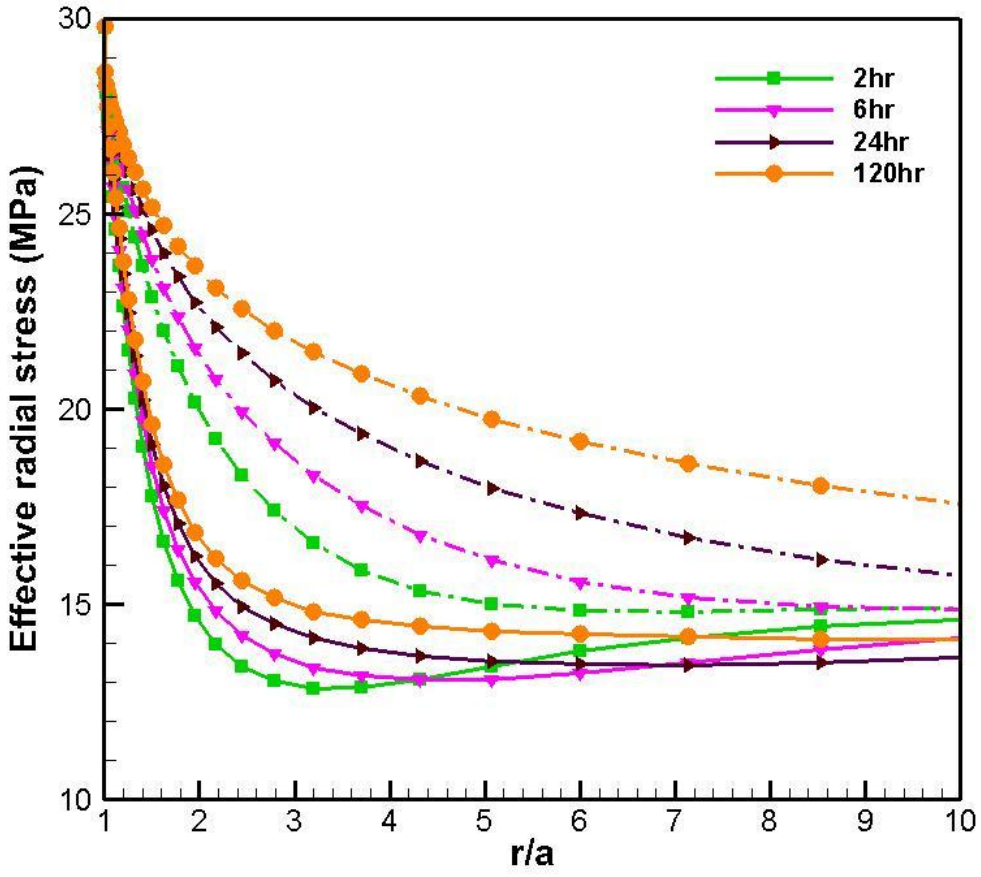

Figure 45 Influence of gas desorption on the evolution of total effective radial stress in the x-direction (compression +; solid curves: with desorption; dashed lines: without desorption).

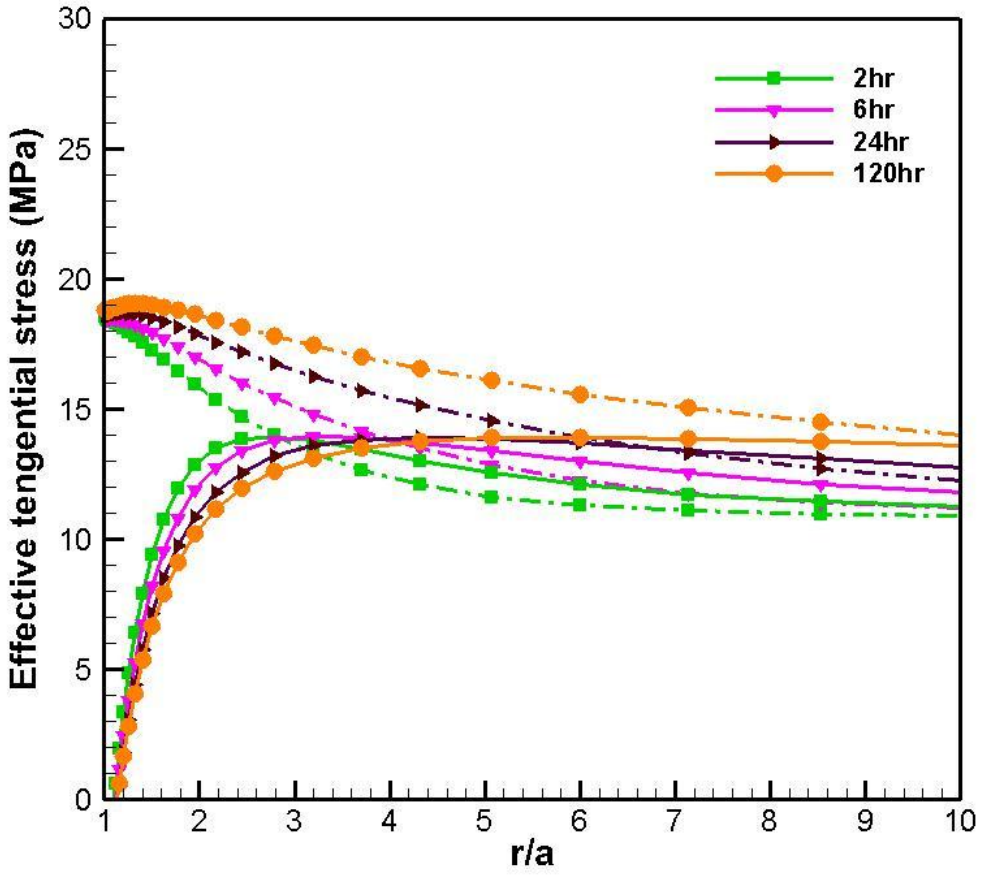

Figure 46 Influence of gas desorption on the evolution of total effective tangential stress in the x-direction (solid curves: with desorption; dashed lines: without desorption); due to gas desorption, total effective tangential stress becomes slightly negative at wellbore (r/a=1) in this case study.

5.2 Wellbore problem-dual permeability

In this session, geomechanical evolution of a fractured reservoir during gas production is simulated by using the non-linear fully coupled poroelastic DPM-FEM model. Geomechanical parameters given in Table 5 and the finite element mesh presented in Figure 11 and 31 are also used for the analysis. The reservoir is assumed to be subjected to the following in-situ stress conditions: σ_H =43.34 MPa in the x-direction ($\theta = 0$) and σ_h =39.01 MPa in the y-direction ($\theta = \pi / 2$). In order to simplify the problem, only methane (single phase and single component) production is considered. And six near-wellbore fractures are considered at current stage. Three of them which are marked as Frac1, 3 and 5 in Figure 47, are perpendicular to the minimum in-situ stress direction to represent hydraulic fractures. The others three, which are named as Frac2, 4 and 6 in Figure 45, are pre-existing natural fractures.

The gas pressure variations (both spatial and temporal) around the wellbore due to the gas depletion are given in Figure 47-49. In these three diagrams, the gas pressure decreases with the time across the whole reservoir. However, as expected, the contour of gas pressure is highly affected by the presence of fractures whose locations are outlined by the solid dark lines in each of these three diagrams. The gas pressure in the region around the fractures is depleted more rapidly compared to the rest of the reservoir.

Poisson's ratio, ν	0.25	0.25
Young's modulus, E	20.684GPa	3.0×10^{6} psi
Shear modulus, G	8.274GPa	1.2×10^{6} psi
Initial porosity, ϕ	0.04	0.04
Biot's coefficient, α	0.6354	0.6354
Initial permeability, k	1.0×10^{-19} m^2	0.1 μD
Bulk modulus, K	13.790GPa	2.0×10^{6} psi
Solid bulk modulus, K_s	37.820GPa	5.5×10^{6} psi
Initial reservoir pressure, p_0	8.274MPa	1200psi
Bottom hole pressure, p_{wf}	5.516MPa	800psi
Average system temperature, T	90^0C	194^0F
Density of gas shale, ρ_r	2.4×10^{3} kg/m^3	150lb/ft^3
Min in-situ stress, σ_h	39.011MPa	5658psi
Max in-situ stress, σ_H	43.340MPa	6286psi
Langmuir pressure constant, P_L	1.517MPa	220psi
Langmuir volume constant, V_L	0.0172 m^3/kg	0.275ft^3/lb
Langmuir volumetric strain constant, ε_L	0.02295	0.02295
Aperture without any normal stress, a_0	0.0001m	3.94×10^{-3} in
Empirical constant, A	1.0	1.0
90% closure stress, B	50MPa	7252psi

Table 5 Input geomechanical parameters used in the wellbore case study

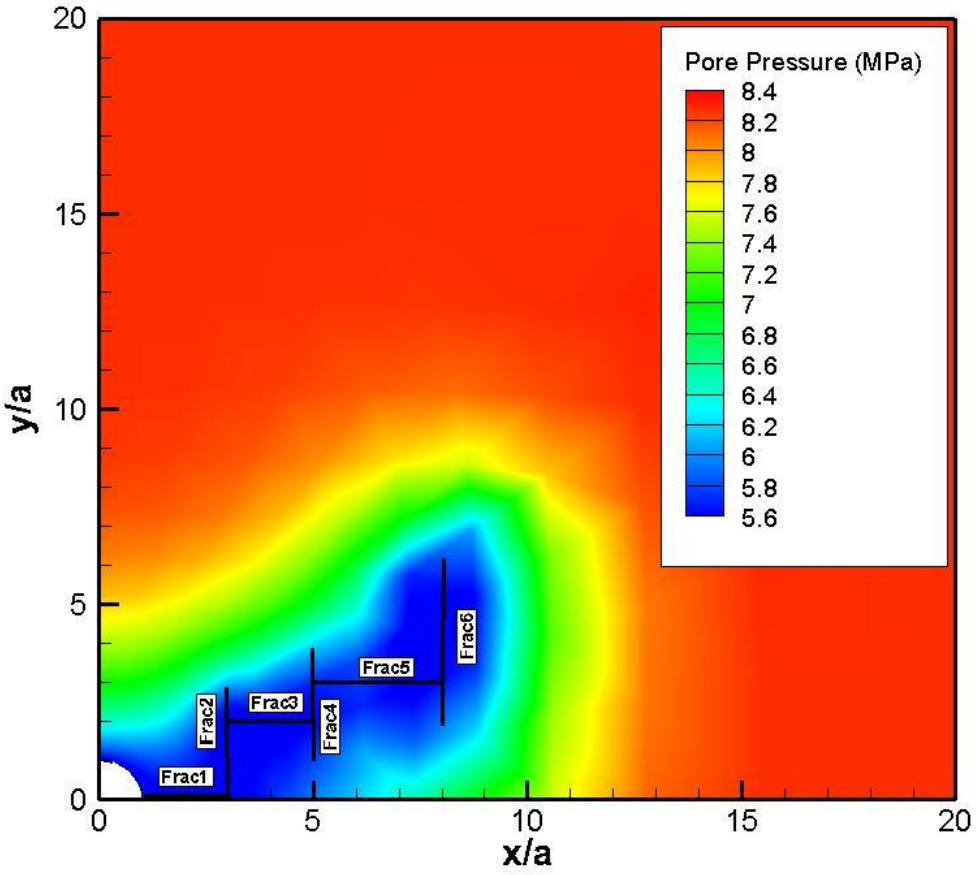

Figure 47 Distribution of gas pressure after 1 day depletion.

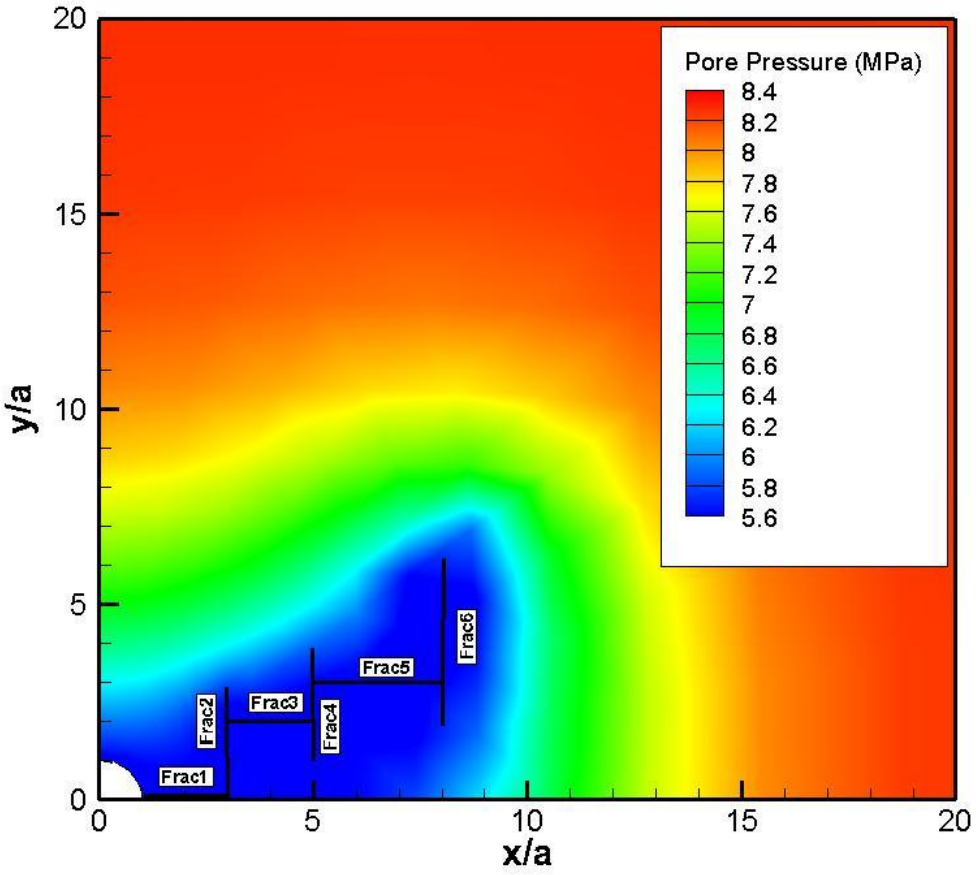

Figure 48 Distribution of gas pressure after 3 days depletion.

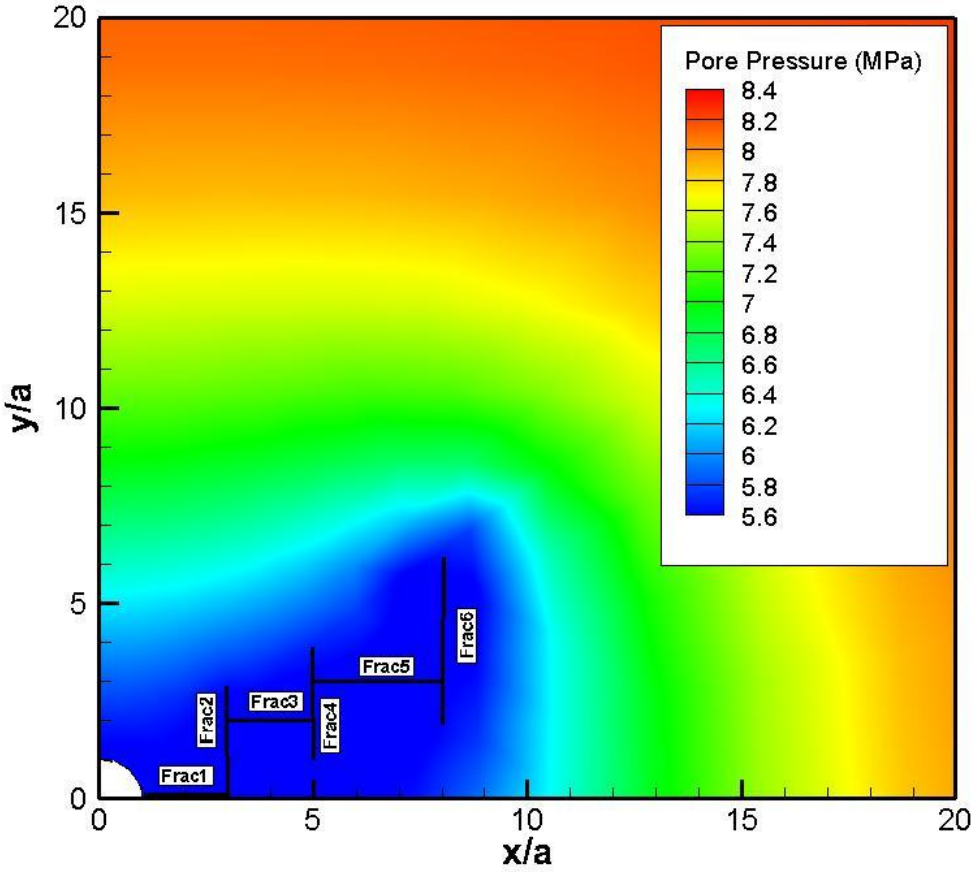

Figure 49 Distribution of gas pressure after 10 days depletion.

Then, two different simulation cases are studied to quantify the influence of desorption-induced matrix deformation: (i) only free gas is drained; (ii) free plus desorption gas is produced. The results in terms of time evolution of fracture aperture for both cases are discussed below.

As shown in Figure 50, the time evolutions of fracture aperture along the dimensionless fracture length are plotted for Frac1 for both cases. The fracture aperture is not uniform along its length in either case. In the 1st case, the fracture aperture slightly increases with time, especially in the near-wellbore region. For some time, the fracture aperture is a bit lower near its end that is close to the wellbore. In the 2nd case, the fracture behavior has a similar trend. However, the fracture aperture variation for the same time span is more significant when compared with that in the 1st case. The fracture will open a bit in this case, especially for the near the wellbore region which is compatible with the effective tangential stress (Huang and Ghassemi, 2011). These anomalies can be attributed to the impacts of gas desorption mechanism. Close to the wellbore, a greater pore pressure reduction is generated and hence a larger amount of adsorbed gas is released which in turn, decreases the effective tangential stresses and enhances the desorption-induced matrix deformation. With relatively lower effective tangential stresses, fractures tend to open a bit in the vicinity of the wellbore upon gas desorption.

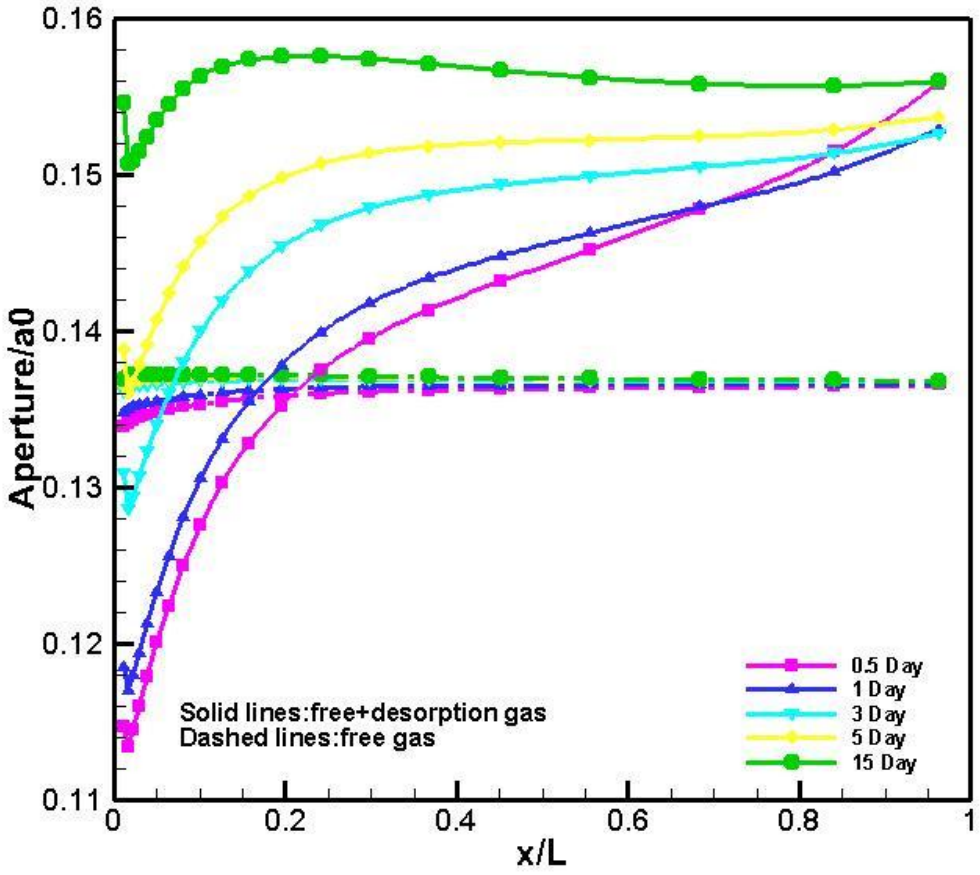

Figure 50 Time evolution of dimensionless aperture of Frac1.

However, the behavior of Frac2 and Frac3 are quite different from that of Frac1, particularly in the 2nd case. In the 1st case, the aperture changes minimally for both Frac2 and Frac3 as depicted in Figure 51 and 52. In the 2nd case, Frac2 closes at both ends and opens near its center for some time. The whole fracture opens first and then closes with time. Frac3 opens continuously as time elapses. The aperture of Frac2 is lower than that of Frac3 as its orientation is normal to the maximum in-situ stress. During gas production, the expected closure of the fractures is associated with a pore pressure reduction that increases the compressive effective stress. However, gas desorption induces tensile stress that works against the influence of pore pressure reduction and causes the fracture open.

In general, fractures that are parallel to the maximum in-situ stress direction will open during gas depletion due to the release of adsorption gas. Fractures that are perpendicular to the maximum in-situ stress tend to close down earlier than those parallel to the maximum in-situ stress with or without gas desorption.

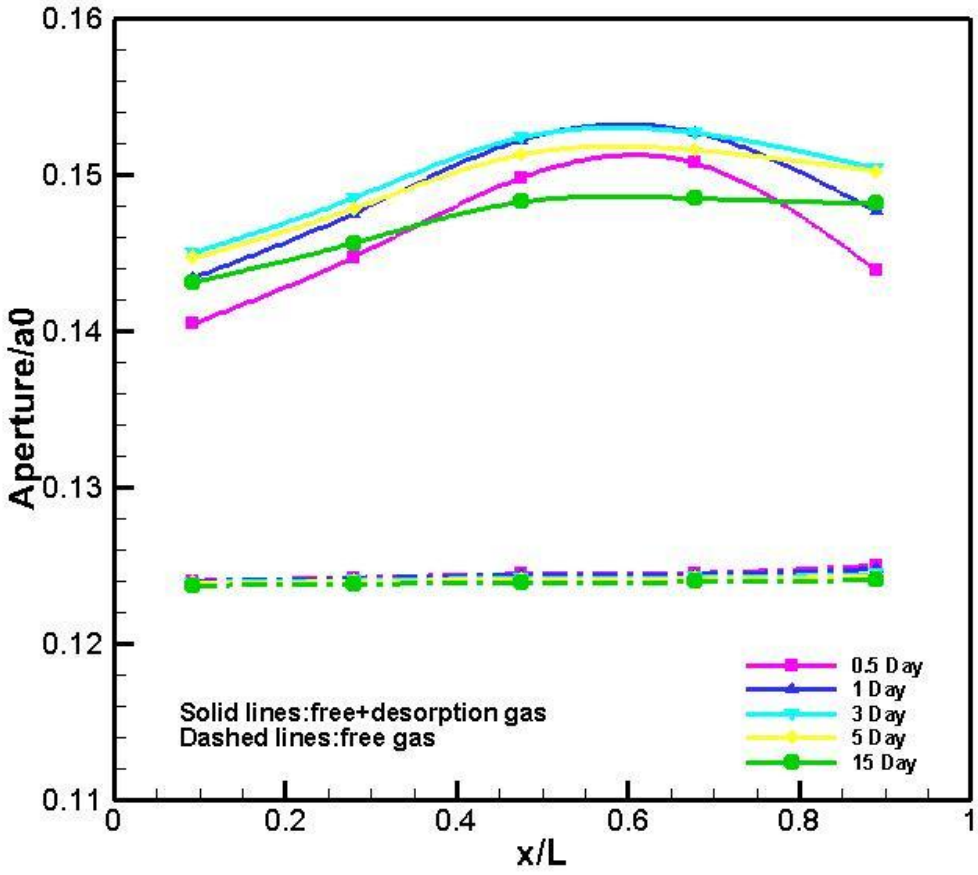

Figure 51 Time evolution of dimensionless aperture of Frac2.

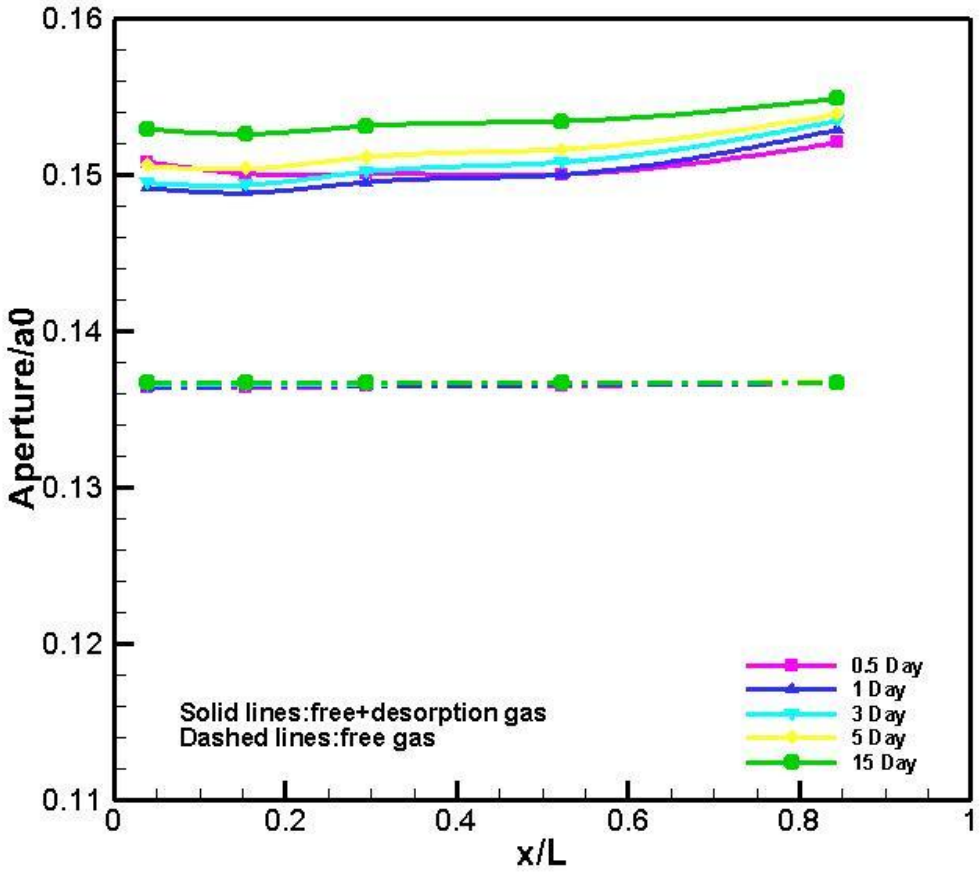

Figure 52 Time evolution of dimensionless aperture of Frac3.

5.3 Field case study

In this session, the non-linear fully coupled poroelastic DPM-FEM model is further applied to a field case to investigate the geomechanical evolution of a fractured reservoir in field scale. In this case study, the reservoir size is $200\text{m}\times 200\text{m}\times 60\text{m}$. Figure 53 shows the whole reservoir domain and its finite element mesh. In total, 10000 eight-node rectangular elements are employed and their size is uniform across the whole domain. As decipted in Figure 53, a horizontal well is placed in the center of the reservoir and is set to parallel to the x-axis. No displacement and no flow conditions are applied to the outer boundary of the reservoir domain. The reservoir is assumed to be subjected to the following in-situ stress conditions: σ_H =43.34 MPa in the y-direction and σ_h =39.01 MPa in the x-direction. Primary geomechanical parameters used in this study are summarized in Table 5.

In order to highlight the matrix deformation induced by gas desorption, the initial reservoir pressure is set to be 8.27 MPa (1200psi) and the bottom hole pressure (BHP) of the horizontal well is 5.52 MPa (800psi), which is kept contant and lower than the reservoir pressure in production period. And the temperature and chemical perturbations are minimized during the numerical simulation. And also, only methane (single phase and single component) production is considered and the reservoir deformation is calculated under plane strain condition in the 2D cases.

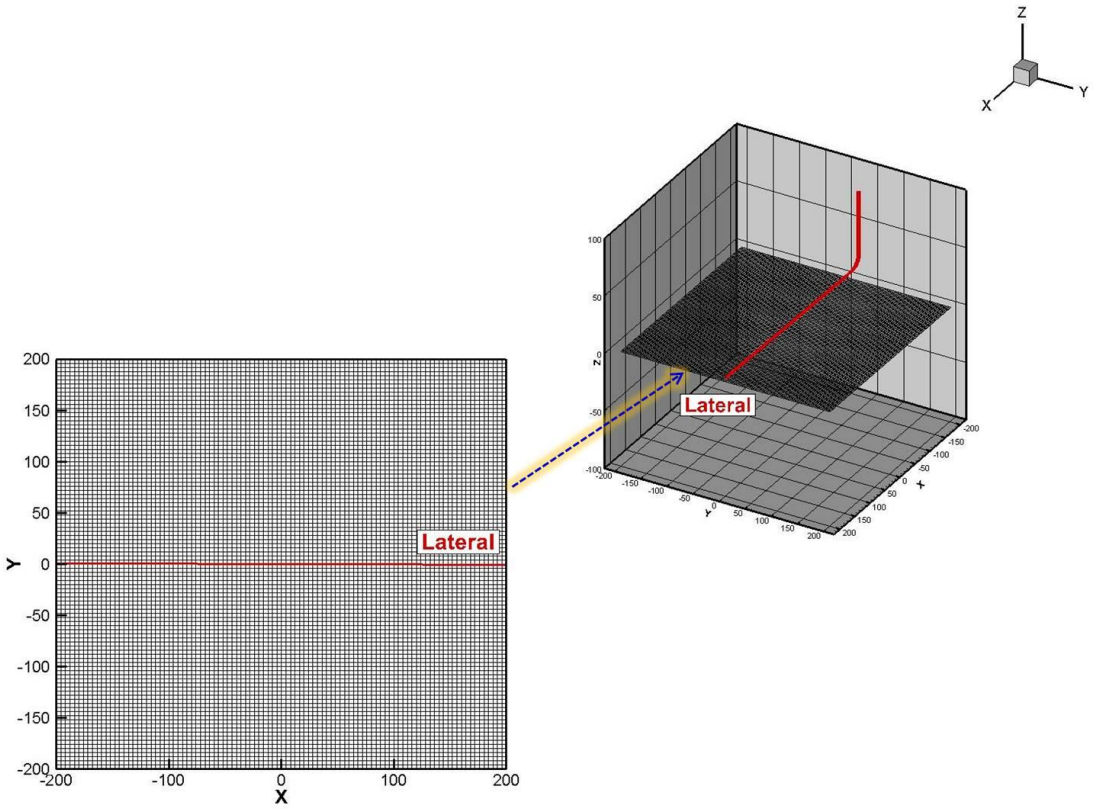

Figure 53 Finite element mesh for field case study

Poisson's ratio, ν	0.25	0.25
Young's modulus, E	20.684GPa	3.0×10^{6} psi
Shear modulus, G	8.274GPa	1.2×10^{6} psi
Initial porosity, ϕ	0.04	0.04
Biot's coefficient, α	0.6354	0.6354
Intrinsic permeability, k_{∞}	1.0×10^{-18} m^2	1.0 μD
Bulk modulus, K	13.790GPa	2.0×10^{6} psi
Solid bulk modulus, K_s	37.820GPa	5.5×10^{6} psi
Initial reservoir pressure, p_0	8.274MPa	1200psi
Bottom hole pressure, p_{wf}	5.516MPa	800psi
Average system temperature, T	90^0C	194^0F
Density of gas shale, ρ_r	2.4×10^{3} kg/m^3	150lb/ft^3
Min in-situ stress, σ_h	39.011MPa	5658psi
Max in-situ stress, σ_H	43.340MPa	6286psi
Langmuir pressure constant, P_L	3.447MPa	500psi
Langmuir volumetric strain constant, ε_L	0.0023	0.0023
Shear dilation angle, φ_{dil}	3^0	3^0
Friction angle, φ_f	31^0	31^0
Shear stiffness of fracture, K_{sh}	1.0GPa	1.45×10^{5} psi
Stress-free aperture, a_m	0.001m	3.937×10^{-2} in
90% closure stress, σ'_{ref}	40MPa	5802psi

Table 6 Input parameters for field case study

5.3.1 Effect of desorption

The influences of gas desorption on reservoir deformation and hence the gas production is first investigated. In order to simplify the problem, a simple geometry is considered in this case. Only one large transverse hydraulic fracture, whose length is 100m (328ft), intersects the horizontal well as shown in Figure 54. As stated in Chapter 3, the fracture aperture and permeability are all pressure dependent and governed by Eq. (3.45) and Eq.(3.15) respectively. Therefore, the fracture condnctivity is not a constant in these numerical tests.

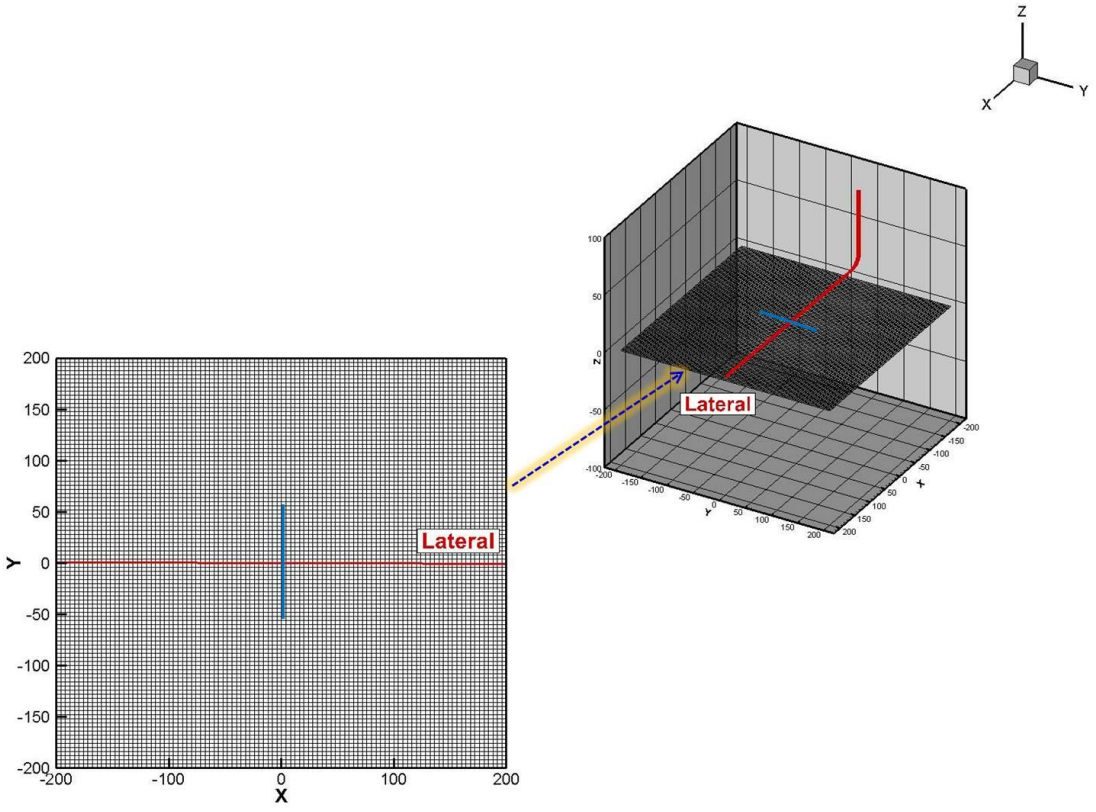

Figure 54 Schematic diagram of a horizontal gas well (red curve) with one transverse fracture (blue line)

As for the matrix permeability, the Beskok-Karniadakis microflow model is used in our simulator. Different adsorption isotherms for a typical Barnett Shale sample can be obtained from Montgomery et al. (2005). The gas content for adsorbed gas inceases with the Langmuir volume constant V_L for a fixed reservoir pressure as illustrated in Figure 55. These three representative values for Langmuir volume constant are used in the parametric tests to demonstrate the influence of the gas desorption on production.

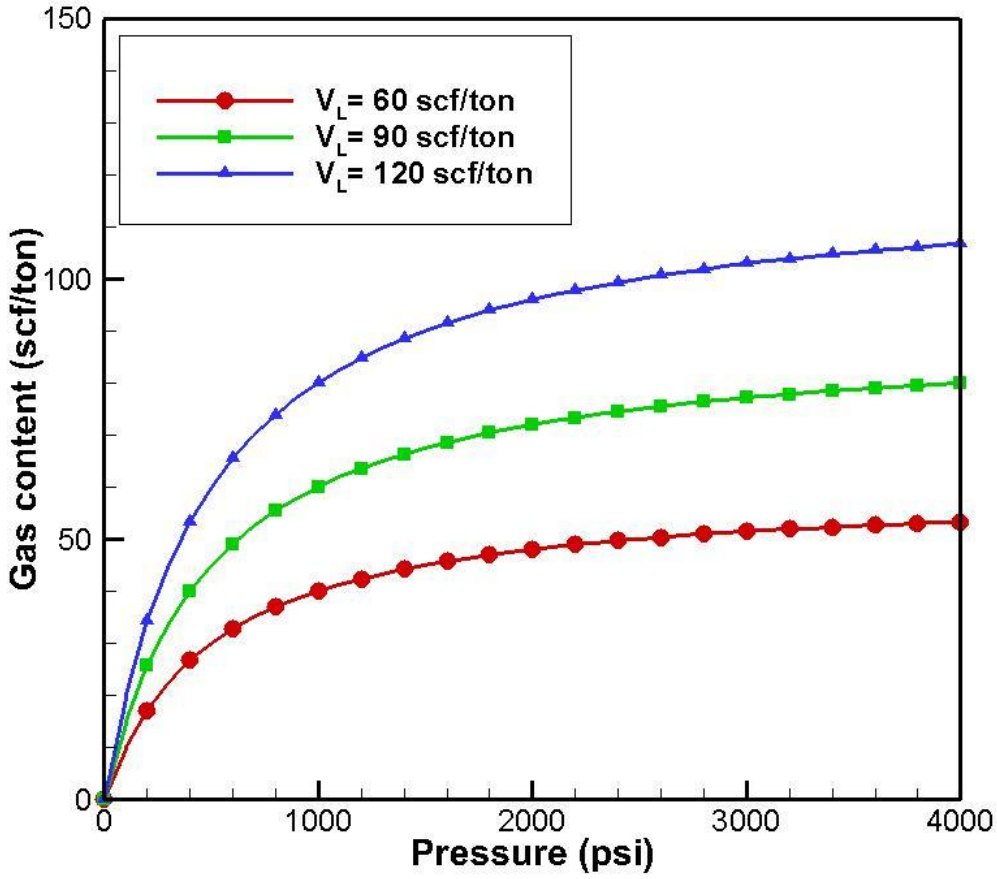

Figure 55 Three typical adsorption isotherms for Barnett shale: $V_L = 60$ scf/ton (red curve), $V_L = 90$ scf/ton (green curve), $V_L = 120$ scf/ton (blue curve), respectively

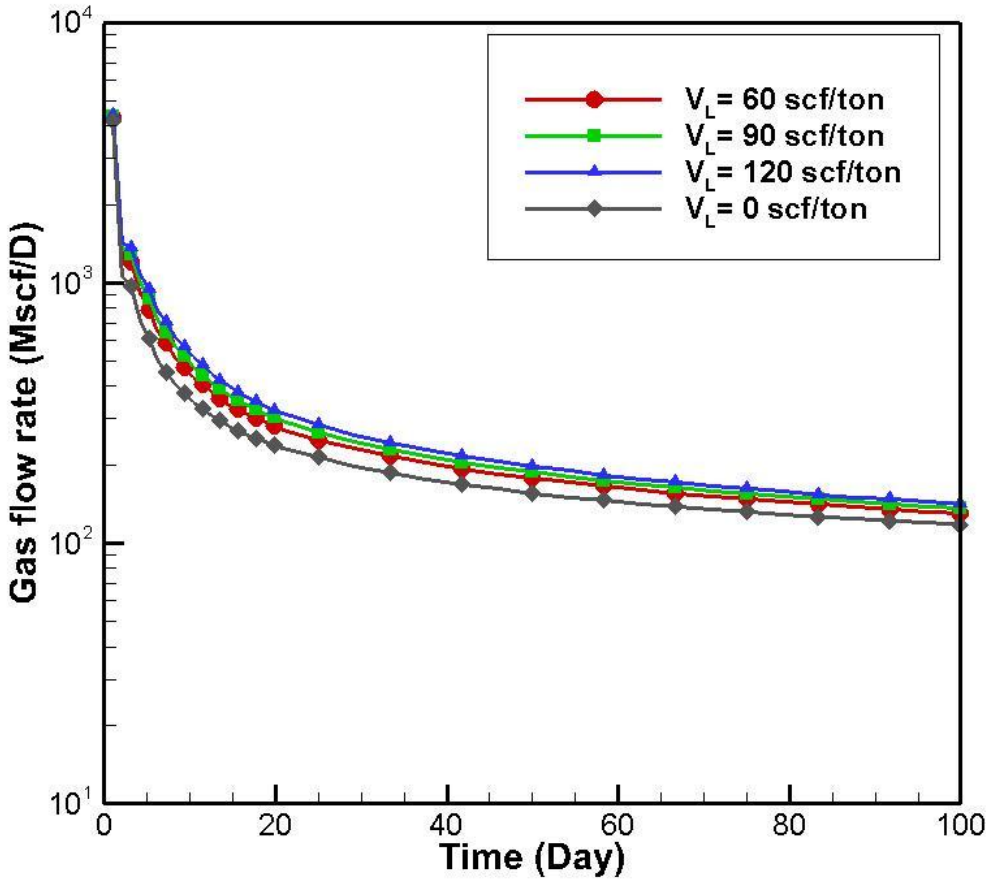

Figure 56 Effect of adsorption on gas flow rate

In Figure 56, the four different runs correspond to the three dinstinct gas desorption isotherms given in figure 55 and none desorption gas case ($V_L = 0$ scf/ton). With varying desorptive contribution, the gas flow rate changes apparently. It indicates that the gas flow rate accelerates with increasing the sorptive storage of gas (value of V_L). However, the gas flow rate declines steeply in the early time, around 1 month, in all the four runs. The gas desorptive contribution can only slightly retard but barely prevent the decline.

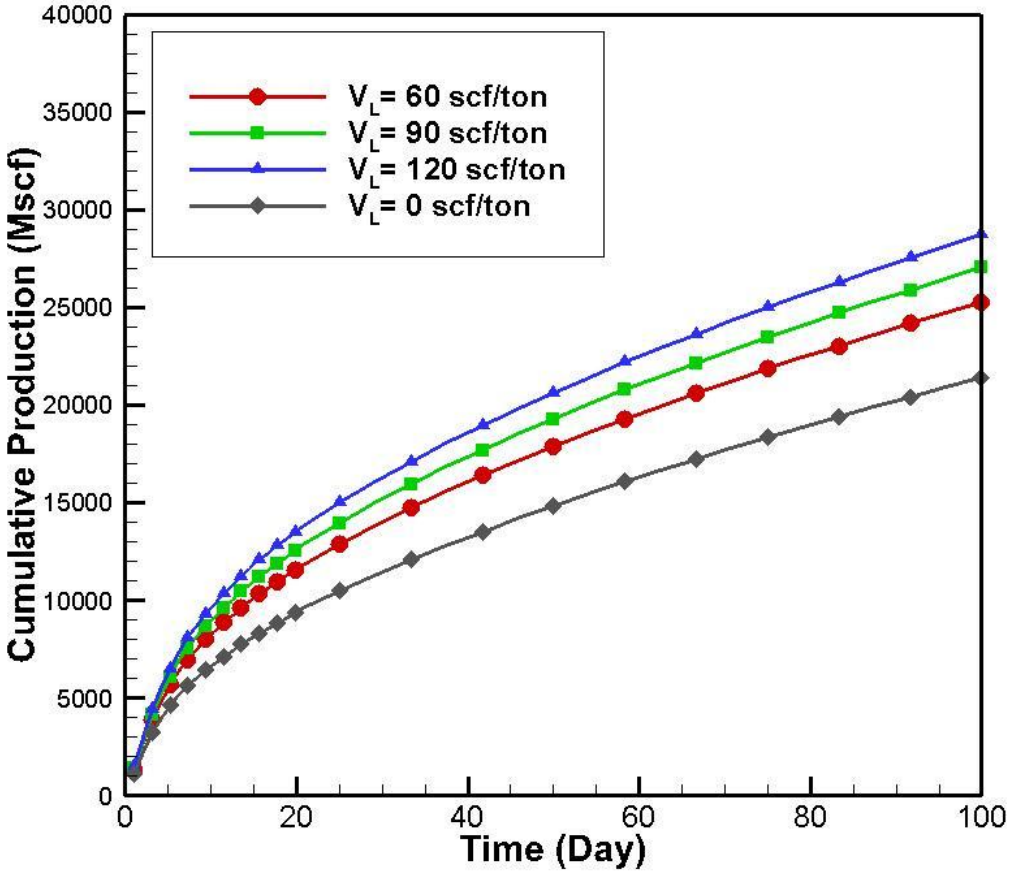

Figure 57 Effect of adsorption on cumulative gas production

In Figure 57, the cumulative gas production curves for the four runs in Figure 55 are presented for comparison. We observed that contribution of desorptive gas on production becomes more significant with greater sorptive storage. After 100 days depletion, nearly 30% difference on the production yields between the cases of $V_L = 120$ scf/ton and $V_L = 0$ scf/ton.

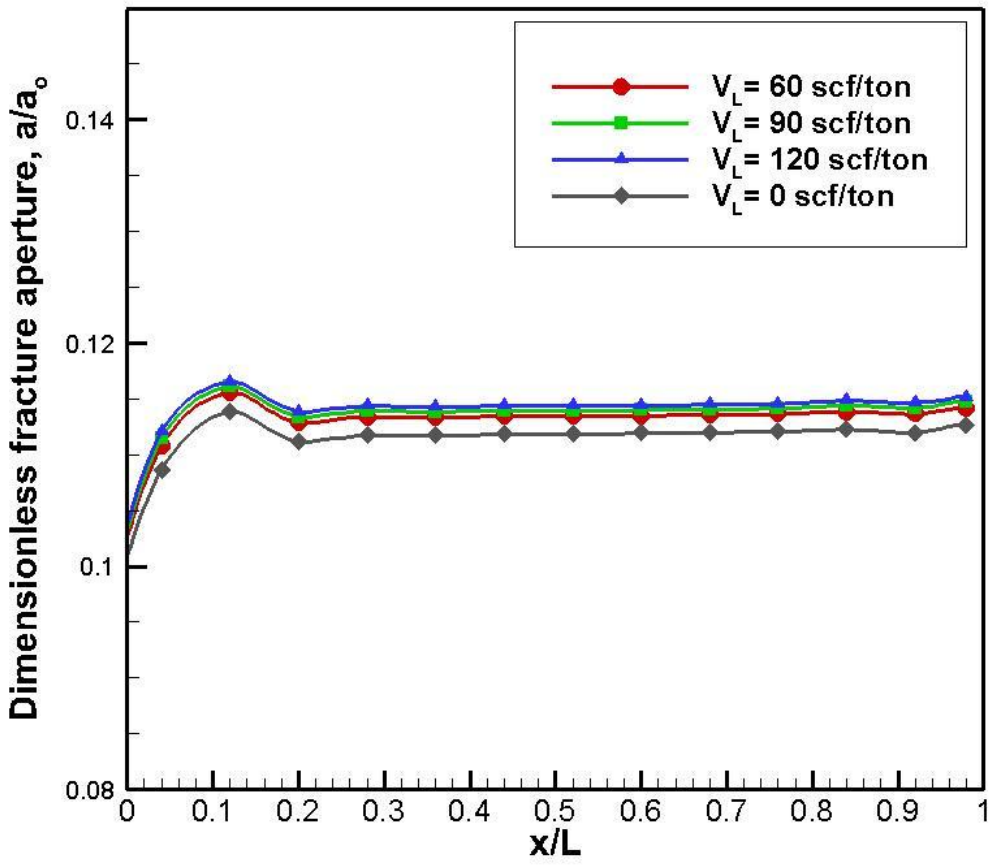

Figure 58 Effect of adsorption on fracture aperture after 25days production

The fracture mechanical responses to the four runs are illustrated In Figure 58. Due to the symmetry of the fracture geometry, only one wing of the fracture is plotted in Figure 58. The dimensionless length $x/L=0$ denotes the place of the horizontal well and $x/L=1.0$ is one end of the fracture. For all the four runs, the fracture aperture is not uniform along its length and is lower in the vincinity of the wellbore ($x/L=0$) due to the greater pore pressure reduction and hence the effective stresses increase. However,

the desorption gas can overcome the increase of effective stresses and force the fracture to relatively "open" by comparing to the case without desorption gas ($V_L = 0$ scf/ton). Figure 58 shows greater fracture aperture corresponds to higher sorptive storage (V_L).

5.3.2 Effect of fracture geometry

As single bi-wing shape fracture geometry is not sufficient to represent the complex fracture network, some fracture complexity need to be considered in the numerical simulator to predict gas production and assess fracture design in gas shale reservoirs. In this session, the influence of the fracture geometry on the gas production is addressed. Three selected fracture geometry models are shown in Figure 57: in the left one, one big hydraulic fracture (210 m in length) intersects two natural fractures (120m in length); in the middle one, both wings of the hydraulic fracture are offseted by the natural fractures; in the right one, the hydraulic fracture intersects more natural fractures to creat an irregular fracture network. In all these three runs, the same sorptive storage ($V_L = 90$ scf/ton) is used to diminish the gas desorption influence. And the total surface area of the hydraulic fractures and the natural fractures are maintained as constants. The results for the three runs are given in Figure 60-64.

The time evolutions of pore pressure distribution for the three models are given in Figure 60-62. Severe pressure depletion is observed in the near fracture region and the depletion area expands from the fracture-face with time in all three runs. Due to different fracture geometry (intersection between natural fractures and hydraulic fractures), the shape of

the depletion area varies from case to case, which might impact the production behavior of the reservoir.

Figure 63 presents three curves of gas flow rate, which correspond to the three different geometry models. Apparently, model 1 gives the highest flow rate among the three, and model 3 demonstrates the lowest one. As fracture segments are placed close to their adjacent ones, when they drain the same area, they will compete with each other to influence the production. And during gas depletion, the effective stress normal to the fracture face of a fracture segment is elevated by the pore pressure drop in the matrix rock and hence forces the fracture segment to close. The perturbation of the effective stress is maximum at the fracture face and declines away from the fracture. If the two fracture segments are set close to each other, the stress perturbation can radiate from one to the other and further reduce the fracture aperture and hence its conductivity. As in model 1, the fractures are set far away from each other to minimize the stress influence between the neighbor ones. As the fracture network becomes more complicated (model 3), more fracture segments are placed close to their adjacent ones and the stress interactions between them get increased, which can lower the fracture apertures when compared to model 1. However, the rapid drop of the flow rate still exists in the early time for the three runs. This steep decline is slightly decelerated in model 1.

In Figure 64, three curves of cumulative gas production for the three models are depicted. It can be seen that model 1 produces most gas during the entire production period when compared with the other two and model 3 presents the least production among the three, which is related to the stress influence between the adjacent fractures.

As the distance between the adjacent fractures gets smaller, when they drain the same area, the fluid production of adjacent fractures will repel each other and the stress influence between the two will become more significant and hence affect the fracture behavior and fluid flow through them.

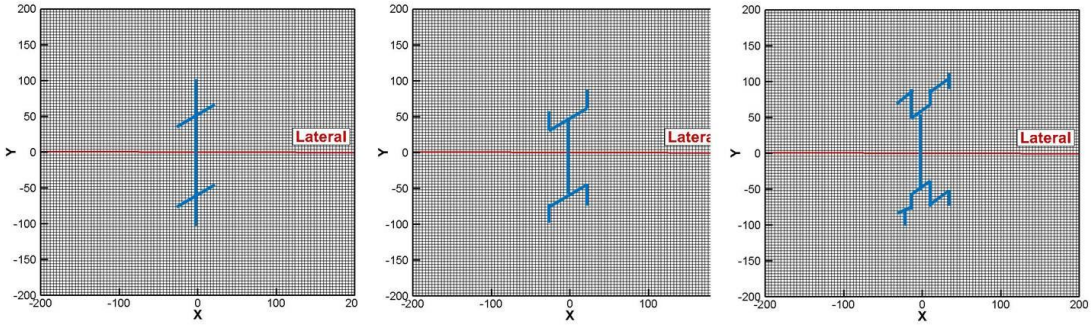

Figure 59 Three different frature geometry models for simulation; Total length of the hydraulic fracture is 210m and the total length of the nature fractures is 120m. The initial aperture of each segments is determined by the initial stress acting on it at the beginig of simulation.

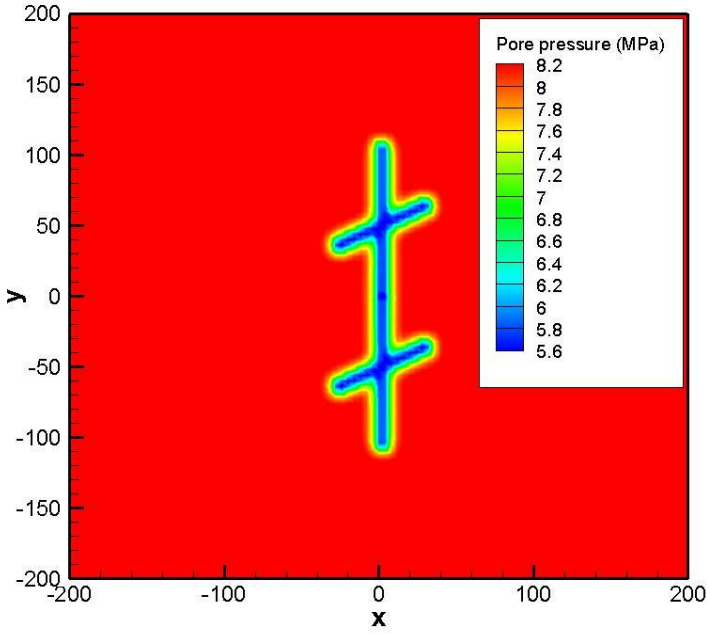
Pore pressure (MPa)
8.2
8
7.8
7.6
7.4
7.2
7
6.8
6.6
6.4
6.2
6
5.8
5.6
200
150
100
50
0
-50
-100
-150
-200
y
-200
-100
0
100
200
x

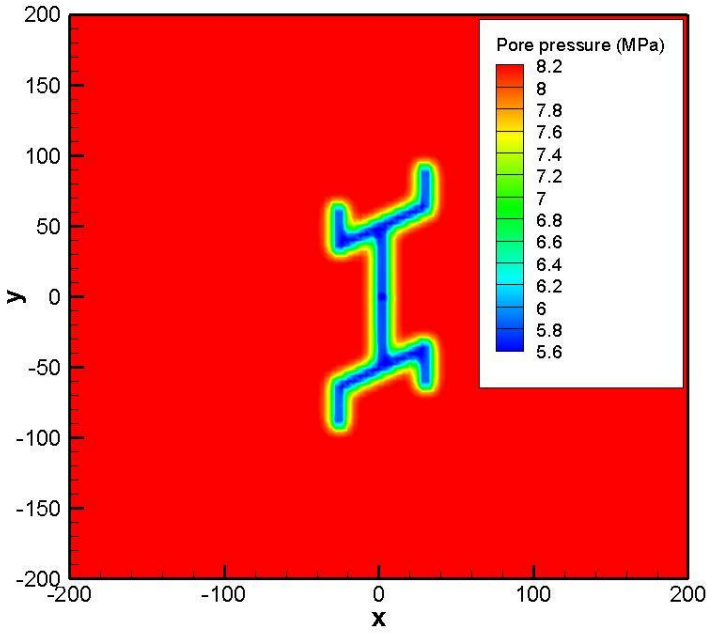
Pore pressure (MPa)
8.2
8
7.8
7.6
7.4
7.2
7
6.8
6.6
6.4
6.2
6
5.8
5.6
200
150
100
50
0
-50
-100
-150
-200
y
-200
-100
0
100
200
x

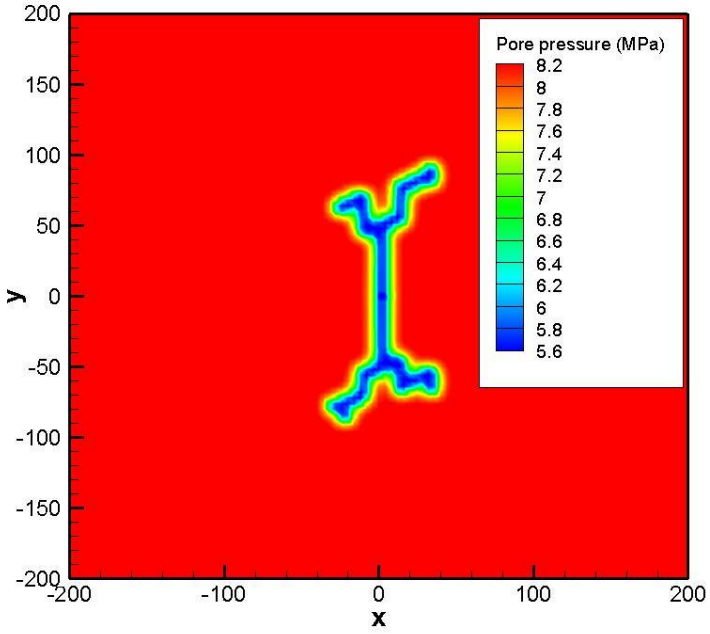

Figure 60 Pore pressure distribution at 25 days

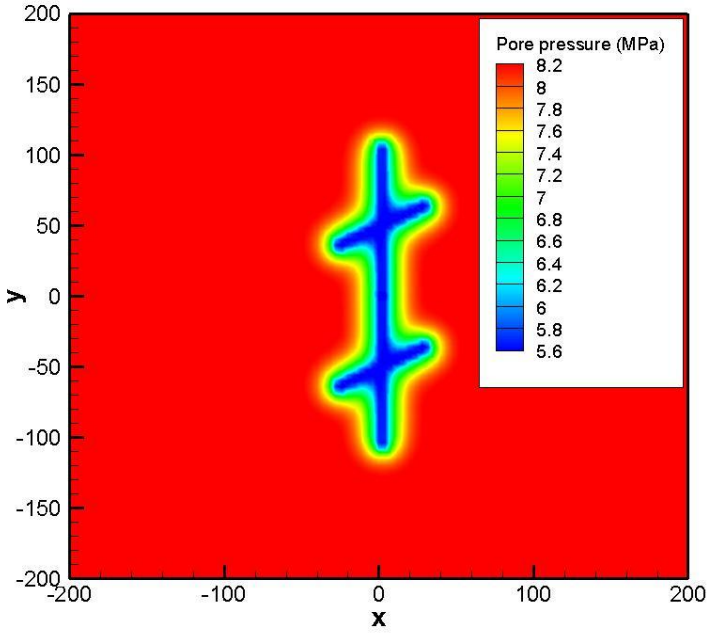
Pore pressure (MPa)
8.2
8
7.8
7.6
7.4
7.2
7
6.8
6.6
6.4
6.2
6
5.8
5.6
200
150
100
50
0
-50
-100
-150
-200
y
-200
-100
0
100
200
x

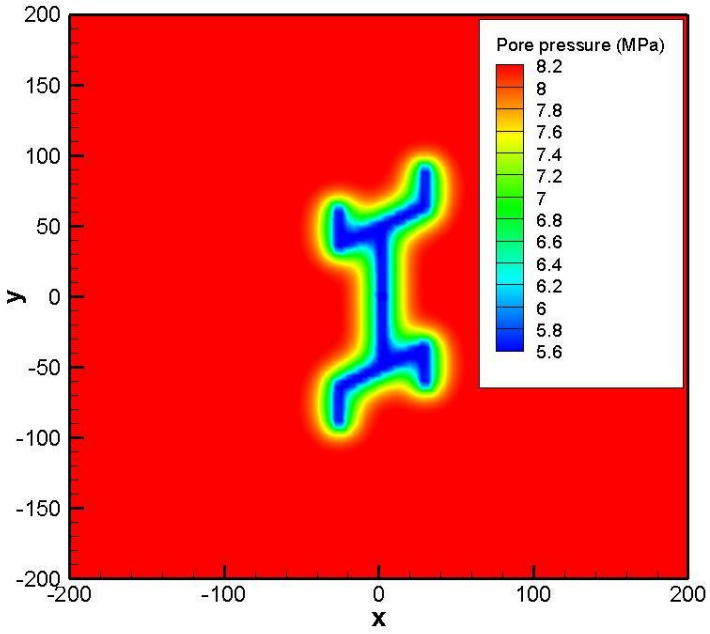
Pore pressure (MPa)
8.2
8
7.8
7.6
7.4
7.2
7
6.8
6.6
6.4
6.2
6
5.8
5.6
200
150
100
50
0
-50
-100
-150
-200
y
-200
-100
0
100
200
x

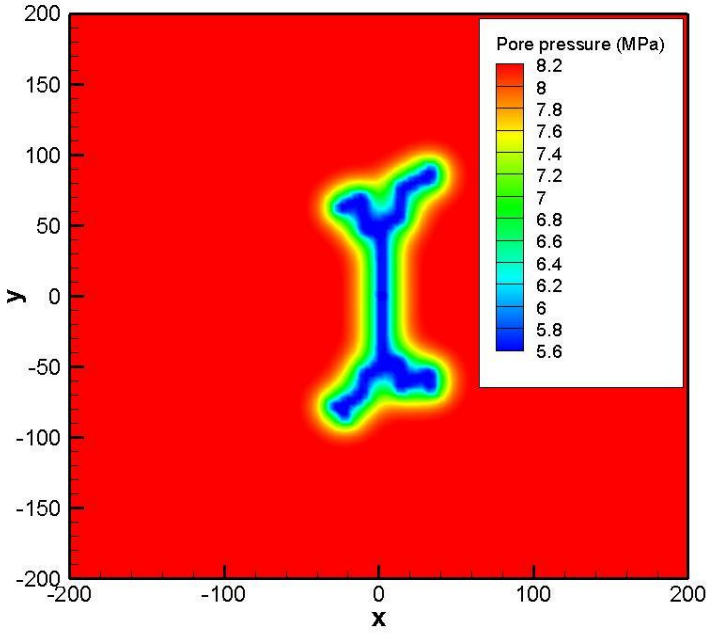

Figure 61 Pore pressure distribution at 100 days

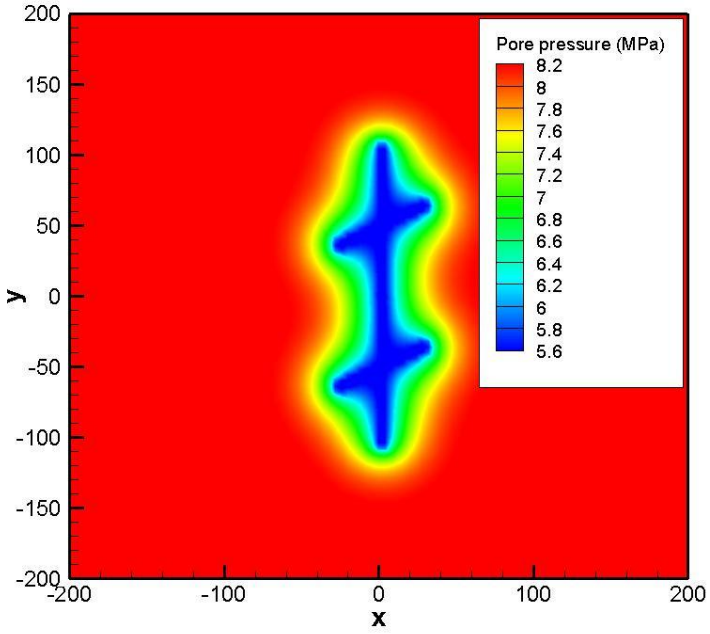
Pore pressure (MPa)
8.2
8
7.8
7.6
7.4
7.2
7
6.8
6.6
6.4
6.2
6
5.8
5.6
200
150
100
50
0
-50
-100
-150
-200
y
-200
-100
0
100
200
x

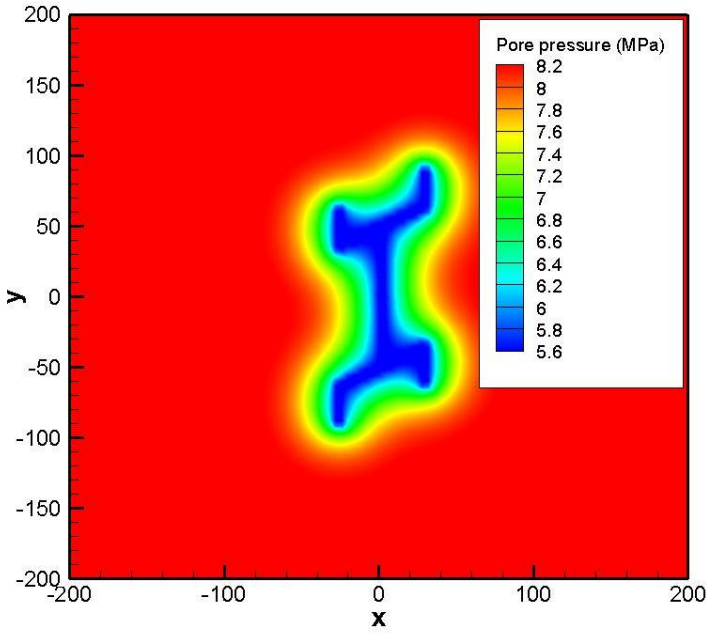
Pore pressure (MPa)
8.2
8
7.8
7.6
7.4
7.2
7
6.8
6.6
6.4
6.2
6
5.8
5.6
200
150
100
50
0
-50
-100
-150
-200
y
-200
-100
0
100
200
x

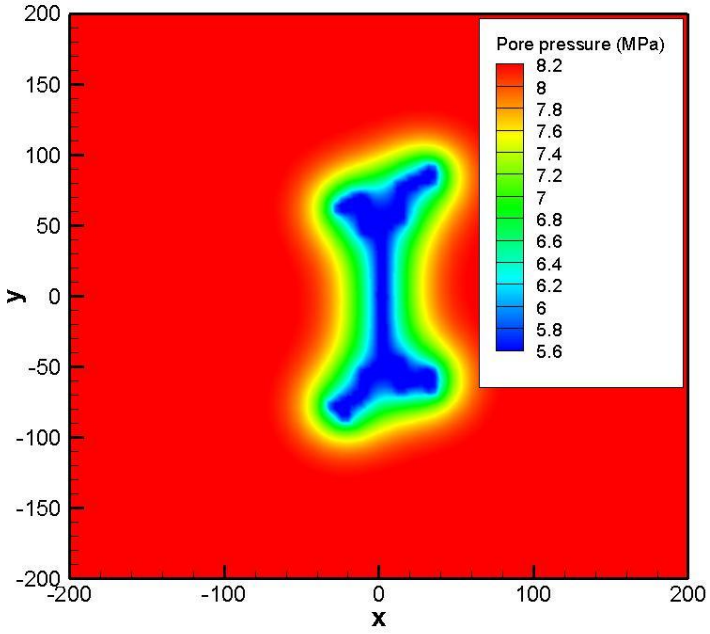

Figure 62 Pore pressure distribution at 400 days

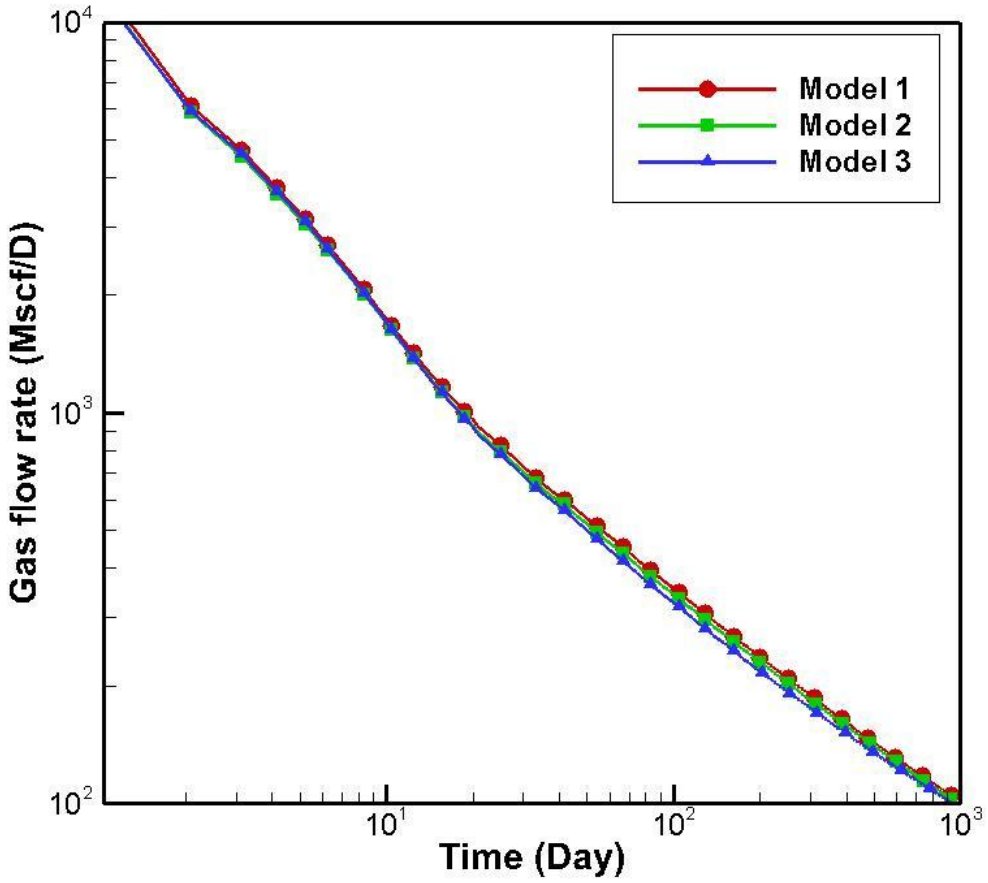

Figure 63 Effect of fracture geometry on gas flow rate

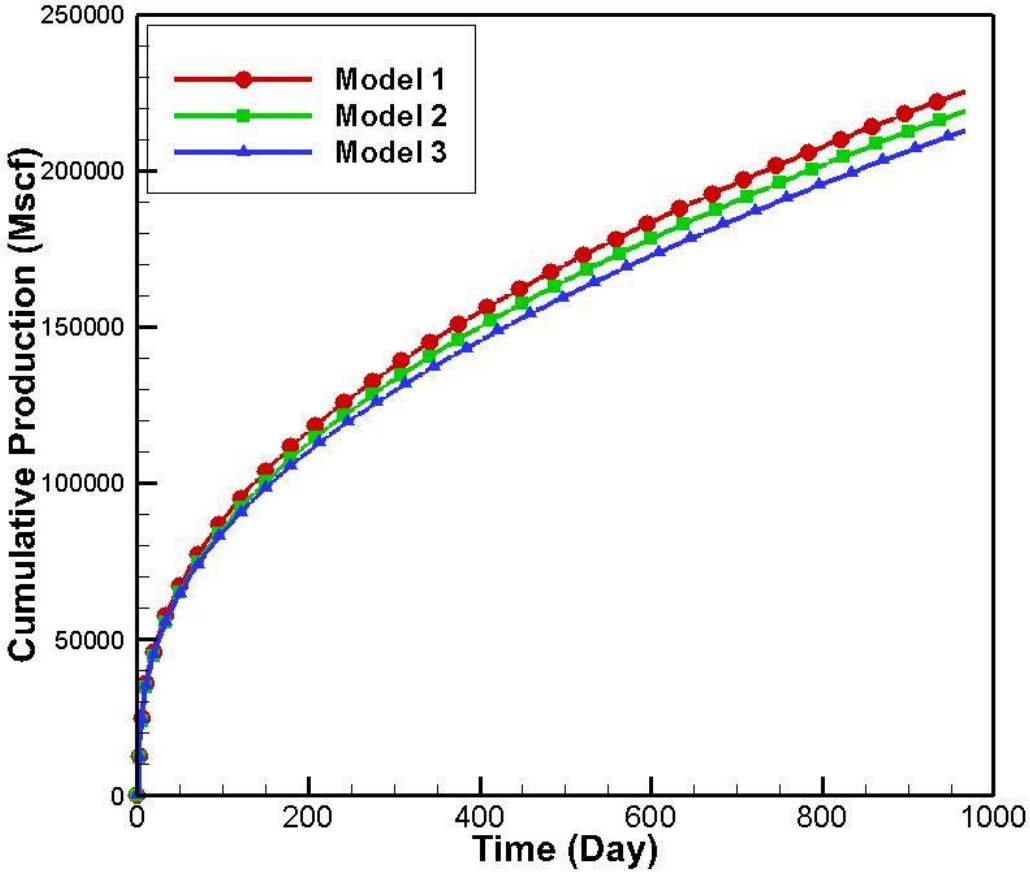

Figure 64 Effect of fracture geometry on cumulative gas production

5.3.3 Effect of viscoelastic deformation

In Chapter 4, a coupled poroviscoelastic model was proposed based on the Maxwell model. The model is applied to a field case in this Section to investigate the viscoelastic effect in the gas depletion process (using point source to represent the well). Two different runs are carried to quantify the influence of viscoelastic deformation of reservoir rock: (i) using a fully coupled poroelastic model given in Chapter 3; (ii) using a fully coupled poroviscoelastic model developed in Chapter 4. In order to minimize other effects, the moajor geomechanical parameters used in these two runs are kept the same and lised in Table 5. And the sorptive storage (V_L) is set to 0 scf/ton and only one large hydraulic fracture (200m in length) presents in the reservoir for both runs. No flow condition and constant stress are applied to all the outer boundaries.

The initial shear viscosity of the formation is $\eta_{s0} = 1.0 \times 10^9 \text{pa} \cdot \text{s}$ (extracted from experimental data (Li and Ghassemi, 2012)). A typical value of the power law exponent of the damage model is given as $n = 3$ (Simakin and Ghassemi, 2005). The dimensionless value of the kinetic healing parameter A is 1 and the ratio of B/A is kept as a constant, e.g. 8, during the process (Simakin and Ghassemi, 2005).

Figure 65 demonstrates the time evolution of the fracture aperture in two runs. Only one wing of the fracture is plotted due to the symmetry of the fracture geometry. The dimensionless length $x/L = 0.5$ corresponds to the location of the horizontal well and $x/L = 0$ denotes one end of the fracture. For the poroelastic model, the fracture aperture decreases with time due to pore pressure reduction and hence effective stress increase in

matrix. However, for the poroviscoelastic model, the fracture closes more rapidly compared to the poroelastic case. This anomaly can be attributed to the creep phenomenon of the reservoir rock, during which the increasing of the volumetric strain of the matrix can further increase the effective stress acting on the fracture surface and push the fracture to close. Based on the cubic law, this reduction of the fracture aperture can decrease the permeability of the fracture and consequently lessen the final production, which is illustrated in Figure 67 and 68.

Figure 66 shows the pore pressure distribution during production for the two runs. It is obvious that the differences between the results of the two runs are small. In the fluid transport equation (Eq.(4.46)), the first term ($\alpha(\nabla \cdot \dot{u})$), which denotes the solid deformation, is negligible when comparing with the fluid diffusion process caused by the high pressure perturbation around the fracture, especially for a geological time scale. It indicates that for the rheology used, the change of solid deformation rate between the elastic and viscoelastic regime is so minute that the viscous deformation of reservoir rock can only slightly impact the fluid diffusion process during a long term production.

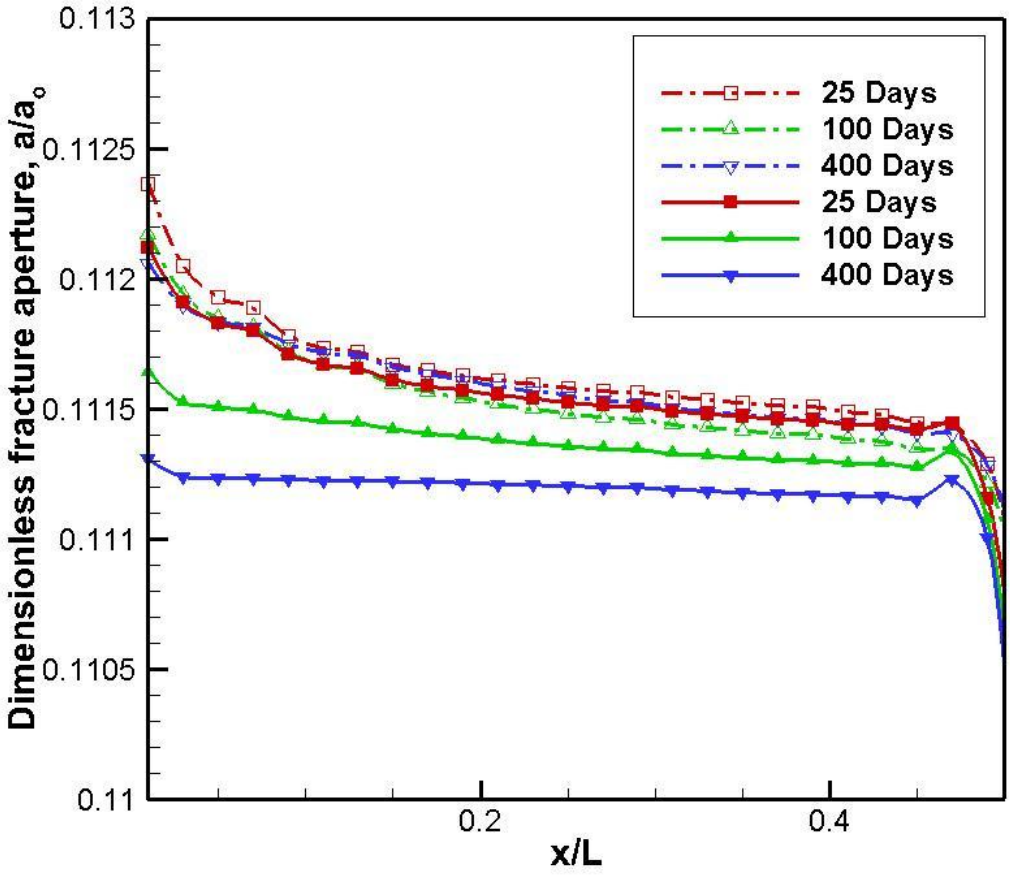

Figure 65 Comparison of poroviscoelastic model results (solid curve) with the poroelastic model results (dashed curves) for the time evolution of fracture aperture (one wing). Effective normal stresss acting on the fracture causes closure.

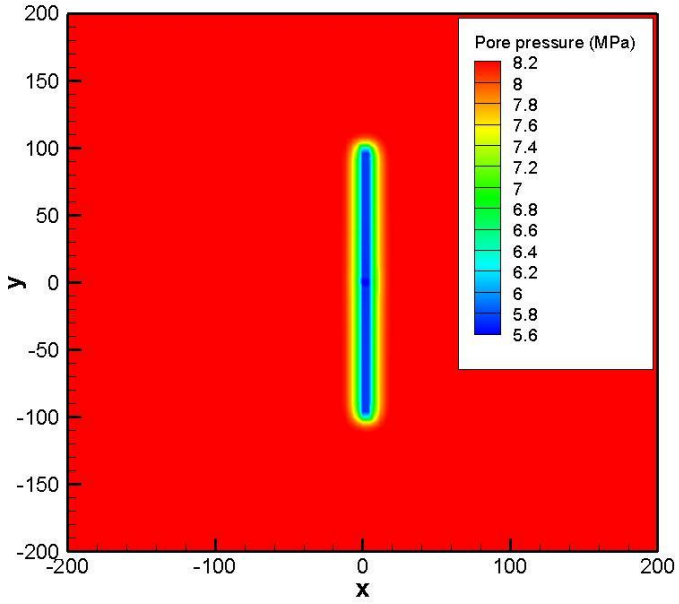

a. poroelastic model, 25days.

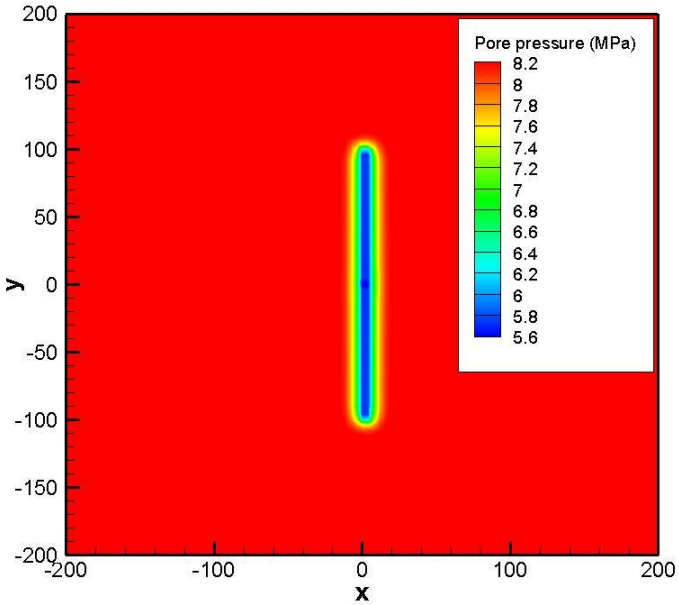

b. poroviscoelastic model, 25days.

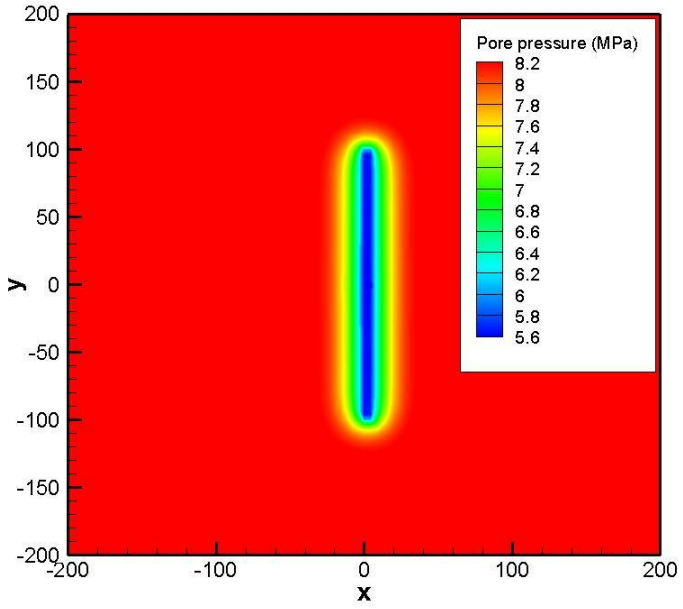

c. poroelastic model, 100days.

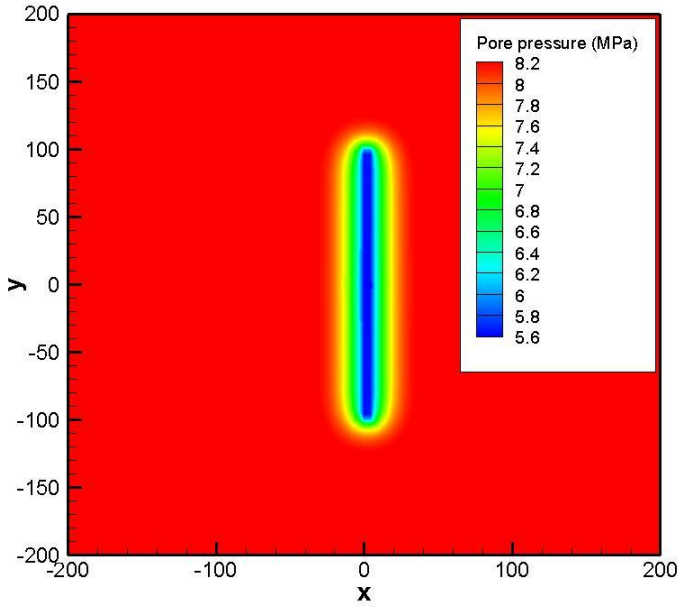

d. poroviscoelastic model, 100days.

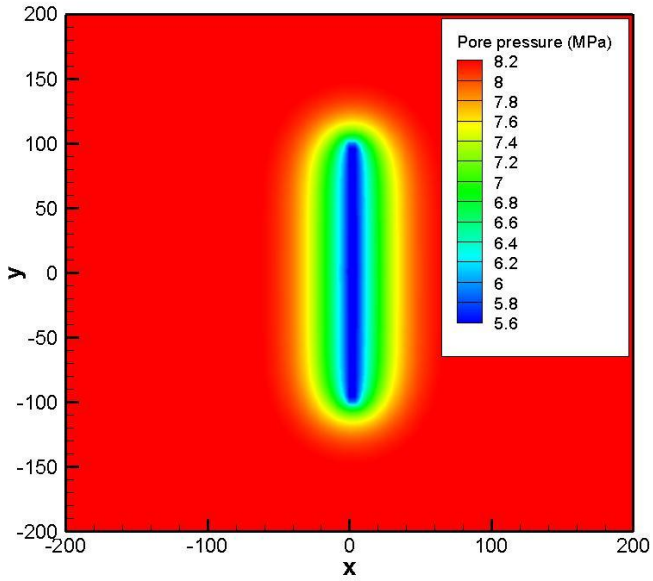

e. poroelastic model, 400days.

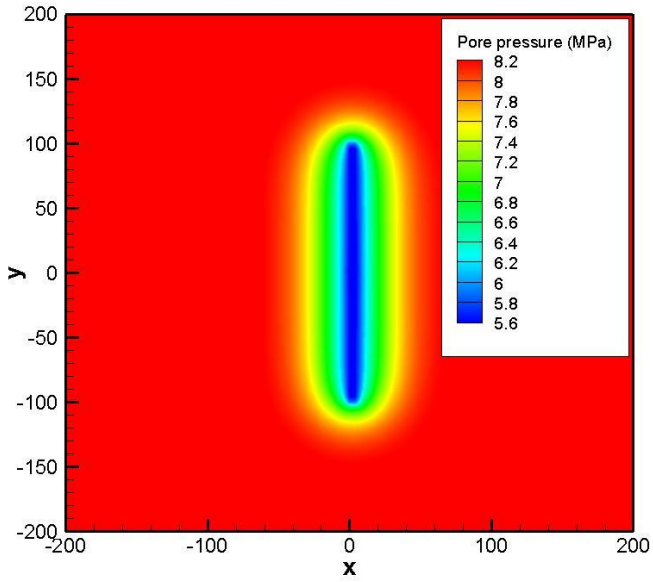

f. poroviscoelastic model, 400days.

Figure 66 Pore pressure distribution during gas production.

In Figure 68, we observe the similar trends of the gas flow rate for both poroelastic and poroviscoelastic cases. In the early stage of the production (<100Days), the two curves almost overlap each other; however, the divergence between the two cases rises with time for a long term production. According to this divergence, the difference in the cumulative production between the two cases grows with time, as decipted in Figure 69. Even the viscous deformation of reservoir rock can hardly affect the fluid diffusion process it can project significant impact on the fracture deformation and force the fracture to "heal" due to creep behavoir. In the poroviscoelastic case, the increase of the effective stress acting on the fracture walls is caused by two processes: (1) pore pressure reduction in matrix due to gas depletion; (2) continuous increase of the compressive strain with time in the matrix during creep. Therefore, the gas flow rate and cumulative production can be stalled by the viscous deformation of the reservoir rock.

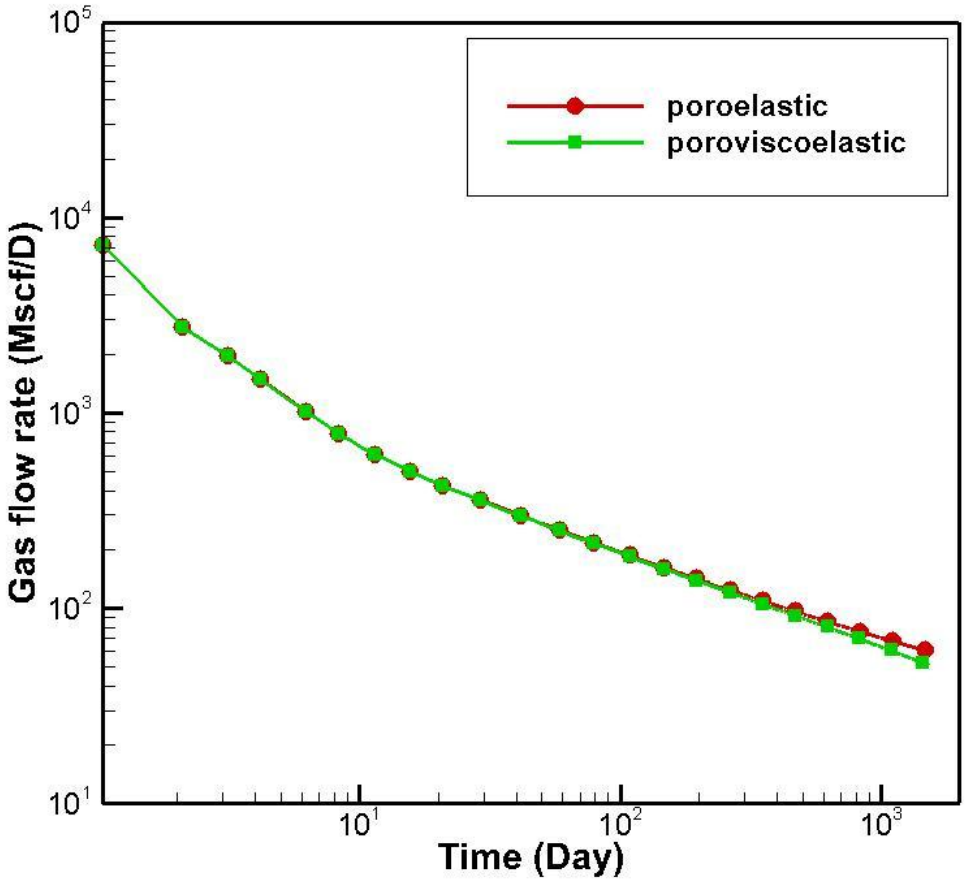

Figure 67 Effect of viscous deformation on gas flow rate

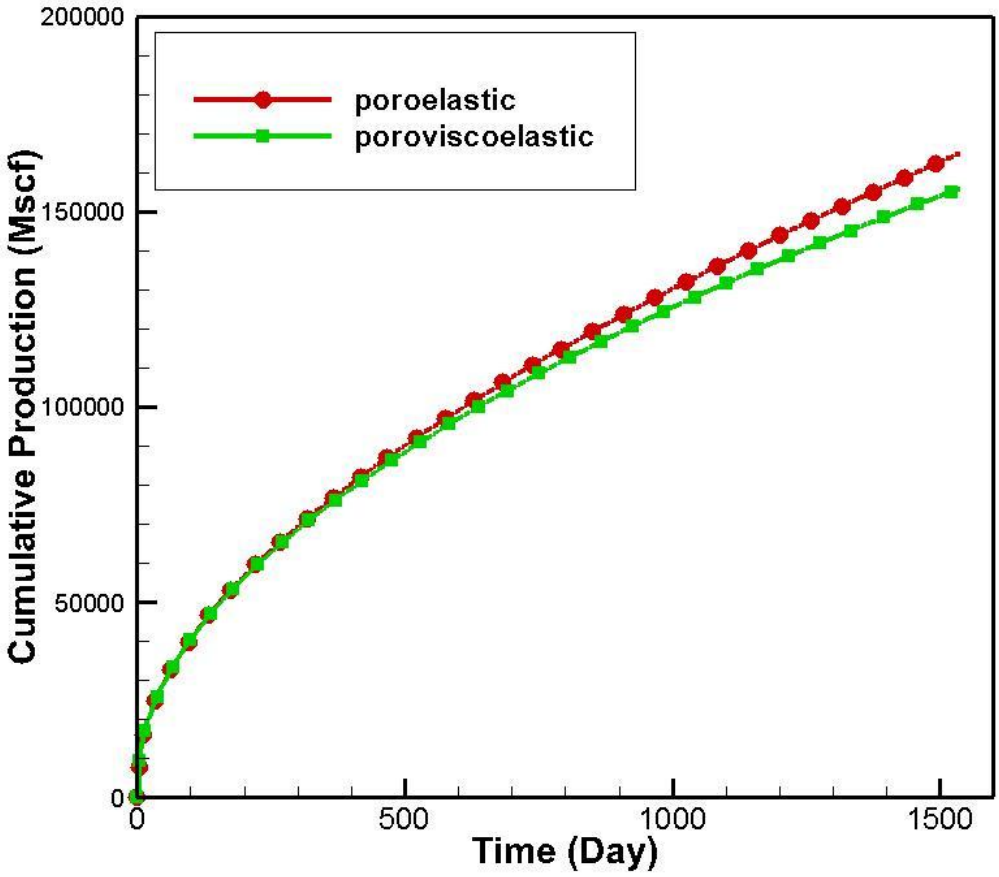

Figure 68 Effect of viscous deformation on cumulative gas production (6% difference at large times)

CHAPTER VI

DISCUSSION AND CONCLUSION

The mechanical response of fractutured gas shale reservoirs to gas depletion and compressible fluid flow can interact with each other and hence significantly impact the gas production. There exist coupled fluid-machnical interactions in the fractured gas shale reservoir: (i) matrix solid deformation caused by pore fluid reduction; (ii) gas desorption induced matrix deformation; (iii) fluid volume and pressure change in response to matrix solid deformation; (iv) fracture deformation, either normal and shear-dilation, induced by stress evolution within the reservoir; (v) pore fluid variation due to permeability change, either in matrix and fracture; (vi) fluid response to viscous deformation of reservoir rock. To take all these processes into consideration, a coupled numerical model was constructed step by step in this work.

In Chapter 2, a coupled poroelastic constitutive relation is developed to investigate the geomechanical reservoir response to gas production process. The gas transport equation for single phase flow was developed by considering the mass conservation of gas content, including both free and absorbed phase gas within shale matrix, and a real gas law. The amount of adsorbed gas was modelled through Langmuir isotherms. The rock constitutive equation and gas transport equation were coupled through the general porosity model and matrix permeability was modeled by Beskok-Karniadakis microflow model during production. All the field equations were solved by Galerkin's Finite Element Method (GFEM) and verified with the appropriate analytical solution.

Then, this single permeability was further developed by incorporating the dual continuum concept to simulate fracture network in heterogeneous reservoirs such as gas shale and coal-bed methane in Chapter 3. In the dual permeability model (DPM), elements without fracture were treated as conventional single permeability grids whereas the dual permeability treatment was applied for the elements with fractures. Both matrix and fracture subdomains were assumed to be permeable to allow fluid to pass through both. Within the framework of this DPM-FEM model, each element, either with or without fractures, featured its own permeability tensor as well as other geomechanical properties. The fractures, especially large scale hydraulic fractures, were discretely depicted by small segments and their geometry and mechanical behavior were handled on element-by element basis. The Barton-Bandis model was used to describe the local mechanical deformation of fractures, either induced by normal stress or shear displacement. The implementation of DPM to the non-linear fully coupled poroelastic FEM model was verified with single permeability model.

In Chapter 4, a fully coupled poroviscoelastic model was constructed to study the the interactions between solid viscous deformation and fluid flow during gas production. The Maxwell model was employed herein to develop the constitutive relations and the viscoelastic effect was considered in both deviatoric and symmetric effective stresses. A reservoir simulator was constructed by incorporating this poroviscoelastic model into the DPM-FEM model developed in Chapter 3 to investigate viscoelastic effect in fracture deformation and hence the final gas production for a long period. This newly constructed

mechanical model was verified with analytical solution and compared to the poroelastic results in consolidation problems.

Finally, several different case studies, from wellbore to field scale, were conducted by applying the comprehensive geomechanical reservoir simulator in Chapter 5. Based on these numerical analyses, the main conclusions are summarized as:

(i) Gas in the near-fracture region (including both natural and induced fractures) is produced through the fracture at a tremendous rate at early time. And then, gas, which moves from the matrix to the fracture at a very low rate, becomes dominated in production. This is the cause of the rate decline behavior of the gas shale reservoirs. Due to the ultra-low permeability of shale matrix, steep pressure gradient is formed in the near fracture region and migrates away from the fracture-face with time, which is the driving force for gas depletion.

(ii) Simulation results show that the fluid flow and reservoir mechanical behavior are strongly influenced by desorption gas during production. The growth of the gas flow rate can be observed along with the increase of desorptive contribution. However, the gas desorptive contribution can slow down but cannot prevent the decline of gas flow rate.

(iii) The intersection or interaction between hydraulic fratures and natural fractures can change the effective fracture surface area during the production. And some small change of the fracture geoemtry might significantly influence the reservoir mechanical behavior and impact the final production.

(iv) Vviscous deformation is a slow but chronic effect. It can only slightly affect the fluid diffusion process. However, the mechanical response of the fracture is very sensitive to the creep behavior of the reservoir rock. Therefore, it can still provide significant impact on the gas production in a long term sense.

Gas desorption, fracture deformation and reservoir viscous deformation are all important processes and should be taken into consideration in accurately assessing hydraulic fracture design and predicting the production of gas shale reservoirs.

6.1 Recommendations for Future Work

In this project, both the poroelastic and poroviscoelastic constitutive relationships and compressible fluid mechanics and fracture mechanics are successfully incorporated into the finite element models to investigate the reservoir geomechnics of gas shale. However, during the constructing and utilizing the numerical models, there still exist some additional improvements for future work.

An issue is that the poroviscoelatic behavior is the temperature component. The solid viscosity is highly dependent on the reservoir temperature and can dramatical reduce with elevated temperature and the presence of fluid. In the current version of the program, we just conduct all the analyses under the isothermal conditions and uniform solid viscosity is adopted in each run by excluding the temperature influences, which might not be correct in the in-situ conditions, especially for the HPHT (high pressure high temperature) reservoirs.

In this work, a very simple viscoelastic model (Maxwell model) is used to construct the linear poroviscoelastic model. However, the Maxwell is only a two-element model and is not an ideal candidate to simulate strain creep during loading process. Normally, increasing the number of mechanical elements in a model can highly improve its quality in predicting the mechanical response of viscoelastic materials. In the future, Burgers model or some other comprehensive models can be incorporated into the numerical model to accurately address the strain creep of the viscoelastic materials. However, more mechanical properties are demanded in more complicated model, whose measurement might be difficult or infeasible through experiments.

Throughout the work, all the mechanical models to simulate fracture deformation, including both normal deformation and shear dilation, are derived for elastic medium in the literature. However, these available elastic models are adopted and directly applied to the poroelastic and poroviscoelastic models in this project. In the poroviscoelstic models, these fracture deformation models need to be further developed and verified with experimental data by incorporating the viscous component in Young's modulus and shear modulus, which are not constant under viscous deformation.

Besides all above, this model was conceptually developed for single phase flow and applied to two dimensional plane strain cases. In the future, three dimensional models can be developed to simulate the multi-phase flow in gas shale and other unconventional reservoirs.

In the poroelastic models, the pressure perturbation (difference between the bottomhole pressure and reservoir pressure) cannot be too high, as exceeds 40MPa. Even when we try to use the ideal gas law, this limitation still exsits. It might be related to the gas compressibity and the stability of the finite element algorithm and need to be further investigate.

In the poroviscoelatic cases, the viscosity of the rock formation can not be too low, as lower than $1.0\times10^{9}\,\mathrm{pa}\cdot\mathrm{s}$ for both the wellbore and field cases. If the viscosity of the sample is beyond the lower limit, the resultant internal force will be too significant to get the iterations converged. Using very small time step might solve the problem in the wellbore cases; however, it is not applicable to the field cases, which need to conduct the prediction in several years.

REFERENCES

Abousleiman, Y., Cheng, A.H.-D., Jiang, C. et al. 1993. A Micromechanically Consistent Poroviscoelksticity Theory for Rock Mechanics Applications. Paper presented at the The 34th U.S. Symposium on Rock Mechanics (USRMS), Madison, WI. American Rock Mechanics Association ARMA-93-0573.

Aifantis, E.C. 1977. Introducing a Multi-Porous Medium. *Dev. Mech.* **8** (37): 209-211.

Al-Hussainy, R., Jr., H.J.R., and Crawford, P.B. 1966. The Flow of Real Gases through Porous Media. *Journal of Petroleum Technology* **18** (5): 624-636.

Al-Huthali, A.H. and Datta-Gupta, A. 2004. Streamline Simulation of Water Injection in Naturally Fractured Reservoirs. Paper presented at the SPE/DOE Symposium on Improved Oil Recovery, Tulsa, Oklahoma. Society of Petroleum Engineers 00089443.

Al-Jawad, M.S. 1997. Reverse Calculation of Pressure from Pseudopressure. *Polymer-Plastics Technology and Engineering* **36** (4): 501-511.

Al-kobaisi, M., Kazemi, H., Ramirez, B. et al. 2009. A Critical Review for Proper Use of Water/Oil/Gas Transfer Functions in Dual-Porosity Naturally Fractured Reservoirs: Part Ii. *SPE Reservoir Evaluation & Engineering* **12** (2): 211-217.

Alamdari, B.B., Kiani, M., and Kazemi, H. 2012. Experimental and Numerical Simulation of Surfactant-Assisted Oil Recovery in Tight Fractured Carbonate Reservoir Cores. Paper presented at the SPE Improved Oil Recovery Symposium, Tulsa, Oklahoma, USA. Society of Petroleum Engineers SPE-153902-MS.

Ambrose, R.J., Clarkson, C.R., Youngblood, J.E. et al. 2011. Life-Cycle Decline Curve Estimation for Tight/Shale Reservoirs. Paper presented at the SPE Hydraulic Fracturing Technology Conference, The Woodlands, Texas, USA. Society of Petroleum Engineers SPE-140519-MS.

Anderson, C.A. and Bridwell, R.J. 1980. A Finite Element Method for Studying the Transient Non-Linear Thermal Creep of Geological Structures. *International Journal for Numerical and Analytical Methods in Geomechanics* **4** (3): 255-276.

Bai, M., Elsworth, D., and Roegiers, J.-C. 1993. Multiporosity/Multipermeability Approach to the Simulation of Naturally Fractured Reservoirs. *Water Resour. Res.* **29** (6): 1621-1633.

Baihly, J.D., Altman, R.M., Malpani, R. et al. 2010. Shale Gas Production Decline Trend Comparison over Time and Basins. Paper presented at the SPE Annual Technical Conference and Exhibition, Florence, Italy. Society of Petroleum Engineers SPE-135555-MS.

Bang, S.H. and Jeon, S. 2009. Comparisons of 2d and 3d Hydraulic Behaviors of a Fractured Rock Mass by Discrete Fracture Network Analysis. Paper presented at the ISRM International Symposium on Rock Mechanics - SINOROCK 2009, The University of Hong Kong, China. International Society for Rock Mechanics and the University of Hong Kong. ISRM-SINOROCK-2009-075.

Barenblatt, G.I., Zheltov, I.P., and Kochina, I.N. 1960. Basic Concepts in the Theory of Seepage of Homogeneous Liquids in Fissured Rocks Strata. *Journal of Applied Mathematics and Mechanics* **24** (5): 1286-1303.

Barton, N., Bandis, S., and Bakhtar, K. 1985. Strength, Deformation and Conductivity Coupling of Rock Joints. *International Journal of Rock Mechanics and Mining Sciences & Geomechanics Abstracts* **22** (3): 121-140.

Bello, R.O. and Wattenbarger, R.A. 2008. Rate Transient Analysis in Naturally Fractured Shale Gas Reservoirs. Paper presented at the CIPC/SPE Gas Technology Symposium 2008 Joint Conference, Calgary, Alberta, Canada. Society of Petroleum Engineers SPE-114591-MS.

Beskok, A. and Karniadakis, G.E. 1999. Report: A Model for Flows in Channels, Pipes, and Ducts at Micro and Nano Scales. *Microscale Thermophysical Engineering* **3** (1): 43-77.

Biot, M.A. 1935. A General Property of Two-Dimensional Thermal Stress Distribution. *Philosophical Magazine Series 7* **19** (127): 540-549.

Biot, M.A. 1941. General Theory of Three-Dimensional Consolidation. *Journal of Applied Physics* **12** (2): 155-164.

Biot, M.A. 1956. Theory of Deformation of a Porous Viscoelastic Anisotropic Solid. *Journal of Applied Physics* **27** (5): 459-467.

Blanton, T.L. and Teufel, L.W. 1983. A Field Test of the Strain Recovery Method of Stress Determination in Devonian Shale. Paper presented at the SPE Eastern Regional Meeting, Pittsburgh, Pennsylvania. Society of Petroleum Engineers of AIME 00012304.

Blaskovich, F.T., Cain, G.M., Sonier, F. et al. 1983. A Multicomponent Isothermal System for Efficient Reservoir Simulation. Paper presented at the Middle East Oil Technical Conference and Exhibition, Bahrain. Society of Petroleum Engineers SPE-11480-MS.

Bloch, M., Cui, L., Roegiers, J.C. et al. 1999. Poroviscoelastic Effects in Anelastic Strain Recovery Tests. Paper presented at the The 37th U.S. Symposium on Rock Mechanics, Vail, CO. American Rock Mechanics Association ARMA-99-1165.

Brunauer, S., Emmett, P.H., and Teller, E. 1938. Adsorption of Gases in Multimolecular Layers. *Journal of the American Chemical Society* **60** (2): 309-319.

Bumb, A.C. and McKee, C.R. 1988. Gas-Well Testing in the Presence of Desorption for Coalbed Methane and Devonian Shale. *SPE Formation Evaluation* **3** (1): 179-185.

Bustin, A.M.M., Bustin, R.M., and Cui, X. 2008. Importance of Fabric on the Production of Gas Shales. Paper presented at the SPE Unconventional Reservoirs Conference, Keystone, Colorado, USA. Society of Petroleum Engineers SPE-114167-MS.

Carlson, E.S. 1994. Characterization of Devonian Shale Gas Reservoirs Using Coordinated Single Well Analytical Models. Paper presented at the SPE Eastern Regional Meeting, Charleston, West Virginia. Society of Petroleum Engineers SPE-29199-MS.

Chaudhri, M.M. 2012. Numerical Modeling of Multifracture Horizontal Well for Uncertainty Analysis and History Matching: Case Studies from Oklahoma and Texas Shale Gas Wells. Paper presented at the SPE Western Regional Meeting, Bakersfield, California, USA. Society of Petroleum Engineers SPE-153888-MS.

Chawathe, A., Ertekin, T., and Grader, A. 1996. Numerical Simulation of Multimechanistic Gas-Water Flow in Fractured Reservoirs. Paper presented at the Permian Basin Oil and Gas Recovery Conference, Midland, Texas. Society of Petroleum Engineers 00035186.

Chazal, C. and Moutou Pitti, R. 2011. Incremental Constitutive Formulation for Time Dependent Materials: Creep Integral Approach. *Mechanics of Time-Dependent Materials* **15** (3): 239-253.

Chen, Z., Liu, J., Elsworth, D. et al. 2009. Investigation of Co₂ Injection Induced Coal-Gas Interactions. Paper presented at the 43rd U.S. Rock Mechanics Symposium & 4th U.S. - Canada Rock Mechanics Symposium, Asheville, North Carolina. American Rock Mechanics Association ARMA-09-099.

Christensen, R.M. 1971. *Theory of Viscoelasticity: An Introduction*. New York: Academic Press.

Cicek, O. 2005. Numerical Simulation of Steam Displacement of Oil in Naturally Fractured Reservoirs Using Fully Implicit Compositional Formulation: A Comparative Analysis of the Effects of Capillary and Gravitational Forces in Matrix/Fracture Exchange Term. Paper presented at the SPE Annual Technical Conference and Exhibition, Dallas, Texas, U.S.A. Society of Petroleum Engineers SPE-97005-MS.

Cipolla, C.L., Lolon, E., and Mayerhofer, M.J. 2009. Reservoir Modeling and Production Evaluation in Shale-Gas Reservoirs. Paper presented at the International Petroleum Technology Conference, Doha, Qatar. International Petroleum Technology Conference IPTC-13185-MS.

Cipolla, C.L., Lolon, E.P., Erdle, J.C. et al. 2010. Reservoir Modeling in Shale-Gas Reservoirs. *SPE Reservoir Evaluation & Engineering* **13** (4): 638-653.

Civan, F. 2010. Effective Correlation of Apparent Gas Permeability in Tight Porous Media. *Transport in Porous Media* **82** (2): 375-384.

Clemo, T.M. and Smith, L. 1989. Solute Transport in Fractured Media: Dual Permeability Models. *Eos Trans. AGU* **70** (43).

Cook, J.R. 2011. Predicting Production from the Marcellus Shale with Two-Layer Dynamic Inflow Performance Curves. Paper presented at the Canadian Unconventional Resources Conference, Alberta, Canada. Society of Petroleum Engineers SPE-146947-MS.

Cox, J.C. 1988. What You Should Know About Gas Compressibility Factors. *World Oil*: 69-72.

Cramer, D.D. 2008. Stimulating Unconventional Reservoirs: Lessons Learned, Successful Practices, Areas for Improvement. Paper presented at the SPE Unconventional Reservoirs Conference, Keystone, Colorado, USA. Society of Petroleum Engineers SPE-114172-MS.

Cui, X. and Bustin, R.M. 2005. Volumetric Strain Associated with Methane Desorption and Its Impact on Coalbed Gas Production from Deep Coal Seams. *AAPG Bulletin* **89** (9): 1181-1202.

Curran, J. and Carvalho, J.L. 1987. A Displacement Discontinuity Model for Fluid-Saturated Porous Media. Paper presented at the 6th ISRM Congress, Montreal, Canada. International Society for Rock Mechanics ISRM-6CONGRESS-1987-014.

Curtis, J.B. 2002. Fractured Shale-Gas Systems. *AAPG Bulletin* **86** (11): 1921-1938.

da Silva, F.V. 1989. Primary and Enhanced Recovery of Ekofisk Field: A Single- and Double-Porosity Numerical Simulation Study. Paper presented at the SPE Annual Technical Conference and Exhibition, San Antonio, Texas. Society of Petroleum Engineers SPE-19840-MS.

Dean, R.H. and Lo, L.L. 1988. Simulations of Naturally Fractured Reservoirs. *SPE Reservoir Engineering* **3** (2): 638-648.

Dershowitz, B., LaPointe, P., Eiben, T. et al. 2000. Integration of Discrete Feature Network Methods with Conventional Simulator Approaches. *SPE Reservoir Evaluation & Engineering* **3** (2): 165-170.

Detournay, E. and Cheng, A.H.D. 1993. Fundamentals of Poroelasticity. In *Comprehensive Rock Engineering: Principles, Practice & Projects*, New York: Pergamon Press. 2.

Diek, A. and Ghassemi, A. 2004. *A Thermoporoelastic Theory of Fluid Saturated Argillaceous Rocks*. Grand Forks, ND: Dept. of Geology & Geological Engineering, University of North Dakota.

Ding, Y., Basquet, R., and Bourbiaux, B. 2006. Upscaling Fracture Networks for Simulation of Horizontal Wells Using a Dual-Porosity Reservoir Simulator. *SPE Reservoir Evaluation & Engineering* **9** (5): 513-520.

Donato, G.D., Huang, W., and Blunt, M. 2003. Streamline-Based Dual Porosity Simulation of Fractured Reservoirs. Paper presented at the SPE Annual Technical Conference and Exhibition, Denver, Colorado. Society of Petroleum Engineers SPE-84036-MS.

Dranchuk, P.M. and Kassem, H.A.-. 1975. Calculation of Z Factors for Natural Gases Using Equations of State. *Journal of Canadian Petroleum Technology* **14** (3): 34-36.

Du, C., Zhang, X., Zhan, L. et al. 2010. Modeling Hydraulic Fracturing Induced Fracture Networks in Shale Gas Reservoirs as a Dual Porosity System. Paper presented at the International Oil and Gas Conference and Exhibition in China, Beijing, China. Society of Petroleum Engineers SPE-132180-MS.

Energy Information Administration. Annual Energy Outlook 2012. http://www.eia.gov/forecasts/aeo/pdf/0383(2012).pdf.

Florence, F.A., Rushing, J., Newsham, K.E. et al. 2007. Improved Permeability Prediction Relations for Low Permeability Sands. Paper presented at the Rocky Mountain Oil & Gas Technology Symposium, Denver, Colorado, U.S.A. Society of Petroleum Engineers SPE-107954-MS.

Forchheimer, P. 1901. Wasserbewegung Durch Boden. *Forschtlft ver. D. Ing.* **45**: 1782-1788.

Freeman, C., Moridis, G.J., Ilk, D. et al. 2010. A Numerical Study of Transport and Storage Effects for Tight Gas and Shale Gas Reservoir Systems. Paper presented at the International Oil and Gas Conference and Exhibition in China, Beijing, China. Society of Petroleum Engineers SPE-131583-MS.

Freeman, C.M., Moridis, G.J., Ilk, D. et al. 2009. A Numerical Study of Performance for Tight Gas and Shale Gas Reservoir Systems. Paper presented at the SPE Annual Technical Conference and Exhibition, New Orleans, Louisiana. Society of Petroleum Engineers SPE-124961-MS.

Fung, L.S.-K. 1993. Numerical Simulation of Naturally Fractured Reservoirs. Paper presented at the Middle East Oil Show, Bahrain. Society of Petroleum Engineers SPE-25616-MS.

Ganzer, L.J. 2002. Simulating Fractured Reservoirs Using Adaptive Dual Continuum. Paper presented at the SPE/DOE Improved Oil Recovery Symposium, Tulsa, Oklahoma. Society of Petroleum Engineers SPE-75233-MS.

Gatens III, J.M., Lee, W.J., Lane, H.S. et al. 1989. Analysis of Eastern Devonian Gas Shales Production Data. *SPE Journal of Petroleum Technology* **41** (5): 519-525.

Gatens III, J.M., Lee, W.J., and Rahim, Z. 1985. Application of an Analytical Model to History Match Devonian Shales Production Data. Paper presented at the SPE Eastern Regional Meeting, Morgantown, West Virginia. Society of Petroleum Engineers SPE-14509-MS.

Ghafouri, H.R. and Lewis, R.W. 1996. A Finite Element Double Porosity Model for Heterogeneous Deformable Porous Media. *International Journal for Numerical and Analytical Methods in Geomechanics* **20** (11): 831-844.

Ghazlan, G., Caperaa, S., and Petit, C. 1995. An Incremental Formulation for the Linear Analysis of Thin Viscoelastic Structures Using Generalized Variables. *International Journal for Numerical Methods in Engineering* **38** (19): 3315-3333.

Ghedan, S.G., Aljawad, M.S., and Poettmann, F.H. 1993. Compressibility of Natural Gases. *Journal of Petroleum Science and Engineering* **10** (2): 157-162.

Gioda, G. 1981. A Finite Element Solution of Non-Linear Creep Problems in Rocks. *International Journal of Rock Mechanics and Mining Sciences & Geomechanics Abstracts* **18** (1): 35-46.

Goodman, R.E. 1976. *Methods of Geological Engineering in Discontinuous Rocks*. St. Paul, Minnesota: West Pub. Co.

Goodman, R.E. 1980. *Introduction to Rock Mechanics*. New York: John Wiley & Sons.

Gringarten, A.C., Henry J. Ramey, J., and Raghavan, R. 1974. Unsteady-State Pressure Distributions Created by a Well with a Single Infinite-Conductivity Vertical Fracture. *Society of Petroleum Engineers Journal* **14** (4): 347-360.

Guo, J., Li, Y., Zhao, J. et al. 2004. Numerical Simulation of Fracturing Naturally Fractured and Low-Permeability Reservoirs with Macro-Fracture. Paper presented at the Canadian International Petroleum Conference, Calgary, Alberta. Petroleum Society of Canada PETSOC-2004-012.

Gurpinar, O., Kalbus, J., and List, D. 1999. Numerical Modeling of a Triple Porosity Reservoir. Paper presented at the SPE Asia Pacific Improved Oil Recovery Conference, Kuala Lumpur, Malaysia. Society of Petroleum Engineers SPE-57277-MS.

Gurpinar, O. and Kossack, C.A. 2000. Realistic Numerical Models for Fractured Reservoirs. Paper presented at the SPE International Petroleum Conference and Exhibition in Mexico, Villahermosa, Mexico. Copyright 2000, Society of Petroleum Engineers, Inc. SPE-59041-MS.

Hagin, P.N. and Zoback, M.D. 2007. Predicting and Monitoring Long-Term Compaction in Unconsolidated Reservoir Sands Using a Dual Power Law Model. *Geophysics* **72** (5): 165-173.

Harpalani, S. and Schraufnagel, A. 1990. Measurement of Parameters Impacting Methane Recovery from Coal Seams. *Geotechnical and Geological Engineering* **8** (4): 369-384.

Heidug, W.K. and Wong, S.W. 1996. Hydration Swelling of Water-Absorbing Rocks: A Constitutive Model. *International Journal for Numerical and Analytical Methods in Geomechanics* **20** (6): 403-430.

Hicks, T.W., Pine, R.J., Willis-Richards, J. et al. 1996. A Hydro-Thermo-Mechanical Numerical Model for Hdr Geothermal Reservoir Evaluation. *International Journal of Rock Mechanics and Mining Sciences & Geomechanics Abstracts* **33** (5): 499-511.

Hill, A.C. and Thomas, G.W. 1985. A New Approach for Simulating Complex Fractured Reservoirs. Paper presented at the Middle East Oil Technical Conference and Exhibition, Bahrain. Society of Petroleum Engineers SPE-13537-MS.

Hill, D.G. and Nelson, C.R. 2000. Gas Productive Fractured Shales-an Overview and Update. *GasTIPS* **7** (2): 11-16.

Holditch, S.A. 2009. Ss: Unlocking the Unconventional Oil and Gas Reservoirs: Stimulation of Tight Gas Sands. Paper presented at the Offshore Technology Conference, Houston, Texas. Offshore Technology Conference OTC-20267-MS.

Huang, H. and Ayoub, J.A. 2008. Applicability of the Forchheimer Equation for Non-Darcy Flow in Porous Media. *SPE Journal* **13** (1): 112-122.

Huang, J. and Ghassemi, A. 2011. Poroelastic Analysis of Gas Production from Shale. Paper presented at the 45th U.S. Rock Mechanics / Geomechanics Symposium, San Francisco, California. American Rock Mechanics Association ARMA-11-479.

Huang, R., Zhou, Z., and Deng, J. 1987. The Creep Characteristics of Shale Formation and the Analysis of Its Loading on the Oil Well Casing. Paper presented at the 6th ISRM Congress, Montreal, Canada. International Society for Rock Mechanics. ISRM-6CONGRESS-1987-024.

Jaeger, J.C., Cook, N.G.W., and Zimmerman, R. 2007. *Fundamentals of Rock Mechanics*. New York: John Wiley & Sons.

Jarvie, D.M., Hill, R.J., Ruble, T.E. et al. 2007. Unconventional Shale-Gas Systems: The Mississippian Barnett Shale of North-Central Texas as One Model for Thermogenic Shale-Gas Assessment. *AAPG Bulletin* **91** (4): 475-499.

Jayakumar, R., Sahai, V., and Boulis, A. 2011. A Better Understanding of Finite Element Simulation for Shale Gas Reservoirs through a Series of Different Case Histories. Paper presented at the SPE Middle East Unconventional Gas Conference and Exhibition, Muscat, Oman. Society of Petroleum Engineers SPE-142464-MS.

Kale, S.V., Rai, C.S., and Sondergeld, C.H. 2010. Petrophysical Characterization of Barnett Shale. Paper presented at the SPE Unconventional Gas Conference, Pittsburgh, Pennsylvania, USA. Society of Petroleum Engineers SPE-131770-MS.

Kang, S.M., Fathi, E., Ambrose, R.J. et al. 2010. Carbon Dioxide Storage Capacity of Organic-Rich Shales. Paper presented at the SPE Annual Technical Conference and Exhibition, Florence, Italy. Society of Petroleum Engineers SPE-134583-MS.

Karimi-Fard, M. and Firoozabadi, A. 2001. Numerical Simulation of Water Injection in 2d Fractured Media Using Discrete-Fracture Model. Paper presented at the SPE Annual Technical Conference and Exhibition, New Orleans, Louisiana. Society of Petroleum Engineers SPE-71615-MS.

Karimi-Fard, M. and Firoozabadi, A. 2003. Numerical Simulation of Water Injection in Fractured Media Using the Discrete-Fracture Model and the Galerkin Method. *SPE Reservoir Evaluation & Engineering* **6** (2): 117-126.

Kay, W. 1936. Gases and Vapors at High Temperature and Pressure - Density of Hydrocarbon. *Industrial & Engineering Chemistry* **28** (9): 1014-1019.

Kazemi, H., Gilman, J.R., and Elsharkawy, A.M. 1992. Analytical and Numerical Solution of Oil Recovery from Fractured Reservoirs with Empirical Transfer Functions (Includes Associated Papers 25528 and 25818). *SPE Reservoir Engineering* **7** (2): 219-227.

Kazemi, H., Merrill JR., L.S., Porterfield, K.L. et al. 1976. Numerical Simulation of Water-Oil Flow in Naturally Fractured Reservoirs. *Society of Petroleum Engineers Journal* **16** (6): 317-326.

Kim, H.O. and Kuhlemeyer, R.L. 1977. A Finite Element Formulation for Creep Analysis. *International Journal for Numerical Methods in Engineering* **11** (12): 1865-1877.

Kim, T.H. and Schechter, D.S. 2007. Estimation of Fracture Porosity of Naturally Fractured Reservoirs with No Matrix Porosity Using Fractal Discrete Fracture Networks. Paper presented at the SPE Annual Technical Conference and Exhibition, Anaheim, California, U.S.A. Society of Petroleum Engineers SPE-110720-MS.

Kim, T.H. and Schechter, D.S. 2009. Estimation of Fracture Porosity of Naturally Fractured Reservoirs with No Matrix Porosity Using Fractal Discrete Fracture Networks. *SPE Reservoir Evaluation & Engineering* **12** (2): 232-242.

King, G.R. 1993. Measurement of Inflow Performance Parameters for Coal Seam and Devonian Shale Gas Reservoirs and Its Implication in Numerical Reservoir Simulation. Paper presented at the SPE Annual Technical Conference and Exhibition, Houston, Texas. Society of Petroleum Engineers SPE-26631-MS.

Klinkenberg, L.J. 1941. The Permeability of Porous Media to Liquids and Gases. Paper presented at the Drilling and Production Practice, New York. American Petroleum Institute API-41-200.

Kozier, G. 1984. Devonian Shale Production Data Analysis. Paper presented at the SPE Unconventional Gas Recovery Symposium, Pittsburgh, Pennsylvania. Society of Petroleum Engineers of AIME SPE-12871-MS.

Kundt, A. and Warburg, E. 1875. On Friction and Thermal Conductivity in Rarefied Gases. *Philosophical Magazine* **50** (4): 53-62.

Kuuskraa, V.A., Sedwick, K., and Yost II, A.B. 1985. Technically Recoverable Devonian Shale Gas in Ohio, West Virginia, and Kentucky. Paper presented at the SPE Eastern Regional Meeting, Morgantown, West Virginia. Society of Petroleum Engineers SPE-14503-MS.

Lamb, A.R., Gorman, G., Gosselin, O.R. et al. 2010. Finite Element Voupled Deformation and Fluid Flow in Fractured Porous Media. Paper presented at the SPE EUROPEC/EAGE Annual Conference and Exhibition, Barcelona, Spain. Society of Petroleum Engineers SPE-131725-MS.

Lancaster, D.E., McKetta, S.F., Hill, R.E. et al. 1992. Reservoir Evaluation, Completion Techniques, and Recent Results from Barnett Shale Development in the Fort Worth Basin. Paper presented at the SPE Annual Technical Conference and Exhibition, Washington, D.C. Society of Petroleum Engineers SPE-24884-MS.

Lane, H.S., Lancaster, D.E., and Watson, A.T. 1990. Estimating Gas Desorption Parameters from Devonian Shale Well Test Data. Paper presented at the SPE Eastern Regional Meeting, Columbus, Ohio. Society of Petroleum Engineers SPE-21272-MS.

Lane, H.S., Watson, A.T., and Lancaster, D.E. 1989. Identifying and Estimating Desorption from Devonian Shale Gas Production Data. Paper presented at the SPE Annual Technical Conference and Exhibition, San Antonio, Texas. Society of Petroleum Engineers SPE-19794-MS.

Langmuir, I. 1916. The Constitution and Fundamental Properties of Solids and Liquids. Part I. Solids. *Journal of the American Chemical Society* **38** (11): 2221-2295.

Lavrov, A., Papamichos, E., and Cerasi, P. 2005. Numerical Modeling of Sand-Production Mechanisms with Displacement Discontinuity Method. Paper presented at the SPE Europec/EAGE Annual Conference, Madrid, Spain. Society of Petroleum Engineers SPE-93981-MS.

Lee, A.L., Gonzalez, M.H., and Eakin, B.E. 1966. The Viscosity of Natural Gases. *Journal of Petroleum Technology* **18** (8): 997-1000.

Lee, J., Choi, S.-U., and Cho, W. 1999. A Comparative Study of Dual-Porosity Model and Discrete Fracture Network Model. *KSCE Journal of Civil Engineering* **3** (2): 171-180.

Lee, W.J. and Gatens III, J.M. 1985. Analysis of Eastern Devonian Gas Shales Production Data. Paper presented at the SPE Eastern Regional Meeting, Morgantown, West Virginia. Society of Petroleum Engineers SPE-14506-MS.

Lewis, A.M. and Hughes, R.G. 2008. Production Data Analysis of Shale Gas Reservoirs. Paper presented at the SPE Annual Technical Conference and Exhibition, Denver, Colorado, USA. Society of Petroleum Engineers 116688-MS.

Lewis, R.W. and Ghafouri, H.R. 1997. A Novel Finite Element Double Porosity Model for Multiphase Flow through Deformable Fractured Porous Media. *International Journal for Numerical and Analytical Methods in Geomechanics* **21** (11): 789-816.

Li, L. and Lee, S.H. 2006. Efficient Field-Scale Simulation for Black Oil in a Naturally Fractured Reservoir Via Discrete Fracture Networks and Homogenized Media. Paper presented at the International Oil & Gas Conference and Exhibition in China, Beijing, China. Society of Petroleum Engineers SPE-103901-MS.

Li, L. and Lee, S.H. 2008. Efficient Field-Scale Simulation of Black Oil in a Naturally Fractured Reservoir through Discrete Fracture Networks and Homogenized Media. *SPE Reservoir Evaluation & Engineering* **11** (4): 750-758.

Li, Y. and Ghassemi, A. 2012. Creep Behavior of Barnett, Haynesville, and Marcellus Shale. Paper presented at the 46th US Rock Mechanics / Geomechanics Symposium, Chicago, Illinois. American Rock Mechanics Association ARMA-2012-330.

Lim, K.T. and Aziz, K. 1995. Matrix-Fracture Transfer Shape Factors for Dual-Porosity Simulators. *Journal of Petroleum Science and Engineering* **13** (3): 169-178.

Lin, W. 2010. Gas Sorption and the Consequent Volumetric and Permeability Change of Coal. Doctor of Philosophy Dissertation, California, Stanford University.

Liu, J., Chen, Z., Elsworth, D. et al. 2010. Linking Gas-Sorption Induced Changes in Coal Permeability to Directional Strains through a Modulus Reduction Ratio. *International Journal of Coal Geology* **83** (1): 21-30.

Liu, X. and Civan, F. 1995. Formation Damage by Fines Migration Including Effects of Filter Cake, Pore Compressibility, and Non-Darcy Flow - a Modeling Approach to Scaling from Core to Field. Paper presented at the SPE International Symposium on Oilfield Chemistry, San Antonio, Texas. Society of Petroleum Engineers SPE-28980-MS.

Loeb, L.B. 1934. *The Kinetic Theory of Gases*. New York and London: McGraw-Hill Book Company, Inc.

Londono, F.E., Archer, R.A., and Blasingame, T.A. 2005. Correlations for Hydrocarbon-Gas Viscosity and Gas Density- -Validation and Correlation of Behavior Using a Large-Scale Database. *SPE Reservoir Evaluation & Engineering* **8** (6): 561-572.

Lu, X., Li, F., and Watson, A.T. 1995. Adsorption Measurements in Devonian Shales. *Fuel* **74** (4): 599-603.

Marji, M.F., Goshtasbi, K., Gholamnejad, J. et al. 2010. On the Displacement Discontinuity Analysis of Radial Cracks Emanating from Circular Blast Holes in Rock Blasting. Paper presented at the ISRM International Symposium - 6th Asian Rock Mechanics Symposium, New Delhi, India. International Society for Rock Mechanics ISRM-ARMS6-2010-126.

Martin, R., Baihly, J.D., Malpani, R. et al. 2011. Understanding Production from Eagle Ford-Austin Chalk System. Paper presented at the SPE Annual Technical

Conference and Exhibition, Denver, Colorado, USA. Society of Petroleum Engineers SPE-145117-MS.
Martineau, D.F. 2007. History of the Newark East Field and the Barnett Shale as a Gas Reservoir. *AAPG Bulletin* **91** (4): 399-403.
Mayerhofer, M.J., Lolon, E.P., Youngblood, J.E. et al. 2006. Integration of Microseismic Fracture Mapping Results with Numerical Fracture Network Production Modeling in the Barnett Shale. Paper presented at the SPE Annual Technical Conference and Exhibition, San Antonio, Texas, USA. Society of Petroleum Engineers SPE-102103-MS.
McBane, R.A. and Thompson, T.W. 1984. Exploration/Production Studies of the Devonian Gas Shales. Paper presented at the SPE Unconventional Gas Recovery Symposium, Pittsburgh, Pennsylvania. Society of Petroleum Engineers of AIME SPE-12833-MS.
McKee, C.R., Bumb, A.C., and Koenig, R.A. 1988. Stress-Dependent Permeability and Porosity of Coal and Other Geologic Formations. *SPE Formation Evaluation* **3** (1): 81-91.
Medeiros, F., Kurtoglu, B., Ozkan, E. et al. 2010. Analysis of Production Data from Hydraulically Fractured Horizontal Wells in Shale Reservoirs. *SPE Reservoir Evaluation & Engineering* **13** (3): 559-568.
Medeiros, F., Ozkan, E., and Kazemi, H. 2006. A Semianalytical, Pressure-Transient Model for Horizontal and Multilateral Wells in Composite, Layered, and Compartmentalized Reservoirs. Paper presented at the SPE Annual Technical Conference and Exhibition, San Antonio, Texas, USA. Society of Petroleum Engineers SPE-102834-MS.
Meyer, B.R. and Bazan, L.W. 2011. A Discrete Fracture Network Model for Hydraulically Induced Fractures: Theory, Parametric and Case Studies. Paper presented at the SPE Hydraulic Fracturing Technology Conference, The Woodlands, Texas, USA. Society of Petroleum Engineers SPE-140514-MS.
Moinfar, A., Narr, W., Hui, M.-H. et al. 2011. Comparison of Discrete-Fracture and Dual-Permeability Models for Multiphase Flow in Naturally Fractured Reservoirs. Paper presented at the SPE Reservoir Simulation Symposium, The Woodlands, Texas, USA. Society of Petroleum Engineers SPE-142295-MS.
Moinfar, A., Varavei, A., Sepehrnoori, K. et al. 2012. Development of a Novel and Computationally-Efficient Discrete-Fracture Model to Study Ior Processes in Naturally Fractured Reservoirs. Paper presented at the SPE Improved Oil Recovery Symposium, Tulsa, Oklahoma, USA. Society of Petroleum Engineers SPE-154246-MS.
Montgomery, S.L., Jarvie, D.M., Bowker, K.A. et al. 2005. Mississippian Barnett Shale, Fort Worth Basin, North-Central Texas: Gas-Shale Play with Multi-Trillion Cubic Foot Potential. *AAPG Bulletin* **89** (2): 155-175.
Nakagawa, M., JIANG, Y., and ESAKI, T. 1999. A New Modelling of Mechanical Behavior of Discontinuities for Discontinuum Analysis. Paper presented at the Ninth International Congress on Rock Mechanics, Paris, France. International Society for Rock Mechanics ISRM-9CONGRESS-1999-188.

Naumenko, K. 2006. Modeling of High-Temperature Creep for Structural Analysis Applications. Doctor of Philosophy Dissertation, the Martin-Luther-University Halle-Wittenberg, Germany.

Nguyen, V.U. 1989. A Fortran Program for Modeling Methane Gas Desorption from Coal. *Computers & Geosciences* **15** (5): 695-707.

Nobakht, M. and Clarkson, C.R. 2012a. A New Analytical Method for Analyzing Linear Flow in Tight/Shale Gas Reservoirs: Constant-Flowing-Pressure Boundary Condition. *SPE Reservoir Evaluation & Engineering* **15** (3): 370-384.

Nobakht, M. and Clarkson, C.R. 2012b. A New Analytical Method for Analyzing Linear Flow in Tight/Shale Gas Reservoirs: Constant-Rate Boundary Condition. *SPE Reservoir Evaluation & Engineering* **15** (1): 51-59.

Noriyuki, M. 1986. On the Finite Element Formulation of Bifurcation Mode of Creep Buckling of Axisymmetric Shells. *Computers & Structures* **23** (3): 357-363.

Olorode, O.M., Freeman, C.M., Moridis, G.J. et al. 2012. High-Resolution Numerical Modeling of Complex and Irregular Fracture Patterns in Shale Gas and Tight Gas Reservoirs. Paper presented at the SPE Latin America and Caribbean Petroleum Engineering Conference, Mexico City, Mexico. Society of Petroleum Engineers SPE-152482-MS.

Olsson, W.A. 1980. Stress-Relaxation in Oil Shale. Paper presented at the The 21st U.S. Symposium on Rock Mechanics, Rolla, Missouri. American Rock Mechanics Association ARMA-80-0517.

Palmer, I. and Mansoori, J. 1998. How Permeability Depends on Stress and Pore Pressure in Coalbeds: A New Model. *SPE Reservoir Evaluation & Engineering* **1** (6): 539-544.

Palmer, I.D., Moschovidis, Z.A., and Cameron, J.R. 2007. Modeling Shear Failure and Stimulation of the Barnett Shale after Hydraulic Fracturing. Paper presented at the SPE Hydraulic Fracturing Technology Conference, College Station, Texas, U.S.A. Society of Petroleum Engineers SPE-106113-MS.

Pollastro, R.M. 2007. Total Petroleum System Assessment of Undiscovered Resources in the Giant Barnett Shale Continuous (Unconventional) Gas Accumulation, Fort Worth Basin, Texas. *AAPG Bulletin* **91** (4): 551-578.

Pollastro, R.M., Jarvie, D.M., Hill, R.J. et al. 2007. Geologic Framework of the Mississippian Barnett Shale, Barnett-Paleozoic Total Petroleum System, Bend Arch-Fort Worth Basin, Texas. *American Association of Petroleum Geologists Bulletin* **91** (4): 405-436.

Priest, S.D. 1984. Boundary Element Methods in Solid Mechanics by S. L. Crouch and A. M. Starfield. *Quarterly Journal of Engineering Geology and Hydrogeology* **17** (4): 399-400.

Rahman, M.K., Hossain, M.M., and Rahman, S.S. 2002. A Shear-Dilation-Based Model for Evaluation of Hydraulically Stimulated Naturally Fractured Reservoirs. *International Journal for Numerical and Analytical Methods in Geomechanics* **26** (5): 469-497.

Ramirez, B., Kazemi, H., Al-kobaisi, M. et al. 2009. A Critical Review for Proper Use of Water/Oil/Gas Transfer Functions in Dual-Porosity Naturally Fractured Reservoirs: Part I. *SPE Reservoir Evaluation & Engineering* **12** (2): 200-210.

Regueiro, R. 2006. Embedded Discontinuity Finite Element Modeling of Three-Dimensional Strong Discontinuities in Rocks. Paper presented at the The 41st U.S. Symposium on Rock Mechanics, Golden, CO. American Rock Mechanics Association ARMA-06-1069.

Remvik, F. 1995. Shale-Fluid Interaction and Its Effect on Creep. Paper presented at the 8th ISRM Congress, Tokyo, Japan. International Society for Rock Mechanics. ISRM-8CONGRESS-1995-064.

Rice, J.R. and Cleary, M.P. 1976. Some Basic Stress Diffusion Solutions for Fluid-Saturated Elastic Porous Media with Compressible Constituents. *Rev. Geophys.* **14** (2): 227-241.

Robertson, E.P. 2005. Modeling Permeability in Coal Using Sorption-Induced Strain Data. Paper presented at the SPE Annual Technical Conference and Exhibition, Dallas, Texas. Society of Petroleum Engineers SPE-97068-MS.

Robertson, E.P. and Christiansen, R.L. 2006. A Permeability Model for Coal and Other Fractured, Sorptive-Elastic Media. Paper presented at the SPE Eastern Regional Meeting, Canton, Ohio, USA. Society of Petroleum Engineers SPE-104380-MS.

Robertson, E.P. and Christiansen, R.L. 2008. A Permeability Model for Coal and Other Fractured, Sorptive-Elastic Media. *SPE Journal* **13** (3): 314-324.

Ross, D.J.K. and Bustin, R.M. 2007. Impact of Mass Balance Calculations on Adsorption Capacities in Microporous Shale Gas Reservoirs. *Fuel* **86** (17-18): 2696-2706.

Ross, D.J.K. and Bustin, R.M. 2009. The Importance of Shale Composition and Pore Structure Upon Gas Storage Potential of Shale Gas Reservoirs. *Marine and Petroleum Geology* **26** (6): 916-927.

Rossen, R.H. 1977. Simulation of Naturally Fractured Reservoirs with Semi-Implicit Source Terms. *Society of Petroleum Engineers Journal* **17** (3): 201-210.

Rushing, J.A., Oliver, S.J.P., and Scheper, R.J. 1989. Reservoir Simulation of the Antrim Shale in the Michigan Basin. Paper presented at the SPE Eastern Regional Meeting, Morgantown, West Virginia. Society of Petroleum Engineers SPE-19313-MS.

Rushmer, T. 1995. An Experimental Deformation Study of Partially Molten Amphibolite: Application to Low-Melt Fraction Segregation. *J. Geophys. Res.* **100** (B8): 15681-15695.

Saghafi, A., Faiz, M., and Roberts, D. 2007. Co2 Storage and Gas Diffusivity Properties of Coals from Sydney Basin, Australia. *International Journal of Coal Geology* **70** (1-3): 240-254.

Saidi, A.M. 1983. Simulation of Naturally Fractured Reservoirs. Paper presented at the SPE Reservoir Simulation Symposium, San Francisco, California. Society of Petroleum Engineers of AIME SPE-12270-MS.

Samandarli, O., Ahmadi, H.A.A., and Wattenbarger, R.A. 2011a. A New Method for History Matching and Forecasting Shale Gas Reservoir Production Performance

with a Dual Porosity Model. Paper presented at the North American Unconventional Gas Conference and Exhibition, The Woodlands, Texas, USA. Society of Petroleum Engineers SPE-144335-MS.

Samandarli, O., Ahmadi, H.A.A., and Wattenbarger, R.A. 2011b. A Semi-Analytic Method for History Matching Fractured Shale Gas Reservoirs. Paper presented at the SPE Western North American Region Meeting, Anchorage, Alaska, USA. Society of Petroleum Engineers SPE-144583-MS.

Sarda, S., Jeannin, L., Basquet, R. et al. 2002. Hydraulic Characterization of Fractured Reservoirs: Simulation on Discrete Fracture Models. *SPE Reservoir Evaluation & Engineering* **5** (2): 154-162.

Sarda, S., Jeannin, L., and Bourbiaux, B. 2001. Hydraulic Characterization of Fractured Reservoirs: Simulation on Discrete Fracture Models. Paper presented at the SPE Reservoir Simulation Symposium, Houston, Texas. Society of Petroleum Engineers SPE-66398-MS.

Schaaf, S.A. and Chambré, P.L. 1961. *Flow of Rarefied Gases*. Princeton, New Jersey: Princeton University Press.

Schepers, K.C., Gonzalez, R.J., Koperna, G.J. et al. 2009. Reservoir Modeling in Support of Shale Gas Exploration. Paper presented at the Latin American and Caribbean Petroleum Engineering Conference, Cartagena de Indias, Colombia. Society of Petroleum Engineers SPE-123057-MS.

Schön, J.H. 2011. *Physical Properties of Rocks: A Workbook*. Oxford,UK: Elsevier.

Seidle, J.R. and Huitt, L.G. 1995. Experimental Measurement of Coal Matrix Shrinkage Due to Gas Desorption and Implications for Cleat Permeability Increases. Paper presented at the International Meeting on Petroleum Engineering, Beijing, China. Society of Petroleum Engineers SPE-30010-MS.

Shi, J.Q. and Durucan, S. 2004. Drawdown Induced Changes in Permeability of Coalbeds: A New Interpretation of the Reservoir Response to Primary Recovery. *Transport in Porous Media* **56** (1): 1-16.

Simakin, A. and Ghassemi, A. 2005. Modelling Deformation of Partially Melted Rock Using a Poroviscoelastic Rheology with Dynamic Power Law Viscosity. *Tectonophysics* **397** (3–4): 195-209.

Sleep, N.H. 2002. Self-Organization of Crustal Faulting and Tectonics. *International Geology Review* **44** (1): 83-96.

Smith, I.M. and Griffiths, D.V. 1997. *Programming the Finite Element Method*: New York:Wiley.

Snow, D.T. 1965. A Parallel Plate Model of Fractured Permeable Media. Doctor of Philosophy Dissertation, University of California, Berkeley.

Sone, H. 2012. Mechanical Properties of Shale Gas Reservoir Rocks, and Its Relation to the in-Situ Stress Variation Observed in Shale Gas Reservoirs. Doctor of Philosophy Dissertation, California, Stanford University.

Sone, H. and Zoback, M.D. 2011. Visco-Plastic Properties of Shale Gas Reservoir Rocks. Paper presented at the 45th U.S. Rock Mechanics / Geomechanics Symposium, San Francisco, California. American Rock Mechanics Association ARMA-11-417.

Spivey, J.P. and Semmelbeck, M.E. 1995. Forecasting Long-Term Gas Production of Dewatered Coal Seams and Fractured Gas Shales. Paper presented at the Low Permeability Reservoirs Symposium, Denver, Colorado. Society of Petroleum Engineers SPE--29580-MS.

Standing, M.B. and Katz, D.L. 1942. Density of Natural Gases. *Transactions of AIME* **146** (1): 140-149.

Starling, K.E. and Ellington, R.T. 1964. Viscosity Correlations for Nonpolar Dense Fluids. *AIChE Journal* **10** (1): 11-15.

Takacs, G. 1976. Comparisons Made for Computer Z-Factor Calculations. *Oil & Gas Journal* **74**: 64-66.

Tamagawa, T. and Tezuka, K. 2004. Validation of Clustering of Fractures in Discrete Fracture Network Model by Using Fracture Density Distributions Along Boreholes. Paper presented at the SPE Annual Technical Conference and Exhibition, Houston, Texas. Society of Petroleum Engineers SPE-90342-MS.

Tao, Q., Ehlig-Economides, C.A., and Ghassemi, A. 2009. Modeling Variation of Stress and Permeability in Naturally Fractured Reservoirs Using Displacement Discontinuity Method. Paper presented at the 43rd U.S. Rock Mechanics Symposium & 4th U.S. - Canada Rock Mechanics Symposium, Asheville, North Carolina. American Rock Mechanics Association ARMA-09-047.

Texas Railroad Commission. Texas Gas Well Gas Production in the Newark, East (Barnett Shale) Field - 1993-2011. http://www.rrc.state.tx.us/barnettshale/index.php#statistics.

Tezuka, K., Tamagawa, T., and Watanabe, K. 2005. Numerical Simulation of Hydraulic Shearing in Fractured Reservoir. Paper presented at the Proceedings World Geothermal Congress 2005, Antalya, Turkey. International Geothermal Association.

Thompson, D.M. 1988. Fort Worth Basin, in L. L. Sloss, Ed. *The geology of North America: Geological Society of America* **D-2**: 346-352.

Thompson, J.M., Mangha, V.O., and Anderson, D.M. 2011. Improved Shale Gas Production Forecasting Using a Simplified Analytical Method-a Marcellus Case Study. Paper presented at the North American Unconventional Gas Conference and Exhibition, The Woodlands, Texas, USA. Society of Petroleum Engineers SPE-144436-MS.

Tommasi, A., Mainprice, D., Canova, G. et al. 2000. Viscoplastic Self-Consistent and Equilibrium-Based Modeling of Olivine Lattice Preferred Orientations: Implications for the Upper Mantle Seismic Anisotropy. *J. Geophys. Res.* **105** (B4): 7893-7908.

Trube, A.S. 1957. Compressibility of Natural Gases. *Journal of Petroleum Technology* **9** (1): 69-71.

Vanorsdale, C.R. 1987. Evaluation of Devonian Shale Gas Reservoirs. *SPE Reservoir Engineering* **2** (2): 209-216.

Verde, A. and Ghassemi, A. 2013. Efficient Solution of Large-Scale Displacement Discontinuity Problems Using the Fast Multipole Method. Paper presented at the

47th US Rock Mechanics / Geomechanics Symposium, San Francisco, CA. American Rock Mechanics Association.

Vermylen, J.P. 2011. Geomechanical Studies of the Barnett Shale, Texas, USA. Doctor of Philosophy Dissertation, California, Stanford University.

Wardie, L.J. 1984. Displacement Discontinuity Method for Three-Dimensional Stress Analysis of Tabular Excavations in Non-Homogeneous Rock. Paper presented at the The 25th U.S. Symposium on Rock Mechanics, Evanston, IL. American Rock Mechanics Association ARMA-84-0702.

Wardle, L.J. and Enever, J.R. 1983. Application of the Displacement Discontinuity Method to the Planning of Coal Mine Layouts. Paper presented at the 5th ISRM Congress, Melbourne, Australia. International Society for Rock Mechanics ISRM-5CONGRESS-1983-168.

Warpinski, N.R. 1989. Elastic and Viscoelastic Calculations of Stresses in Sedimentary Basins. *SPE Formation Evaluation* **4** (4): 522-530.

Warpinski, N.R., Mayerhofer, M.J., Vincent, M.C. et al. 2008. Stimulating Unconventional Reservoirs: Maximizing Network Growth While Optimizing Fracture Conductivity. Paper presented at the SPE Unconventional Reservoirs Conference, Keystone, Colorado, USA. Society of Petroleum Engineers SPE-114173-MS.

Warren, J.E. and Root, P.J. 1963. The Behavior of Naturally Fractured Reservoirs. *SPE Journal* **3** (3): 245-255.

Willis-Richards, J., Watanabe, K., and Takahashi, H. 1996. Progress toward a Stochastic Rock Mechanics Model of Engineered Geothermal Systems. *J. Geophys. Res.* **101** (B8): 17481-17496.

Witherspoon, P.A., Wang, J.S.Y., Iwai, K. et al. 1980. Validity of Cubic Law for Fluid Flow in a Deformable Rock Fracture. *Water Resour. Res.* **16** (6): 1016-1024.

Xu, W., Li, J., and du, m. 2011. Quick Estimate of Initial Production from Stimulated Reservoirs with Complex Hydraulic Fracture Network. Paper presented at the SPE Annual Technical Conference and Exhibition, Denver, Colorado, USA. Society of Petroleum Engineers SPE-146753-MS.

Xu, W., Thiercelin, M.J., and Walton, I.C. 2009. Characterization of Hydraulically-Induced Shale Fracture Network Using an Analytical/Semi-Analytical Model. Paper presented at the SPE Annual Technical Conference and Exhibition, New Orleans, Louisiana. Society of Petroleum Engineers SPE-124697-MS.

Yacoub, T.E. and Curran, J.H. 1999. Analysis of Post-Peak Pillar Behaviour Using the Enhanced Displacement Discontinuity Method. Paper presented at the The 37th U.S. Symposium on Rock Mechanics, Vail, CO. American Rock Mechanics Association ARMA-99-0169.

Zeng, F., Zhao, G., and Liu, H. 2012. A New Model for Reservoirs with a Discrete-Fracture System. *Journal of Canadian Petroleum Technology* **51** (2): 127-136.

Zhang, H., Liu, J., and Elsworth, D. 2008. How Sorption-Induced Matrix Deformation Affects Gas Flow in Coal Seams: A New Fe Model. *International Journal of Rock Mechanics and Mining Sciences* **45** (8): 1226-1236.

Zhang, X., Du, C., Deimbacher, F. et al. 2009. Sensitivity Studies of Horizontal Wells with Hydraulic Fractures in Shale Gas Reservoirs. Paper presented at the International Petroleum Technology Conference, Doha, Qatar. International Petroleum Technology Conference SPE-13338-MS.

Zhang, X., Koutsabeloulis, N.C., Press, D.J. et al. 2011. Dual-Permeability Models for Coupled Reservoir Geomechanical Modeling: Application to Field Production Data. Paper presented at the SPE Reservoir Characterisation and Simulation Conference and Exhibition, Abu Dhabi, UAE. Society of Petroleum Engineers SPE-148078-MS.

Zhang, X., Morrow, N.R., and Ma, S. 1996. Experimental Verification of a Modified Scaling Group for Spontaneous Imbibition. *SPE Reservoir Engineering* **11** (4): 280-285.

Zhao, H., Givens, N.B., and Curtis, B. 2007. Thermal Maturity of the Barnett Shale Determined from Well-Log Analysis. *AAPG Bulletin* **91** (4): 535-549.

Zhao, Y., Hu, Y., Zhao, B. et al. 2004. Nonlinear Coupled Mathematical Model for Solid Deformation and Gas Seepage in Fractured Media. *Transport in Porous Media* **55** (2): 119-136.

Zhou, W., Banerjee, R., Poe, B.D. et al. 2012. Semi-Analytical Production Simulation of Complex Hydraulic Fracture Network. Paper presented at the SPE International Production and Operations Conference & Exhibition, Doha, Qatar. Society of Petroleum Engineers SPE-157367-MS.

Zhou, X. and Ghassemi, A. 2009. Three-Dimensional Poroelastic Displacement Discontinuity Simulation of Natural Fractures. Paper presented at the 43rd U.S. Rock Mechanics Symposium & 4th U.S. - Canada Rock Mechanics Symposium, Asheville, North Carolina. American Rock Mechanics Association ARMA-09-154.

Zhou, Z.H., Huang, R.Z., and Chen, Y.F. 1992. Constitutive Equations of Shale and Clay Swelling: Theoretical Model and Laboratory Test under Confining Pressure. Paper presented at the International Meeting on Petroleum Engineering, Beijing, China. Society of Petroleum Engineers SPE-22382-MS.

Zienkiewicz, O.C. and Taylor, R.L. 2000. *The Finite Element Method: The Basis*. Oxford, UK: Butterworth-Heinemann.

Zocher, M.A., Groves, S.E., and Allen, D.H. 1997. A Three-Dimensional Finite Element Formulation for Thermoviscoelastic Orthotropic Media. *International Journal for Numerical Methods in Engineering* **40** (12): 2267-2288.

APPENDIX I

ANALYTICAL SOLUTION OF MODE II LOADING OF A WELLBORE

Wellbore Problem Definition:

A vertical borehole is drilled in a porous rock layer subjected to a non-hydrostatic horizontal in situ stress field:

$$\sigma_{xx} = -(P_0 - S_0) \tag{I-1}$$

$$\sigma_{yy} = -(P_0 + S_0) \tag{I-2}$$

$$\sigma_{xy} = 0 \tag{I-3}$$

$$p = p_0 \tag{I-4}$$

where P_0 is the far-field mean stress and S_0 is stress deviator and p_0 is the pore pressure.

Two assumptions need to be addressed in order to analyze this problem:

(1) under plane strain condition;

(2) instantaneous drilling process is simulated by removing at $t = 0^+$ the stresses and pore pressure which were acting on the borehole boundary initially.

Boundary conditions at the borehole wall under mode II loading are given as below:

$$\sigma_{rr} = 0 \qquad \sigma_{r\theta} = 0 \qquad p = -p_0 \tag{I-5}$$

Both the induced stress and pore pressure will vanish at infinity.

Diffusion Equation:

Under the condition of planar deformation and axisymmetry, the displacement field is obviously irrotational and characterized by the only non-zero component, $u_r(r,t)$. Then the pore pressure diffusion equation takes the following form:

$$\frac{\partial p}{\partial t} - c\left(\frac{1}{r}\frac{\partial p}{\partial r} + \frac{\partial^2 p}{\partial r^2}\right) = -\frac{\eta(1-\nu)}{GS}\frac{d}{dt}(\sigma_{rr} + \sigma_{\theta\theta} + 2\eta p) \tag{I-6}$$

Because of the vanishing stress condition at infinity, in this case, the pore pressure is governed by a homogeneous diffusion equation:

$$\frac{\partial^2 p}{\partial r^2} + \frac{1}{r}\frac{\partial p}{\partial r} = \frac{1}{c}\frac{\partial p}{\partial t} \tag{I-7}$$

Analytical Solution:

Laplace transform $\tilde{f} = \int_{-\infty}^{+\infty} e^{-ht} f(t)dt$ (h is the transform parameter)

with $h\tilde{f} = \int_{-\infty}^{+\infty} e^{-ht} f'(t)dt$

Apply the Laplace transformation to diffusion equation (I-7)

$$\frac{\partial^2 \tilde{p}}{\partial r^2} + \frac{1}{r}\frac{\partial \tilde{p}}{\partial r} - \frac{h}{c}\tilde{p} = 0 \tag{I-8}$$

Diffusion Eq.(I-8) can be regarded as a modified Bessel's differential equation

And its general solution is $\tilde{p} = D_1 K_0\left(r\sqrt{\frac{h}{c}}\right)$ (I-9)

where K_0 is the modified Bessel function of second kind of order 0; D_1 is a constant.

Now, we just restrict our attention to the special case in which the displacement field is irratational without any body force. Then it can be derived from a scalar potential Φ as

$$u_i = \Phi_{,i} \tag{I-10}$$

according to the Helmholtz decomposition of a vector field.

Then, the Navier type equation: $G\nabla^2 u_i + \frac{G}{1-2\nu} u_{k,ki} = \alpha p_{,i} - F_i$ (I-11)

can be reduced to: $\Phi_{,ikk} = \frac{\eta}{G} p_{,i}$ (I-12)

It can be integrated to yield

$$\varepsilon = u_{i,i} = \frac{\eta}{G} p + g(t) \tag{I-13}$$

where $g(t)$ is generally an unknown function of time only and it should be identically zero for the irrotational displacement in infinite or semi-infinite domain (Detournay and Cheng, 1993).

For this problem: $\varepsilon = \frac{\eta}{G} p$ (I-14) (because of the vanishing stress condition at infinity)

Applying the Laplace transformation to Eq. (I-14) and substituting $\tilde{p}$ with Eq.(I-9), one can get $\tilde{\varepsilon} = \frac{\eta}{G} \tilde{p} = \frac{\eta}{G} D_1 K_0(r\sqrt{\frac{h}{c}})$ (I-15)

Apply the Laplace transformation to equation $\varepsilon = \frac{1}{r} \frac{\partial}{\partial r}(r u_r)$ (I-16)

$$\Rightarrow \tilde{\varepsilon} = \frac{1}{r} \frac{\partial}{\partial r}(r \tilde{u}_r) = \frac{\eta}{G} D_1 K_0(r\sqrt{\frac{h}{c}}) \tag{I-17}$$

As $\frac{d}{dx}[x^n K_n(x)] = -x^n K_{n-1}(x) \Rightarrow \frac{d}{dx}[x K_1(x)] = -x K_0(x)$ (I-18)

$$d(r\tilde{u}_r) = \frac{\eta}{G} D_1 K_0(r\sqrt{\frac{h}{c}}) r dr$$

$$\Rightarrow d(r\tilde{u}_r) = \frac{\eta}{G} D_1 \frac{c}{h} K_0(r\sqrt{\frac{h}{c}})(r\sqrt{\frac{h}{c}}) d(r\sqrt{\frac{h}{c}}) \quad \text{(I-19)}$$

$$\Rightarrow d(r\tilde{u}_r) = -\frac{\eta}{G} D_1 \frac{c}{h} d[(r\sqrt{\frac{h}{c}}) K_1(r\sqrt{\frac{h}{c}})]$$

Integrating on both sides of Eq.(I-19), it yields

$$r\tilde{u}_r = -\frac{\eta}{G} D_1 \frac{c}{h} (r\sqrt{\frac{h}{c}}) K_1(r\sqrt{\frac{h}{c}}) + D_2$$

$$\Rightarrow \tilde{u}_r = -\frac{\eta}{G} D_1 \sqrt{\frac{c}{h}} K_1(r\sqrt{\frac{h}{c}}) + \frac{D_2}{r} \quad \text{(I-20)}$$

Checking Boundary conditions: $\sigma_{rr} = \sigma_{r\theta} = 0$ and $p = -p_0$ at r=a

$$p = -p_0 \Rightarrow \tilde{p}(a) = -\frac{p_0}{h} \Rightarrow D_1 K_0(a\sqrt{\frac{h}{c}}) = -\frac{p_0}{h}$$

$$\Rightarrow D_1 = -\frac{p_0}{h K_0(a\sqrt{\frac{h}{c}})} \quad \text{(I-21)}$$

If Let $\beta = a\sqrt{\frac{h}{c}}$, the expression for D_1 can be rewritten as

$$D_1 = -\frac{p_0}{h K_0(\beta)} \quad \text{(I-22)}$$

Then, we could get the solution of pore pressure in Laplace domain:

$$\frac{h\tilde{p}}{p_0} = -\frac{K_0(r\sqrt{\frac{h}{c}})}{K_0(\beta)} \quad \text{(I-23)}$$

For Hooke's law $\sigma_{rr} = 2G\varepsilon_{rr} + \frac{2G\nu}{1-2\nu}\varepsilon - \alpha p$ (I-24)

Apply Laplace transformation

$$\tilde{\sigma}_{rr} = 2G\frac{\partial \tilde{u}_r}{\partial r} + \frac{2G\nu}{1-2\nu}\tilde{\varepsilon} - \alpha\tilde{p} \tag{I-25}$$

By replacing $\tilde{u}_r$ and $\tilde{\varepsilon}$ with Eq.(I-20) and (I-17) respectively, Eq.(I-25) is given as

$$\tilde{\sigma}_{rr} = 2G[-\frac{\eta}{G}D_1\sqrt{\frac{c}{h}}\frac{dK_1(r\sqrt{\frac{h}{c}})}{dr} - \frac{D_2}{r^2}] + \frac{2G\nu}{1-2\nu}[\frac{\eta}{G}D_1K_0(r\sqrt{\frac{h}{c}})] - \alpha(-\frac{p_0}{h})$$

Due to $\sigma_{rr} = 0$ at r=a , with $K_n'(x) = -K_{n-1}(x) - \frac{n}{x}K_n(x)$

$$\Rightarrow 0 = 2G[-\frac{\eta}{G}D_1(-K_0(\beta) - \frac{K_1(\beta)}{\beta}) - \frac{D_2}{a^2}] + \frac{2G\nu}{1-2\nu}[\frac{\eta}{G}D_1K_0(\beta)] - \alpha(-\frac{p_0}{h})$$

$$\Rightarrow 0 = -2\eta D_1[-K_0(\beta) - \frac{K_1(\beta)}{\beta}] - \frac{2G}{a^2}D_2 + \frac{2\eta\nu}{1-2\nu}D_1K_0(\beta) + \alpha\frac{p_0}{h}$$

$$\Rightarrow \frac{2G}{a^2}D_2 = 2\eta D_1[K_0(\beta) + \frac{K_1(\beta)}{\beta} + \frac{\nu}{1-2\nu}K_0(\beta)] + \alpha\frac{p_0}{h}$$

$$\Rightarrow \frac{2G}{a^2}D_2 = 2\eta(-\frac{p_0}{hK_0(\beta)})[\frac{K_1(\beta)}{\beta} + \frac{1-\nu}{1-2\nu}K_0(\beta)] + \alpha\frac{p_0}{h}$$

$$\Rightarrow \frac{2G}{a^2}D_2 = -2\eta\frac{p_0}{h}[\frac{K_1(\beta)}{\beta K_0(\beta)} + \frac{1-\nu}{1-2\nu}] + \alpha\frac{p_0}{h}$$

Constant D_2 is solved: $D_2 = -2\eta\frac{a^2}{2G}\frac{p_0}{h}\frac{K_1(\beta)}{\beta K_0(\beta)}$ (I-26)

From Eq. (I-20), it is obtained:

$$\Rightarrow \tilde{u}_r = -\frac{\eta}{G} D_1 \sqrt{\frac{c}{h}} K_1(r\sqrt{\frac{h}{c}}) + \frac{D_2}{r}$$

$$\Rightarrow \tilde{u}_r = -\frac{\eta}{G}(-\frac{p_0}{hK_0(\beta)})\sqrt{\frac{c}{h}} K_1(r\sqrt{\frac{h}{c}}) + \frac{1}{r}(-2\eta \frac{a^2}{2G}\frac{p_0}{h}\frac{K_1(\beta)}{\beta K_0(\beta)})$$

$$\Rightarrow \tilde{u}_r = \frac{\eta}{G}\frac{p_0\sqrt{\frac{c}{h}}}{h}\frac{K_1(r\sqrt{\frac{h}{c}})}{K_0(\beta)} - \frac{\eta}{G}\frac{p_0}{h}\frac{a^2}{r}\frac{K_1(\beta)}{\beta K_0(\beta)} \qquad \text{(I-27)}$$

$$\Rightarrow \frac{2Gh\tilde{u}_r}{p_0 a} = 2\eta[\frac{K_1(r\sqrt{\frac{h}{c}})}{\beta K_0(\beta)} - \frac{K_1(\beta)}{r\sqrt{\frac{h}{c}}K_0(\beta)}]$$

From eq. (I-25), it is obtained:

$$\tilde{\sigma}_{rr} = 2G\frac{\partial \tilde{u}_r}{\partial r} + \frac{2G\nu}{1-2\nu}\tilde{\varepsilon} - \alpha\tilde{p}$$

$$\Rightarrow \tilde{\sigma}_{rr} = 2G[-\frac{\eta}{G}D_1\sqrt{\frac{c}{h}}\frac{dK_1(r\sqrt{\frac{h}{c}})}{dr} - \frac{D_2}{r^2}] + \frac{2G\nu}{1-2\nu}[\frac{\eta}{G}D_1K_0(r\sqrt{\frac{h}{c}})] - \alpha[D_1K_0(r\sqrt{\frac{h}{c}})]$$

$$\Rightarrow \tilde{\sigma}_{rr} = 2G\{-\frac{\eta}{G}D_1[-K_0(r\sqrt{\frac{h}{c}}) - \frac{K_1(r\sqrt{\frac{h}{c}})}{r\sqrt{\frac{h}{c}}}] - \frac{D_2}{r^2}\} + \frac{2G\nu}{1-2\nu}[\frac{\eta}{G}D_1K_0(r\sqrt{\frac{h}{c}})] - \alpha[D_1K_0(r\sqrt{\frac{h}{c}})]$$

$$\Rightarrow \tilde{\sigma}_{rr} = 2\eta D_1[K_0(r\sqrt{\frac{h}{c}}) + \frac{K_1(r\sqrt{\frac{h}{c}})}{r\sqrt{\frac{h}{c}}} + \frac{\nu}{1-2\nu}K_0(r\sqrt{\frac{h}{c}}) - \frac{\alpha}{2\eta}K_0(r\sqrt{\frac{h}{c}})] - \frac{2G}{r^2}D_2$$

$$\Rightarrow \tilde{\sigma}_{rr} = 2\eta(-\frac{p_0}{hK_0(\beta)})\frac{K_1(r\sqrt{\frac{h}{c}})}{r\sqrt{\frac{h}{c}}} - \frac{2G}{r^2}D_2$$

$$\Rightarrow \tilde{\sigma}_{rr} = 2\eta(-\frac{p_0}{hK_0(\beta)})\frac{K_1(r\sqrt{\frac{h}{c}})}{r\sqrt{\frac{h}{c}}} - \frac{2G}{r^2}(-2\eta\frac{a^2}{2G}\frac{p_0}{h}\frac{K_1(\beta)}{\beta K_0(\beta)})$$

$$\Rightarrow \frac{h\tilde{\sigma}_{rr}}{p_0} = -2\eta[\frac{K_1(r\sqrt{\frac{h}{c}})}{r\sqrt{\frac{h}{c}}K_0(\beta)} - \frac{a^2}{r^2}\frac{K_1(\beta)}{\beta K_0(\beta)}] \tag{I-28}$$

For planestrain

$$\sigma_{kk} + 2\eta p = \frac{2G}{1-2\nu} g(t) = 0 \tag{I-29}$$

$g(t)$ is generally an unknown function of time only and it should be identically zero for the irrotational displacement in infinite or semi-infinite domain (Detournay and Cheng, 1993).

After applying Laplace transformation to Eq. (I-29), finally one can get the solution of tangential stress in Laplace domain:

$$\tilde{\sigma}_{rr} + \tilde{\sigma}_{\theta\theta} = -2\eta\tilde{p}$$
$$\Rightarrow \tilde{\sigma}_{\theta\theta} = -2\eta\tilde{p} - \tilde{\sigma}_{rr}$$
$$\Rightarrow \tilde{\sigma}_{\theta\theta} = 2\eta\frac{p_0}{h}\frac{K_0(r\sqrt{\frac{h}{c}})}{K_0(\beta)} + 2\eta\frac{p_0}{h}[\frac{K_1(r\sqrt{\frac{h}{c}})}{r\sqrt{\frac{h}{c}}K_0(\beta)} - \frac{a^2}{r^2}\frac{K_1(\beta)}{\beta K_0(\beta)}]$$
$$\Rightarrow \frac{h\tilde{\sigma}_{\theta\theta}}{p_0} = 2\eta[\frac{K_0(r\sqrt{\frac{h}{c}})}{K_0(\beta)} + \frac{K_1(r\sqrt{\frac{h}{c}})}{r\sqrt{\frac{h}{c}}K_0(\beta)} - \frac{a^2}{r^2}\frac{K_1(\beta)}{\beta K_0(\beta)}] \tag{I-30}$$

APPENDIX II

ANALYTICAL SOLUTION OF 1D CONSOLITION

Terzaghi's one-dimensional consolidation(Mechanical)

Assumptions:

1).A soil layer of thickness L, resting on a rigid impermeability base

2).A constant load is applied to the surface of the layer under drained conditions;

3).Boundary conditions: p=0 at x=0 and $\partial p / \partial x = 0$ at x=L

Initial pore pressure field p(x,0), induced by loading of the layer, is given by

$$p(0,x) = \eta p^* / GS \tag{II-1}$$

Under uniaxial strain condition: $p = -\frac{\eta}{GS}\sigma_{xx}$ (II-2)

σ_{xx} is the only non-zero strain in this situation;

Diffusion equation is given as: $\frac{\partial p}{\partial t} - C\frac{\partial^2 p}{\partial x^2} = -\frac{\eta}{GS}\frac{d\sigma_{xx}}{dt}$ (II-3)

Since the stress (σ_{xx}) is a constant, a homogeneous diffusion equation is given:

$$\frac{\partial p}{\partial t} - C\frac{\partial^2 p}{\partial x^2} = 0 \tag{II-4}$$

Let $p(x,t) = \phi(x)g(t)$

Then Eq.(II-4) is transformed to: $\phi(x)g'(t) - C\phi''(x)g(t) = 0$ (II-5)

Separate variables: $\frac{g'(t)}{g(t)} = C\frac{\phi''(x)}{\phi(x)}$

By assuming $\frac{\phi''(x)}{\phi(x)} = \mu^2$, Eq. (II-5) can be rewritten as:

$$\phi''(x) - \mu^2 \phi(x) = 0 \qquad \text{(II-6)}$$

$\phi(x) = C_1 e^{\mu x} + C_2 e^{-\mu x}$ (II-7) is the general solution for Eq.(II-6)

where C_1 and C_2 are constants;

By applying boundary conditions

$$p(0,t) = \phi(0) g(t) = 0 \Rightarrow \phi(0) = 0 \Rightarrow \phi(0) = C_1 + C_2 = 0 \Rightarrow C_2 = -C_1 \qquad \text{(II-7)}$$

$$p'(L,t) = \phi'(L) g(t) = 0 \Rightarrow \phi'(L) = 0$$
$$\Rightarrow \phi'(L) = \mu C_1 (e^{\mu L} + e^{-\mu L}) = 0$$
$$\Rightarrow e^{2\mu L} = -1$$

If let $\mu = i\omega$ (ω is real) (II-8)

$$e^{i2\omega L} = \cos(2\omega L) + i \sin(2\omega L) = -1$$
$$\Rightarrow 2\omega L = (2n+1)\pi \qquad \text{(II-9)}$$
$$\Rightarrow \omega = \frac{(2n+1)\pi}{2L}$$

By taking Eq.(II-7)-(II-9) into Eq.(II-7), it yields

$$\phi(x) = C_1 e^{i\omega x} - C_1 e^{-i\omega x} = 2iC_1 \sin(\omega x) = 2iC_1 \sin(\frac{2n+1}{2L}\pi x) \qquad \text{(II-10)}$$

If let $\phi_n(x) = \sin(\frac{2n+1}{2L}\pi x)$ (II-11)

Then the following two equations can be obtained

$$\mu_n^2 = -\frac{(2n+1)^2 \pi^2}{4L^2} \qquad \text{(II-12)}$$

$$p_n(x,t) = \phi_n(x) g_n(t) \qquad \text{(II-13)}$$

By substituting Eq.(II-12) and (II-13) into Eq.(II-6), the general solution of $p_n(x,t)$ can be derived:

$$\frac{g_n'(t)}{g_n(t)} = C\frac{\phi_n''(x)}{\phi_n(x)} = C\mu^2 = -C\frac{(2n+1)^2\pi^2}{4L^2}$$
$$\Rightarrow g_n'(t) = -C\frac{(2n+1)^2\pi^2}{4L^2}g_n(t)$$
$$\Rightarrow g_n(t) = B*e^{-C\frac{(2n+1)^2\pi^2 t}{4L^2}} \qquad \text{(II-14)}$$
$$\Rightarrow p_n(x,t) = \sin(\frac{2n+1}{2L}\pi x)*e^{-C\frac{(2n+1)^2\pi^2 t}{4L^2}}$$

So the general product solutions to Eq.(II-4) is given as:

$$p(x,t) = \sum_{n=0}^{\infty} A_n \sin(\frac{2n+1}{2L}\pi x)*e^{-C\frac{(2n+1)^2\pi^2 t}{4L^2}} \qquad \text{(II-15)}$$

As $p(x,0) = \eta p^* / GS$ (II-16)

$$\Rightarrow p(x,0) = \sum_{n=0}^{\infty} A_n \sin(\frac{2n+1}{2L}\pi x) = \frac{\eta p^*}{GS}$$
$$\Rightarrow A_n = \frac{2}{L}\int_0^L \sin(\frac{2n+1}{2L}\pi x)*\frac{\eta p^*}{GS}dx = \frac{\eta p^*}{GS}\frac{2}{L}\int_0^L \sin(\frac{2n+1}{2L}\pi x)dx \qquad \text{(II-17)}$$
$$\Rightarrow A_n = \frac{\eta p^*}{GS}\frac{2}{L}\frac{2L}{(2n+1)\pi}[-\cos(\frac{2n+1}{2L}\pi x)\Big|_0^L] = \frac{\eta p^*}{GS}\frac{4}{(2n+1)\pi}$$

Then, the solution for the homogeneous diffusion equation (Eq.(II-4)) is

$$p(x,t) = \frac{\eta p^*}{GS}\sum_{n=0}^{\infty}\frac{4}{(2n+1)\pi}\sin(\frac{2n+1}{2L}\pi x)*e^{-C\frac{(2n+1)^2\pi^2 t}{4L^2}} \qquad \text{(II-18)}$$

Calculating displacement field

Let the displacement $u_x = u_x^u + \Delta u_x$ (II-19)

where Δu_x is the time-dependent incremental component; u_x^u is the initial undrained elastic displacement;

Under uniaxial strain condition $\sigma_{xx} = \frac{2G(1-\nu_u)}{1-2\nu_u}\varepsilon_{xx} - \alpha M\xi$ (II-20)

For Mode I loading: $\xi = 0$ under undrained condition, with $u_x = 0$ at x=L

$$p^* = -\frac{2G(1-\nu_u)}{1-2\nu_u}\varepsilon_{xx} = -\frac{2G(1-\nu_u)}{1-2\nu_u}\frac{\partial u_x^u}{\partial x}$$
$$\Rightarrow u_x^u = \int_x^L \frac{p^*(1-2\nu_u)}{2G(1-\nu_u)}dx = \frac{p^*(1-2\nu_u)}{2G(1-\nu_u)}(L-x) \quad \text{(II-21)}$$

From navier equation: $\frac{2G(1-\nu)}{1-2\nu}\frac{\partial^2 u_x}{\partial x^2} - \alpha\frac{\partial p}{\partial x} = 0$, we could get

$$\frac{\partial^2 u_x}{\partial x^2} = \frac{1-2\nu}{2G(1-\nu)}\alpha\frac{\partial p}{\partial x} \quad \text{(II-22)}$$

Replacing p in Eq.(II-22) by Eq.(II-18), the following expression is obtained

$$\frac{\partial^2 u_x}{\partial x^2} = \frac{1-2\nu}{2G(1-\nu)}\alpha\frac{\eta p^*}{GS}\sum_{n=0}^{\infty}\frac{4}{(2n+1)\pi}\frac{2n+1}{2L}\pi\cos(\frac{2n+1}{2L}\pi x) * e^{-C\frac{(2n+1)^2\pi^2 t}{4L^2}} \quad \text{(II-23)}$$

Let $\tau_n = e^{-C\frac{(2n+1)^2\pi^2 t}{4L^2}}$, above equation could be simplified to:

$$\frac{\partial^2 u_x}{\partial x^2} = \frac{p^*(\nu_u-\nu)}{2G(1-\nu)(1-\nu_u)}\sum_{n=0}^{\infty}\frac{2}{L}\cos(\frac{2n+1}{2L}\pi x)\tau_n \quad \text{(II-24)}$$

Let defining $M = \frac{p^*(\nu_u-\nu)}{2G(1-\nu)(1-\nu_u)}$ (II-25), Eq.(II-24) can be rewritten as

$$\frac{\partial^2 u_x}{\partial x^2} = M\sum_{n=0}^{\infty}\frac{2}{L}\cos(\frac{2n+1}{2L}\pi x)\tau_n \quad \text{(II-25)}$$

Integrating on both sides of Eq.(II-25) by x, it yields

$$\int_0^x \frac{\partial^2 u_x}{\partial x^2} dx = \int_0^x M \sum_{n=0}^{\infty} \frac{2}{L} \cos(\frac{2n+1}{2L}\pi x)\tau_n dx$$

$$\Rightarrow \frac{\partial u_x}{\partial x}\Big|_0^x = M \sum_{n=0}^{\infty} \frac{2}{L} \frac{2L}{(2n+1)\pi} [\sin(\frac{2n+1}{2L}\pi x)\Big|_0^x]\tau_n \qquad \text{(II-26)}$$

$$\Rightarrow \frac{\partial u_x}{\partial x} - \frac{\partial u_x}{\partial x}\Big|_{x=0} = M \sum_{n=0}^{\infty} \frac{4}{(2n+1)\pi} \sin(\frac{2n+1}{2L}\pi x)\tau_n$$

Let $\frac{\partial u_x}{\partial x}\Big|_{x=0} = Q$ (constant), the following equation is derived

$$\frac{\partial u_x}{\partial x} = M \sum_{n=0}^{\infty} \frac{4}{(2n+1)\pi} \sin(\frac{2n+1}{2L}\pi x)\tau_n + Q \qquad \text{(II-27)}$$

Again, integrating on both sides of Eq.(II-27) by x, one can get

$$\Rightarrow \int_x^L \frac{\partial u_x}{\partial x} dx = \int_x^L [M \sum_{n=0}^{\infty} \frac{4}{(2n+1)\pi} \sin(\frac{2n+1}{2L}\pi x)\tau_n + Q]dx$$

$$\Rightarrow \Delta u_x\Big|_x^L = M \sum_{n=0}^{\infty} \frac{4}{(2n+1)\pi} \frac{2L}{(2n+1)\pi} [-\cos(\frac{2n+1}{2L}\pi x)\Big|_x^L]\tau_n + Qx\Big|_x^L \qquad \text{(II-28)}$$

$$\Rightarrow -\Delta u_x = M \sum_{n=0}^{\infty} \frac{8L}{(2n+1)^2\pi^2} \cos(\frac{2n+1}{2L}\pi x)\tau_n + Q(L-x)$$

With boundary condition: t=0, $\tau_n = 1 \Rightarrow \Delta u_x = 0$ (II-29)

$$\Rightarrow Q(L-x) = -M \sum_{n=0}^{\infty} \frac{8L}{(2n+1)^2\pi^2} \cos(\frac{2n+1}{2L}\pi x)$$

$$\Rightarrow \Delta u_x = M \sum_{n=0}^{\infty} \frac{8L}{(2n+1)^2\pi^2} \cos(\frac{2n+1}{2L}\pi x)(1-\tau_n) \qquad \text{(II-30)}$$

$$\Rightarrow \Delta u_x = \frac{p^*(\nu_u - \nu)}{2G(1-\nu)(1-\nu_u)} \sum_{n=0}^{\infty} \frac{8L}{(2n+1)^2\pi^2} \cos(\frac{2n+1}{2L}\pi x)(1-e^{-C\frac{(2n+1)^2\pi^2 t}{4L^2}})$$

Thus, the total displacement is found

$$u_x = \frac{p^*(1-2\nu_u)}{2G(1-\nu_u)}(L-x) + \frac{p^*(\nu_u-\nu)}{2G(1-\nu)(1-\nu_u)}\sum_{n=0}^{\infty}\frac{8L}{(2n+1)^2\pi^2}\cos(\frac{2n+1}{2L}\pi x)(1-e^{-C\frac{(2n+1)^2\pi^2 t}{4L^2}})$$

(II-31)

The surface displacement is given as:

$$u^* = u_x(0,t) = \frac{p^*(1-2\nu_u)}{2G(1-\nu_u)}L + \frac{p^*(\nu_u-\nu)}{2G(1-\nu)(1-\nu_u)}\sum_{n=0}^{\infty}\frac{8L}{(2n+1)^2\pi^2}(1-e^{-C\frac{(2n+1)^2\pi^2 t}{4L^2}}) \qquad \text{(II-32)}$$

If let $\tau = \frac{Ct}{4L^2}$, $f(\tau) = \sum_{n=0}^{\infty}\frac{8}{(2n+1)^2\pi^2}(1-e^{-(2n+1)^2\pi^2\tau})$, the surface settlement is

$$u^* = \frac{p^*L(1-2\nu_u)}{2G(1-\nu_u)}[1 + \frac{\nu_u-\nu}{(1-\nu)(1-2\nu_u)}f(\tau)] \qquad \text{(II-33)}$$

Hydraulic consolidation(Mode II loading)

Homogeneous diffusion equation: $\frac{\partial p}{\partial t} - C\frac{\partial^2 p}{\partial x^2} = 0$ (II-34)

With boundary conditions: p=p* at x=0 and $\partial p / \partial x = 0$ at x=L,

Initial pore pressure p(x, 0) =0

First try to find a steady state solution p(x, t) =V(x)

Then the diffusion equation (Eq.(II-34)) becomes to

$$CV''(x) = 0 \Rightarrow V(x) = ax + b \quad \text{(II-35)}$$

Where a and b are both constants.

After applying boundary conditions, one can get

$$\begin{aligned} p(0,t) &= V(0) = b = p^* \\ p'(L,t) &= V'(L) = a = 0 \end{aligned} \quad \text{(II-36)}$$

Sbustituing Eq.(II-36) into Eq.(II-35), it yields

$$V(x) = p^* \quad \text{(II-37)}$$

If let $\hat{p}(x,t) = p(x,t) - V(x)$ (II-38)

Putting Eq.(37) and (38) into Eq.(34), we can get

$$\begin{aligned} &\frac{\partial \hat{p}(x,t)}{\partial t} = \frac{\partial p(x,t)}{\partial t} - \frac{\partial V(x)}{\partial t} = C\frac{\partial^2 p(x,t)}{\partial x^2} \\ &\frac{\partial^2 \hat{p}(x,t)}{\partial x^2} = \frac{\partial^2 p(x,t)}{\partial x^2} - \frac{\partial^2 V(x)}{\partial x^2} = \frac{\partial^2 p(x,t)}{\partial x^2} \\ &\Rightarrow \frac{\partial \hat{p}(x,t)}{\partial t} = C\frac{\partial^2 \hat{p}(x,t)}{\partial x^2} \end{aligned} \quad \text{(II-39)}$$

Then the boundary condition can be expressed as:

$$\begin{aligned}
&\hat{p}(0,t) = p(0,t) - V(0) = p^* - p^* = 0 \\
&\hat{p}'(L,t) = p'(L,t) - V'(L) = 0 - 0 = 0 \\
&\hat{p}(x,0) = p(x,0) - V(x) = 0 - p^* = -p^*
\end{aligned} \tag{II-40}$$

According to the B.C. (Eq.(II-40)), the general solution for $\hat{p}(x,t)$ (homogeneous part) should be the same as the solution we got in mode I loading:

$$\hat{p}(x,t) = \sum_{n=0}^{\infty} A_n \sin(\frac{2n+1}{2L}\pi x) * e^{-C\frac{(2n+1)^2\pi^2 t}{4L^2}} \tag{II-41}$$

As $\hat{p}(x,0) = -p^* \Rightarrow \sum_{n=0}^{\infty} A_n \sin(\frac{2n+1}{2L}\pi x) = -p^*$

$$\begin{aligned}
&\Rightarrow A_n = \frac{2}{L}\int_0^L (-p^*)\sin(\frac{2n+1}{2L}\pi x)dx = -p^*\frac{2}{L}\int_0^L \sin(\frac{2n+1}{2L}\pi x)dx \\
&\Rightarrow A_n = -p^*\frac{2}{L}\frac{2L}{(2n+1)\pi}[-\cos(\frac{2n+1}{2L}\pi x)\Big|_0^L] = -\frac{4p^*}{(2n+1)\pi}
\end{aligned} \tag{II-42}$$

By taking Eq.(II-42) into Eq.(II-41), the solution of pore pressure can be given by

$$\Rightarrow \hat{p}(x,t) = -p^*\sum_{n=0}^{\infty}\frac{4}{(2n+1)\pi}\sin(\frac{2n+1}{2L}\pi x) * e^{-C\frac{(2n+1)^2\pi^2 t}{4L^2}} \tag{II-43}$$

Combing Eq.(37), (38) and (43), the following expression is derived

$$\Rightarrow p(x,t) = \hat{p}(x,t) + V(x) = p^*[1 - \sum_{n=0}^{\infty}\frac{4}{(2n+1)\pi}\sin(\frac{2n+1}{2L}\pi x) * e^{-C\frac{(2n+1)^2\pi^2 t}{4L^2}}] \tag{II-44}$$

Calculating displacement

For Mode II loading: $u_x = 0$ at x=L and $u_x = 0$ at t=0

From navier equation: $\frac{2G(1-\nu)}{1-2\nu}\frac{\partial^2 u_x}{\partial x^2} - \alpha\frac{\partial p}{\partial x} = 0$ (II-45)

we could get $\frac{\partial^2 u_x}{\partial x^2} = \frac{1-2\nu}{2G(1-\nu)}\alpha\frac{\partial p}{\partial x}$ (II-46)

Replacing p in Eq.(II-46) by the solution of p (Eq.(II-44)) we calculated, one can get

$$\frac{\partial^2 u_x}{\partial x^2} = \frac{1-2\nu}{2G(1-\nu)}\alpha p^*[-\sum_{n=0}^{\infty}\frac{4}{(2n+1)\pi}\frac{2n+1}{2L}\pi\cos(\frac{2n+1}{2L}\pi x)*e^{-C\frac{(2n+1)^2\pi^2 t}{4L^2}}] \quad \text{(II-47)}$$

If let $\tau_n = e^{-C\frac{(2n+1)^2\pi^2 t}{4L^2}}$, Eq.(II-47) could be simplified to:

$$\frac{\partial^2 u_x}{\partial x^2} = \frac{p^*\eta}{G}[-\sum_{n=0}^{\infty}\frac{2}{L}\cos(\frac{2n+1}{2L}\pi x)\tau_n] \quad \text{(II-48)}$$

Integrating on both sides of Eq.(II-48) by x

$$\int_0^x \frac{\partial^2 u_x}{\partial x^2}dx = \int_0^x \frac{p^*\eta}{G}[-\sum_{n=0}^{\infty}\frac{2}{L}\cos(\frac{2n+1}{2L}\pi x)\tau_n]dx$$

$$\Rightarrow \frac{\partial u_x}{\partial x}\Big|_0^x = \frac{p^*\eta}{G}\{-\sum_{n=0}^{\infty}\frac{2}{L}\frac{2L}{(2n+1)\pi}[\sin(\frac{2n+1}{2L}\pi x)\Big|_0^x]\tau_n\} \quad \text{(II-49)}$$

$$\Rightarrow \frac{\partial u_x}{\partial x} - \frac{\partial u_x}{\partial x}\Big|_{x=0} = -\frac{p^*\eta}{G}\sum_{n=0}^{\infty}\frac{4}{(2n+1)\pi}\sin(\frac{2n+1}{2L}\pi x)\tau_n$$

If $\frac{\partial u_x}{\partial x}\Big|_{x=0} = Q$ (constant), Eq.(II-49) can be rewritten as

$$\Rightarrow \frac{\partial u_x}{\partial x} = -\frac{p^*\eta}{G}\sum_{n=0}^{\infty}\frac{4}{(2n+1)\pi}\sin(\frac{2n+1}{2L}\pi x)\tau_n + Q \quad \text{(II-50)}$$

Again, integrating on both sides of Eq.(II-50) by x

$$\Rightarrow \int_x^L \frac{\partial u_x}{\partial x}dx = \int_x^L [-\frac{p^*\eta}{G}\sum_{n=0}^{\infty}\frac{4}{(2n+1)\pi}\sin(\frac{2n+1}{2L}\pi x)\tau_n + Q]dx$$

$$\Rightarrow u_x\Big|_x^L = -\frac{p^*\eta}{G}\sum_{n=0}^{\infty}\frac{4}{(2n+1)\pi}\frac{2L}{(2n+1)\pi}[-\cos(\frac{2n+1}{2L}\pi x)\Big|_x^L]\tau_n + Qx\Big|_x^L$$

$$\Rightarrow -u_x = -\frac{p^*\eta}{G}\sum_{n=0}^{\infty}\frac{8L}{(2n+1)^2\pi^2}\cos(\frac{2n+1}{2L}\pi x)\tau_n + Q(L-x)$$

$$\Rightarrow u_x = \frac{p^*\eta}{G}\sum_{n=0}^{\infty}\frac{8L}{(2n+1)^2\pi^2}\cos(\frac{2n+1}{2L}\pi x)\tau_n - Q(L-x) \quad \text{(II-51)}$$

Apply B.C. at t=0, $\tau_n = 1 \Rightarrow u_x = 0$

$$\Rightarrow Q(L-x) = \frac{p^*\eta}{G}\sum_{n=0}^{\infty}\frac{8L}{(2n+1)^2\pi^2}\cos(\frac{2n+1}{2L}\pi x)$$

$$\Rightarrow u_x = \frac{p^*\eta}{G}\sum_{n=0}^{\infty}\frac{8L}{(2n+1)^2\pi^2}\cos(\frac{2n+1}{2L}\pi x)(\tau_n - 1)$$

$$\Rightarrow u_x = \frac{p^*\eta}{G}\sum_{n=0}^{\infty}\frac{8L}{(2n+1)^2\pi^2}\cos(\frac{2n+1}{2L}\pi x)(e^{-C\frac{(2n+1)^2\pi^2 t}{4L^2}} - 1) \quad \text{(II-52)}$$

Then, the surface displacement can be obtained

$$u^* = u_x(0,t) = \frac{p^*\eta}{G}\sum_{n=0}^{\infty}\frac{8L}{(2n+1)^2\pi^2}(e^{-C\frac{(2n+1)^2\pi^2 t}{4L^2}} - 1) \quad \text{(II-53)}$$

Let $\tau = \frac{Ct}{4L^2}$, $f(\tau) = \sum_{n=0}^{\infty}\frac{8}{(2n+1)^2\pi^2}(1 - e^{-(2n+1)^2\pi^2\tau})$ (II-54)

Eq.(II-53) can be stated as $u^* = -\frac{p^*\eta L}{G} f(\tau)$ (II-55)

APPENDIX III

POROSITY MODEL WITH DIFFERENT PHASES

The volumetric strain of the gas shale could be rewritten as:

$$\varepsilon_v = -\frac{1}{K}(\bar{\sigma} - \alpha p) \tag{III-1}$$

Governing equations for single phase flow:

Local continuity equation is developed by considering the mass conservation of gas content: $\frac{\partial m}{\partial t} + \nabla \cdot (\rho_f v) = \gamma$ (III-2)

where $v = \frac{q}{A}$ is the superficial velocity; ρ_f is the fluid density; γ denotes the source density (rate of injected gas content per unit volume of the porous medium); m represents remained fluid content within unit volume of medium:

$$m = \rho_f \phi \tag{III-3}$$

From Darcy's law: $q = -\frac{k_a A}{\mu} \nabla p$ (III-4)

where k_a stands for apparent Darcy permeability.

Substituting Eq.(III-3)-(III-4) into Eq.(III-2), it yields:

$$\frac{\partial}{\partial t}\left(\rho_f \phi\right) - \nabla \cdot (\rho_f \frac{k_a}{\mu} \nabla p) = \gamma \tag{III-5}$$

Porosity model:

For the initial condition, assuming $\varepsilon_{v0} = 0$. So, in the following discussion, we are dealing with the increments of all strain and stress components.

The volumetric response of the porous medium with respect to loading {P, p}could be expressed by the following relations (Detournay and Cheng, 1993):

$$\frac{\Delta V}{V} = -\frac{1}{K}(\dot{P} - \alpha \dot{p}) \tag{III-6}$$

$$\frac{\Delta V_p}{V_p} = -\frac{1}{K_p}(\dot{P} - \beta \dot{p}) \tag{III-7}$$

With the subscript p denoting pore space and $\beta = 1 - \frac{K_p}{K_s}$.

By applying Betti-Maxwell reciprocal theorem: $\frac{\partial V}{\partial p}\Big|_{\bar{\sigma}} = -\frac{\partial V_p}{\partial \bar{\sigma}}\Big|_p$ (III-8)

The following equation could be obtained: $K_p = \frac{\phi}{\alpha} K$ (III-9)

Applying the definition $V = V_p + V_s$ and $\phi = V_p / V$, the following equations could be readily developed (Detournay and Cheng, 1993)

$$\frac{\Delta V}{V} = \frac{\Delta V_s}{V_s} + \frac{\Delta \phi}{1 - \phi} \tag{III-10}$$

$$\frac{\Delta V_p}{V_p} = \frac{\Delta V_s}{V_s} + \frac{\Delta \phi}{\phi(1 - \phi)} \tag{III-11}$$

Combing Eq.(III-6)-(III-11), $\Delta\phi$ could be solved:

$$\Delta \phi = \phi(\frac{1}{K} - \frac{1}{K_p})(\dot{P} - \dot{p}) = \frac{\phi - \alpha}{K}(\dot{P} - \dot{p}) \tag{III-12}$$

Substituting Eq.(III-1) and (III-9) into Eq.(III-12), one can get:

$$\Delta \phi = (\alpha - \phi)(\dot{\varepsilon}_v + \frac{\dot{p}}{K_s}) \tag{III-13}$$

With the initial condition $\varepsilon_{v0} = 0 : \dot{\varepsilon}_v = \varepsilon_v - \varepsilon_{v0} = -\frac{1}{K}(\dot{\bar{\sigma}} - \alpha \dot{p})$ (III-14)

Then the following relation could be revealed: $\phi - \phi_0 = \Delta\phi$ (III-15)

Substituting Eq.(III-13) and (III-14) into Eq.(III-15), we can obtain:

$$\phi = \frac{1}{1 + S - S_0}[\phi_0 + \alpha(S - S_0)] \quad \text{(III-16)}$$

With $S = \varepsilon_v + \frac{p}{K_s}$ (III-17) and $S_0 = \frac{p_0}{K_s}$ (III-18)

(1) Slightly compressible fluid (as water)

By taking out the time derivation in the LHS of Eq.(III-5)

$$\left(\phi \frac{\partial \rho_f}{\partial p} + \rho_f \frac{\partial \phi}{\partial p}\right)\frac{\partial p}{\partial t} = \nabla \cdot (\rho_f \frac{k_a}{\mu} \nabla p) + \gamma \quad \text{(III-19)}$$

The change of fluid density with respect to pressure is expressed as:

$$\frac{\partial \rho_f}{\partial p} = \frac{\rho_f}{K_f} \quad \text{(III-20)}$$

The total volumetric deformation (ε_v) of the porous medium consists of the pore space change (ε_p) and the deformation of the solid porous matrix (ε_s). The deformation of the solid porous matrix is due to the fluid pressure and effective stress loading:

(i) the effect of fluid pressure (the compression stress or strain is negative)

$$\varepsilon_{s1} = -\frac{p}{K_s}(1 - \phi) \quad \text{(III-21)}$$

(ii) the effect of effective stress loading

$$\varepsilon_{s2} = -\frac{\sigma'_{kk}}{3K_s} \tag{III-22}$$

where K_s is the bulk modulus of the solid and ϕ is the porosity. The average effective stress ($\sigma'_{kk}/3$) has the following relation with the volumetric strain and pore pressure:

$$\frac{\sigma'_{kk}}{3} = \frac{\sigma'_{xx} + \sigma'_{yy} + \sigma'_{zz}}{3} = K\varepsilon_v + \frac{K}{K_s}p \tag{III-23}$$

where K ($K < K_s$) is the bulk modulus of the porous matrix. Combining Eqs. (III-21) and (III-22), and substituting Eq. (III-23) result in the deformation of the solid porous matrix: $\varepsilon_s = \frac{K}{K_s}\varepsilon_v + \frac{p}{K_s}\left[\frac{K}{K_s} - (1-\phi)\right]$ (III-24)

The pore space change is obtained by subtracting the deformation of the solid porous matrix from the total volumetric strain and using the definition of Biot's coefficient, α ($\alpha = 1 - K/K_s$): $\varepsilon_p = \alpha\varepsilon_v + (\alpha - \phi)\frac{p}{K_s}$ (III-25)

Then, the pore volume change with respect to pressure is expressed as:

$$\frac{\partial\phi}{\partial p} = \frac{\partial\varepsilon_p}{\partial p} = \alpha\frac{\partial\varepsilon_v}{\partial p} + \frac{\alpha - \phi}{K_s} \tag{III-26}$$

Substituting Eq.(III-20) and Eq.(III-26) into Eq.(III-19), one can get

$$\alpha\frac{\partial\varepsilon_v}{\partial t} + \left(\frac{\phi}{K_f} + \frac{\alpha - \phi}{K_s}\right)\frac{\partial p}{\partial t} = \nabla\cdot\left(\frac{k_a}{\mu}\nabla p\right) + \gamma \tag{III-27}$$

As $\frac{\phi}{K_f} + \frac{\alpha - \phi}{K_s} = \frac{1}{M}$ where M is the Biot modulus, Eq.(III-27) could be rewritten as:

$$\alpha \frac{\partial \varepsilon_v}{\partial t} + \frac{1}{M}\frac{\partial p}{\partial t} = \nabla \cdot (\frac{k_a}{\mu}\nabla p) + \gamma \tag{III-28}$$

This expression of fluid diffusivity eqation is compatible with Diek and Ghassemi's work (2004) and Detournay and Cheng (1993).

(2) Gas flow (only free gas)

Real gas density could be expressed as: $\rho_g = \frac{pM_g}{ZRT}$ (III-29)

Replacing ρ_g in Eq.(III-5) by Eq.(III-30), it yields

$$\frac{\partial}{\partial t}\left(\frac{p\phi}{Z}\right) = \nabla \cdot (k_a \frac{p}{\mu Z}\nabla p) + \gamma \frac{RT}{M_g} \tag{III-30}$$

Expanding the term on the LHS of Eq.(III-30)

$$\begin{aligned}\frac{\partial}{\partial t}\left(\frac{p\phi}{Z}\right) &= \phi \frac{\partial}{\partial t}\left(\frac{p}{Z}\right) + \frac{p}{Z}\frac{\partial \phi}{\partial t} \\ &= \phi \frac{p}{Z}\left(\frac{1}{p/Z}\frac{\partial}{\partial t}\left(\frac{p}{Z}\right) + \frac{1}{\phi}\frac{\partial \phi}{\partial t}\right) \\ &= \phi \frac{p}{Z}\left(\frac{1}{p/Z}\frac{\partial}{\partial p}\left(\frac{p}{Z}\right) + \frac{1}{\phi}\frac{\partial \phi}{\partial p}\right)\frac{\partial p}{\partial t}\end{aligned} \tag{III-31}$$

The change of gas density with respect to pressure is expressed as:

$$\frac{1}{p/Z}\frac{\partial}{\partial p}\left(\frac{p}{Z}\right) = \frac{1}{\rho_g}\frac{d\rho_g}{\partial p} = C_g = \frac{1}{K_g} \tag{III-32}$$

where C_g is the gas compressibility ; the inverse of the gas compressibility gives gas bulk modulus K_g

And the pore volume change with respect to pressure is expressed the same as Eq. (III-26):

$$\frac{\partial \phi}{\partial p} = \frac{\partial \varepsilon_p}{\partial p} = \alpha \frac{\partial \varepsilon_v}{\partial p} + \frac{\alpha - \phi}{K_s} \tag{III-33}$$

Substituting Eq.(III-32) and (III-33) into Eq.(III-31), one can get:

$$\frac{\partial}{\partial t}\left(\frac{p\phi}{Z}\right) = \frac{p}{Z}\left(\frac{\phi}{K_g} + \alpha \frac{\partial \varepsilon_v}{\partial p} + \frac{\alpha - \phi}{K_s}\right)\frac{\partial p}{\partial t} \tag{III-34}$$

As $\frac{\phi}{K_g} + \frac{\alpha - \phi}{K_s} = \frac{1}{M}$ where M is the Biot modulus, Eq.(III-34) could be rewritten as:

$$\frac{\partial}{\partial t}\left(\frac{p\phi}{Z}\right) = \frac{p}{Z}\left(\frac{1}{M} + \alpha \frac{\partial \varepsilon_v}{\partial p}\right)\frac{\partial p}{\partial t} \tag{III-35}$$

Substituting Eq.(III-35) into Eq.(III-30), yields:

$$\frac{p}{Z}\left(\frac{1}{M} + \alpha \frac{\partial \varepsilon_v}{\partial p}\right)\frac{\partial p}{\partial t} = \nabla \cdot (k_a \frac{p}{\mu Z} \nabla p) + \gamma \frac{RT}{M_g} \tag{III-36}$$

As the gas properties are not constant with pressure change, the pseudo-pressure is introduced: $m(p) = 2\int_{p_1}^{p_2} \frac{p}{\mu Z} dp$ (III-37)

By applying Liebnitz's rule to differentiate the above integral, we obtain:

$$\frac{\partial m(p)}{\partial x} = 2 \frac{p}{\mu Z} \frac{\partial p}{\partial x} \tag{III-38}$$

And $$\frac{\partial m(p)}{\partial t} = 2 \frac{p}{\mu Z} \frac{\partial p}{\partial t} \tag{III-39}$$

Substituting Eq.(III-38) and (III-39) into Eq.(III-36):

$$\left(\frac{1}{M} + \alpha \frac{\partial \varepsilon_v}{\frac{\mu Z}{2p}\partial m(p)}\right)\frac{p}{Z}\frac{\mu Z}{2p}\frac{\partial m(p)}{\partial t} = \nabla \cdot (k_a \frac{p}{\mu Z}\frac{\mu Z}{2p}(\nabla m(p))) + \gamma \frac{RT}{M_g} \tag{III-40}$$

Assuming constant k_a, finally one can get:

$$\left(\frac{1}{M}+\alpha\frac{2p}{\mu Z}\frac{\partial\varepsilon_v}{\partial m(p)}\right)\frac{\partial m(p)}{\partial t}=\frac{k_a}{\mu}\nabla^2 m(p)+\gamma\frac{2RT}{\mu M_g} \tag{III-41}$$

It could be expressed as:

$$\alpha\frac{2p}{\mu Z}\frac{\partial\varepsilon_v}{\partial t}+\frac{1}{M}\frac{\partial m(p)}{\partial t}=\frac{k_a}{\mu}\nabla^2 m(p)+\gamma\frac{2RT}{\mu M_g} \tag{III-42}$$

(3) Gas flow (free gas + desorption gas)

The volumetric strain of the gas (free gas and desorption gas) could be rewritten as:

$$\varepsilon_v=-\frac{1}{K}(\bar{\sigma}-\alpha p)+\varepsilon_s \tag{III-43}$$

where ε_s is defined as gas sorption-induced strain

Governing equations for gas flow:

Local continuity equation is developed by considering the mass conservation of gas content: $\frac{\partial m}{\partial t}+\nabla\cdot(\rho_g v)=\gamma$ (III-44)

where $v=\frac{q}{A}$ is the superficial velocity; ρ_g is the gas density; γ denotes the source density (rate of injected gas content per unit volume of the porous medium); m represents remained gas content within unit volume of medium, including both free and absorbed gas (Saghafi et al., 2007):

$$m=\rho_g\phi+\rho_g\rho_r\frac{V_L p}{p+P_L} \tag{III-45}$$

where ρ_{sc} denotes gas density at standard condition; ρ_r is the density of gas shale; V_L and P_L represent Langmuir volume and pressure constant respectively.

Real gas density could be expressed as: $\rho_g = \frac{pM_g}{ZRT}$ (III-46)

where M_g is the gas molecular mass; Z is the compressibility factor with $Z_{sc} \approx 1$.

Then $\rho_{sc} = \frac{p_{sc} M_g}{RT_{sc}}$ (III-47)

With p_{sc} and T_{sc} denoting the pressure and temperature under standard condition.

From Darcy's law: $q = -\frac{k_a A}{\mu} \nabla p$ (III-48)

where k_a stands for apparent gas permeability.

Substituting Eq.(III-45)-(III-48) into Eq.(III-44), it yields:

$$\frac{\partial}{\partial t}\left(\frac{p\phi}{Z}\right) + \frac{\partial}{\partial t}\left(\frac{p}{Z}\rho_r \frac{V_L p}{p+P_L}\right) = \nabla \cdot (k_a \frac{p}{\mu Z} \nabla p) + \gamma \frac{RT}{M_g} \quad \text{(III-49)}$$

Porosity model:

For the initial condition, assuming $\varepsilon_{v0} = 0$. So, in the following discussion, we are dealing with the increments of all strain and stress components.

The volumetric response of the porous medium with respect to loading {P, p}could be expressed by the following relations (Detournay and Cheng, 1993)

$$\frac{\Delta V}{V} = -\frac{1}{K}(\dot{P} - \alpha \dot{p}) \quad \text{(III-50)}$$

$$\frac{\Delta V_p}{V_p} = -\frac{1}{K_p}(\dot{P} - \beta \dot{p}) \quad \text{(III-51)}$$

With the subscript p denoting pore space and $\beta = 1 - \frac{K_p}{K_s}$.

Recalling Eq.(III-43), a similar expression could be stated in this case study:

$$\frac{\Delta V}{V} = -\frac{1}{K}(\dot{\bar{\sigma}} - \alpha \dot{p}) + \dot{\varepsilon}_s \tag{III-52}$$

If we assume that sorption-induced strain projects the same effect on bulk rock and pore space, another relation for pore space could be proposed:

$$\frac{\Delta V_p}{V_p} = -\frac{1}{K_p}(\dot{\bar{\sigma}} - \beta \dot{p}) + \dot{\varepsilon}_s \tag{III-53}$$

By applying Betti-Maxwell reciprocal theorem: $\frac{\partial V}{\partial p}\Big|_{\bar{\sigma}} = -\frac{\partial V_p}{\partial \bar{\sigma}}\Big|_p$ (III-54)

The following equation could be obtained: $K_p = \frac{\phi}{\alpha} K$ (III-55)

Applying the definition $V = V_p + V_s$ and $\phi = V_p / V$, the following equations could be readily developed (Detournay and Cheng, 1993):

$$\frac{\Delta V}{V} = \frac{\Delta V_s}{V_s} + \frac{\Delta \phi}{1 - \phi} \tag{III-56}$$

$$\frac{\Delta V_p}{V_p} = \frac{\Delta V_s}{V_s} + \frac{\Delta \phi}{\phi(1 - \phi)} \tag{III-57}$$

Combing Eq.(III-52)-(III-57), $\Delta\phi$ could be solved:

$$\Delta \phi = \phi(\frac{1}{K} - \frac{1}{K_p})(\dot{\bar{\sigma}} - \dot{p}) \tag{III-58}$$

Substituting Eq.(III-43) and (III-55) into Eq.(III-58), one can get:

$$\Delta\phi = (\alpha - \phi)(\dot{\varepsilon}_v - \dot{\varepsilon}_s + \frac{\dot{p}}{K_s}) \quad \text{(III-59)}$$

ε_s is defined as gas sorption-induced strain. A Langmuir type equation is developed to compute ε_s (Zhang et al., 2008)

$$\varepsilon_s = \varepsilon_L \frac{p}{P_L + p} \quad \text{(III-60)}$$

where ε_L is the Langmuir volumetric strain, which denotes the maximum volumetric strain that could be induced to the bulk rock as fully saturated with gas (Shi and Durucan, 2004).

With the initial condition $\varepsilon_{v0} = 0 : \dot{\varepsilon}_v = \varepsilon_v - \varepsilon_{v0} = -\frac{1}{K}(\dot{\bar{\sigma}} - \alpha \dot{p}) + \dot{\varepsilon}_s$ (III-61)

Then the following relation could be revealed: $\phi - \phi_0 = \Delta\phi$ (III-62)

Substituting Eq.(III-59) and (III-61) into Eq.(III-62), we can obtain:

$$\phi = \frac{1}{1 + S - S_0}[\phi_0 + \alpha(S - S_0)] \quad \text{(III-63)}$$

with $S = \varepsilon_v - \varepsilon_s + \frac{p}{K_s}$ (III-64) and $S_0 = \frac{p_0}{K_s} - \varepsilon_{s0} = \frac{p_0}{K_s} - \varepsilon_L \frac{p_0}{P_L + p_0}$ (III-65)

The total volumetric deformation (ε_v) of the porous medium consists of the pore space change (ε_p), the deformation of the solid porous matrix (ε_{sm}) and gas sorption-induced strain (ε_s). The deformation of the solid porous matrix is due to the fluid pressure and effective stress loading:

(iii) the effect of fluid pressure (the compression stress or strain is negative)

$$\varepsilon_{sm1} = -\frac{p}{K_s}(1-\phi) \tag{III-64}$$

(iv) the effect of effective stress loading

$$e_{sm2} = \frac{\sigma'_{kk}}{3K_s} \tag{III-65}$$

where K_s is the bulk modulus of the solid and ϕ is the porosity. The average effective stress ($\sigma'_{kk}/3$) has the following relation with the volumetric strain and pore pressure:

$$\frac{\sigma'_{kk}}{3} = \frac{\sigma'_{xx}+\sigma'_{yy}+\sigma'_{zz}}{3} = K(\varepsilon_v - \varepsilon_s) + \frac{K}{K_s}p \tag{III-66}$$

where K ($K < K_s$) is the bulk modulus of the porous matrix. Combining Eqs. (III-64) and (III-65), and substituting Eq. (III-66) result in the deformation of the solid porous matrix:

$$\varepsilon_{sm} = \frac{K}{K_s}(\varepsilon_v - \varepsilon_s) + \frac{p}{K_s}\left[\frac{K}{K_s} - (1-\phi)\right] \tag{III-67}$$

The pore space change is obtained by subtracting the deformation of the solid porous matrix from the total volumetric strain and using the definition of Biot's coefficient, α, ($\alpha = 1 - K/K_s$):

$$\varepsilon_p = \alpha(\varepsilon_v - \varepsilon_s) + (\alpha - \phi)\frac{p}{K_s} \tag{III-68}$$

Expanding the first term on the LHS of Eq.(III-49)

$$\begin{aligned}\frac{\partial}{\partial t}\left(\frac{p\phi}{Z}\right) &= \phi\frac{\partial}{\partial t}\left(\frac{p}{Z}\right) + \frac{p}{Z}\frac{\partial\phi}{\partial t} \\ &= \phi\frac{p}{Z}\left(\frac{1}{p/Z}\frac{\partial}{\partial t}\left(\frac{p}{Z}\right) + \frac{1}{\phi}\frac{\partial\phi}{\partial t}\right) \\ &= \phi\frac{p}{Z}\left(\frac{1}{p/Z}\frac{\partial}{\partial p}\left(\frac{p}{Z}\right) + \frac{1}{\phi}\frac{\partial\phi}{\partial p}\right)\frac{\partial p}{\partial t}\end{aligned} \tag{III-69}$$

The change of gas density with respect to pressure is expressed as:

$$\frac{1}{p/Z}\frac{\partial}{\partial p}\left(\frac{p}{Z}\right)=\frac{1}{\rho_g}\frac{d\rho_g}{\partial p}=C_g=\frac{1}{K_g} \tag{III-70}$$

where C_g is the gas compressibility ; the inverse of the gas compressibility gives gas bulk modulus K_g

By taking Eq.(III-68), the pore volume change with respect to pressure is given as:

$$\frac{\partial\phi}{\partial p}=\frac{\partial\varepsilon_p}{\partial p}=\alpha\left(\frac{\partial\varepsilon_v}{\partial p}-\frac{\partial\varepsilon_s}{\partial p}\right)+\frac{\alpha-\phi}{K_s} \tag{III-71}$$

Substituting Eq.(III-70) and (III-71) into Eq.(III-69) and replacing ε_s by Eq.(III-60), it yields:

$$\frac{\partial}{\partial t}\left(\frac{p\phi}{Z}\right)=\frac{p}{Z}\left(\frac{\phi}{K_g}+\alpha\left(\frac{\partial\varepsilon_v}{\partial p}-\frac{\varepsilon_L P_L}{(P_L+p)^2}\right)+\frac{\alpha-\phi}{K_s}\right)\frac{\partial p}{\partial t} \tag{III-72}$$

As $\frac{\phi}{K_g}+\frac{\alpha-\phi}{K_s}=\frac{1}{M}$ where M is the Biot modulus, Eq.(III-72) could be rewritten as:

$$\frac{\partial}{\partial t}\left(\frac{p\phi}{Z}\right)=\frac{p}{Z}\left(\frac{1}{M}+\alpha\frac{\partial\varepsilon_v}{\partial p}-\alpha\frac{\varepsilon_L P_L}{(P_L+p)^2}\right)\frac{\partial p}{\partial t} \tag{III-73}$$

B_g is the gas formation volume factor with the definition as:

$$B_g=\frac{V}{V_{sc}}=\frac{p_{sc}}{p}\frac{T}{T_{sc}}\frac{Z}{Z_{sc}}$$

where Z is the compressibility factor with $Z_{sc}\approx 1$.

Then, $p_{sc}=B_g\frac{p}{Z}\frac{T_{sc}}{T}$ (III-74)

Substituting Eq.(III-74) into the second term on the LHS of Eq.(III-49)

$$\frac{p_{sc}\rho_r V_L P_L}{(p+P_L)^2}\frac{T}{T_{sc}}\frac{\partial p}{\partial t}=\frac{B_g\rho_r V_L P_L}{(p+P_L)^2}\frac{p}{Z}\frac{\partial p}{\partial t} \tag{III-75}$$

Substituting Eq.(III-73) and (III-75) into Eq.(III-49), one can get:

$$\frac{p}{Z}\left(\frac{1}{M}+\alpha\frac{\partial\varepsilon_v}{\partial p}-\alpha\frac{\varepsilon_L P_L}{(P_L+p)^2}\right)\frac{\partial p}{\partial t}+\frac{B_g\rho_r V_L P_L}{(p+P_L)^2}\frac{p}{Z}\frac{\partial p}{\partial t}=\nabla\cdot(k_a\frac{p}{\mu Z}\nabla p)+\gamma\frac{RT}{M_g} \tag{III-76}$$

As the gas properties are not constant with pressure change, the pseudo-pressure is introduced: $m(p)=2\int_{p_1}^{p_2}\frac{p}{\mu Z}dp$ (III-77)

By applying Liebnitz's rule to differentiate the above integral, we obtain:

$$\frac{\partial m(p)}{\partial x}=2\frac{p}{\mu Z}\frac{\partial p}{\partial x} \tag{III-78}$$

And $$\frac{\partial m(p)}{\partial t}=2\frac{p}{\mu Z}\frac{\partial p}{\partial t} \tag{III-79}$$

Substituting Eq.(III-78) and (III-79) into Eq.(III-76):

$$\left(\frac{1}{M}-\alpha\frac{\varepsilon_L P_L}{(P_L+p)^2}+\alpha\frac{\partial\varepsilon_v}{\frac{\mu Z}{2p}\partial m(p)}\right)\frac{p}{Z}\frac{\mu Z}{2p}\frac{\partial m(p)}{\partial t}+\frac{B_g\rho_r V_L P_L}{(p+P_L)^2}\frac{p}{Z}\frac{\mu Z}{2p}\frac{\partial m(p)}{\partial t}$$
$$=\nabla\cdot(k_a\frac{p}{\mu Z}\frac{\mu Z}{2p}(\nabla m(p)))+\gamma\frac{RT}{M_g} \tag{III-80}$$

Assuming constant k_a, finally one can get:

$$\alpha\frac{2p}{\mu Z}\frac{\partial\varepsilon_v}{\partial t}+\left(\frac{1}{M}+\frac{\left(B_g\rho_r V_L-\alpha\varepsilon_L\right)P_L}{(p+P_L)^2}\right)\frac{\partial m(p)}{\partial t}=\frac{k_a}{\mu}\nabla^2 m(p)+\gamma\frac{2RT}{\mu M_g} \tag{III-81}$$

APPENDIX IV

PVT GAS PROPERTIES

Z-factor

The real gas equation of state, which is commonly used in industry, is defined as following: $PV = ZnRT$ (IV-1)

where P = pressure; V =volume; T =temperature; n =the number of moles; R =the universal gas constant, whose value is depend on the above unites; Z is called the Z-factor or compressibility factor, which is dimensionless.

The Z-factor is applied to correct the ideal gas law, especially the pressure, to fit the real gas behavior. The Z-factor is a function of both pressure and temperature. However, it only varies with pressure in reservoir engineering, as reservoir temperature is almost constant and merely changes during production.

There are several experimental and numerical ways to determine the Z-factor. Among them, Standing-Katz correlation is widely accepted and used with confidence in industry, which correlates the Z-factor to pseudo-reduced pressure P_{pr} and temperature T_{pr} (Standing and Katz, 1942).

Prior to use the Standing-Katz correlation, the pseudo critical pressure P_{pc} and temperature T_{pc} of gas mixture should be calculated by applying the Kay's rules (Kay, 1936): $P_{pc} = \sum y_j P_{cj}$ $T_{pc} = \sum y_j T_{cj}$ (IV-2)

where P_{cj} and T_{cj} are the critical pressure and temperature of j^{th} component respectively; y_j is the mole fraction of corresponding component. Then, the pseudo-reduced pressure P_{pr} and temperature T_{pr} could be determined:

$$P_{pr} = P / P_{pc} \qquad T_{pr} = T / T_{pc} \qquad \text{(IV-3)}$$

where P and T are reservoir pressure and temperature.

With these two terms (P_{pr} and T_{pr}), the Z-factor could be readily read from the Standing-Katz correlation chart.

Though the Standing-Katz correlation is proved to be reliable by the industry over years, some computer solutions for calculating the Z-factor are developed in gas reservoir engineering programs. A number of different methods for reproducing the Z-factor chart had been reviewed and compared by Takacs (1976). Based on his work, the Dranchuk and Abou-Kassem method, which utilizes equation of state of 11 factors to compute Z-factors, is the most accurate. Its absolute error is only as low as 0.316% (Dranchuk and Kassem, 1975). A computer-based procedure is constructed to reproduce the Standing-Katz Z-factor chart by using the Dranchuk and Abou-Kassem equation and then incorporated into the FEM numerical simulator.

The Dranchuk and Abou-Kassem equation is shown as below:

$$Z = 1 + \left(A_1 + \frac{A_2}{T_{pr}} + \frac{A_3}{T_{pr}^3} + \frac{A_4}{T_{pr}^4} + \frac{A_5}{T_{pr}^5} \right) \rho_{pr} + \left(A_6 + \frac{A_7}{T_{pr}} + \frac{A_8}{T_{pr}^2} \right) \rho_{pr}^2 - A_9 \left(\frac{A_7}{T_{pr}} + \frac{A_8}{T_{pr}^2} \right) \rho_{pr}^5 + A_{10} \left(1 + A_{11} \rho_{pr}^2 \right) \frac{\rho_{pr}^2}{T_{pr}^3} \exp\left(-A_{11} \rho_{pr}^2 \right) \quad \text{(IV-4)}$$

where $\rho_{pr} = \dfrac{0.27 P_{pr}}{Z T_{pr}}$ (IV-5)

The constants are given as follows:

$A_1 = 0.3265$, $A_2 = -1.0700$, $A_3 = -0.5339$, $A_4 = 0.01569$, $A_5 = -0.05165$, $A_6 = 0.5475$, $A_7 = -0.7361$, $A_8 = 0.1844$, $A_9 = 0.1056$, $A_{10} = 0.6134$, $A_{11} = 0.7210$.

By expressing Z as a function of reduced density ρ_{pr} from Eq. (IV-5) and then substituting it in Eq. (IV-4), the following non-linear equation could be obtained:

$$1 + \left(A_1 + \frac{A_2}{T_{pr}} + \frac{A_3}{T_{pr}^3} + \frac{A_4}{T_{pr}^4} + \frac{A_5}{T_{pr}^5} \right) \rho_{pr} + \left(A_6 + \frac{A_7}{T_{pr}} + \frac{A_8}{T_{pr}^2} \right) \rho_{pr}^2 - A_9 \left(\frac{A_7}{T_{pr}} + \frac{A_8}{T_{pr}^2} \right) \rho_{pr}^5 + A_{10} \left(1 + A_{11} \rho_{pr}^2 \right) \frac{\rho_{pr}^2}{T_{pr}^3} \exp\left(-A_{11} \rho_{pr}^2 \right) - \frac{0.27 P_{pr}}{\rho_{pr} T_{pr}} = 0 \quad \text{(IV-6)}$$

For simple, this equation can be rewritten as: $f(\rho_{pr}) = 0$ (IV-7)

It can be readily solved for ρ_{pr} by using the Newton-Raphson iterative method. The detailed working steps are listed below:

1) make an initial guess of ρ_{pr}^i, as $\rho_{pr}^1 = 0.1$, where i is the number of iteration;

2) replace this value in Eq. (IV-6); some non-zero value $f^i(\rho_{pr}^i)$ will be generated unless the correct ρ_{pr}^i has been selected in step (1);

3) updated estimate of ρ_{pr} could be determined as:

$$\rho_{pr}^{i+1} = \rho_{pr}^i - f^i \Big/ \frac{df^i}{d\rho_{pr}} \tag{IV-8}$$

where $\frac{df}{d\rho_{pr}}$ is expressed as the derivative of Eq. (IV-6)

$$\frac{df}{d\rho_{pr}} = \left(A_1 + \frac{A_2}{T_{pr}} + \frac{A_3}{T_{pr}^3} + \frac{A_4}{T_{pr}^4} + \frac{A_5}{T_{pr}^5} \right) + 2\left(A_6 + \frac{A_7}{T_{pr}} + \frac{A_8}{T_{pr}^2} \right)\rho_{pr} - 5A_9\left(\frac{A_7}{T_{pr}} + \frac{A_8}{T_{pr}^2} \right)\rho_{pr}^4 + \left(\frac{2A_{10}\rho_{pr}}{T_{pr}^3} + \frac{2A_{10}A_{11}\rho_{pr}^3}{T_{pr}^3} - \frac{2A_{10}A_{11}^2\rho_{pr}^5}{T_{pr}^3} \right)\exp\left(-A_{11}\rho_{pr}^2\right) + \frac{0.27P_{pr}}{\rho_{pr}^2 T_{pr}} \tag{IV-9}$$

4) repeat the step(2) and (3) until the convergence condition is satisfied, as $\left|\rho_{pr}^{i+1} - \rho_{pr}^i\right| \le 0.001$;

5) Finally, the Z-factor can be resulted by substituting the computed value of ρ_{pr} in Eq. (IV-5).

This method is applicable over the ranges (Cox, 1988):

$$0.20 \le P_{pr} \le 30. \qquad \text{and} \qquad 1.0 \le T_{pr} \le 3.0 \tag{IV-10}$$

A FORTRAN subroutine calcGAS is written based on this procedure. Each time we need to input the Tpr(pseudo-reduced temperature) to computer each isotherm of Z-factor.

As shown in the diagram below (Figure 68), the Z-factor first decreases and then increases with increasing Ppr along each isothermal. A linear relationship with positive slope is established between the Z-factor and Ppr on each isothermal, if the pseudo-reduced pressure is higher enough, as greater than 5. However, the slope of this linear relationship gradually reduces with increasing pseudo-reduced temperature. Our numerical result is highly compatible with the origin Standing-Katz correlation chart, but one thing need to be pointed out that the Z value for Ppr=0.2 is always negative. I think this is related to the current convergence condition which we specified in the iteration process. If we try to improve the accuracy of our results, we need to sacrifice the computation time by orders. Another important issue is that this procedure is invalid for HPHT reservoir.

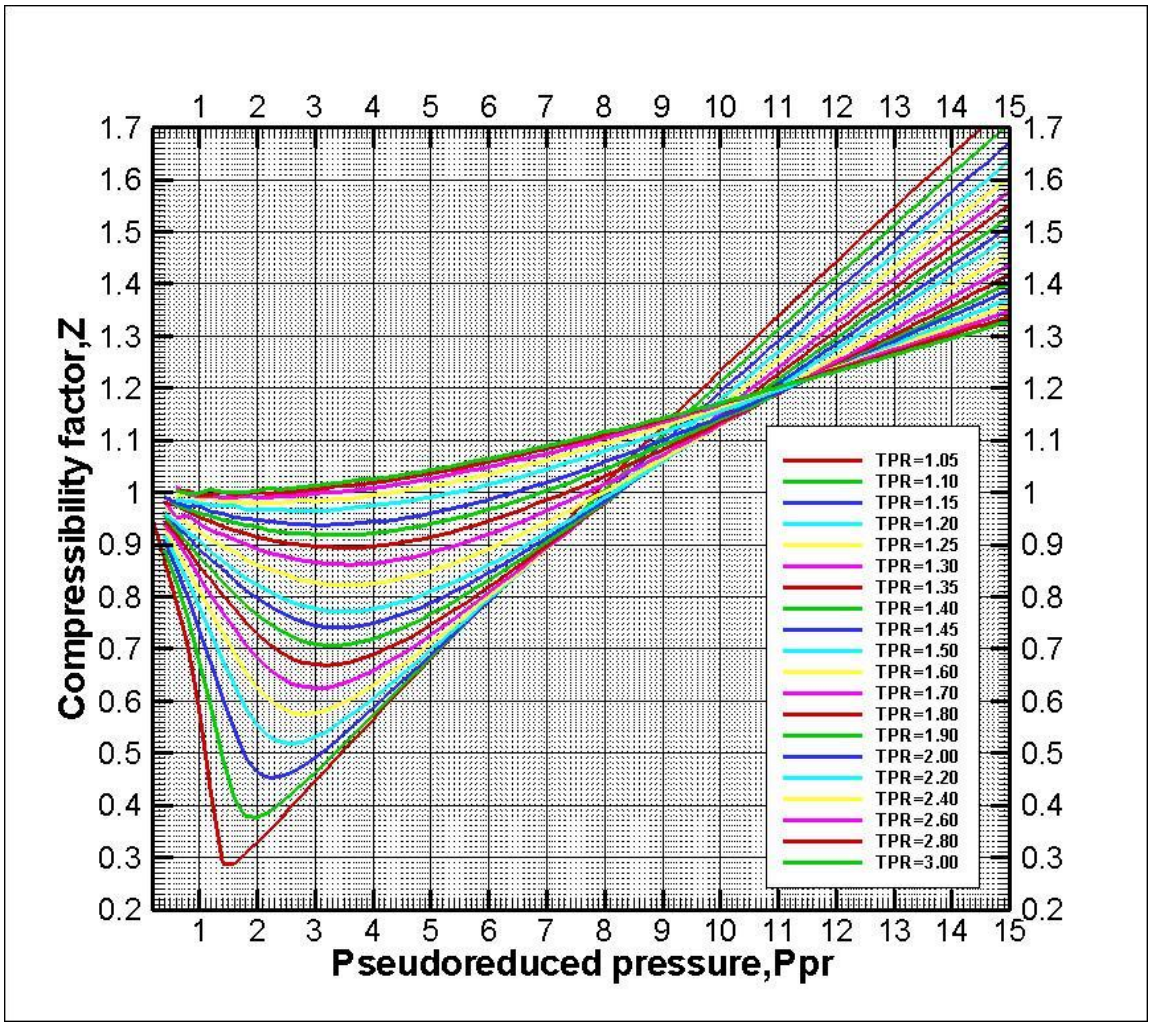

Figure 69 Reproduce Standing-Katz correlation chart for pure methane by applying subroutine calcZ

Isothermal compressibility

The coefficient of isothermal compressibility of gas c_g (gas compressibility) is defined as: $c_g = -\frac{1}{V}\left(\frac{\partial V}{\partial P}\right)_T$ (IV-11)

According to the real gas equation (IV-1), the coefficient of isothermal compressibility could be expressed as: $c_g = \frac{1}{P} - \frac{1}{Z}\left(\frac{\partial Z}{\partial P}\right)_T$ (IV-12)

Pseudo-reduced compressibility is introduced by Trube (1957) $c_g = \frac{c_{pr}}{P_{pc}}$ (IV-13)

Then, by combing Eq. (IV-12) and (IV-13), the dimensionless c_{pr} could be defined as:

$$c_{pr} = c_g P_{pc} = \frac{1}{P_{pr}} - \frac{1}{Z}\left(\frac{\partial Z}{\partial P_{pr}}\right)_{T_{pr}} \quad \text{(IV-14)}$$

The expression of Z-factor could be obtained from Eq. (IV-5)

$$Z = \frac{0.27 P_{pr}}{\rho_{pr} T_{pr}} \quad \text{(IV-15)}$$

By differentiating Eq.(IV-15), $\left(\frac{\partial Z}{\partial P_{pr}}\right)_{T_{pr}} = \frac{0.27\left(\frac{\partial Z}{\partial \rho_{pr}}\right)_{T_{pr}}}{Z T_{pr} + \rho_{pr} T_{pr}\left(\frac{\partial Z}{\partial \rho_{pr}}\right)_{T_{pr}}}$ (IV-16)

Substituting $\left(\frac{\partial Z}{\partial P_{pr}}\right)_{T_{pr}}$ in Eq. (IV-14) by Eq. (IV-16), an expression for dimensionless c_{pr} could be obtained as:

$$c_{pr} = \frac{1}{p_{pr}} - \frac{0.27}{Z T_{pr}}\left(\frac{\left(\frac{\partial Z}{\partial \rho_{pr}}\right)_{T_{pr}}}{Z + \rho_{pr}\left(\frac{\partial Z}{\partial \rho_{pr}}\right)_{T_{pr}}}\right) \quad \text{(IV-17)}$$

By running subroutine calcZ, Z and ρ_{pr} could be computed. By differentiating Eq. (IV-4) on both sides, term $\left(\frac{\partial Z}{\partial \rho_{pr}}\right)_{T_{pr}}$ could also be evaluated:

$$\left(\frac{\partial Z}{\partial \rho_{pr}}\right)_{T_{pr}} = \left(A_1 + \frac{A_2}{T_{pr}} + \frac{A_3}{T_{pr}^3} + \frac{A_4}{T_{pr}^4} + \frac{A_5}{T_{pr}^5}\right) + 2\left(A_6 + \frac{A_7}{T_{pr}} + \frac{A_8}{T_{pr}^2}\right)\rho_{pr} - 5A_9\left(\frac{A_7}{T_{pr}} + \frac{A_8}{T_{pr}^2}\right)\rho_{pr}^4 + \left(\frac{2A_{10}\rho_{pr}}{T_{pr}^3} + \frac{2A_{10}A_{11}\rho_{pr}^3}{T_{pr}^3} - \frac{2A_{10}A_{11}^2\rho_{pr}^5}{T_{pr}^3}\right)\exp\left(-A_{11}\rho_{pr}^2\right) \quad \text{(IV-18)}$$

Then, the dimensionless c_{pr} can be calculated. Henceforth, coefficient of isothermal compressibility of gas c_g can be determined from Eq.(IV-13). Our numerical results (Figure 69) are quite close to some numerical simulation results in literature (Trube, 1957; Ghedan et al., 1993).

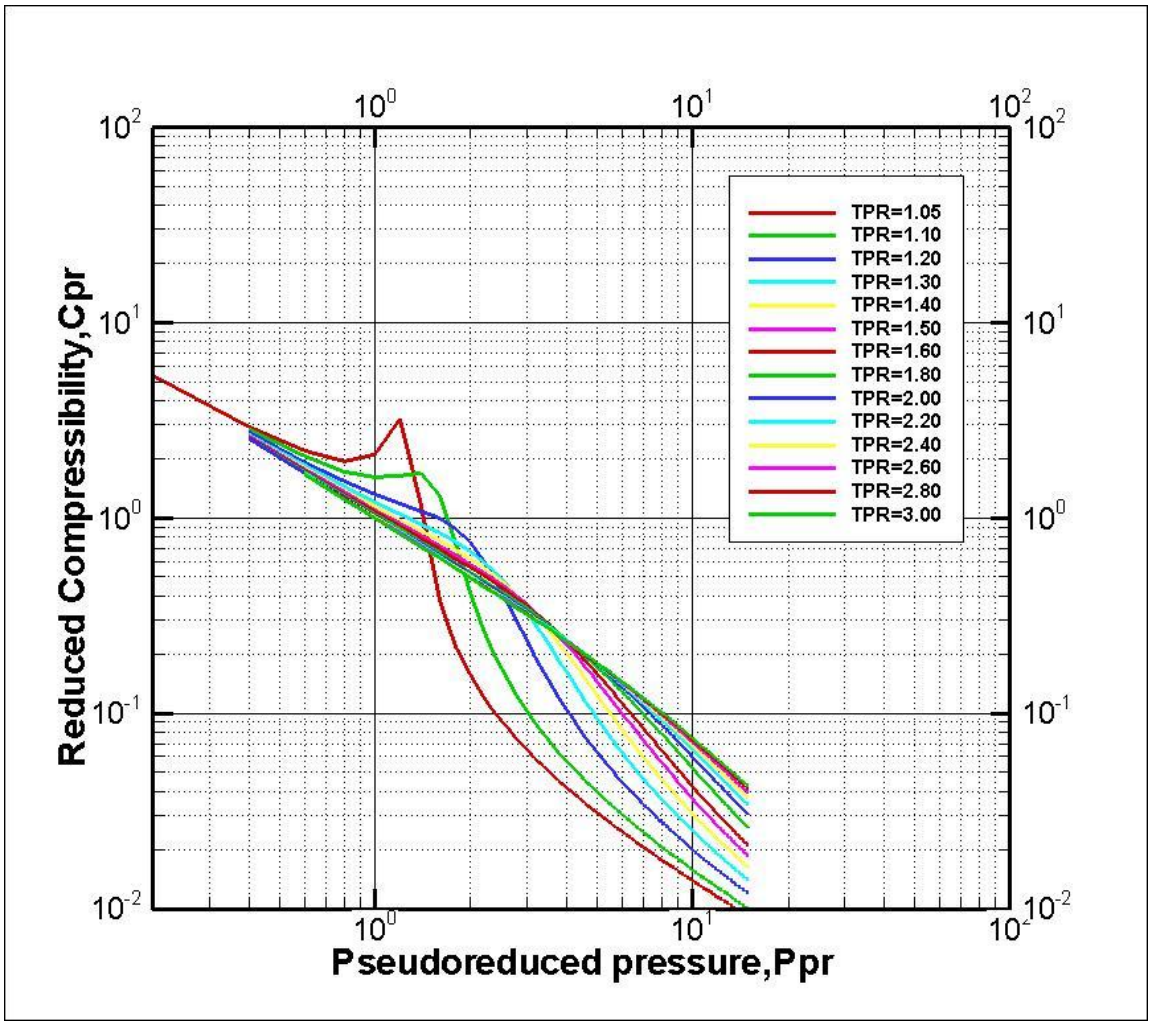

Figure 70 Isotherms of reduced compressibility Vs. reduced pressure curves of pure methane

Gas viscosity

Gas viscosity is frequently estimated through different empirical correlations. Among them, the Lee, Gonzalez, and Eakin (LGE) correlation is widely used in petroleum literature.

After modifying Starling and Ellington correlation (1964), the LGE correlation is proposed by Lee et al. (1966) based on the experimental data of eight samples of natural gas whose specific gravities are less than 0.77. The direct measurement of gas viscosity is conducted on gas samples composed by pure hydrocarbon components; however, the non-hydrocarbon components (or impurities) are not taken into account in this correlation. The LGE correlation expresses the gas viscosity as a function of temperature, gas molecular weight and density at relevant reservoir conditions:

$$\mu_g = 10^{-4} A \exp\left(B\rho_g^C\right) \tag{IV-19}$$

where

$$A = \frac{\left(9.379 + 0.01607M\right)T^{1.5}}{209.2 + 19.26M + T} \tag{IV-20}$$

$$B = 3.448 + \frac{986.4}{T} + 0.01009M \tag{IV-21}$$

$$C = 2.447 - 0.2224B \tag{IV-22}$$

And ρ_g is the gas density (in gm/cc) at specific temperature and pressure; M is the gas molecular weight (in lb/lb-mole); T represents reservoir temperature (in deg R); μ_g is the gas viscosity with unit in cp.

This correlation is quite accurate for gases of specific gravity less than 1.0, with 2% average absolute error at low pressure and 4% average absolute error at high pressure. The correlation is applicable to the pressure range between 100 and 8000 psia and the temperature range between 100 and 340 deg F (Lee et al., 1966). It is proven to be reliable to predict viscosities of gas with low quantities of impurities at common reservoir conditions (Londono et al., 2005). It is inadequate to use this correlation to predict gas viscosities of HPHT reservoir.

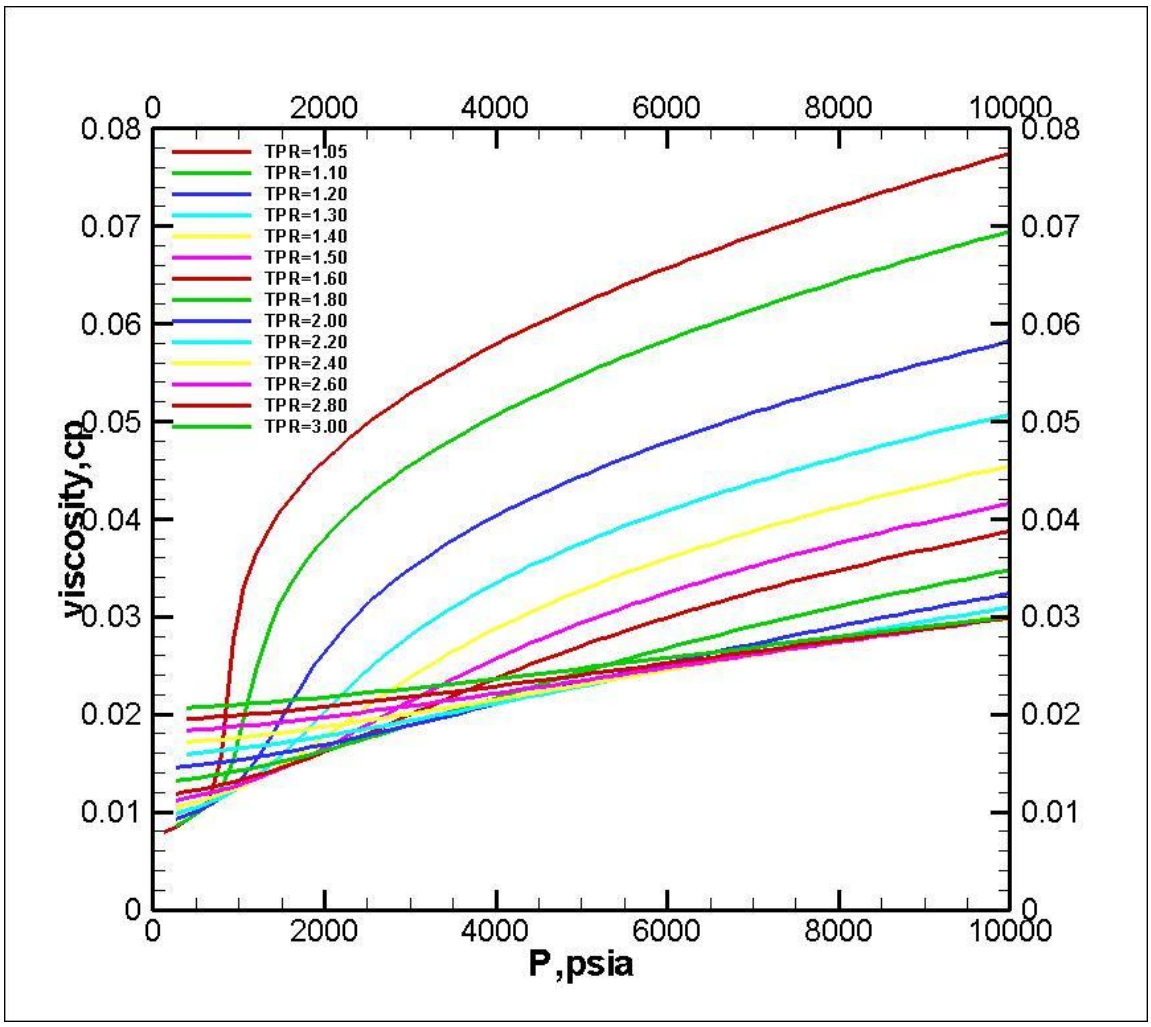

Figure 71 Viscosity of pure methane Vs. reservoir pressure

Pseudopressure

In gas reservoir engineering, the real gas pressure and its corresponding pseudopressure are the two most significant parameters. As the gas properties are not constant with pressure variation, the common method for computing pseudo-pressure is numerical integration (Al-Hussainy et al., 1966) $m(p) = 2\int_{p_1}^{p_2} \frac{p}{\mu(p)Z(p)} dp$ (IV-23)

where p_1 is any arbitrary base pressure (usually standard condition).

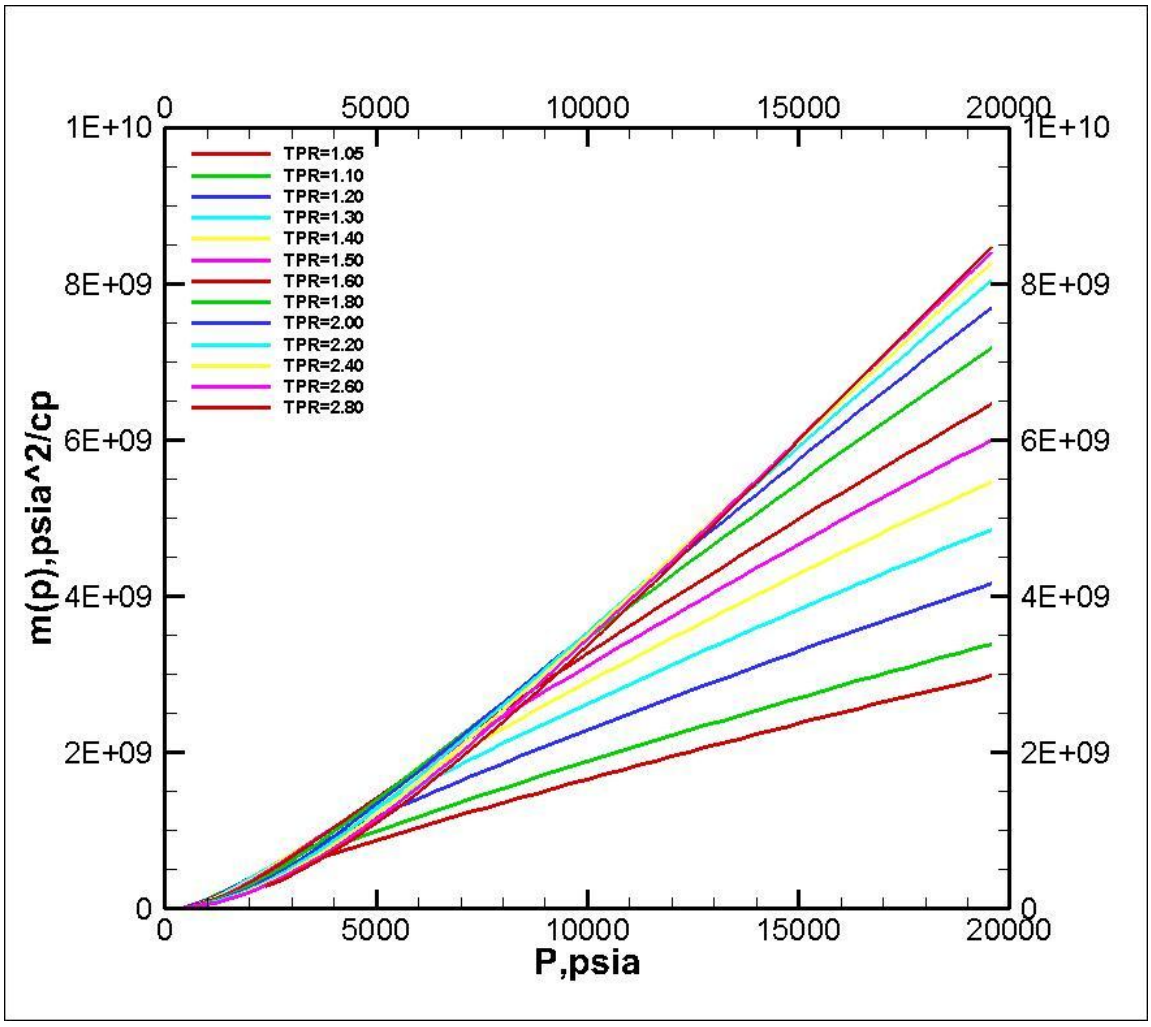

Figure 72 Pseudopressure of pure methane Vs. pressure

Reverse computation

As pseudopressure(m(p)) has no physical meaning, a reverse computation should be run to convert it to its corresponding pressure during reservoir simulation process. Interpolation or table read might be the easiest way to do this job in literature. However, both of them are not feasible or sufficient for an accurate reservoir simulator. For this purpose, the Newton-Raphson iterative method is adopted in this work to realize such conversions. For a given pseudopressure, the reservoir pressure is root of the following equation: $2\int_{p_1}^{p_2} \frac{p}{\mu(p)Z(p)} dp - m(p) = 0$ (IV-24)

For simplicity, this equation can be written as: $f(p) = 0$ (IV-25)

p can be easily evaluated by using the Newton-Raphson iterative method, as what have done for calculating Z factor. The detailed working steps are listed below:

1) make an initial guess of p^i, as $p^1 = \sqrt{\frac{m(p)*0.012}{2}}$ (Al-Jawad, 1997) (IV-26), where i is the number of iteration;
2) replace this value in Eq.(IV-25); some non-zero value $f^i(p^i)$ will be generated unless the correct p^i has been selected in step (1);
3) updated value of p could be determined by:

$$p^{i+1} = p^i - \frac{f^i}{\frac{df^i}{dp}} \quad \text{(IV-27)}$$

where $\frac{df^i}{dp}$ is obtained by differentiating eq.(IV-24) to p

$$\frac{\partial f(p)}{\partial p} = \frac{2p^i}{\mu(p^i)Z(p^i)} \tag{IV-28}$$

where $\mu(p^i)$ and $Z(p^i)$ is computed from subroutine calcGAS which has been discussed before.

4) repeat the step(2) and (3) until the convergence condition is satisfied, as

$$\left|\frac{p^{i+1} - p^i}{p^i}\right| \le 0.001; \tag{IV-29}$$

A FORTRAN subroutine p4mp is written to convert pseudopressure to its corresponding pressure based on the above procedure.

Pressure(psi)	m(p)psi^2/cP	Pressure(psi)	Difference(%)
399.84	5.83.E+06	400.01	0.042
799.68	6.36.E+07	799.93	0.031
1199.52	1.58.E+08	1199.48	0.003
1599.36	2.72.E+08	1599.29	0.004
1999.20	3.89.E+08	1999.23	0.001
2399.04	5.01.E+08	2399.09	0.002
2798.88	6.11.E+08	2798.97	0.003
3198.72	7.17.E+08	3198.85	0.004
3598.56	8.21.E+08	3598.73	0.005
3998.40	9.22.E+08	3998.60	0.005
4398.24	1.02.E+09	4398.43	0.004
4798.08	1.12.E+09	4798.27	0.004
5197.92	1.22.E+09	5198.11	0.004
5597.76	1.31.E+09	5597.94	0.003
5997.60	1.40.E+09	5997.76	0.003

Table 7 Pressure recalculated from pseudopressure

The data in the first column in Table 5 are the input pressure data for subroutine pseudopressure with $T_{pr} = 1.20$ and the data in the second column are the output

corresponding pseudopressure by running subroutine pseudopressure, which should also be the input pseudopressure data for subroutine p4mp.Henceforth, the data in the third column are the recalculated pressure from the pseudopressure after running subroutine p4mp. The different between the original and recalculated values of pressure is limited within 0.05%, as shown in the 4^{th} column in Table 5. The number of iterations for pseudopressure conversions is no more than 4, which means Eq. (IV-24) converges very quickly. Based on the efficiency and accuracy of computational process, this numerical model seems to be capable for simulating gas PVT properties and practically acceptable in gas reservoir engineering.

APPENDIX V

INSTRUCTION FOR FEM

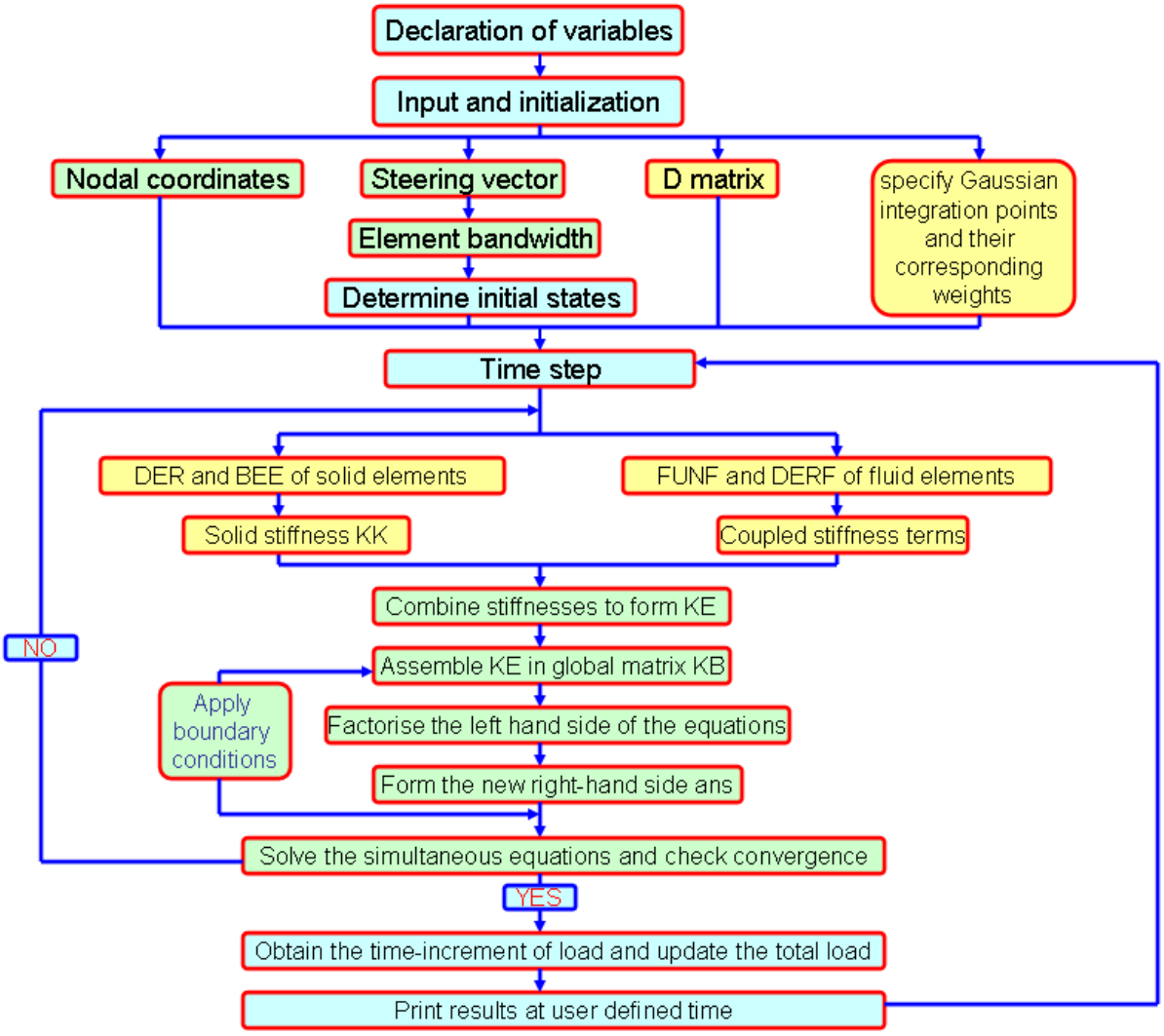

APPENDIX VI

NUMERICAL APPROACH TO CREEP (FEM)

To resemble the basic natures of creep phenomena in viscoelastic medium, inelastic deformations, stress relaxation as well as the weakening of the material strength need to be considered in the mechanical models, either analytical or numerical models. A comprehensive model should be capable of predicting long term deformation and creep behavior of the material regardless of the geometry and the loading history. Obviously, numerical models, as finite element method (FEM) and boundary element method (BEM), are advanced in wide range of applications in simulating creep behavior.

Prior to building the numerical models, a reliable constitutive model need to be constructed or proposed to describe the time dependent deformation associated with creep phenomena. However, no matter which constitutive model is used, the following governing equations should be satisfied:

(1) Strain-displacement relation

$$\varepsilon_{ij} = \frac{1}{2}(u_{i,j} + u_{j,i}) \qquad \text{(VI-1)}$$

Where u_i represents solid displacement vector denoting the movement of the porous medium with respect to a reference configuration; ε_{ij} is the component of strain tensor.

(2) Equilibrium equation

$$\sigma_{ij,j} + f_i = 0 \qquad \text{(VI-2)}$$

Where f_i represents the components of body force; σ_{ij} denotes the component of stress tensor.

In the finite element procedure, The unknowns (u-displacement vector) at any arbitrary point can be approximated by interpolating the variables at nodal points through the following functions (Smith and Griffiths, 1997):

$$\{\mathrm{u}\}=[\mathrm{N_u}]\{\tilde{\mathrm{u}}\} \qquad \text{(VI-3)}$$

where $\mathrm{N_u}$ is the conventional shape function and $\tilde{\mathrm{u}}$ is the vector of the nodal displacement. Based on this approximation, Eq.(VI-1) can be expressed in matrix form:

$$\{\varepsilon\}=[B]\{\tilde{\mathrm{u}}\} \qquad \text{(VI-4)}$$

where B is the strain-displacement matrix and $[B]=[\partial][\mathrm{N_u}]$ with ∂ denoting the differential operator. The expression of B depends on the element type and the formation of the displacement vector.

In matrix form, the stress-strain relationship can be given as generalized Hooke's law:

$$\{\sigma\}=[D]\{\varepsilon\}=[D][B]\{\tilde{\mathrm{u}}\} \qquad \text{(VI-5)}$$

where D is the stress-strain matrix.

In the principle of virtual work (Kim and Kuhlemeyer, 1977; Ghazlan et al., 1995; Zienkiewicz and Taylor, 2000; Chazal and Moutou Pitti, 2011), the sum of the total external and internal virtual work is equal to zero:

$$\delta W_e+\delta W_i=0 \qquad \text{(VI-6)}$$

$$\int_V \{\sigma\}\{\delta\varepsilon\}\,dV = \int_V \{f_V\}\{\delta u\}\,dV + \int_S \{f_A\}\{\delta u\}\,dA \qquad \text{(VI-7)}$$

where $\delta\varepsilon$ and δu denote virtual strain and displacement respectively; f_V and f_A represent volumetric force and surface traction.

By taking the finite element approximation (Eq.(VI-4) and (VI-5)) into the equilibrium equation (VI-7), it yields the following incremental formula:

$$K\Delta u = \Delta R \qquad \text{(VI-8)}$$

where $K = \int_V B^{\mathrm{T}} DB dV$ is the global stiffness matrix; ΔR is the increments of loading vector, including both the external force and resultant internal force. In the elasticity regime, the expressions for K and R are simple and identical in literature. However, for the viscoelastic or creep problems, those expressions vary from case to case.

Roughly, there are two different ways, initial strain and initial stress respectively, to solve the non-linear time-dependent creep problems by using the finite element method (Kim and Kuhlemeyer, 1977).

i) In the initial strain method, the creep strain at any time interval is defined by the stress history through the constitutive laws. The creep strain increments are converted into induced nodal forces and the stiffness matrix is constant within each time interval. In the creep problem, the total strain (ε_T) is composed by two different parts (Gioda, 1981; Naumenko, 2006): elastic (ε_e) and creep (ε_{cr}).

$$\dot{\varepsilon}_T = \dot{\varepsilon}_e + \dot{\varepsilon}_{cr} \qquad \text{(VI-9)}$$

By substituting Eq. (VI-9) into the equilibrium equation (VI-7), the following linear equation can be obtained:

$$K\{\Delta u\} = \{\Delta R\} + \{\Delta f^{cr}\} \qquad \text{(VI-10)}$$

where $\Delta f^{cr} = \int_V [B]^{\mathrm{T}} [D] \{\dot{\varepsilon}_{cr}\} dV$ denotes the internal force induced by creep. In this method, the stress-strain matrix D is kept the same during each time step, and all the creep effect are put into the vector Δf^{cr}, which is also adopted in this work. The detailed expression of vector Δf^{cr} depends on the constitutive model. Within this framework, Gioda (Gioda, 1981) developed the finite element model for creep problems by using a general non-linear viscoplastic rheological law and incorporating the primary, secondary and tertiary creep regime in a cylinder test. Ghazlan et al. (Ghazlan et al., 1995) proposed an incremental formulation by dividing the creep compliance into elastic and inelastic (creep) part and generalized Kelvin model and Laplace transformation were employed to derive the creep part of the compliance. Naumenko (Naumenko, 2006) presented the derivation of FEM formula by taking both thermal and viscoelastic effect into consideration and gave out the explicit time procedure for how to solve the problem numerically. Other than the incremental formula, Naumenko (Naumenko, 2006) derived his formula in full form, thus the vector Δf^{cr} in that work reflected the whole history of the strain. Chazal and Moutou Pitti (Chazal and Moutou Pitti, 2011) proposed an incremental constitutive equation by using a pseudo fourth order tensor for non-ageing viscoelastic materials and then applied the finite element method to discretize the formulation and solve the boundary viscoelastic problems. In this work, the vector Δf^{cr}

is derived step by step by using the Maxwell model and the viscoelastic effect is addressed in both deviatoric and mean effective stresses.

ii) In the initial stress method, the total stress at any time interval is governed by the strain history through the constitutive laws. Thus, both the stiffness matrix and induced internal or pseudo force term are functions of stress state and its change during each time interval. Kim and Kuhlemeyer (Kim and Kuhlemeyer, 1977) applied this method for creep analysis and used the principle of virtual work to derived the following FEM formula:

$$K_E \{u\} = \{P_E\} \qquad \text{(VI-11)}$$

where $K_E = \int_V [B]^T [D(t)][B] dV$; $D(t)$ and P_E are all stress (deviatoric stress) dependent variables during tests and need to be updated within each time step. Anderson and Bridwell (Anderson and Bridwell, 1980) developed a finite element procedure to study the long term thermal creep of materials by following an arbitrary constitutive law. In their model, current stress, instead of initial stress, was used in the creep calculation and the geometry change was taking into account in updating the stress state to predict large deformation. Noriyuki (Noriyuki, 1986) proposed an incremental formulation to investigate the creep deformation of cylindrical shell under axial compression. In his work, it was assumed that the creep remained constant and used as initial strain across a time interval. Zocher et al. (Zocher et al., 1997) presented another finite element algorithm by taking the integral form of the constitutive equations and assumed constant strain rate within a time step to predict both creep and relaxation behavior. And Dirichlet-Prony series was used to represent the relaxation moduli in the integral form.

The procedure to solve the non-linear equations in the FEM procedure is briefly given as below:

(i) Unknowns (u, $m(p_m)$ and $m(p_f)$) from a previous time step are used to "guess" the initial stiffness matrix in current time step;

(ii) In current time step, the FEM formulation is solved to obtain the increment of unknown variables (Δu, $\Delta m(p_m)$ and $\Delta m(p_f)$);

(iii) The newly updated Δu, $\Delta m(p_m)$ and $\Delta m(p_f)$ is used to compute the strain, stress at current time step and then update the fracture aperture, boundary conditions, internal force and stiffness matrix;

(iv) Step (ii) is repeated to get the new Δu, $\Delta m(p_m)$ and $\Delta m(p_f)$ for the next iteration; if Δu, $\Delta m(p_m)$ and $\Delta m(p_f)$ are close enough to those in the presvious iteration, the iteration is terminated and the next time step is proceeded.